Analysis and Control of Variable Stiffness Robots

Author(s):
Petit, Florian Patrick

Publication Date:
2014

Permanent Link:

https://doi.org/10.3929/ethz-a-010404874 →

DISS. ETH NO. 22134

Analysis and Control of Variable Stiffness Robots

A thesis submitted to attain the degree of
DOCTOR OF SCIENCES of ETH ZURICH
(Dr. sc. ETH Zurich)

presented by

Florian Patrick Petit

Diplom-Ingenieur Univ., Technische Universität München

born on 21 September 1982
citizen of Germany

accepted on the recommendation of

Prof. Dr. Robert Riener, ETH Zürich
Prof. Dr. Jonas Buchli, ETH Zürich
Prof. Dr. Alin Albu-Schäffer, Technische Universität München

2014

Contents

Acknowledgements

First of all, I would like to thank my supervisors Alin Albu-Schäffer and Robert Riener. Without their kind support this thesis would not have been possible. I am very thankful for the chance to work at the Institute of Robotics and Mechatronics of the German Aerospace Center. Likewise, the atmosphere at the Sensory-Motor Systems Lab at ETH Zurich was always refreshing and opened up many new perspectives. I am also grateful that Jonas Buchli agreed to join my committee.

Furthermore, I want to thank all my colleagues who supported this work. Foremost these are the people of the DLR Hand Arm System team, Dominik Lakatos, Werner Friedl, Alex Dietrich, Maxime Chalon, and David Braun who are great collaborators and researchers. I also like to thank my students Reinhard Neureiter, Andreas Daasch, and Matthias Meiner for their contributions and trust in me as a supervisor.

Finally, I am deeply grateful to my family for their never-ending support in all my endeavors, and to my love Julia.

Munich, July 2014

Abstract

This dissertation addresses the analysis and control of variable stiffness actuated robots aiming at precise, sensitive, robust, and dynamic interaction with their environment and especially humans. The focus is the adjustment of impedance properties, namely adjusting the robot equilibrium position, the stiffness, and damping. Highest demands are met by the development of new control concepts and the transfer of state-of-the-art techniques from related fields.
Physical interaction is a common task of robotic systems. Aiming at providing service and support for humans, robots need to be able to collaborate with humans and in human environments. The ability to perceive the surrounding and react in a sensitive way is a key factor for robots. Another one is the role of mechanical compliance as it allows to attenuate contact forces and both the environment and the robot can be protected. A step towards this goal is the class of torque controlled robots, where active control generates the compliant features using joint torque sensory information. A further advancement of this technology are the recently developed variable stiffness (VS) robots. There, a main feature is the deliberate introduction of a mechanically variable, elastic element in the robot joints. This passive spring provides the desired compliance properties: it increases the mechanism robustness by absorbing shock impacts and its energy storing capabilities allow to achieve highly dynamic motions. Additionally, the spring stiffness can be adjusted and thereby, the robot can be tuned to the task on a mechanical level. A further important property of the elastic elements is its joint torque sensing capability.
In this work new control methods are developed and combined with well-established techniques to exploit the full potential of variable stiffness robots. The research has been conducted at the Institute of Robotics and Mechatronics of the German Aerospace Center (DLR), where an integrated variable stiffness robot, the DLR Hand Arm System, has been developed. An introductory part of this thesis is dedicated to the analysis and modeling of variable stiffness actuators (VSA) which is a basis for the later controller designs. An abstract dynamic model is presented describing the variable stiffness actuators and the integration in the multi-joint robot system. The properties of the model and the nonlinear and varying elastic elements are elaborated. To further deepen the actuator understanding, the bidirectional antagonistic variable stiffness (BAVS) setup is evaluated in a case study. Furthermore, the functionality of the BAVS joint and torque and stiffness properties are analysed. Major results are the existence, transition, and stiffness properties of a helping mode, which allows to fully exploit the torque capabilities of the joint. An analytical model of this mode is developed, which facilitates analysis and design of the joint's stiffness properties. This model is used to synthesize cam disc-based BAVS setups, which are evaluated in experiments. Such, an insight into VS joint design and realization is given and additionally a contribution to actuator development is provided.
The major part of this thesis is dedicated to the development of control algorithms to adjust the impedance properties of robots. The impedance control formulation is a main reason for the success of torque controlled robots. It allows to solve many tasks in an intuitive manner by providing flexible adjustment of the properties of the robot such as equilibrium position, stiffness,

and damping. To proof the general capability of variable stiffness actuated robots, it is considered to be of fundamental importance to be able to adjust their impedance parameters. Three prime control objectives are intended. The first task is end-effector position regulation. Advanced control methods are required as the joint elasticities deflect under gravitational load resulting in positioning inaccuracy of the end-effector. Additionally, the separation of the motor and link by the elastic element leads to a non-collocation of the control input and measurement output and hardens controller design. Here, an energy-based controller is adapted which is able to cope with the joint properties such as elasticity and nonlinearity and provides precise, quasi-static link side position control. The flexibility of the method regarding task coordinate choice is a benefit as it simplifies and broadens the controller applicability. The second impedance control objective is to tune the robot stiffness to the task. It is a distinct feature of variable stiffness actuators to adjust the joint stiffness on a mechanical level. The performance of the mechanical tuning capability of multi-joint VSA robots is analysed respecting the limitations given by the joint-wise actuator mounting and the bounded stiffness variation range. This allows to formulate two approaches to exploit the stiffness capability where one method combines active impedance control with the passive joint stiffness. The second method relies on configuration adjustment to vary the end-effector stiffness. In both cases it is aimed to provide flexible stiffness adjustment on the one side and mechanical robustness and energy storage on the other side. The third impedance control task is the control of the robot damping. The low damping of variable stiffness joints is the basis for the torque measurement and dynamic capabilities of VSA robots, but active damping injection by control is required for most manipulation tasks. Three damping control approaches with different properties are presented. First, a backstepping method allows the theoretical treatment of noisy sensor signals. Second, a state feedback controller with physically motivated gain design matched to the robot shows excellent performance and robustness. Third, a state-based approach requires only minimal model knowledge. Summarizing it can be said, that using the presented techniques the excellent performance of the impedance control methods known from classical state-of-the-art robots is available for variable stiffness actuated robots. Additionally, this new class of systems adds beneficial properties that are not covered by classically designed manipulators. An outlook into methods exploiting the dynamic capabilities of variable stiffness actuators is provided by an approach to excite oscillatory motions.

An emphasis of this work is the thorough evaluation of the developed methods on a real robotic system. Most of the methods are therefore tested on the DLR Hand Arm System and in few cases on a bidirectional antagonistic variable stiffness actuator test rig. The obtained results prove the capability of the methods and the variable stiffness setup and clarify their contribution towards the development of a versatile service robotic system.

Kurzfassung

Diese Dissertation behandelt die Analyse und Regelung von Robotern mit einstellbarer Gelenksteifigkeit, die das Ziel haben präzise, feinfühlig, robust und dynamisch mit ihrer Umgebung und vor allem Menschen interagieren zu können. Der Fokus liegt auf der Anpassung der Impedanzeigenschaften des Roboters wie der Gleichgewichtsposition, der Steifigkeit und Dämpfung. Durch die Entwicklung neuer Regelungkonzepte und dem Transfer von modernen Techniken werden hierbei höchsten Anforderungen erfüllt.
Die Interaktion mit der Umwelt ist eine übliche Aufgabe für Robotersysteme. Mit dem Ziel Serviceaufgaben für Menschen zu erledigen, müssen Roboter mit Menschen und in menschlichen Umgebungen arbeiten können. Hierfür sind die Fähigkeiten die Umgebung wahrnehmen zu können und in einer feinfühligen Art und Weise reagieren zu können Schlüsselfaktoren für Roboter. Eine wichtige Rolle spielt auch die mechanische Nachgiebigkeit durch die Kontaktkräfte abgemildert werden können und somit die Umgebung und der Roboter geschützt werden können. Ein Schritt in diese Richtung stellt die Klasse der drehmomentgeregelten Roboter dar, bei der die Nachgiebigkeitseigenschaften durch aktive Regelung und Drehmomentsensoren erreicht wird. Eine neuartige Weiterentwicklung dieser Technologie sind Roboter mit variabler Gelenksteifigkeit (VS Roboter). Das Herausstellungsmerkmal sind hier die variabel elastischen Elemente in den Robotergelenken. Diese passiven Federelemente erzeugen die gewünschten Nachgiebigkeitseigenschaften: Kraftspitzen können abgefedert werden und dadurch wird die Systemrobustheit erhöht, und die Energiespeicherung kann zur Erzeugung von hochdynamischen Bewegungen genutzt werden. Zusätzlich erlaubt die Verstellbarkeit der Steifigkeit die mechanische Anpassung des Robotersystems an die gestellte Aufgabe. Eine weitere wichtige Eigenschaft der Federelemente ist die mögliche Drehmomentschsätzung.
In dieser Arbeit werden neuartige Regelungsmethoden entwickelt und mit modernen Techniken kombiniert um das Potenzial von Robotern mit einstellbarer Gelenksteifigkeit voll ausnutzen zu können. Die Forschungstätigkeit wurde am Institut für Robotik und Mechatronik des Deutschen Zentrums für Luft- und Raumfahrt durchgeführt, wo ein integriertes Robotersystem mit einstellbarer Gelenksteifigkeit, das DLR Hand Arm System, entwickelt wurde. Der Erste Teil dieser Arbeit behandelt die Analyse und Modellierung von Gelenken mit einstellbarer Steifigkeit (variable stiffness actuator, VSA), und stellt die Basis für die späteren Reglerentwicklungen dar. Hierin wird ein abstraktes Robotermodell vorgestellt, das die VSA Gelenkmodule selbst und deren Integration in das Robotersystem beschreibt. Die Eigenschaften des Modells und der nichtlinearen und veränderlichen elastischen Elemente werden ausgearbeitet. Um ein tiefergehendes Verständnis von Antrieben mit einstellbarer Steifigkeit zu erlangen, wird das bidirektional antagonistische Gelenk (BAVS) in einer Fallstudie untersucht. Dazu wird die Funktionalität und die Drehmoment- und Steifigkeitseigenschaften analysiert. Ein herausragendes Ergebnis ist die Identifikation eines 'helfenden' Modus und dessen Übergangs- und Steifigkeitseigenschaften, der es erlaubt die Drehmomentmöglichkeiten des Gelenkes voll auszunutzen. Es wird ein analytisches Modell entwickelt, das es ermöglicht die Steifigkeitseigenschaften des Gelenks zu analysieren und

zu entwerfen. Dieses Modell wird dann verwendet um Kurvenscheiben-basierte BAVS Gelenke zu entwerfen und in Experimenten zu untersuchen. So können tiefergehende Einblicke in den Entwurf von VS Gelenken gewonnen werden also auch ein Beitrag zur Antriebsentwicklung geleistet werden. Der Hauptteil dieser Arbeit befasst sich mit der Entwicklung von Regelungsalgorithmen zur Einstellung der Impedanzparameter des Roboters. Die Formulierung des Impedanzregelgesetzes ist ein Hauptgrund für den Erfolg von drehmomentgeregelten Robotern. Durch dieses Regelgesetz können viele Aufgaben in einer intuitiven Art und Weise gelöst werden, da Eigenschaften wie Gleichgewichtsposition, Steifigkeit oder Dämpfung des Roboters flexibel angepasst werden können. Um die Leistungsfähigkeit von Robotern mit einstellbarer Gelenksteifigkeit zu zeigen, wird die Möglichkeit die Impedanzparameter einzustellen als grundliegend wichtig eingeschätzt. Drei Impedanzregelaufgaben werden betrachtet. Die erste Aufgabe ist die Positionsregelung des Endeffektors. Fortschrittliche Regelungsmethoden sind hierfür notwendig, da sich die Gelenkelastizitäten im Gravitationsfeld längen und zu Positionsungenauigkeit führen. Zusätzlich führt die Trennung von Motor und Abtrieb durch das elastische Modul zu einer nichtkollokiertheit des Antriebs und Messausgangs, das den Reglerentwurf weiterhin erschwert. Um diese Eigenschaften auszugleichen wird in dieser Arbeit ein energiebasiertes Regelgesetz angewendet, das quasi-statische Positionsregelung ermöglicht.
Die zweite Impedanzregelaufgabe ist die Gelenksteifigkeit der Roboteraufgabe anzupassen. Ein Herausstellungsmerkmal von Antrieben mit einstellbarer Gelenkelastizität ist der mechanische Eingriff auf die Gelenksteifigkeit. Daher werden die Auswirkungen dieses Stelleingriffs auf die resultierende Robotersteifigkeit unter Berücksichtigung der baubedingten Begrenzungen untersucht. Es werden zwei Methoden vorgestellt, wobei in der einen aktive Impedanzregelung mit der passiven Gelenksteifigkeit kombiniert wird. In der anderen wird die Roboterkonfiguration zur Steifigkeitsverstellung verwendet. Beide Methoden zielen darauf ab eine flexible Steifigkeitseinstellung zu gewähren und gleichzeitig mechanische Robustheit und Energiespeicherung zu ermöglichen. Die dritte Impedanzregelaufgabe ist die Dämpfungsregelung des Roboters. Geringe Gelenksdämpfung ermöglicht einerseits die Gelenkdrehmomentschätzung und dynamische Bewegungen, erfordert jedoch aktive Schwingungsunterdrückung für die meisten Manipulationsaufgaben. Drei Ansätze zur Dämpfungsregelung werden vorgestellt. Ein erster Ansatz basiert auf einer Backstepping-Methode und erlaubt die theoretisch korrekte Behandlung von rauschbehafteten Signalen. Ein zweiter Ansatz verwendet komplette Zustandsrückführung und einen Algorithmus um die Verstärkungsfaktoren physikalisch motiviert auszulegen und ermöglicht hervorragende Effektivität und Robustheit. Ein dritter Ansatz bedarf nur eines minimalen Robotermodells. Zusammenfassend kann gesagt werden, dass durch die entwickelten Impedanzregelungsmethoden Robotern mit variabler Gelenksteifigkeit eine vergleichbare Leistungsfähigkeit wie bekannte moderne Roboter erreichen können. Zusätzlich ermöglicht diese neue Systemklasse weitere Fähigkeiten, die über die klassischen Roboter hinausgehen. Anschließend folgt noch ein Ausblick in eine Methoden, die die dynamischen Eigenschaften von variabel elastischen Gelenken ausnutzt und oszillatorische Bewegungen anregt.
Ein Schwerpunkt dieser Arbeit ist die umfangreiche Erprobung der entwickelten Methoden auf

einem robotischen System. Die meisten Methoden wurden auf dem DLR Hand Arm System getestet und in einigen Fällen wurden Untersuchungen auf einem bidirektionalen antagonistischen Testsystem durchgeführt. Die Messergebnisse zeigen eindrücklich die Leistungsfähigkeit der entwickelten Methoden und generell von Robotern mit einstellbaren, elastischen Gelenkantrieben und verdeutlichen deren Beitrag zur Weiterentwicklung von vielfältig einsetzbaren Robotersystemen.

1. Introduction

1.1. Motivation and Problem Description

Robotic systems find application in many areas today. Well known is the industrial field, where robots execute tasks which require high accuracy, fast execution cycles, or the handling of heavy objects. The production line in a car factory is such an example, where handling and welding tasks are performed. There, robots operate in separated areas and execute fixed motion patterns programmed by an expert in advance. In general the jobs of such robots can often be described by the three Ds, which are tasks that are dull, dangerous, or dirty. The robots are accordingly built to withstand such harsh conditions which reflects in their look and feel.
The digital revolution of the recent years led to a flooding of highly integrated electronic devices in everyday life. Various types of sensory information and enormous computation power are omnipresent. Robotic systems can benefit from this advancement in the way that they are able to gather and process information regarding their surrounding. Together with the development of advanced control and artificial intelligence methods an often envisioned perspective may become reality: robots aim to act in an intelligent way, where decisions are made autonomously considering and reflecting multiple modalities to achieve a certain task. Such tasks may go beyond the mentioned three Ds and require robots to do "jobs that require memorization, keen perceptual skills, and service-orientation", as it also expected by non-specialists [1]. There, robots act hand in hand with humans and cooperate with people rather than work in place of people. One important cornerstone for this goal is the ability of robots to interact with their environment, especially with humans. Physical interaction requires a robot technology that is able to act and react in an aware and appropriate way to its surrounding, be it in an active or a passive way.

1.1.1. Soft Robotics

A purely geometric perspective, where paths and relationships are specified in a geometric manner, is sufficient to describe many robotic tasks. Such an approach requires a structured and predictable environment, where interaction is known in advance. This prerequisite is often not given for physical interaction tasks with humans or in dynamic environments. In these scenarios deviations between the geometric model and the reality arise, which have to be accounted for. A reliable approach to handle geometric deviations, and thereby physical interaction, is the deliberate introduction of compliance [2]. Compliant behaviour is defined as a force reaction due to

acting motions, here. This elasticity is beneficial for interaction as it allows to overcome position inaccuracy. If a rigid manipulator comes into contact with another rigid object high contact forces result, possibly harming the robot or its environment [3]. If the manipulator acts compliantly, the robot will deflect during interaction and the arising forces are limited. The robotics community is well aware of the beneficial properties of compliance and associated the term *soft robotics* to describe the capability to interact performant and safe with the environment, likewise humans and objects [4]. Soft robotics has been explored on multiple levels. One way of introducing compliance is by using passive elastic elements, like mechanical springs or pneumatic systems [5, 6]. An example is the remote center of compliance (RCC) [7]. It provides a passive elasticity implemented by spring elements at the end effector of a rigid robot. Typical applications are insertion tasks such as peg-in-hole [8]. Another way of realizing compliant behaviour is by an active compliance. This approach finds application in robots which are equipped with torque sensors in the robot joints. Torque sensory information is fed back in a control loop to generate the compliant behaviour artificially [9]. In particular the impedance control formulation [10] is very popular and provides an intuitive interpretation: the controlled robot behaves like a mass-spring-damper system. The torque control technology shows great success, both in the research community [11, 12] and in industrial applications [13, 14, 15].
Both approaches have considerable advantages. Elastic elements provide mechanical energy storage and thereby enable dynamic behaviour and mechanical robustness. Active compliance generated by feedback controllers shows great adaptability regarding stiffness adjustment or choice of task coordinate frame [10, 16]. An approach to integrate the best of both methods is variable stiffness actuation which will be discussed in the following.

1.1.2. Variable Stiffness Actuation

The variable stiffness actuator (VSA) technology is an advancement of the flexible joint technology of torque controlled lightweight robots (LWRs) [12]. The joints of the LWRs show a mechanical compliance originated mainly by the gear boxes and the torque measurement devices, resulting in a stiffness around $10000-20000\,\mathrm{Nm/rad}$.[1] The soft robotic features are realized by control. Prominent examples are active damping control of the lightweight robot structure [18], Cartesian impedance control [19], or collision detection and reaction [20]. The mechatronic limitations (given by the control system, sensors, actuators, etc.) result in commanded Cartesian task stiffness in the range of $0-5000\,\mathrm{Nm/rad}$ [21]. The variable stiffness technology in contrast aims at implementing some of the soft robotic features on a mechanical level [4]. Such, the arm joint stiffness is ranging in between $50-850\,\mathrm{Nm/rad}$ for the robot used in this work, more than one order of magnitude lower than flexible joints of the LWR. Furthermore an additional actuator is introduced as not only the joint position/torque has to be set, but also the joint stiffness itself. A key factor enabling the advantages is the separated structure, where the motor is detached from the link by the elastic element. It provides a certain decoupling whereby the individual

[1] Please remark that the joint stiffness of classical industrial robots is around $10^5\,\mathrm{Nm/rad}$ [17].

properties of the two subsystems can be exploited. The main goals and advantages of the VSA technology are:

- **Mechanism robustness.** The mechanism robustness with respect to external impacts can be increased as the link mass and joint elasticity yield a mechanical low pass filter. This is especially relevant for fragile[2] mechanisms as fingers of robotic hands, where rigid impacts occur on a regular basis [22].
- **Increased dynamic performance and energy efficiency.** The ability to store mechanical energy can be exploited to overcome motor velocity limitations. Advanced dynamic capabilities like throwing can be achieved [23]. Some legged robots [24] exploit this fact, too. Additionally, it can be used to increase the energy efficiency during repetitive motion tasks [25].
- **Task adaptability.** The variability of the stiffness characteristics allows to adapt the system to tasks on a mechanical level. For this so-called task embodiement [26], the joint stiffness is tuned such that minimal active control influence is necessary to achieve a task.

The separated structure is also given for flexible joint robots - even though in an attenuated form. There, the elasticity is provided mainly by the gearbox and strain gauges (or similar technology). While the former is parasitic, the latter is introduced intentionally and used for torque measurement: the resulting microscopic deflection is measured by an electric or optic device. Based upon the known material properties the deflection is then correlated to applied forces. Hooke's law $F = k\Delta x$, with the force F, the spring characteristics k and the relative deflection Δx, describes the situation in a basic configuration.
The similar setup of the variable stiffness technology enables torque sensing as well. Elementary are the deliberate introduction of the compliant element and certain preconditions for the system. The torque measurement is realized by a deflection measurement of the elastic element and the known elastic displacement characteristic. The difference to strain gauge torque sensors is the macroscopic displacement in the millimeter or centimeter range. Furthermore, while Hooke's law involves a linear relation between torque and displacement, variable stiffness actuators may have a nonlinear relation $f : F = f(\Delta x)$. This does not hinder the measurement principle, as long as the mapping f is known. An important precondition to enable this torque measurement is a preferably ideal spring characteristics, with as little friction as possible. Any friction effects render the torque estimation more difficult and require a more complex model or prohibit a precise estimation at all. Therefore, high efforts are undertaken to realize variable stiffness actuators enabling high quality joint torque estimation.
Besides of the added value, the separation and nonlinear elastic elements rise additional effort and pose a robotic problem par excellence. Mechanism- , electric- , and control design have to be well-matched to each other to provide the desired performance. One has to keep in mind that the joint torque dynamics and the link side dynamics are in the same frequency range. The

[2]Objects are considered to be fragile, if forces in contact situations are in the range of their nominal forces.

spring nonlinearity and motor- and link dynamics depict a complex system and need careful and precise control. The goal of the control algorithms is to exploit this structure in a beneficial way and simultaneously reduce the downsides.
The similarity of flexible joints and variable stiffness joints immediately suggests the use of similar control methods. Indeed, efforts of the community attest such an approach [27, 28, 29]. The goal of this thesis is the adaptation and development of several controllers for variable stiffness actuated robots, as stated in more detail in the following section.

1.2. Problem Statement

The variable stiffness actuator technology promises several advantages. A main goal is to perform well in classical applications solved by flexible joint and rigid joint robots. Many of such tasks can be successfully approached by the ability to adjust the impedance behaviour of a robot. A main difficulty of the control of the impedance parameters of VSA robots is the dynamics introduced by the separation of motor and link side and the nonlinear elasticity. The goal of this thesis is to tackle this problem and can be subsumed to adjust the impedance behaviour of multi-joint VSA robots (see also Fig. 1.1):
First, it is desired to adjust the link equilibrium position. This is required to adjust the pose of the robot for manipulation or handling tasks. A main difficulty is the deviation of the elastic elements under gravity load. It is convenient to be able to freely choose intuitive task coordinate systems, such as Cartesian coordinates.
Second, the robot stiffness needs to be adjusted to the task. Following the embodiment design idea to tune mechanical joint properties, this is preferably achieved by changing the passive elasticity. The mechanical limitations and joint wise deployment impose restriction on this approach. Torque controlled active compliance may overcome these limits and enables the well known zero stiffness case, where the robot mass is gravity compensated.
Third, variable stiffness robots show low intrinsic damping of the nonlinear elastic element. Controlling an appropriate damping value is a key factor for the safety, performance, and success of interaction tasks.
A further aim is to exploit the dynamic capabilities provided by the elastic joint elements. Therefore, exciting oscillations of elastic robots in a controlled way is desired.
Precise robot modeling is fundamental for mathematical system understanding. The control goals can be tackled with controllers of different levels of model knowledge. A particular solution may be chosen depending upon the robot setting.
This outlines some of the control problems of variable stiffness actuators which are approached in this thesis. Main challenges are the multi-dimensionality of the robot system, the nonlinear robot dynamics, and the nonlinear VSA characteristics which shows low intrinsic damping.

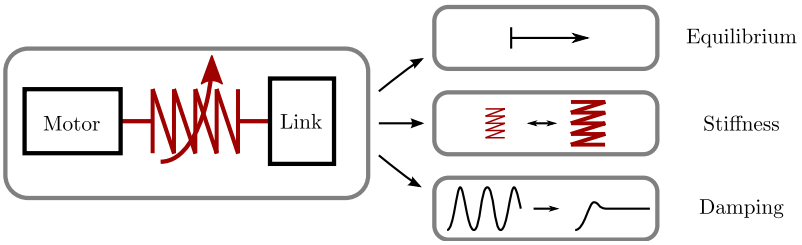

Figure 1.1.: An overview graphics of the different controllers developed. Basic task execution requires the adjustment of the link side equilibrium position, the damping properties and the stiffness properties.

1.3. Related Work

An overview of the research on compliant actuators and robots is provided in the following. While we focus mostly on electro-mechanical actuators, it is to mention, that technological solutions range from hydraulic [30] and pneumatic [6] [31] to unconventional ideas like electro-active polymers [32] or carbon nanotubes [33].
The idea of adjusting impedance parameters [10] of robots on a mechanical level has been researched by several groups in the 90s. Such, a 'programmable' mechanism has been described by Laurin-Kovitz et al. [5]. Besides of theoretical results, a prototypical implementation of a joint mechanism with mechanically variable springs and dampers has been presented. Morita and Sugano objected the beneficial properties of passive impedance for the use in grasping applications [34]. Leaf springs and brakes have been integrated in a finger mechanism to ensure soft grasping. A 1-DoF testbed of such a finger has been build and used for experimental validation of the ideas. This research on mechanical impedance for grasping has led to the development of a seven DoF robot, called MIA ARM [35]. The authors mention the advantage of high compliance similar to force controlled robots, and the need for high tracking performance. The stiffness and tracking performance of the prototype passive elastic arm is evaluated in experiments.
Biology has motivated the development of antagonistic joint actuators. A setup using spring elements to imitate the compliance of the skeleto-muscular system has been described by Koganezawa et al. [36]. It is shown, that a nonlinear stiffness profile is necessarry to vary the joint stiffness. In a later work, a control scheme to independently control stiffness and position of an antagonistically driven, multi DoF robot joint is presented [37]. Another antagonistic actuator which is able to control stiffness and motion has been developed by English and Russel [38]. Independence of joint deflection and stiffness on a mechanical level has been a focus and a nonlinear (quadratic) stiffness profile fulfilling the requirement has been found.
In the work of Okada et al. the performance increasing properties of a programmable passive compliance mechanism are evaluated [39]. A shoulder joint mechanism is designed able to be mechanically programmed to a task (ball throwing). Bicchi et al. are examining the role of

programmable passive compliance for safety in human robot collaboration [40]. They designed a 3 DoF arm using pneumatic McKibbon actuators to change the stiffness properties. In a subsequent work of Bicchi et al. the field of performant yet safe robot joints is treated [41]. Among other possibilities variable stiffness transmission (VST) and variable stiffness actuation (VSA) is considered to be an alternative able to achieve these goals. The class of such actuators can be summarized as variable impedance actuators (VIA). In the following years, many research groups developed a variety of variable impedance actuators.

Hurst et al. [42] designed a variable stiffness actuator for highly dynamic legged locomotion. A prototype was constructed and the desired properties of variable stiffness and low damping/high energy efficiency are evaluated in experiments. The group of Prof. Bicchi designed several VSA actuators using electric motors and variable transmissions to achieve a nonlinear spring behaviour [43, 28]. The latter paper presents the realization of an extended antagonistic scheme, the bidirectional antagonism, first described in [44]. A simple mechanical setup still guaranteeing independent stiffness and equilibrium position control is realized in the MACCEPA designs by Van Ham and Vanderborght with their co-authors [45, 25]. A planar cam disc mechanism modulates a linear spring to achieve a nonlinear stiffness characteristics. The joint setup is popular among many research groups due to its ease of reproducability. Highly integrated and powerful variable stiffness joints have been developed at the German Aerospace Center (DLR) [46, 47, 48]. The focus here is high integration while providing low damping and the desired active stiffness variation capability. A key element for their dense mechanical packing is the incorporation of a Harmonic Drive gear. A systematic classification of the design choices to build VSAs using Harmonic Drive Gears has been described in [49].

A VSA based on the lever arm principle with a variable fixation point to modulate stiffness is developed by Jafari et al. [50]. The obtained stiffness characteristics is close to be linear. While most groups focus on building variable stiffness actuators, Laffranchi et al. [51] suggested an actuator with variable passive damping. The stiffness characteristic of the actuator is similar to a constant spring series elastic characteristic [52] with similar drawbacks. The topic of energy efficient stiffness variation has been researched at the University of Twente. Following an analysis and design framework [53], a rotational variable stiffness actuator has been developed [54].

The mechanical robustness properties of VSA as needed in robotic hands are exploited by Grebenstein in [55, 22].

The publications [56, 57, 58] give a further overview of the field of variable impedance actuators. It can be concluded, that the basic functionality of the joints is similar and the main differences are related to mechanical solutions for adjusting stiffness, damping, and position.

Many of the mentioned joint technologies have been implemented in multi-joint robots, where active or passive compliant systems can be distinguished. In the class of active compliant systems, the most successful system (in manufactured units) is the Light Weight Robot (LWR) III [12], developed at the German Aerospace Center and now commercialized by KUKA Roboter GmbH [15]. Another well known torque controlled robot is the Robonaut R2 from NASA [59]. A whole generation of robots has been developed at MIT, where series elastic actuators (SEA) have been

used as joint actuators. The upper body system COG [60] was the starting point and DOMO [61] is the latest member of robots developed at the university before the developments lead to a commercialization by MEKA Robotics [62] and the MEKA Arm 2. A further industrial robot based upon the SEA joint technology is the robot BAXTER [63]. Continuous research on compliant robotic arms and torsos has been conducted in the Sugano Laboratory at Waseda University. Developments are the robot Wendy [64] with its two MIA Arms [35] equipped with variable stiffness actuators [34]. An advanced version called TWENDY-ONE has been recently presented [65] where a passive elastic joint actuator including a visco-elastic damper is used [66]. Active and passive compliant systems have been developed at IIT, where prominent systems are the quadrupedal walking machine HyQ [30], the humanoid robot iCub [67] (both active compliant) and the robot COMAN [68] (passive compliant). Furthermore, a compliant robot arm with variable damping has been developed [69]. Last but not least we want to point out the developments of variable stiffness actuated robots at the German Aerospace Center, where the work described in this thesis was conducted. Besides of the several VS actuators which have been designed and evaluated at the institute, an integrated robotic arm has been constructed based upon some of the concepts [70]. This system is used for the evaluation and experimental validation of the control concepts presented in this thesis.
This is an outline of systems developed in the field. Further literature is referred to in the relating chapters.

1.4. Thesis Outline and Contributions

1.4.1. Organization

Motivated by the problem formulation the organization of this work is sketched in Fig. 1.2. The details of the chapters are given in the following.

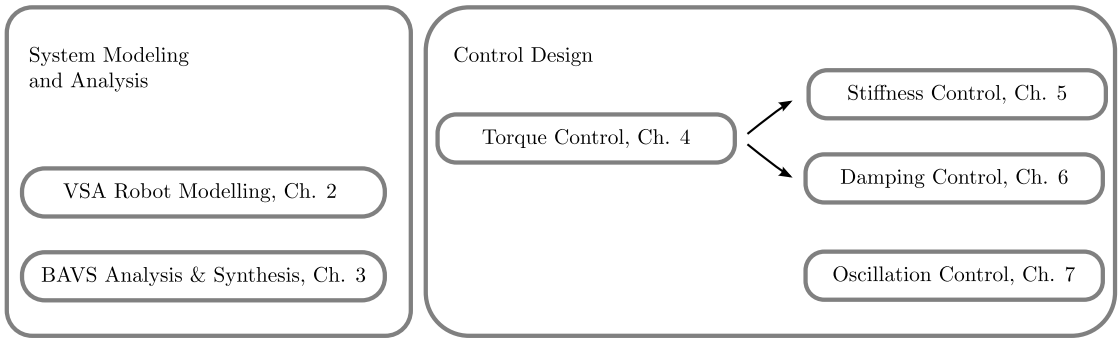

Figure 1.2.: Thesis overview.

An introduction to variable stiffness robot modeling is given in **Chapter 2**. The modeling approach is fundamental for the designs and analyses in the subsequent sections. Important

properties of variable stiffness actuators are provided. A typical variable stiffness robot as used for the experimental validation is presented.
An in detail case study of a variable stiffness actuator setup, the bidirectional antagonistic variable stiffness joint, is given in **Chapter 3**. The basic functionality is discussed along with torque and stiffness properties of the joint. Furthermore, implementation details and experimental measurement data are provided.
Two torque controllers, well known from flexible joint robots, are adapted to variable stiffness robots in **Chapter 4**. They can be interpreted as shaping of the potential and kinetic energy of the robot. Such, the equilibrium position of the underactuated system and its dynamic performance can be adjusted. The formulation allows for flexibility regarding the task coordinate frame, which allows to formulate a Cartesian impedance controller. The controllers depict a basis for several of the following control approaches.
An analysis of the achievable Cartesian stiffness range depending upon the robot joint stiffness and nullspace optimization is presented in **Chapter 5**. To fully benefit from the robot stiffness potential the combination of feedback control with the passive joint stiffness is investigated in detail. Furthermore, a nullspace stiffness controller is discussed.
Elastic joint elements show low damping. Interaction tasks may induce disturbances, which lead to unwanted oscillatory motion. To suppress the oscillations, active damping control is a powerful solution, as discussed in **Chapter 6**. Three different controllers are included ranging from high performance model-based to requiring minimal model- and state information.
In the last technical section **Chapter 7** the dynamic properties of variable stiffness actuators are addressed. It is shown how damping is connected to stimulating oscillations in a flexible system.

1.4.2. Publications

The author of this thesis has been first author and co-author of several scientific publications, see Appendix B. Original content of the author in these publications (text, graphics, etc.) has been partly used in this thesis. The exact publications are cited in the corresponding sections. These works may be subject to copyright protection.

2. Setup and Modeling of Variable Stiffness Robots

A fundamental basis of robot control is a proper understanding of the robotic system. Analytic models enable this understanding and are a key factor in control design as presented in this thesis. This section introduces the setup and modeling of a typical variable stiffness actuated robot. The analysis is conducted using the variable stiffness robot DLR Hand Arm System as an example. This system is later on used also for the experimental validation of the control concepts. We start by giving an quick overview of the system. Then, the model of the variable stiffness actuators of the arm is introduced. After this, the general dynamic model of a multi-joint VSA robot is presented. The chapter is finished by outlining some practical aspects of VSA robots affecting control.
The use of the DLR Hand Arm System as an example and platform for experimental controller validation does not limit the generality of the results of this work. All models and controllers are formulated in a generalized way.

2.1. The DLR Hand Arm System

The DLR Hand Arm System consists of two main components. First, an antropomorphic tendon driven hand with 19 degrees of freedom (DoF) attached to a two DoF wrist. The drive units (19+2 DoF, overall 42 motors) are mounted in the forearm. Second, an arm with five degrees of freedom, ten motors in total. The first three axes of the arm form the shoulder, followed by an elbow. The joints are actuated by Flexible Spring Joints (FSJ) [46] which are able to generate up to 67 Nm of torque and vary their stiffness in a range of 52 Nm/rad up to 827 Nm/rad. The elbow is connected to the lower arm rotation joint based upon a bidirectional antagonistic variable stiffness principle (BAVS, see Chapter 3). A photo of the DLR Hand Arm System can be seen in Fig. 2.1. The DLR Hand Arm System is a highly integrated robot where most electric and mechanic components are mounted in the system. Only power supply cables and optical bus cables for the real-time control computers are required to be connected. This setup is chosen to design more complex robots in a modular way. The controllers are implemented using Matlab Simulink and run on a QNX real-time operating system with a maximum rate of 3 kHz [70].
Further properties of the DLR Hand Arm System are introduced in the following.

Figure 2.1.: The DLR Hand Arm System.

2.2. Variable Stiffness Actuators

Many different drive concepts have been used for the design of variable stiffness actuators so far. The joints considered here and build into the DLR Hand Arm System use electric motors as torque sources, for which system design and control is well developed and nominal torque capacity and bandwidth are high. Mechanical compliance is introduced by a linear stiffness element in combination with a kinematic setup, which produces the desired nonlinear output behavior by a nonlinear transmission.

2.2.1. The General Variable Stiffness Actuator Model

A schematic of a general variable stiffness setup is shown in Fig. 2.2. It consists of a motor which connects to the link by a nonlinear and variable elastic element. The validity of the abstract model is shown in the following.
Several types of variable stiffness actuators are used in the DLR Hand Arm System. In all joints harmonic drive gears transform the motion of the fast spinning rotors into the torque and velocity

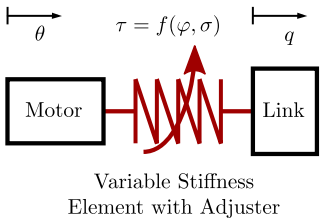

Figure 2.2.: A schematic of the simplified variable stiffness setup. The motor is coupled by a variable stiffness actuator to the link. The adjuster input is assumed to be kinematic. The serial structure results in a diagonal shape of the dynamic model, see (2.9).

desired at the output. The kinematics of the harmonic drive gears is described by

$$\dot{q}_c = \alpha \dot{q}_f + \beta \dot{q}_w, \tag{2.1}$$

where q_c, q_f, and q_w denote the circular spline, the flex spline, and the wave generator coordinate, respectively. The dot indicates the time derivatives $\partial/\partial t$ and such the velocities. The parameters $\alpha = N/(N+1)$ and $\beta = 1/(N+1)$ result from the transmission ratio N of the gear.

The Floating Spring Joint

The harmonic drive gears are popular choices to implement VS joints, as their structure allows for various implementation arrangements [49]. One simple arrangement achieves a pure reduction gear. This setup is used in the floating spring joint (FSJ) [48] and depicted in Fig. 2.3. Herein, the circular spline is attached to the base. As the rotor is fixed to the wave generator and no flexibility of the joint is assumed, the motor coordinate θ is defined to be

$$\theta = q_f = -1/N q_w. \tag{2.2}$$

The dynamic model of the joint arrangement can be obtained using Lagrange's equation. It requires to formulate the mechanical energy of the joint. The kinetic energy of the system is given by

$$T = \frac{1}{2} J_\theta \dot{\theta}^2 + \frac{1}{2}(J_\sigma + J_{cd})\dot{\sigma} + \frac{1}{2}(J_q + 2J_{cd} + J_\sigma)\dot{q}^2 \tag{2.3}$$

where σ is the adjuster coordinate and q the link coordinate. J_θ is the rotor and wave generator inertia, reflected to the link side, and the inertia added from the spring and roller mechanism. J_σ is the reflected inertia[1] of the adjuster mechanism, and J_{cd} is the inertia added by the cam discs. Furthermore, J_q is the link inertia. The potential energy is given purely by the elastic element

$$V = \frac{1}{2} k (f_{cd}(\varphi + \sigma) + f_{cd}(-\varphi - \sigma))^2, \tag{2.4}$$

[1]The adjuster motor motion is also transmitted by a gear box.

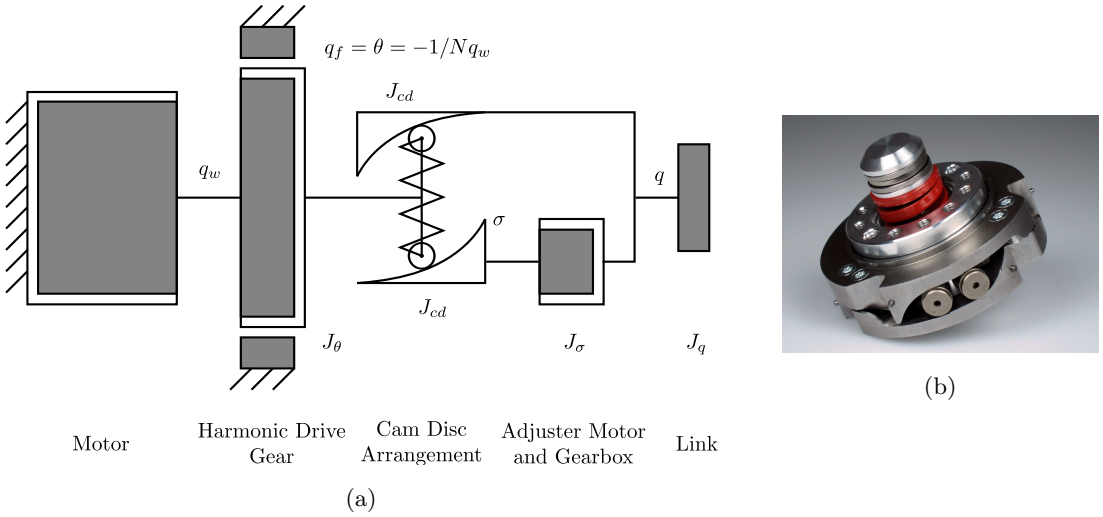

Figure 2.3.: A sketch of the FSJ arrangement (a) and a photo of the cam disc mechanism with the elastic element (b). The harmonic drive is used as a simple reduction gear. The VS mechanism is mounted between the flex spline q_f and the link q.

with $\varphi = \theta - q$ and k is the spring constant of the linear spring, mounted between the two cam discs. The nonlinear function f_{cd} describes the geometry of the cam discs. The Lagrangian [71] of the system is defined by

$$L(\boldsymbol{x}, \dot{\boldsymbol{x}}) = T(\boldsymbol{x}, \dot{\boldsymbol{x}}) + V(\boldsymbol{x}), \tag{2.5}$$

where

$$\boldsymbol{x} = \begin{pmatrix} q \\ \theta \\ \sigma \end{pmatrix} \in \mathbb{R}^3 \tag{2.6}$$

is a vector containing the coordinates. The equations of motion can be derived using the Euler-Lagrange equations

$$\frac{d}{dt}\frac{\partial L(\boldsymbol{x}, \dot{\boldsymbol{x}})}{\partial \dot{\boldsymbol{x}}} - \frac{\partial L(\boldsymbol{x}, \dot{\boldsymbol{x}})}{\partial \boldsymbol{x}} = \boldsymbol{Q}, \tag{2.7}$$

where $\boldsymbol{Q} \in \mathbb{R}^3$ is the vector representing the generalized forces corresponding to $\boldsymbol{x}$. It follows

$$\begin{bmatrix} J_q + 2J_{cd} + J_\sigma & 0 & 0 \\ 0 & J_\theta & 0 \\ 0 & 0 & J_\sigma + J_{cd} \end{bmatrix} \begin{bmatrix} \ddot{q} \\ \ddot{\theta} \\ \ddot{\sigma} \end{bmatrix}$$
$$+k(f_{cd}(\varphi + \sigma) + f_{cd}(-\varphi - \sigma)) \begin{bmatrix} j_1 - j_2 \\ -j_1 + j_2 \\ -j_1 + j_2 \end{bmatrix} = \begin{bmatrix} \tau_{\text{ext}} \\ \tau_\theta \\ \tau_\sigma \end{bmatrix} \tag{2.8}$$

with $j_1 = \frac{df_{cd}(x)}{dx}, j_2 = \frac{df_{cd}(-x)}{dx}$. The torques τ_θ and τ_σ act as control input to the joint and the stiffness motor, respectively. The inner torque control loops of the motors are operated at 100 kHz [70] and the torque dynamics result to be much faster than the mechanical dynamics ($>> 100$). Such, the motors can be assumed to be ideal torque sources. Furthermore, τ_{ext} is an external torque acting on the joint. The diagonal structure[2] of this joint setup is beneficial and allows for a common simplification of the dynamic model [72]

$$\begin{bmatrix} m_i & 0 \\ 0 & b_i \end{bmatrix} \begin{bmatrix} \ddot{q}_i \\ \ddot{\theta}_i \end{bmatrix} + \begin{bmatrix} -\tau_i(\varphi_i, \sigma_i) \\ \tau_i(\varphi_i, \sigma_i) \end{bmatrix} = \begin{bmatrix} \tau_{ext,i} \\ \tau_{m,i} \end{bmatrix}, \tag{2.9a}$$

$$\tau_i(\varphi_i, \sigma_i) = k(f_{cd,i}(\varphi_i + \sigma_i) + f_{cd,i}(-\varphi_i - \sigma_i))(-j_{1,i} + j_{2,i}). \tag{2.9b}$$

An important assumption of this model is to consider the adjuster coordinate σ_i as an kinematic control input. Thereby, similarity to the well researched flexible joint robot model is ensured [73]. It results a serial setup, where the motor is connected to the link by the varying elastic element, see Fig. 2.2. This structure is advantageous for controller design and will be exploited later on. Many joint designs can be described by the model (2.9), among them the ones presented in [46], [47], and [48]. In some cases outer diagonal terms arise, which often can be neglected in the practical case.

Remark: The notation of (2.9) will be used in the remainder of this thesis to be consistent with the multi-joint systems treated. Indices $i \in 1 \dots n$ represent the i^{th} joint and indicate that each of the VSA joints in a robot can be described by this model. Furthermore, we will use vector and matrix notation to generalize the representation. The already defined variables are collected in the following manner:

$$\boldsymbol{q} = (q_1, \cdots, q_n)^T \tag{2.10a}$$

$$\boldsymbol{\theta} = (\theta_1, \cdots, \theta_n)^T \tag{2.10b}$$

$$\boldsymbol{f}(\boldsymbol{\varphi}, \boldsymbol{\sigma}) = (f_1(\varphi_1, \sigma_1), \cdots, f_n(\varphi_n, \sigma_n))^T \tag{2.10c}$$

$$\cdots .$$

The Bidirectional Antagonistic Variable Stiffness Joint

Another joint concept developed at DLR is the bidirectional antagonistic variable stiffness joint (BAVS joint). The main difference between the FS joint and the BAVS joint is the way the joint stiffness is altered. While in the FSJ a more powerful main joint motor is separated from the less powerful stiffness adjuster motor, the BAVS setup includes two motors of equal size. The properties of the BAVS setup are analysed later in Chapter 3 in more detail, here, we only introduce the general setup and the dynamic model. From the sketch in Fig. 2.4 it follows that

[2] This particular joint setup results in a diagonal structure. This is not true for all possible arrangements, however most setups can be approximated by a diagonal model [72].

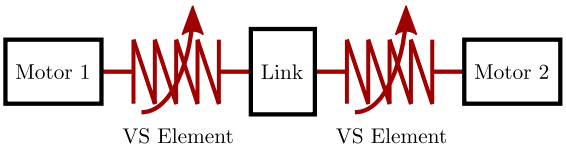

Figure 2.4.: A schematic of the bidirectional antagonistic variable stiffness setup. Each motor is coupled by a variable stiffness actuator to the link. The serial structure results in a diagonal shape of the dynamic model.

also the BAVS model is of diagonal structure

$$\begin{bmatrix} m_i & 0 & 0 \\ 0 & b_{i,1} & 0 \\ 0 & 0 & b_{i,2} \end{bmatrix} \begin{bmatrix} \ddot{q}_i \\ \ddot{\theta}_{i,1} \\ \ddot{\theta}_{i,2} \end{bmatrix} + \begin{bmatrix} -\tau_{i,1}(\varphi_{i,1}) - \tau_{i,2}(\varphi_{i,2}) \\ \tau_{i,1}(\varphi_{i,1}) \\ \tau_{i,2}(\varphi_{i,2}) \end{bmatrix} = \begin{bmatrix} \tau_{ext,i} \\ \tau_{m,i,1} \\ \tau_{m,i,2} \end{bmatrix}, \tag{2.11a}$$

$$\tau_{i,1}(\varphi_{i,1}) = f_{i,1}(\varphi_{i,1}), \quad \tau_{i,2}(\varphi_{i,2}) = f_{i,2}(\varphi_{i,2}) \tag{2.11b}$$

where $f_{i,j}(\varphi_{i,j})$ are functions of the displacement parameter $\varphi_{i,j} = \theta_{i,j} - q_i$. Besides of the additional motor the difference is the non-existence of the stiffness adjusters. Therefore, the stiffness elements do not have the stiffness adjusting inputs σ_i.

2.2.2. The Variable Stiffness Element

A main part of each variable stiffness actuator is the elastic element and its characteristics. In general, the elements are implemented to show an ideal stiffness with as little damping as possible. The low damping of the springs has several benefits:

- It allows to estimate the torques acting on the elastic element using

  $$\boldsymbol{\tau} = \boldsymbol{f}(\boldsymbol{\varphi}, \boldsymbol{\sigma}) \tag{2.12}$$

  (c.f. (2.9b)) and a pure position measurement of $\boldsymbol{\theta}, \boldsymbol{q}$, and $\boldsymbol{\sigma}$ (similarly possible for the BAVS case). Uniqueness of the solution is assumed. The conditions for the existence of the unique solution are given below.

- Adjusting a motor position $\boldsymbol{\theta}_d$ and a stiffness setting $\boldsymbol{\sigma}$, the link side position $\boldsymbol{q}_d$ can be precisely estimated purely using the model (2.9). An approach relying on this fact is discussed in Section 4.1.

- Energy can be stored into the spring element and recovered with little loss. This enables highly dynamic motions. An approach which makes use of the energy storage capability is presented in Chapter 7.

Besides of these general features, some important theoretical properties of the elastic elements are summarized here.

- The instantaneous (incremental) **joint stiffness** of the spring at $\boldsymbol{\varphi}, \boldsymbol{\sigma}$ is given by

$$\boldsymbol{k}(\boldsymbol{\varphi}, \boldsymbol{\sigma}) = \frac{\partial \boldsymbol{f}(\boldsymbol{\varphi}, \boldsymbol{\sigma})}{\partial \boldsymbol{\varphi}}. \tag{2.13}$$

- An important property of the spring function is the **uniqueness of an equilibrium solution**. Uniqueness is given if the following conditions are valid

$$\frac{\partial V(\boldsymbol{x})}{\partial \boldsymbol{x}} - \boldsymbol{\tau}_e = \boldsymbol{0} \quad \text{and} \quad \frac{\partial^2 V(\boldsymbol{x})}{\partial \boldsymbol{x}^2} > \boldsymbol{0}, \tag{2.14}$$

  where $V(\boldsymbol{x})$ is the potential of the elastic element, $\boldsymbol{x} = (\boldsymbol{\theta}, \boldsymbol{q}, \boldsymbol{\sigma})$ is the generalized coordinates vector, and $\boldsymbol{\tau}_e \in \mathbb{R}^{3n}$. These conditions are true for most developed VSA joints and are assumed in the following.

- From (2.14) it follows that the **elastic element inverses** can be evaluated to be

$$\boldsymbol{\varphi} = \boldsymbol{f}_{\varphi}^{-1}(\boldsymbol{\tau}_e, \boldsymbol{\sigma}), \tag{2.15a}$$

$$\boldsymbol{\sigma} = \boldsymbol{f}_{\sigma}^{-1}(\boldsymbol{\tau}_e, \boldsymbol{\varphi}) \tag{2.15b}$$

The exact characteristics of the stiffness element (2.12), in particular the function $f_{cd,i}$ (2.9b), is subject to mechanical design. Many possibilities exist which can be assigned to three main categories:

Linear stiffness: The use of linear springs in robotic actuators has been explored by e.g. [52, 60] in their work on Series Elastic Actuators (SEA). Although not limited to, the series elasticity used in their setup shows a constant spring rate $k = const.$ The joint torques result to be

$$\boldsymbol{\tau}(\boldsymbol{\varphi}, \boldsymbol{\sigma}) = \boldsymbol{K}\boldsymbol{\varphi}, \tag{2.16}$$

with $\boldsymbol{K} \in \mathbb{R}^{n \times n}$ a positive definite stiffness matrix. For most robots, the matrix is diagonal $\boldsymbol{K} = \mathrm{diag}(\boldsymbol{k})$. In case joint couplings exist (comparable to biarticular muscles in humans) this matrix has outer diagonal entries. Robots equipped with SEAs are the Meka Arm A2 [62] or the CompAct arm [69]. Due to the constant spring rate, the SEAs show a force bandwidth limitation. A similar model is the reduced flexible joint model described in [73] and found in light weight robots [12, 18]. There, joint stiffness is higher than in the SEA case at around 10000-20000 Nm/rad.

Linear, variable stiffness: Recent developments aim to overcome the force bandwidth limitation by introducing a spring with variable stiffness in series. In one class of actuators the constant spring stiffness k from (2.16) is replaced by a variable spring stiffness with an additional stiffness variation input

$$\boldsymbol{\tau}(\boldsymbol{\varphi}, \boldsymbol{\sigma}) = \boldsymbol{K}(\boldsymbol{\sigma})\boldsymbol{\varphi}. \tag{2.17}$$

Examples for joints with such a characteristics are the vsaUT-II and AWAS joints [54, 74].

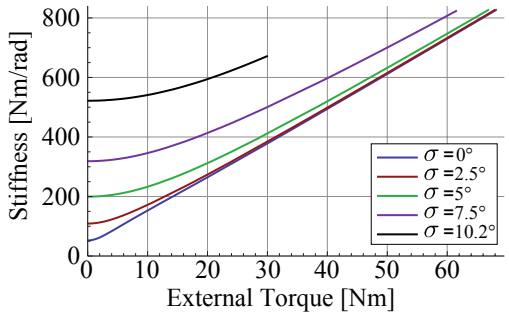

Figure 2.5.: The stiffness-torque characteristics of the FS joint. The stiffness increases nonlinearly with increasing joint torques. Furthermore, the stiffness adjuster input σ allows to vary the joint stiffness independent of the joint torque/position over a wide range.

Nonlinear, variable stiffness: Many other joint setups implement a nonlinear and varying joint stiffness. Such, $\tau(\varphi, \sigma)$ can be of arbitrary nonlinear shape and has the additional input σ to vary the stiffness characteristics. The multi-joint model is given by

$$\boldsymbol{\tau}(\boldsymbol{\varphi}, \boldsymbol{\sigma}) = \boldsymbol{f}(\boldsymbol{\varphi}, \boldsymbol{\sigma}). \tag{2.18}$$

A common choice for the single joint torque function $f(\varphi, \sigma)$ is a progressive shape of the joint stiffness. It has the properties $\partial f/\partial\varphi > 0$, $\partial^3 f/\partial\varphi^3 > 0$ for all σ. A progressive stiffness shape profile produces increasing stiffness w.r.t. joint deflection and is chosen out of several reasons. One is to generate maximal forces at the joints limits and thereby prevent the mechanism from damage.[3] Another one results from stiffness variation possibility. Details regarding this are discussed in a case study in Chapter 3. Examples for joints implementing such a characteristic are the MACCEPA joints [45, 25] or the FS joints, as used in the DLR Hand Arm System [48]. The stiffness profiles of the FSJ are depicted in Fig 2.5.

2.3. The VSA Robot Model

The derivation of the complete VSA robot model follows tightly the derivation of the flexible joint model [73]. The dynamic model can be achieved using the Euler-Lagrange method and requires the formulation of the kinetic energy term given by the links and the rotors. They are

$$T(\boldsymbol{q}, \dot{\boldsymbol{q}}, \dot{\boldsymbol{\theta}}) = \frac{1}{2} \begin{pmatrix} \dot{\boldsymbol{q}} \\ \dot{\boldsymbol{\theta}} \end{pmatrix}^T \begin{bmatrix} \boldsymbol{M}_r(\boldsymbol{q}) + \boldsymbol{M}_l(\boldsymbol{q}) & \boldsymbol{S}(\boldsymbol{q}) \\ \boldsymbol{S}(\boldsymbol{q})^T & \boldsymbol{B} \end{bmatrix} \begin{pmatrix} \dot{\boldsymbol{q}} \\ \dot{\boldsymbol{\theta}} \end{pmatrix} = \begin{pmatrix} \dot{\boldsymbol{q}} \\ \dot{\boldsymbol{\theta}} \end{pmatrix}^T \boldsymbol{H}(\boldsymbol{q}) \begin{pmatrix} \dot{\boldsymbol{q}} \\ \dot{\boldsymbol{\theta}} \end{pmatrix} \tag{2.19}$$

The inertia components of the rotors are collected in the generalized inertia matrix $\boldsymbol{M}_r(\boldsymbol{q}) \in \mathbb{R}^{n \times n}$ which has diagonal structure due to symmetry assumption. The link inertia matrix $\boldsymbol{M}_l(\boldsymbol{q}) \in$

[3] Limits are imposed by the mechanical joint setup. E.g. a maximal deflection of the elastic element is given. Overrunning the maximum values can lead to irreversible damage to the joint mechanism.

$\mathbb{R}^{n\times n}$ contains the inertia properties of the links. The motor inertia matrix $\boldsymbol{B} = \mathrm{diag}(\boldsymbol{b}) \in \mathbb{R}^{n\times n}$ contains the terms of the inertia tensor of the rotors along their axes of rotation, c.f. (2.9). Furthermore, outer diagonal terms $\boldsymbol{S}(\boldsymbol{q}) \in \mathbb{R}^{n\times n}$ arise due to an energy contribution to the rotational part of the kinetic energy of the rotors by the link motion and vice versa. This part is neglected in the flexible joint model [73] $\boldsymbol{S}(\boldsymbol{q}) = \boldsymbol{0}$. The term is also ignored in our case as the motor velocity is normally much higher than the link velocity due to the high gear ratio $N_i > 100$. In some joint designs, coupling terms depending upon the full robot state $\boldsymbol{S}(\boldsymbol{x})$ appear. The resulting systems pose additional control effort (non-minimum phase) and are not treated in the following.

Furthermore, the potential energy of the system is calculated, consisting of the gravitational potential $V_g(\boldsymbol{q})$ and the elastic element potential $V_k(\boldsymbol{q}, \boldsymbol{\theta}, \boldsymbol{\sigma})$ as introduced in (2.4)

$$V(\boldsymbol{q}, \boldsymbol{\theta}) = V_g(\boldsymbol{q}) + V_k(\boldsymbol{q}, \boldsymbol{\theta}, \boldsymbol{\sigma}). \tag{2.20}$$

The gravity potential only depends on the link position due to the symmetric setup of the rotors and alignment of the rotor axis and the joint axis. The elastic element potential also depends on the motor and adjuster positions, c.f. (2.4).

Using (2.19) and (2.20) together with the Lagrangian formalism results in the equations of motions

$$\boldsymbol{M}(\boldsymbol{q})\ddot{\boldsymbol{q}} + \boldsymbol{C}(\boldsymbol{q}, \dot{\boldsymbol{q}})\dot{\boldsymbol{q}} + \boldsymbol{g}(\boldsymbol{q}) = \boldsymbol{\tau} + \boldsymbol{\tau}_{\text{ext}}, \tag{2.21a}$$

$$\boldsymbol{B}\ddot{\boldsymbol{\theta}} + \boldsymbol{\tau} = \boldsymbol{\tau}_m, \tag{2.21b}$$

$$\boldsymbol{\tau} = \boldsymbol{f}(\boldsymbol{\theta} - \boldsymbol{q}, \boldsymbol{\sigma}), \tag{2.21c}$$

where the mass matrix $\boldsymbol{M}(\boldsymbol{q}) \in \mathbb{R}^{n\times n}$ consists of the remaining entries of $\boldsymbol{M}_r(\boldsymbol{q}) + \boldsymbol{M}_l(\boldsymbol{q})$ and the Coriolis/centrifugal terms are given by $\boldsymbol{C}(\boldsymbol{q}, \dot{\boldsymbol{q}}) \in \mathbb{R}^{n\times n}$. The gravity torque is given by

$$\boldsymbol{g}(\boldsymbol{q}) = \left(\frac{\partial V_g(\boldsymbol{q})}{\partial \boldsymbol{q}}\right)^T. \tag{2.22}$$

The model (2.21) is the basis for many of the controllers developed in this work. Note the diagonal structure, similar to the one in (2.9) with the only coupling between the motor and the link given by the elastic element.

In the case of BAVS joint actuators, two motors with dynamics are present while no kinematic stiffness variation input exists. The model (2.21) can be extended in a straight forward way to allow for arbitrary combinations of both VS concepts. The equations of motion result to be

$$\boldsymbol{M}(\boldsymbol{q})\ddot{\boldsymbol{q}} + \boldsymbol{C}(\boldsymbol{q}, \dot{\boldsymbol{q}})\dot{\boldsymbol{q}} + \boldsymbol{g}(\boldsymbol{q}) = \boldsymbol{T}\boldsymbol{\tau} + \boldsymbol{\tau}_{\text{ext}}, \tag{2.23a}$$

$$\boldsymbol{B}\ddot{\boldsymbol{\theta}} + \boldsymbol{\tau} = \boldsymbol{\tau}_m, \tag{2.23b}$$

$$\boldsymbol{\tau} = \boldsymbol{f}(\boldsymbol{\theta} - \boldsymbol{T}^T\boldsymbol{q}, \boldsymbol{\sigma}), \tag{2.23c}$$

where a mapping matrix $\boldsymbol{T} \in \mathbb{R}^{n\times m}$ is introduced. It maps the m motor coordinates to the n link coordinates. The dimensions of the variables are $\boldsymbol{q}, \boldsymbol{g}(\boldsymbol{q}), \boldsymbol{\tau}_{\text{ext}} \in \mathbb{R}^n$, $\boldsymbol{M}(\boldsymbol{q}), \boldsymbol{C}(\boldsymbol{q}, \dot{\boldsymbol{q}}) \in \mathbb{R}^{n\times n}$, $\boldsymbol{\theta}, \boldsymbol{\tau}, \boldsymbol{\tau}_m \in \mathbb{R}^m$, and $\boldsymbol{B} \in \mathbb{R}^{n\times n}$. For BAVS joints $\boldsymbol{\sigma}$ is omitted.

2.4. Further Effects

The controller development as conducted in this thesis is mainly based on (2.21). This model is an abstraction of the robot and implies several simplifications. Abstraction is a powerful and necessary tool to be able to apply many of the theoretical methods as used in this work. The presented models have been evaluated by qualitative and quantitative comparisons of experimental and simulation results. If a model is sufficiently accurate is heavily dependent on the used controller. The models 2.21 and 2.23 have been found to be accurate enough for the subsequently presented controllers under the reported circumstances. Still, often side effects are visible during practical evaluation resulting from limitations of the used model. Therefore these limitations have to be kept in mind during the control design and are often implicitly accounted for. We indicate such consequences in the related sections.
Important constraints are:

- **Friction**, is present at several places in the joint. Assuming viscous friction, the model (2.21) can be extended

$$\boldsymbol{M}(\boldsymbol{q})\ddot{\boldsymbol{q}} + \boldsymbol{C}(\boldsymbol{q},\dot{\boldsymbol{q}})\dot{\boldsymbol{q}} + \boldsymbol{D}_q\dot{\boldsymbol{q}} + \boldsymbol{g}(\boldsymbol{q}) = \boldsymbol{\tau} + \boldsymbol{\tau}_{\text{ext}}, \tag{2.24a}$$

$$\boldsymbol{B}\ddot{\boldsymbol{\theta}} + \boldsymbol{D}_\theta\dot{\boldsymbol{\theta}} + \boldsymbol{\tau} = \boldsymbol{\tau}_m, \tag{2.24b}$$

$$\boldsymbol{\tau} = \boldsymbol{f}(\boldsymbol{\theta} - \boldsymbol{q}, \boldsymbol{\sigma}) + \boldsymbol{D}_\tau\dot{\boldsymbol{\tau}}. \tag{2.24c}$$

  The aim of variable stiffness joints is to provide as little link and spring friction as possible, therefore $\boldsymbol{D}_q$ and $\boldsymbol{D}_\tau$ can be neglected in most cases. The effect of motor friction can be reduced to great extend by using friction observers [75]. We understand that it is a strong assumption to neglect friction, however controllers which are able to cope with it provide great practical avail and applicability. We will discuss this assumption at points where it effects controller design or performance.

- **Saturations**, encountered especially as joint torque and motor velocity saturations, have effects on the controller and trajectory design. Concerning a saturation-aware trajectory design, the interested reader may refer to recent approaches on the DLR Hand Arm System such as ball-throwing [76, 23].

- **Real-time**: The implemented control algorithms are subject to real-time computation with a control frequency of 3 kHz. Within one control cycle, all sensory information relevant for the system state have to be gathered (35 sensors), the control output has to be computed, and the actuator commands have to be applied (14 actuators). These contrary restrictions (real-time compliance, system complexity) demand a great deal of control design effort and impede the use of computationally expensive control techniques such as nonlinear model predictive control [77] so far[4]. To relax the computational limitations, approaches to run

[4] Please remark that through the enormous increase of computing power and advances in optimization based control, such approaches may soon be ready for real-time application.

the closed loop error controllers at the fastest rate while computing the controller gains at a slower rate exist and are used [78].

- **Control bandwidth**: The limited control bandwidth is mostly introduced by delays in the signal path, and it bounds the effective controller gains. Therefore, theoretically elegant solutions such as feedback linearization or diverse high-gain methods can only be applied with care. Violating these constraints results in over-compensation at best and leads to instability at worst. A practical solution is given by control algorithms which allow to select control gains in physically reasonable ranges.

- **Sensor noise** effects hinder the reconstruction of state signals. The measurements obtained on the motor and link side are exposed to noise. Particularly when deriving higher order derivatives, various filter designs come into consideration [79]. In view of the control bandwidth and the computational costs, usually low order filters are deployed. Another solution is the reconstruction of states via model-based methods.

2.5. Discussion

This chapter gives an introduction to the modelling of variable stiffness actuators and variable stiffness robots. After a motivating presentation of the used hardware platform, the DLR Hand Arm System, important variable stiffness joint setups are reported. Then, the most common stiffness characteristics used in the setups are summarized. It is shown that in a popular class of actuators the stiffness adjuster mechanism can be treated as an independent input where its dynamics can be omitted. It results a serial setup of the motor, the elastic element, and the link. The advantage of the reported VSA robot model is its similarity to the flexible joint model. An important difference is the introduction of the variable, elastic element. The shape of the elastic element needs to hold several properties, such that controller design is enabled. The chapter is concluded with an outlook on the most important effects additionally arising in a real-world VSA robot.
The contribution is the presentation of the different variable stiffness joint setups and modeling of the complete VSA robot in a condensed and integral form also relating to concepts reported in the literature.

3. Case study: The Bidirectional Antagonistic Variable Stiffness Joint

A multitude of VSA joints has been presented in the past. The reported setups differ in several aspects. Especially the torque characteristics and implementation of the elastic elements and the arrangement and relative dimensioning of the motors distinguish the approaches. One type of joints involves a bigger motor to adjust the joint torque/position and another smaller motor to adjust the joint stiffness. The advantage is the clear differentiation between joint torque/position and joint stiffness adjustment. A disadvantage is that the stiffness adjuster motor cannot support the joint motor and vice versa in many designs due to a serial setup of the joint and stiffness motors. Another approach is an antagonistic arrangement, similar to human muscle actuation. In this case study, an in-depth analysis of a variable stiffness actuation concept called the Bidirectinal Antagonistic Variable Stiffness (BAVS) joint is presented.
This chapter first introduces the bidirectional antagonistic variable stiffness joint setup and functionality. An analysis of the achievable joint stiffness range is presented. One of the outcomes is a stiffness synthesis method. Afterwards, the class of cam disc based mechanisms to realize nonlinear elastic elements is chosen and several implementation issues like number of cam discs and springs are discussed regarding achievable stiffness curves. Finally, the gained insights are discussed and evaluated on a BAVS joint realization as used in the DLR Hand Arm System, where several experiments validate the theoretical findings. All considerations focus on achieving independently a certain joint torque/position and stiffness and are quasi static. As far as possible, an analytic approach is chosen.
This section is based on the publications [80] and [81].

3.1. Setup and Functionality

3.1.1. Antagonistic Joint Setup

The antagonistic joint setup is motivated by the antagonistic arrangement of muscles as found in the skeletal system of living creatures. Opposing muscles, often called agonist and antagonist, act on a movable part such as a joint. The setup accounts for the property of muscles to only be able to exert pulling forces. Contracting one muscle induces a motion at the joint, and the opposing muscle is passively lengthened. After one muscle was contracted, the opposing muscle is able to

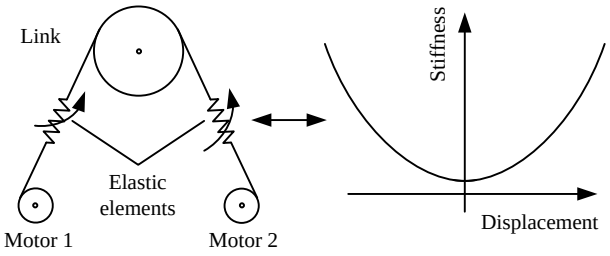

Figure 3.1.: On the left a normal antagonistic setup with actuators acting only in the pulling direction is shown. A progressive stiffness-displacement profile is depicted (right side), which enables stiffness variation and aims to prevent the mechanism to run into hardware limits.

generate a force which brings the shortened muscle back to its original length. Contracting both sides at the same time (co-contraction) increases the joint stiffness due to the nonlinear muscle stiffness.

A straight forward technical transfer of this concept incorporates two equally sized actuators and one output (the link), see Fig. 3.1. Several actuation technologies to be used in antagonistic setups have been reported in the literature [82, 83, 84]. We focus on electric motors in combination with gearboxes, due to their excellent power density and controllability. Passive elastic elements decouple the motors and the link [36, 85]. In the following, one motor with its elastic elements coupling it to the link is called a motor-spring unit or simply side of the antagonism. The model (2.11) is considered where we restrict our analysis to one joint, leading to a simplified notation. The elastic elements in conjunction with position controlled motors enable the use of the motor-spring units as torque sources

$$\begin{aligned} \tau_1 &= f_1(\varphi_1, \sigma) = f(\theta_1 + \sigma - q), \\ \tau_2 &= f_2(\varphi_2, \sigma) = f(\theta_2 - \sigma - q) \end{aligned} \tag{3.1}$$

where it is assumed, that the i-th motor position θ_i is a control input.[1] The link coordinate is denoted by q and σ is an offset used for co-contraction (stiffness adjustment).

The function of a technical antagonism setup is similar to a muscle antagonism. If only one motor-spring unit contracts, a torque at the link is created, called output torque. The spring of the other (opposite) side is passively deflected. To change the joint stiffness, internal torques are generated, where the two sides co-contract. An important precondition for this functionality is a nonlinear torque-displacement characteristic $f(.)$ of the elastic element. We focus here on a progressive shape, see Fig. 3.1 right side.

[1] In practice, e.g. a standard regulation PD control loop on the motor coordinate can be used $\tau_{m,i} = K_P(\theta_{d,i} - \theta_i) - K_D\dot{\theta}_i$. Here, $\tau_{m,i}$ is the i-th motor torque, θ_d the desired motor position and K_P and K_D the proportional and derivative controller gains.

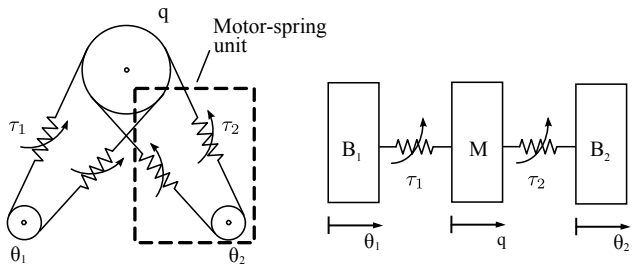

Figure 3.2.: Sketches of two possible bidirectional antagonism realizations. On the left a setup using tendons with pretensioned, unidirectional nonlinear spring elements. On the right a realization with bidirectional nonlinear spring elements. Both setups are functionally equivalent but differ in implementation issues, see Section 3.4.

3.1.2. Bidirectional Antagonistic Variable Stiffness Joint Setup

In contrast to muscles, electric motors can turn into two directions. By setting up a connection that is able to transmit forces in two directions at the joint, this bidirectionality allows to extend the antagonistic setup into the bidirectional antagonism. This extends the role of the agonist and antagonist in the antagonistic setup, as now the actuators can work co-directional: Both actuators can apply torques in both directions at the link and therefore they can support each other. The modification toward the bidirectional setup still allows for all operation modes of the standard antagonistic setup and additionally enables a helping mode, where the actuators work actively co-directional. Thus, the helping mode provides improved torque performance. Possible scenarios are the compensation of an external load or an application where energy has to be stored into the springs like for throwing. Furthermore, BAVS joints show high power to size ratio as all the motor power can be made available at the link.
The torque and stiffness composition of the bidirectional antagonistic variable stiffness setup can be analysed by identifying that the two motor-spring units are mounted in a parallel arrangement. The torque of each unit contributes to the overall joint torque τ

$$\tau = \tau_1 + \tau_2 \qquad |\tau_i| \leq \tau_{stall} \; \forall \; i. \tag{3.2}$$

Assuming sufficient spring capacity, the unit torque is limited only by the motor stall torque τ_{stall}. Here, the difference to the normal antagonism is visible, as there only unidirectional torques $-\tau_{stall} \leq \tau_1 \leq 0$ and $0 \leq \tau_2 \leq \tau_{stall}$ can be exerted.
The link stiffness[2] k results from the unit stiffness $k_i(\tau_i)$ to be

$$k = k_1(\tau_1) + k_2(\tau_2) \qquad k_i(\tau_i) \geq 0 \; \forall \; \tau_i. \tag{3.3}$$

A mechanical realization is achieved by replacing the single elastic tendon in Fig. 3.1 with a loop around each motor and the joint, see Fig. 3.2 left. A sketch of the general arrangement is

[2]Definition from (2.13).

shown on the right, where bidirectional elastic elements are assumed. Implementation details are discussed in Section 3.4.

3.2. Operating Modes

The modification towards the bidirectional antagonism allows to use the operating mode of the standard antagonistic setup (called normal mode) and enables the additional helping mode. In the helping mode the motors are able to support each other, see Fig. 3.3. While the normal mode has a broad stiffness adjustment capability for low external torques, the helping mode significantly extends the torque operating region still allowing some stiffness variation.

3.2.1. Normal Antagonistic Mode

In this mode, the torques generated oppose each other. Their magnitudes can be equal or different:

- When the torques are of equal magnitude but have different signs, e.g. $\tau_1 = -\tau_2 = \tau_0$, internal torques are generated that compensate for each other and no net output torque is generated. This produces a zero link torque in accordance with (3.2)

$$\tau = \tau_1 + \tau_2 = 0. \tag{3.4}$$

  Although no output torque is generated, the link stiffness k is increased. This is due to the fact that the internal torques load the elastic elements

$$k = k_1(\tau_1) + k_2(\tau_2) > k_1(0) + k_2(0). \tag{3.5}$$

  Here, $k_i(0)\ \forall\ i$ is the stiffness of the units for the unloaded case. Therefore, internal opposing torques can be used to control the stiffness of the joint in absence of an external torque. This is the well known co-contraction property of antagonistic setups to increase the joint stiffness.

  In the following, this operation to increase stiffness by internal torques is referred to as pretensioning of the joint and τ_0 is the torque used for pretension.

- Torques of different magnitude and opposing signs, e.g. $\tau_1 < 0 < \tau_2$, compensate for each other up to a certain limit, creating internal torques. However, the difference of the two torques generates an external torque at the link. For example

$$\underbrace{\tau_0 + \tau_{\text{ext}}}_{\tau_1}\underbrace{-\tau_0}_{\tau_2} = \tau_{\text{ext}} = \tau \tag{3.6}$$

  with τ_{ext} as the torque available at the link. This case is the solution of (3.2) for a link torque and internal torques of different magnitudes but still different signs.

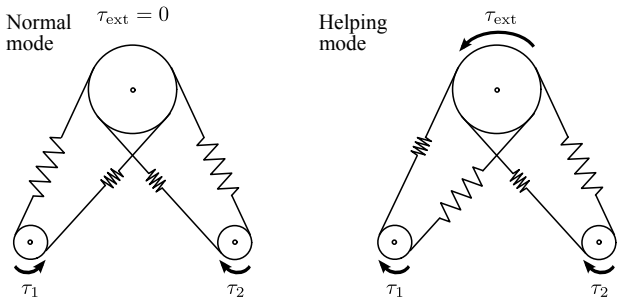

Figure 3.3.: The modes of operation of the bidirectional antagonistic setup. Each motor is able to apply bidirectional torques at the links. In the normal mode, the units generate internal torques which cancel out each other, whereas the link stiffness is increased. In the helping mode, the motors support each other and generate a higher external torque.

The described two cases can be identified in the torque plots belonging to (3.2), see Fig. 3.4. In the relaxed case with no external torque applied, both motor-spring unit torque curves superimpose and generate twice the joint stiffness (the joint torque curve has twice the slope). By pretensioning, internal torques are generated and the stiffness is increased, as the curves move apart. If no external torque is generated, the system is at the origin of the torque-displacement curve. By increasing the external torque, the operating point slides along the torque curve τ meaning one motor gets loaded while the other is deloaded. If the external torque is such big that one motor is completely deloaded $\tau_{1|2} = 0$, the motor torques are no longer working against each other. Instead, from this point on the two motors will provide a torque in the same direction and thereby support each other. This is the new mode of operation, the helping mode, and will be discussed in the next section.

3.2.2. Helping Antagonistic Mode

The helping mode uses torques in the same direction to allow the motors to support each other. Therefore, for motor-spring unit torques $\text{sign}(\tau_1) = \text{sign}(\tau_2)$ is fulfilled. To establish a force equilibrium, an external torque is essentially required and has to be directed against the τ_i

$$-2\tau_{stall} \leq \tau = \tau_{\text{ext}} = \sum_{i=1,2} \tau_i \leq 2\,\tau_{stall}, \tag{3.7}$$

see Fig. 3.3 right. Without any external torque the helping mode does not activate. The helping mode allows the creation of up to twice the stall torque of a single motor at the link. The cooperation of the two motors enables a further stiffness variation in the helping mode: By varying the torque contribution of each motor to support the external load, also varied stiffness of each unit is generated, which results in a different link stiffness.

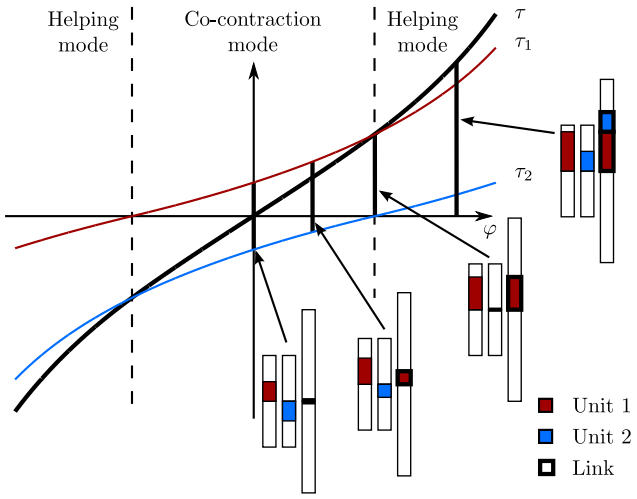

Figure 3.4.: A plot of the two motor-spring unit torques (red, τ_1 and blue, τ_2) and the resulting link torque (thick, τ). Please note the s-shape of τ due to symmetry reasons. The unit torque curves have moved out of the center and summed up to a steeper link torque curve (link stiffness is increased). The passive transition from the normal (co-contraction) to the helping mode can be identified. The bar graphs illustrate the loading of the motor-spring units. At the center, the units generate opposing torques leading to increased stiffness. Once an external torque is applied, the units get loaded unequally. At the transition point from normal to helping mode, only one motor is loaded. If the joint is further loaded, the helping mode activates and the two motors support each other.

To exploit the stiffness variation capabilities during the helping mode, the following load distribution approach is used.
The joint torque behavior by distributing the load is given by

$$\tau = \tau_1 + \tau_2 = \alpha\,\tau_{\text{ext}} + (1-\alpha)\,\tau_{\text{ext}},\ \alpha\ \in\ \{\alpha \in \mathbb{R} | 0 \leq \alpha \leq 1\}, \tag{3.8}$$

where the coefficient α indicates the load distribution. With (3.3) it results for the joint stiffness

$$k = k_1(\alpha\,\tau_{\text{ext}}) + k_2((1-\alpha)\,\tau_{\text{ext}}). \tag{3.9}$$

Two extreme cases of the load sharing can be identified. First, only one motor compensates for the complete external load, while the second motor is idle ($\alpha = 1$ or $\alpha = 0$). Second, the two motors contribute the equal amount to the joint torque ($\alpha = \frac{1}{2}$). These two cases describe the limits for the stiffness variation. The highest stiffness is achieved by generating the highest possible torque, therefore operating one unit at it's load limit. The lowest stiffness is achieved for

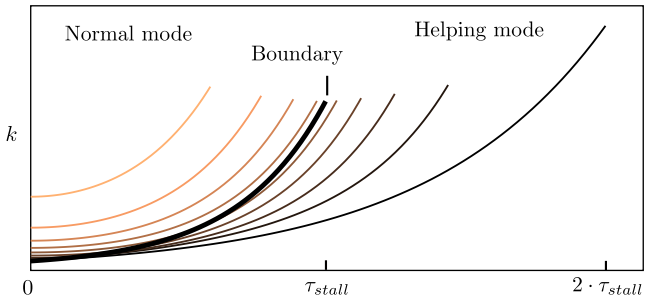

Figure 3.5.: A plot of a torque-stiffness curve. The thin lines are the stiffness curves for increasing pretension of the motors. The thick line represents the boundary between the normal and the helping mode. Each line ends if the stall torque of a spring-motor unit is reached. The helping mode allows the link torque to be twice the motor torque.

the lowest motor-spring unit torques, therefore equal sharing. Please remark, that the stiffness variation mechanism of the normal mode and the helping mode both rely on load distribution between the motor-spring units: In the normal mode internal torques are used and so are external torques in the helping mode.
The stiffness variation capability depends on the exact torque-stiffness curve. An evaluation of the stiffness variation capability and a synthesis method are presented in Section 3.3.

3.3. Joint Stiffness Characteristic

A stiffness variation is even possible in the helping mode. To analyse the achievable joint stiffness, first the use of torque-stiffness plots is motivated. Afterwards a synthesis method to generate a desired joint stiffness behaviour is discussed.

3.3.1. Torque-Stiffness Plots

For the specification of a robotic task the motion reaction of a robot to forces acting on it, namely the compliant behavior, is of big relevance. These parameters are difficult to describe by abstract numbers like maximal joint load or equilibrium position stiffness. To characterize a BAVS joint performance in a general way, torque-stiffness plots as depicted in Fig. 3.5 will be used. A torque-stiffness plot provides stiffness information regarding applied external torques and the current internal state (pretension) of the joint. The joint position information as used in Fig. 3.4 is only of minor relevance for the joint stiffness performance, as the position can be adjusted independently.[3]

[3]Given a certain external torque $\hat{\tau}_{ext}$ two joint deflections follow $\hat{\varphi}_1, \hat{\varphi}_2$. It is always possible to achieve a certain link position $\hat{q}$ by driving the motors to the positions $\hat{\theta}_1 = \hat{\varphi}_1 + \hat{q}$ and $\hat{\theta}_2 = \hat{\varphi}_2 + \hat{q}$.

An arbitrary torque-stiffness curve for the bidirectional antagonistic setup as shown in Fig. 3.5 can be interpreted as follows: Positive link torques are plotted along the horizontal axis. The vertical axis shows joint stiffness values. Due to the symmetry of the joint setup, the torque-stiffness plot can be mirrored at the vertical axis. A family of curves is depicted, where each curve represents the characteristic for one pretension torque. Here, the step size between the curves equals an increase of pretension of 10 % $\sigma_{\max}$ ($\sigma_{\max}$ is the maximal motor pretension position). The lowest curve equals no pretension (highest achievable link torque $\tau_{\max} = 2\ \tau_{\text{stall}}$). The highest curve equals a pretension of $\sigma = 90\,\%\ \sigma_{\max}$. The stiffness curves are cut off when the stall torque of one motor is exceeded.
The bold curve is the boundary between the normal and the helping mode. Upon crossing it, the motor-spring units no longer work against each other but rather support each other, as also illustrated in Fig. 3.4. Some of the stiffness curves cross this boundary. This transition from normal- to helping mode happens passively when the external load increases. During operation, the crossing of the boundary will happen smoothly, see Fig. 3.4.
As an operating point approaches the end of a curve, the mechanism operates increasingly close to the stall torque of one unit. To further load the joint, it has to be switched to a curve with lower stiffness. In the normal mode, this switching means the reduction of the pretension of the motors to make available more torque at the link. In the helping mode, this switching means a more equal distribution of the link load between the two motors.

3.3.2. Design of the Stiffness Characteristics

The last section analysed that a stiffness variation is even possible in the helping case, although this is not a co-contraction state. The stiffness variation can be managed by altering the two motor spring unit torques to compensate for the external load, as described by (3.8). The two extreme cases $\alpha = \frac{1}{2}$ and $\alpha = 1|0$ are used to outline the silhouette of the torque-stiffness plot. What joint stiffness variation can be achieved depends upon the motor-spring unit stiffness curves. Here, a method to synthesize a desired joint torque-stiffness profile is discussed.
Therefore, first a desired torque-stiffness curve is specified by $k = D(\tau)$, where $D(\tau)$ is the desired function. With (2.13), the differential equation

$$\frac{\partial \tau(\varphi)}{\partial \varphi} = D(\tau(\varphi)) \tag{3.10}$$

can be formulated. By solving this equation, a torque-displacement curve is deduced, as required for analysis and implementation. An analytical solution of (3.10) cannot be found for arbitrary stiffness profiles $D(\tau)$. However, there exist solutions for several prototype cases as discussed below.

Linear Torque-Stiffness Relation: $k(\tau) = c\,\tau$

The first desired characteristic is a linear increasing torque-stiffness curve

$$k(\tau) = c\,\tau, \tag{3.11}$$

where c is a positive real constant of unit [1/rad]. The linear behaviour between force/torque and stiffness was also found in humans (passive) musculoskeletal system [86]. It follows

$$k(\tau) = \frac{\partial \tau(\varphi)}{\partial \varphi} = c\,\tau(\varphi). \tag{3.12}$$

The result for the torque-displacement curve is

$$\tau(\varphi) = \frac{d}{c}\,e^{c\,\varphi}, \tag{3.13}$$

with d [Nm/rad] also a positive real constant and the corresponding stiffness curve is

$$k_{\text{lin}}(\varphi) = \frac{\partial \tau(\varphi)}{\partial \varphi} = d\,e^{c\,\varphi}. \tag{3.14}$$

In this case, stiffness changes linearly with torque. As a result, varying the load between the two motors has no effect, see Fig. 3.6(a). This is due to the fact that any linear combination of the single stiffness always adds up to the same link stiffness, as can be easily verified using (3.3), (3.8) and (3.11):

$$k_{\text{lin}}(\tau_{\text{ext}}) = c\,\tau_1 + c\,\tau_2 = c\,\alpha\,\tau_{\text{ext}} + c\,(1-\alpha)\,\tau_{\text{ext}} = c\,\tau_{\text{ext}} \tag{3.15}$$

Thus, the linear torque-stiffness characteristic is not a good choice if a stiffness variation is desired in the helping mode. This is not in conflict with a linear relation found in humans because of their missing ability to act in a helping mode. To guarantee a large stiffness variation capability in the helping mode, the stiffness change of each actuator should be high for changing torques. Therefore, $D(\tau)$ should be 'as nonlinear as possible'. This will be evaluated in the next subsections.
Please note that $\tau(\varphi) = e^{c\,\varphi}$ is not s-shaped as required in Section 3.2.2. The real implemented torque curve is $\tau = \mathrm{a}\,(e^{\mathrm{b}\,\varphi} - e^{-\mathrm{b}\,\varphi})$, with a and b $\in \mathbb{R}^+$, what results in a s-shaped torque curve. Nonetheless, the assumption of the ideal torque curve holds for a wide range of φ values.

Quadratic Torque-Stiffness Relation $k(\tau) = c\,d\,(1 + \frac{\tau^2}{c^2})$

A moderate nonlinear characteristic is a quadratically increasing stiffness curve:

$$k(\tau) = c\,d\,(1 + \frac{\tau^2}{c^2}), \tag{3.16}$$

c [Nm] and d [1/rad] are real positive constants. Furthermore,

$$\tau(\varphi) = c\,\tan(d\,\varphi). \tag{3.17}$$

For the stiffness-displacement curve the following relation holds

$$k_{\text{quad}}(\varphi) = \frac{\partial\tau(\varphi)}{\partial\varphi} = c\,d\,\frac{1}{\cos^2(d\,\varphi)}. \tag{3.18}$$

This quadratic stiffness curve already demonstrates a reasonable achievable stiffness range for the helping antagonistic case, see Fig. 3.6(b).

Exponential Torque-Stiffness Relation: $k(\tau) = d\,e^{c\,\tau}$

An even more pronounced nonlinearity consists of an exponential relationship. The desired torque-stiffness curve is chosen to be

$$k(\tau) = d\,e^{c\,\tau}. \tag{3.19}$$

$c\,[1/Nm]$ and $d\,[Nm/rad]$ are real positive constants, again. The torque-displacement curve is

$$\tau(\varphi) = -\frac{1}{c}\ln(-c\,d\,\varphi) \qquad \varphi < 0, \tag{3.20}$$

and the stiffness-displacement relationship

$$k_{\text{exp}}(\varphi) = \frac{\partial\tau(\varphi)}{\partial\varphi} = -\frac{1}{c\,\varphi}. \tag{3.21}$$

As the torque curve $\tau(\varphi)$ is only defined for negative displacements, this result has to be modified for practical realization:

$$\tau = -\operatorname{sign}(\varphi)\,\mathrm{a}\ln(-\operatorname{sign}(\varphi)\,\varphi + \mathrm{b}) + \operatorname{sign}(\varphi)\,\mathrm{a}\ln(\mathrm{b}). \tag{3.22}$$

With a and b $\in \mathbb{R}^+$. This is a shifting of the torque-displacement curve along the horizontal axis and does not change the desired property of (3.19). The result can be seen in Fig. 3.6(c).

3.3.3. Achievable Stiffness Range and Adjustability

By inspecting the stiffness characteristics of the quadratic and exponential case (see Fig. 3.6(b), Fig. 3.6(c)) it seems as for $\tau = 0$ the stiffness adjustment range is reduced in comparison to the linear case. This is not true as the range itself can be chosen similar by design, i.e. $k_{\text{lin}}(0)^{max} = k_{\text{quad}}(0)^{max} = k_{\text{exp}}(0)^{max}$ and $k_{\text{lin}}(0)^{min} = k_{\text{quad}}(0)^{min} = k_{\text{exp}}(0)^{min}$. However, the stiffness adjustability is smaller for more nonlinear characteristics: The stiffness adjustability is defined here as the inverse of the change of stiffness per change of adjustment parameter

$$A = \left(\frac{dk(\tau)}{d\tau}\right)^{-1}. \tag{3.23}$$

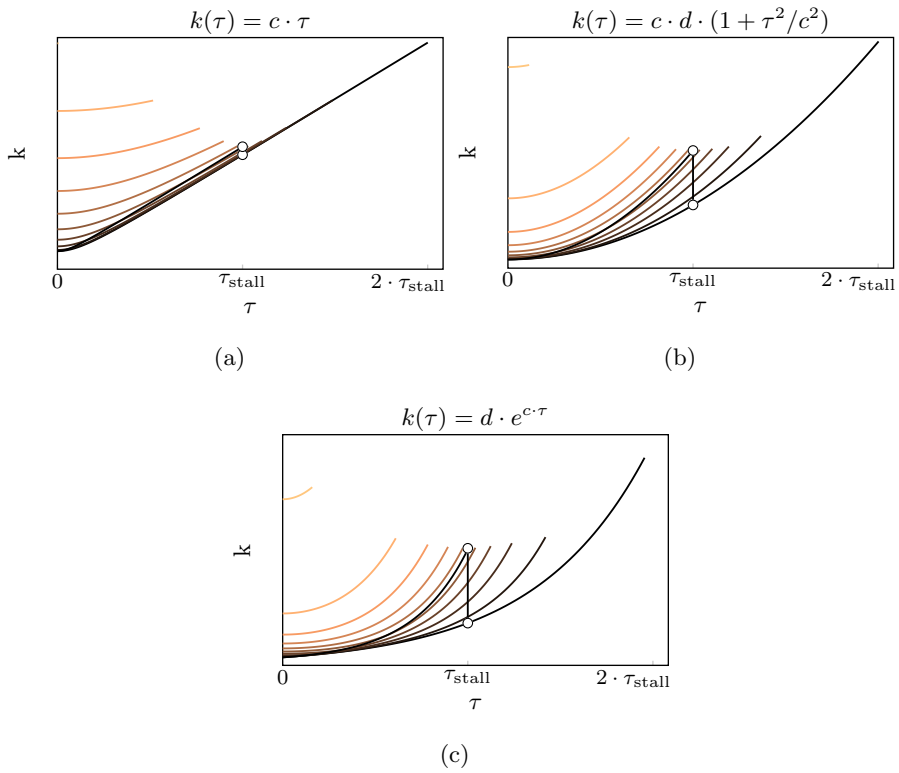

Figure 3.6.: The three torque-stiffness curves (3.11), (3.16), (3.19). The thick curve marks the boundary between the normal and the helping mode region. The vertical lines show the available stiffness range of the helping mode region at $\tau = \tau_{stall}$. The increasing stiffness range from the linear to the exponential plot can be clearly seen.

Assuming first no external torques $\tau_{\text{ext}} = 0$, in the linear case the adjustability is constant and the stiffness can be linearly adjusted by internal torques. In contrast, in the nonlinear case the stiffness adjustability is nonlinear and high internal loads lead to low adjustability and vice versa. For rising external torques $\tau_{\text{ext}} \neq 0$ the same principle applies and the highest stiffness adjustability is given if one motor is unloaded, so around the helping mode boundary. This fact together with the extended stiffness range results in a favourable stiffness-torque area along the helping mode boundary for nonlinear shapes.
This behaviour can be exploited in the context of an application in a robot arm, such as the DLR Hand Arm system. It may be desired to operate the joints at a point in the characteristics where a high adjustability is guaranteed. To generate an optimal stiffness characteristic, joint torque operating regions have to be identified task dependently, using e.g. results from [87]. To give an intuition, shoulder joints are often operated in the middle of the torque range due to gravity loading by the arm weight. Wrist joint torques are often small for the unloaded robot. Therefore, the quadratic or exponential characteristics may be better suited for shoulder joints

and the linear characteristics for the wrist joints. A mathematical description of the desired characteristics may allow the formulation of an optimal control problem.

3.4. Implementation Issues

To increase the practicality and avail of the theoretical analysis from the section before, in the following, implementation issues of a class of BAVS mechanisms are discussed. To preserve the generality of the presentation still an abstract viewpoint is taken with the aim that the presented approach can be applied in other setups. Parts of the analysis are motivated by work from [88].

3.4.1. BAVS Joint Setup

The general setup of a BAVS joint is sketched in Fig. 3.2 right. It requires to decouple the motors from the link by a bidirectional and nonlinear elastic element.
A BAVS setup derived from the normal antagonism using elastic tendons and pulling springs is given in Fig. 3.2 left. A downside of such a realization are the necessary tendon loops which are prone to tendon creep or geometric errors like eccentricity and therefore mechanism failure [22].
Another realization example avoiding tendons is shown in Fig. 3.7 a), where differential gears are used. Often, harmonic drive gears are chosen, where one of the non-actuated parts (flex spline or wave generator) is connected to the link and the other part to the elastic element. Thereby, the spring acts as the decoupling element between the motor and the link, as desired. We use such an arrangement for our following discussions. As the presented approach focuses on stiffness curve design this choice does not limit the generalizability of the obtained results.
A key element of any VSA mechanism is the implementation of the variable stiffness elastic element. The demand to achieve arbitrary motor-spring unit torque shapes as assumed in Section 3.3.2 is challenging for the setups. Many solutions to realize nonlinear elastic elements have been described in literature. A popular approach is based on modulating linear springs with nonlinear kinematic mechanisms. Here, we focus on roller-cam disc setups which turned out to provide great flexibility for the stiffness curve design and have been a popular choice [85, 46, 47, 48, 89]. In the following, several BAVS joint setups based upon cam disc mechanisms are analysed. First, the setup of one single cam disc is treated in the next section.

3.4.2. Basic Cam Disc Properties

The setup of one single cam disc and the linear spring is depicted in Fig. 3.8. This simplified model can be obtained either from a planar realization [85, 89] or from 'unwinding' a revolute joint, e.g. [46]. In the mechanism, a roller is pushed by a linear spring against a cam disc and the spring force together with the inclination of the disc generates a deflecting force.
The resulting forces can be analysed by considering the path of the center of the roller $f_i(\varphi_x)$

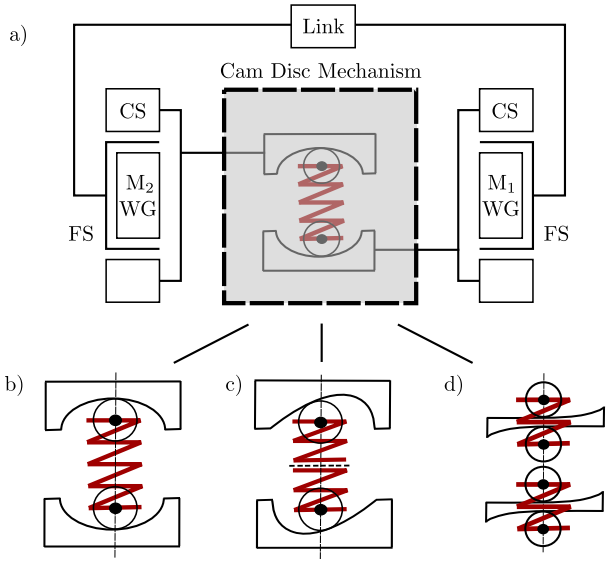

Figure 3.7.: Differential gears are used (harmonic drives: wave generator WG, flex spline FS, circular spline CS) to introduce the elastic coupling in between the link and the motors (M_1, M_2), see a). Three different nonlinear spring solutions as a combination of linear springs and cam discs are considered. In b) the simplest setup with two symmetrical cam discs and one spring is depicted. c) shows the setup of two asymmetrical cam discs with two springs. The schematic d) presents the most complex setup consisting of four asymmetrical cam disc geometries with two springs. Compare also Fig. 3.12 and Fig. 3.13

w.r.t. the deflection φ_x, where i indicates the i-th roller. The geometry of the cam disc[4] is described by the function f_{ci}. This cam disc geometry can be created by taking the cam disc path f_i and sliding the roller along it. The outer convex hull of the resulting shape is the cam disc geometry f_{ci}, see Fig. 3.8. It is used for the mechanical realization of the cam disc.
The repelling force is

$$F_i(\varphi_x) = k_s f_i(\varphi_x) f_i'(\varphi_x), \tag{3.24}$$

where k_s is the spring rate and $f_i'(\varphi_x) = \frac{\partial f_i(\varphi_x)}{\partial \varphi_x}$ is the derivative of the cam disc path. The stiffness of the setup is defined with (2.13) to be

$$k(\varphi_x) = k_s(f_i'(\varphi_x)^2 + f_i(\varphi_x) f_i''(\varphi_x)). \tag{3.25}$$

To design a cam disc path that realizes a certain torque-displacement curve (see Section 3.3.2), the differential equation (3.24) has to be solved for $f_i(\varphi_x)$. Similar as in 3.3.2 an analytical

[4]In the following we will use the term 'cam disc path' to refer to f_i and 'cam disc geometry' for f_{ci}.

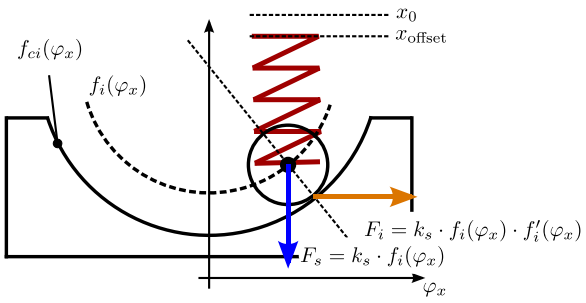

Figure 3.8.: A schematic of a simplified cam disc mechanism. The spring is constrained to a vertical motion. The repelling force F_i is defined by the spring force F_s and the slope of the cam disc path f_i'. The combination of the spring and cam disc generates the required nonlinear stiffness property of the joint. The desired cam disc path f_i can be used together with the roller to generate the cam disc geometry f_{ci}: By sliding the roller along the cam disc path, a shape is generated. The outer convex hull of this shape defines the cam disc geometry f_{ci}.

solution cannot be achieved for arbitrary force-displacement curves $F_i(\varphi_x)$ but exemplary cases can be analysed. This is done in the following subsection for several setups to highlight their properties and the approach.
Independent of a particular solution, some basic constraints and properties of the achievable stiffness can be identified. These can be achieved from (3.25):

- To guarantee proper rolling of the cam roller, the curvature of the cam disc geometry has to be less than the curvature of the cam roller $f_{ci}'' \leq R''$. Please notice, from mechanism side it is possible to realize discontinuities of $f_i(\varphi_x)$ by designing cam disc geometries where $f_{ci} = R$ locally, low tolerances during manufacturing assumed.

- Furthermore, the cam disc path $f_i(\varphi_x)$ influences the stiffness among others in (3.25). Given a certain cam disc path, it is possible to offset the position $f_i(\varphi_x)$ by preloading the spring $x_0 + x_{\text{offset}}$. It results $\tilde{f}_i(\varphi_x) = f_i(\varphi_x) + x_{\text{offset}}$, $\tilde{f}_i'(\varphi_x) = f_i'(\varphi_x)$, $\tilde{f}_i''(\varphi_x) = f_i''(\varphi_x)$. Thereby, the resulting stiffness can be influenced without changing the cam disc path.

  A down side is that a certain amount of spring energy is used for the pretensioning. This is not desirable as the maximum spring energy sets the bounds for the spring dimensions. In other words, the more spring energy is used for pretensioning, the bigger the spring needs to be. This can be undesirable if a small construction space is favoured.

3.4.3. BAVS Mechanism Arrangements

To outline the possibilities of cam disc based BAVS joint mechanisms, here we analyse setups where certain mechanical design parameters are varied as suggested in [88]. The contribution is the analytical approach. The differential gear setup is used where the elastic element is subject to alternations. The analysed arrangements are depicted in Fig. 3.7 and the varied parameters are

- number of springs (1, 2 or 4),
- number of cam discs (2 or 4),
- shape of cam discs (symmetric or asymmetric).

The simplest setup is the *single spring* solution using only one linear spring, as shown in Fig. 3.7 b) with symmetric cam discs. The *double spring* solution uses two instead of only one spring, but in the same setting with two cam discs, see Fig. 3.7 c). The third analysed setup is shown in Fig. 3.7 d) and contains *two springs and four cam discs*. Furthermore, the role of *asymmetric cam discs* is discussed in the following.

Single spring solution

The first possible setup is a combination of one spring and two symmetric cam discs (see Fig. 3.7 b). As only one linear spring is used to implement the two elastic elements, the least parts and construction space of the discussed arrangements is needed. The reaction force obtained from each symmetric cam disc at the link is

$$\tau_i = r_{\text{disc}} k_s (f_1 + f_2)(f_1' + f_2'). \tag{3.26}$$

where $f_1 = f_1(\varphi_{x1}), f_2 = f_2(\varphi_{x2})$. f_1, f_2 and f_1', f_2' are as used in (3.24). The constant r_{disc} is the radius between the center of rotation of the joint and the cam disc, defining the resulting torques from the cam disc forces. In the following, both constants are assumed to be $r_{\text{disc}} = 1$ m and $k_s = 1$ N/m without loss of generality.
To show the implications of this setup, a cam disc profile for a desired $\tau - k$ characteristic is generated. Here, we chose the quadratic torque-stiffness relation (see Section 3.3.2) which shall be achieved for the relaxed case (no pretension, $\sigma = 0$). It is desired to find the corresponding torque-displacement curve. Therefore, the joint torque is equated with the desired shape

$$\tau = \sum_{i=1,2} \tau_i = \tau_1 + \tau_2 = c \tan(d\varphi_x), \tag{3.27a}$$

$$\tau_1 = k_s(f_1 + f_2)f_1', \quad \tau_2 = k_s(f_1 + f_2)f_2'. \tag{3.27b}$$

The parameters c and d are constant. In (3.27b) a consequence of the 'sharing' of the linear spring by the cam discs is visible, as a coupling between the two elastic torques arises: Each

side's torque depends also on the other sides deflection. The coupling terms arise also in (3.26) and are given by

$$f_1 f_2' + f_2 f_1'. \tag{3.28}$$

These coupling terms prohibit independent curve design for each side. To still be able to achieve the torque-displacement curves, symmetrical loading $f_1 = f_2$ is assumed and the differential equation of one cam disc path $f_i(\varphi_x)$ can be formulated

$$\tau_i = \frac{1}{2} c \tan(d\ \varphi_x) = 2 f_i(\varphi_x) \frac{\mathrm{d}f_i(\varphi_x)}{\mathrm{d}\varphi_x}. \tag{3.29}$$

The cam disc path results to be

$$\frac{1}{2} c \int \tan(d\varphi_x) \mathrm{d}\varphi_x = 2 \int f_i(\varphi_x) \mathrm{d}f_i(\varphi_x) \tag{3.30a}$$

$$\Leftrightarrow \qquad f_i(\varphi_x) = \sqrt{-\frac{c}{2d} \log(\cos(d\varphi_x))}. \tag{3.30b}$$

The desired quadratic $\tau - k$ characteristic is achieved in the relaxed case, see Fig. 3.9. However, the characteristics is heavily distorted for pretension states $\sigma \neq 0$. The problem arises due to the coupling terms (3.28) and can be understood by noting that the cam disc paths show a discontinuity at $\varphi_x = 0$. Looking only at the first cam disc[5] with a given pretension $f_1(\sigma) = 0$ while $f_1'(\sigma) \neq 0$, see Fig. 3.10. However, at this pretension the other cam disc $f_2(\sigma) \neq 0$ and therefore the resulting $\tau_1 = f_2(\sigma) f_1'(\sigma) \neq 0$: as the cam disc path derivative $f_1'(\sigma)$ is discontinuous also the resulting τ_1 is so, which causes the effects visible in Fig. 3.9.
The discontinuities can be avoided by imposing the constraint $f_i'(0) = 0$. However, this constraint limits the curve shape design possibilities and hardens the mathematical analysis.
Two alternative setups bypass the discontinuity problem and are considered here.

Double spring solution

A similar joint setup involves using two springs in combination with two symmetrical cam discs. The setup, shown in Fig. 3.7 c) (there depicted with asymmetric cam discs), provides greater flexibility but also requires more parts and little more space. The joint force of the setup is calculated by

$$\tau = r_{\mathrm{disc}} k_s (f_1 f_1' + f_2 f_2'). \tag{3.31}$$

The advantage of the two-spring setup is the independent design of the cam discs. Assuming again a desired quadratic $\tau - k$ characteristic

$$\tau = \sum^{i} \tau_i = \tau_{m1} + \tau_{m2} = c \tan(d\varphi_x), \tag{3.32a}$$

$$\tau_i = f_i f_i', \quad i = 1, 2. \tag{3.32b}$$

[5] The same is true for the other cam disc with index $(.)_2$ for symmetry reasons.

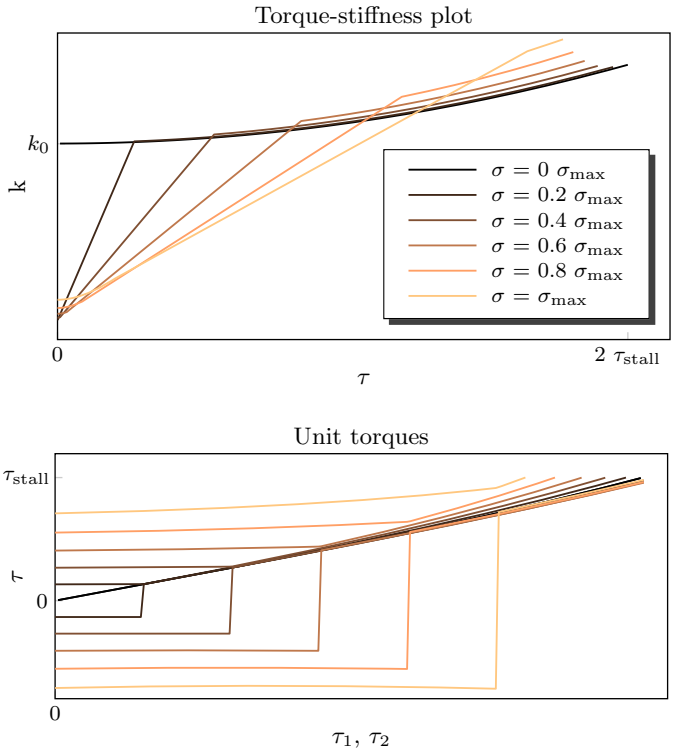

Figure 3.9.: The single spring solution. Upper plot: the desired quadratic $\tau - k$ characteristic is only achieved in the relaxed case for $\sigma = 0$. For any other pretension state, discontinuities due to the coupling terms (3.28) arise. Lower plot: also the resulting unit torques are discontinuous.

The single curves can be independently designed and the cam disc path results to be

$$\tau_{mi} = \frac{1}{2} c \tan(d\varphi_x) = f_i(\varphi_x) \frac{\mathrm{d}f_i(\varphi_x)}{\mathrm{d}\varphi_x} \tag{3.33a}$$

$$\Leftrightarrow \qquad f_i(\varphi_x) = \sqrt{-\frac{c}{d} \log(\cos(d\varphi_x))}. \tag{3.33b}$$

The two-spring setup avoids discontinuities, as no coupling terms appear. In particular, the slopes f_i' of the curves are only discontinuous if $f_i = 0$. Therefore, the product $f_i f_i'$ is zero only if $f_i = 0$. The resulting force and stiffness curves are smooth, see Fig. 3.11.

Two springs and four cam discs

The last setup analysed contains four cam discs with asymmetric shape in combination with two springs see Fig. 3.7 d). The asymmetric cam discs provide a non-zero stiffness at zero deflection, without discontinuity in the cam disc paths. Also, by using two opposing cam discs the linear

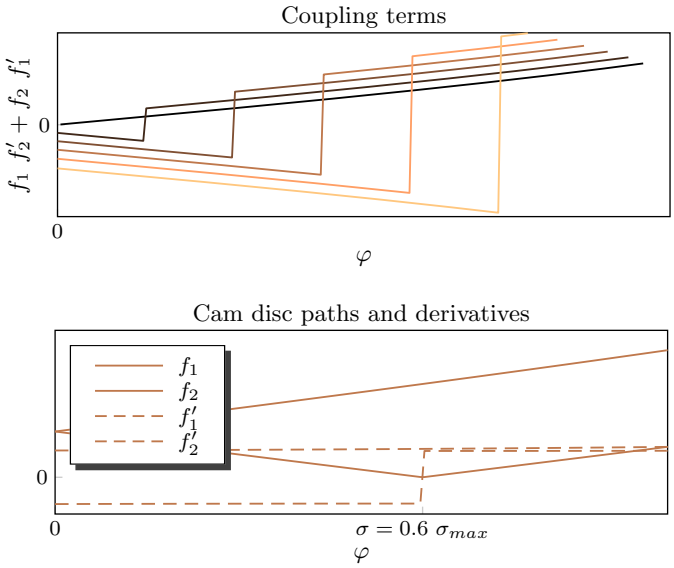

Figure 3.10.: Coupling terms and cam disc shapes for quadratic $\tau - k$ profile. The discontinuity is generated by a stiffness $\neq 0$ at the pretension σ. The discontinuity has an effect on the $\tau - k$ characteristic (see Fig. 3.9), which is caused by the coupling terms.

spring can be initially tensioned without loading the motors. This setup provides great flexibility for stiffness curve design, i.e. all the curves from Section 3.3 can be implemented. A downside is the mechanism complexity. The joint force is

$$\tau = r_{\text{disc}} k_s ((f_1 + f_2)(f_1' + f_2') + (f_3 + f_4)(f_3' + f_4')). \tag{3.34}$$

Asymmetric cam discs

Instead of using symmetric cam disc shapes, also asymmetric shapes can be considered. Asymmetric disc shape means here that the minimum of f_i is not located at $\varphi_x = 0$ mm, see Fig. 3.7 c). Asymmetric shapes allow to achieve high stiffness at the relaxed joint equilibrium position $\varphi_x = 0$ mm without designing cam disc geometries where $f_{ci} = R$ locally. Asymmetric shapes can be interpreted as pretensioned symmetric shapes. A disadvantage is, that for the single and double spring solution the motors are already loaded at the rest position.
In order to achieve a continuous asymmetric shape, e.g. a piecewise function can be used. The offset of the minimum from the center is described in the following by o_a. An example for a cam disc realization with asymmetric disc shape is

$$f_i(\varphi_x) = \begin{cases} R_1 - \sqrt{(R_1^2 - (\varphi_x - o_a)^2)} & : \varphi_x < o_a \\ R_2 - \sqrt{(R_2^2 - (\varphi_x - o_a)^2)} & : \varphi_x > o_a, \end{cases} \tag{3.35}$$

where R_1 and R_2 are different radii. An asymmetric shape is used in the mechanical BAVS joint realization as described in the next section.

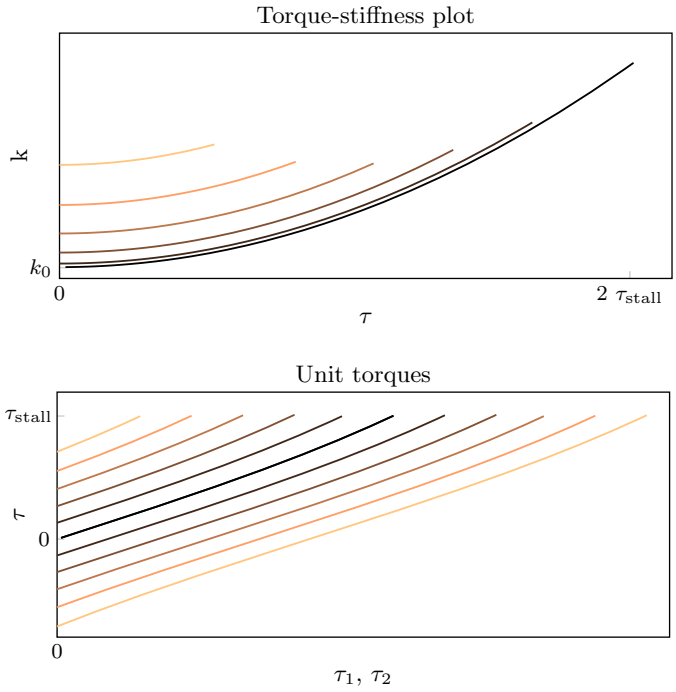

Figure 3.11.: The double spring solution. The desired quadratic $\tau - k$ characteristic is precisely achieved. Furthermore, a smooth behaviour results for all pretension cases.

3.5. Experimental Results

A BAVS implementation is used in the DLR Hand Arm System as a lower arm rotation joint. It is located in the lower arm close to the elbow. The main constraints in this application are necessary small dimensions and high power density, as the lower arm contains further 42 finger and wrist drive units.

A considered mechanism arrangement is the single spring solution which enables small construction space. However, to avoid discontinuities the cam disc path derivative needs to equal zero at $\varphi_x = 0$. This results in low restoring forces around zero deflection and thereby limits the accuracy of the joint in the presence of friction effects, which occur in practice. The four cam disc solution allows for more freedom in cam disc design thus possible higher restoring forces. A downside is the more complex setup as more parts are involved.

The double spring solution with asymmetric cam discs combines the advantages of few parts and good design freedom regarding the torque - stiffness characteristics. Therefore, a BAVS joint based on the double spring solution is used in the DLR Hand Arm System. A simplified sketch of the realization is shown in Fig. 3.12 top. In comparison to Fig. 3.2, the positions of the motors and springs are exchanged, without changing the functionality. The connection to the common link is realized by a bevel gear, as a change of the axis of rotation was necessary in the DLR Hand Arm System. A detailed setup sketch is shown in Fig. 3.12 bottom. The

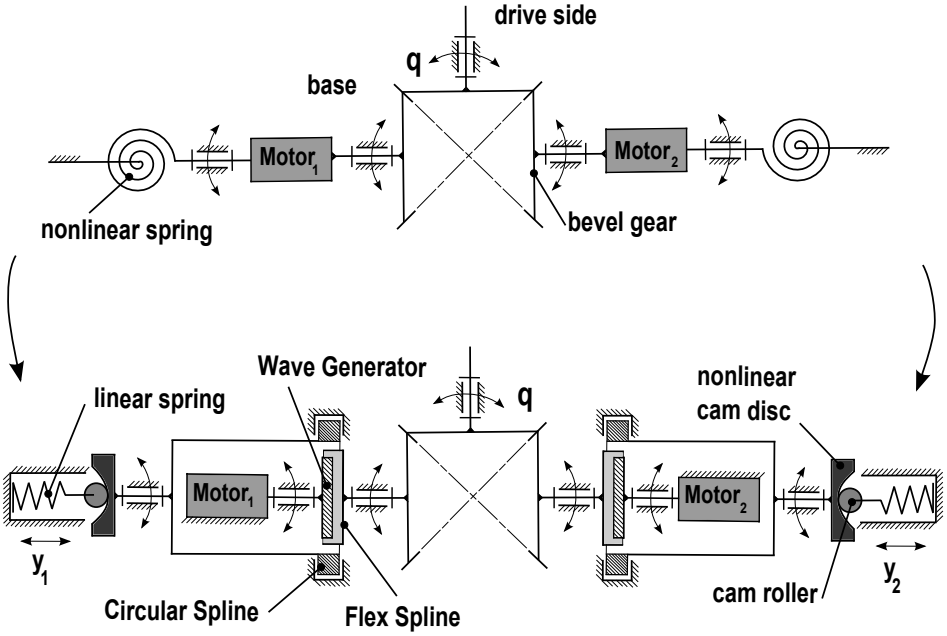

Figure 3.12.: Implementation of the BAVS joint in the Hand Arm System—The upper figure shows a simplified representation, the lower figure a more detailed version of a double spring solution with symmetric cam discs (reprint from [90]).

setup is symmetric and can be mirrored at the link axis. The two nonlinear elastic elements are realized by a rotational arrangement of linear springs and cam discs.[6] Harmonic Drives are used as gearboxes in a differential way. Each circular spline is attached to a nonlinear elastic element. The motors are coupled with the wave generators and the flex splines with the bevel gear. A CAD drawing of the setup is shown in Fig. 3.13.
The cam disc profiles have been chosen according to (3.35) as two circle shapes with the values

Variable	Value	Variable	Value
R_1	9.5 mm	x_{offset}	2 mm
R_2	4.5 mm	r_{disc}	21.65 mm
o_a	1.9 mm	k_s	22.1 N/mm

The range is $\varphi_{xi}^{max} = \pm 5.85$ mm. This planar curve is used in the rotational mechanism and a maximal rotational joint deflection of $\varphi = \pm 0.2758$ rad results. The minimum of the cam disc is located at $\varphi = \pm 0.0873$ rad. The exact values for curve shape are such that the restoring forces are high enough around $\varphi = 0$ rad (stiffness $k \approx 6$ Nm/rad) while not generating too much motor load ($\tau_i(\varphi = 0) \approx 0.22$ Nm).
The measured $\tau - \varphi$ characteristics is given in Fig. 3.14. The ideal characteristics as obtained from theory is also given in the plot as dotted-dashed curves. The resulting $\tau - k$ curves are

[6] Note that in this sketch the lever arm of the two cam discs is depicted in a planar way, but it is set up rotationally.

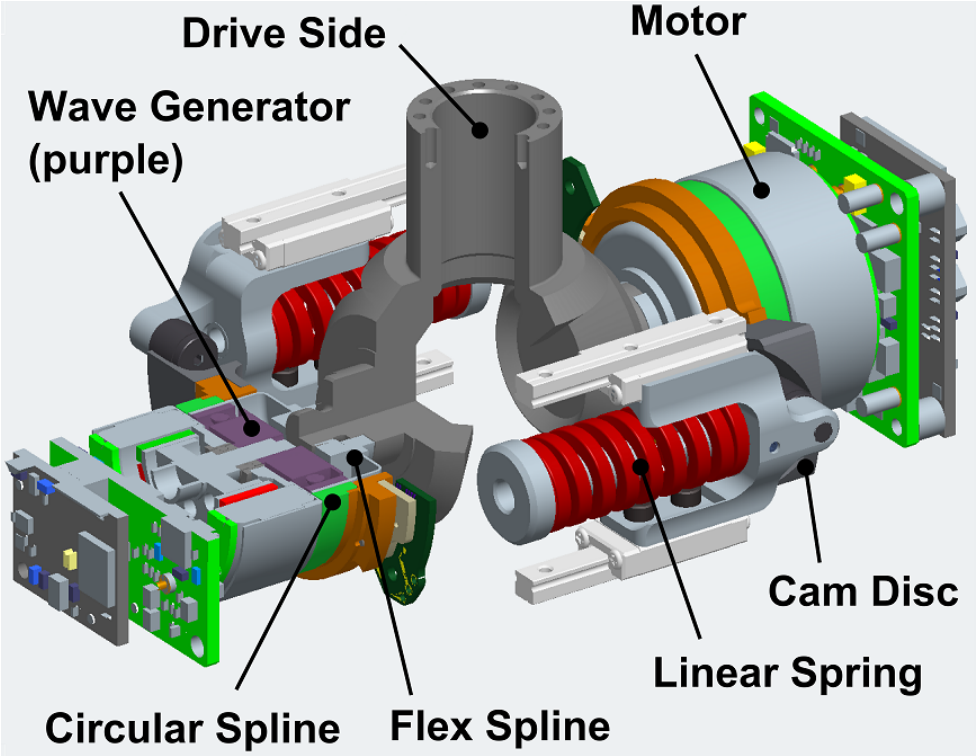

Figure 3.13.: A CAD drawing of the BAVS joint as it is implemented in the forearm rotation of the DLR Hand Arm System with asymmetric cam disc shape and double spring solution. The mechanism dimensions are 95 mm by 56 mm by 45 mm.

plotted in Fig. 3.15. To achieve the plot, the torque curves have been fitted by polynomials and the derivative is used as stiffness. Furthermore, measurements of the helping mode boundary are given in Fig. 3.17. The helping mode boundary is defined as the curve, where the motors start to support each other. In the symmetric cam disc setup, it is measured by fixing one motor and keeping the second spring undeflected (follow the joint deflection with the motor). To measure it for asymmetric cam discs where both springs are deflected for the 'relaxed' ($\sigma = 0$ rad) joint, the link is deflected until one cam disc reaches its minimum. Then, the motor follows the link motion, such that the minimum is maintained. As a results, the helping mode boundary follows the torque curve of the relaxed case until the cam disc minimum at $\varphi = \pm 0.0873$ rad is reached. Afterwards, it crosses the other torque curves. To show the power consumption effects of the asymmetric cam disc, the motor currents of the setup for rising pretensions are given in Fig. 3.16. The motors are drawing power even at $\varphi = 0$ rad as the asymmetric cam discs generate a spring load. It is a general property of BAVS joints that a stiffness increase requires co-contraction of the drive units and thereby increases energy consumption.
The differences between the theoretical curves and the measurements can be attributed to several causes. First, the model used considers an ideal mechanism neglecting parasitic compliance. This

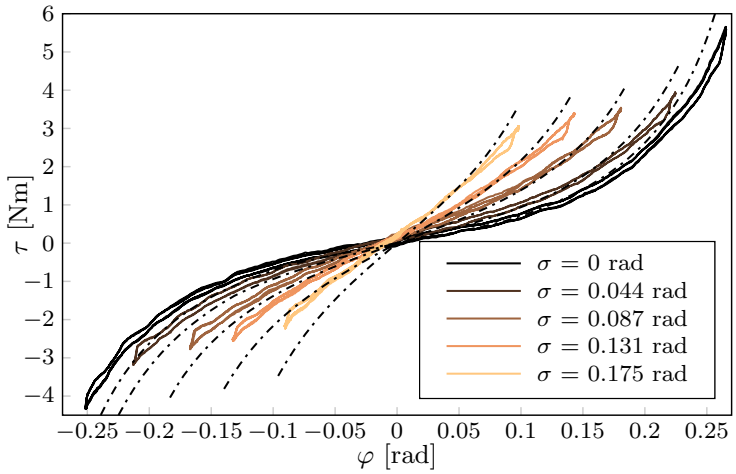

Figure 3.14.: Bold: The measured torque displacement curves of the BAVS joint as used in the lower arm rotation joint of the DLR Hand Arm system. Dotted-dashed: The theoretical curves. Two asymmetric cam discs shapes together with two springs are realized. Several pretension states are shown.

causes the sagging of the stiffness curves in Fig. 3.15 for increasing loads and pretension. Second, tolerances in the manufacturing process distort the results. Last, the measuring apparatus adds further inaccuracy. Summarizing it is to say that the experimental results are qualitatively convincing and confirm the theoretical findings. The validity of the approach can be concluded.

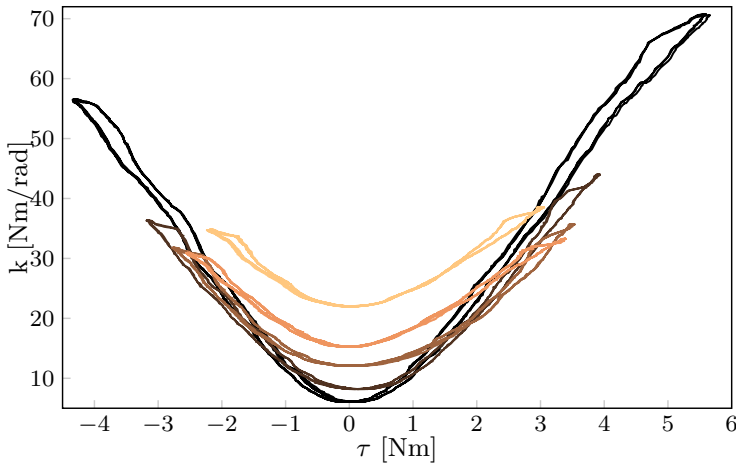

Figure 3.15.: Torque - stiffness curves as resulting from the measurements of Fig. 3.14. To obtain the stiffness, a polynomial fit of the torque curves has been used. The sagging of the curves for higher loads and pretension may be attributed to unmodeled compliance in the joint. Still, the measurements show the validity of the design approach.

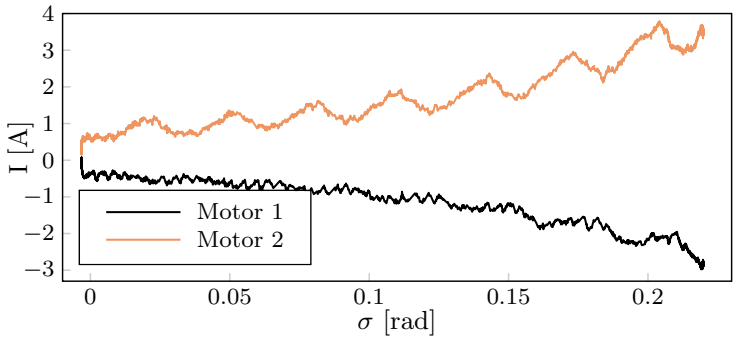

Figure 3.16.: Measurements of the motor currents for increasing stiffness. It can be seen that even at the relaxed case $\sigma = 0$ motor power is required due to the asymmetric cam discs. For higher pretensions higher currents result. The ripples are attributed to the harmonic drives.

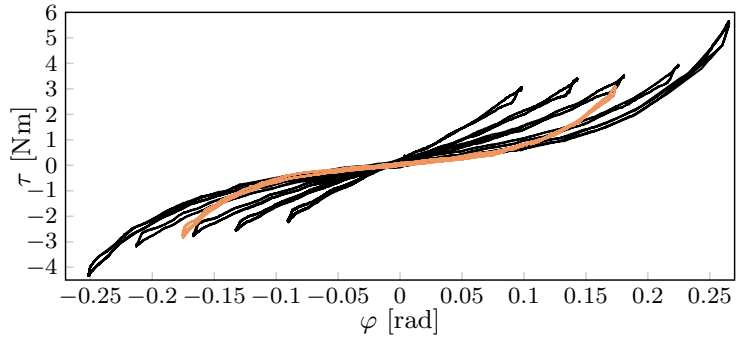

Figure 3.17.: The measured helping mode boundary overlaid on the data of Fig. 3.14. The mechanism is in the normal mode until the minimum of the cam discs is reached at $\varphi = 0.0873$ rad. Therefore the helping mode boundary equals the relaxed mechanism up to this deflection. For higher deflections, the two motors support each other. The improved performance of the BAVS setup with respect to a normal antagonistic joint setup can be seen in this plot: The overall joint load is almost twice the stall torque of one motor.

3.6. Discussion

Robotic joint design allows for a multitude of choices and many solutions exist. In this case study, insights into design possibilities are given, and the complexity of such a design process is revealed.
As a final remark it is to say that stiffness design for BAVS joints is influenced by several effects. The most important points are

- Nonlinear stiffness profiles are required to enable a stiffness variation by co-contraction. The co-contraction generates internal torques. Only if a stiffness dependency upon internal torques exists, the link stiffness is altered.
- The stiffness behaviour of the normal mode has to be considered. Given the nonlinear profile from the point before, a stiffness variation is given.
- The stiffness behaviour of the helping mode has to be considered. The analysis in Section 3.3.2 revealed that certain requirements have to be met to enable a stiffness variation in the helping mode. The design effort to achieve such a property is considerable. To be relevant for an application it has to be analysed if such a stiffness variation in the helping mode is desired and can be achieved by the control system.
- Furthermore the properties of a realization principle have to be regarded. Cam disc setups are often chosen instead of tendon based setups due to their favourable mechanical properties. The analysis in this chapter shows the extent of such a design process.

All these steps require a specific dimensioning using either an analytic approach and/or simulations. The design cannot be evaluated in a decoupled fashion.
In general, torque-stiffness curve design is task dependent. A progressive shape is often used, where reasons range from the protection of hardware limits (see Section 2.2.2), to biological motivation [86]. The antagonistic setup and the bidirectional antagonism in particular justify and provide quantifiable guides for such a stiffness characteristic, see the design method in Section 3.3.2. However, from a controls perspective such a characteristics has to be seen differentiated. The nonlinearity of the joint stiffness has consequences for controller design, see e.g Section 6.1.5 and Section 5.4.
An mentionable advantage of the BAVS setup is the use of two equally sized motor-spring units. High power density and in some cases failure robustness can be achieved. However, the mechanical connection of the units requires additional gearboxes and thereby increases joint friction. Furthermore, the continuously required power to maintain pretension states is a drawback.

4. Energy Shaping Approaches

An approach to control robotic systems is to define a desired system and to construct feedback laws which implement this characteristic in a closed-loop manner. A class of such controllers are energy shaping controllers where the goal system is defined in terms of potential and kinetic energy. This approach is beneficial regarding the required model accuracy as control torques are generated such that the system behaves according to the specified goal dynamics without the exact knowledge of a system model. Additionally, the need for higher derivatives of system state information is reduced. Furthermore, if the resulting system can be interpreted in a physical context, the analysis of stability is facilitated.
Several energy shaping controllers for robotic systems have been reported in the literature. While constructive methods exist for directly actuated (rigid robot) systems [91, 92] energy shaping control of underactuated systems is limited to a subclass of systems. The mathematical challenges and the resulting complexity of the approach are subjects of recent research [93, 94, 95, 96, 18, 97, 98]. Flexible joint robots and the discussed variable stiffness robots represent underactuated systems and such methods are applied in the context.
In this section two energy shaping methods suitable for variable stiffness robots are discussed. The first method allows to formulate a controller to adjust the link side equilibrium position of the robot arm. The second controller uses feedback of non-actuated states which can be physically interpreted to enhance controller performance. The methods have been developed for flexible joint robots in [18, 97] and have been transferred to variable stiffness robots in [98]. Due to their beneficial properties they depict a basis for several of the controllers developed in the remainder of this work.
The two energy shaping techniques are fundamental for several of the controllers presented in this thesis. Due to their passivity and model-structure preserving properties, they can be applied with ease.

4.1. Potential Energy Shaping

Many robotic tasks are defined as trajectories in operational space of the tool center point or in configuration space. That can be theoretically described by specifying all n link side positions $\boldsymbol{q}$ only. However, it is apparent from (2.21) that the input variables $\boldsymbol{\tau}_m$ and the task state variables $\boldsymbol{q}$ are *non-collocated*. Two signals are said to be *collocated* if they constitute a power port of a subsystem. A power port is given if the product of these two variables represents the

instantaneous power flow [99]. This is a force and a velocity (or a linear operator of velocity, such as position). The non-collocation stems from the fact that the motor and the link dynamics are interconnected by an elastic element (2.9b). Therefore, $\boldsymbol{\tau}_m$ and $\boldsymbol{q}$ do not allow to conclude on the power of the link or motor and therefore are non-collocated. Controllers have to take into account, that the motor represents the control input but the link side coordinate does not have a direct input. Controllers which neglect the coupling dynamics are exposed to stability issues. A solution is to only regulate $\boldsymbol{\theta}$ and neglect the compliance. However, due to the introduced mechanical stiffness of VSA, such controllers are prone to large position errors. An elegant way to both ensure stability and accurately execute the task has been subsumed in [98]. The approach is formulated for robots with any sort of joint elasticity. Here, it is adapted to the VSA case and verified in experiments.

4.1.1. Statically Equivalent Joint Coordinates

The main idea is to construct a collocated variable $\bar{\boldsymbol{q}}$ that is statically equivalent to the link side position $\boldsymbol{q}$ but only depends on $\boldsymbol{\theta}$. Therefore, a static version of the equations (2.21) is required, i. e. $\dot{\boldsymbol{x}} = \boldsymbol{0}$, where $\boldsymbol{x} = (\boldsymbol{\theta}, \boldsymbol{q})^T \in \mathbb{R}^k$ is denoting the robot state vector. This can be derived using the robots potential energy term $V(\boldsymbol{x})$ of the Lagrangian (2.5). The static equilibrium is achieved if

$$\boldsymbol{f}_{\boldsymbol{\theta}}(\boldsymbol{\theta}, \boldsymbol{q}) := \frac{\partial V(\boldsymbol{x})}{\partial \boldsymbol{\theta}} = \boldsymbol{\tau}_m \tag{4.1a}$$

$$\boldsymbol{f}_{\boldsymbol{q}}(\boldsymbol{\theta}, \boldsymbol{q}) := \frac{\partial V(\boldsymbol{x})}{\partial \boldsymbol{q}} = \boldsymbol{0} \tag{4.1b}$$

holds. The special properties of (4.1b) are the key elements for the existence of $\bar{\boldsymbol{q}}$. First, the potential function $V(\boldsymbol{\theta}, \boldsymbol{q})$ is positive definite with respect to $\boldsymbol{q}$. This is true for the robot dynamics part and is mainly a constrain on the joint elasticity function. The assumption is fulfilled for all the DLR Hand Arm System joints. Second, the sum of the joint stiffness (2.13) and the Hessian of the gravity potential is bounded

$$\alpha_1 \|\boldsymbol{q}\|^2 > \boldsymbol{q}^T \frac{\partial^2 V(\boldsymbol{\theta}, \boldsymbol{q})}{\partial \boldsymbol{q}^2} \boldsymbol{q} > \alpha_2 \|\boldsymbol{q}\|^2 \tag{4.2a}$$

$$\left| \frac{\partial V(\boldsymbol{\theta}, \boldsymbol{q})}{\partial \boldsymbol{q} \partial \boldsymbol{\theta}} \right| > \alpha_3. \tag{4.2b}$$

These conditions cause the convex nature of $V(\boldsymbol{x})$ and ensure exactly one single solution of $\boldsymbol{q}$ for each $\boldsymbol{\theta}$

$$\exists \bar{\boldsymbol{q}} : \mathbb{R}^n \to \mathbb{R}^n \text{ such that } \boldsymbol{f}_{\boldsymbol{q}}(\boldsymbol{\theta}, \bar{\boldsymbol{q}}(\boldsymbol{\theta})) = \boldsymbol{0}, \forall \boldsymbol{\theta} \in \mathbb{R}^n. \tag{4.3}$$

Thus, $\bar{\boldsymbol{q}}$ is the static equivalent to the link coordinate $\boldsymbol{q}$, solely based upon $\boldsymbol{\theta}$. By differentiating $\boldsymbol{f}_{\boldsymbol{q}}(\boldsymbol{\theta}, \bar{\boldsymbol{q}}(\boldsymbol{\theta}))$ with respect to $\boldsymbol{\theta}$ the partial derivative of $\bar{\boldsymbol{q}}$,

$$\boldsymbol{J}_{\bar{\boldsymbol{q}}}(\boldsymbol{\theta}) = \frac{\partial \bar{\boldsymbol{q}}(\boldsymbol{\theta})}{\partial \boldsymbol{\theta}} = -\left(\frac{\partial^2 V(\boldsymbol{\theta}, \bar{\boldsymbol{q}}(\boldsymbol{\theta}))}{\partial \bar{\boldsymbol{q}}(\boldsymbol{\theta})^2} \right)^{-1} \frac{\partial V(\boldsymbol{\theta}, \bar{\boldsymbol{q}}(\boldsymbol{\theta}))}{\partial \bar{\boldsymbol{q}}(\boldsymbol{\theta}) \partial \boldsymbol{\theta}}, \tag{4.4}$$

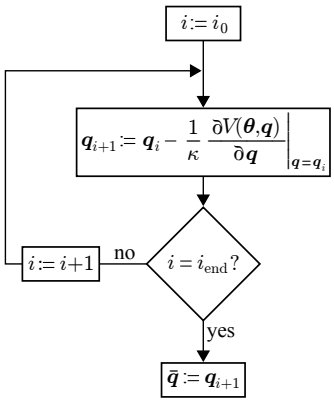

Figure 4.1.: A numerical iteration scheme is used to calculate the static link side equivalent variable $\bar{\boldsymbol{q}}(\boldsymbol{\theta})$. Fast convergence can be guaranteed by the convex nature of the problem and the depicted simplified gradient method. In terms of the implementation on the real system, one has to keep in mind that the numerical costs can be greatly reduced by using the solution from the last time step as starting condition for the current one. The rate of convergence can be controlled via κ to a certain extend.

can be calculated.
The properties (4.2) allow to conclude that the mapping $\bar{\boldsymbol{q}}(\boldsymbol{\theta})$ is a global diffeomorphism, i. e. $\boldsymbol{J}_{\bar{\boldsymbol{q}}}(\boldsymbol{\theta})$ is non-singular,

$$\sup_{\boldsymbol{\theta}\in\mathbb{R}^n} \left\| \boldsymbol{J}_{\bar{\boldsymbol{q}}}(\boldsymbol{\theta})^{-1} \right\| < \infty. \tag{4.5}$$

This inequality is fulfilled as

$$\left\| \boldsymbol{J}_{\bar{\boldsymbol{q}}}(\boldsymbol{\theta})^{-1} \right\| < \left\| \left(\frac{\partial V(\boldsymbol{\theta}, \bar{\boldsymbol{q}}(\boldsymbol{\theta}))}{\partial \bar{\boldsymbol{q}}(\boldsymbol{\theta}) \partial \boldsymbol{\theta}} \right)^{-1} \right\| \left\| \frac{\partial^2 V(\boldsymbol{\theta}, \bar{\boldsymbol{q}}(\boldsymbol{\theta}))}{\partial \boldsymbol{q}(\boldsymbol{\theta})^2} \right\| < \alpha_1 \alpha_3. \tag{4.6}$$

For a detailed derivation see [98]. Finding $\bar{\boldsymbol{q}}(\boldsymbol{\theta})$ requires a numerical algorithm in case of complex nonlinear systems such as VSA robots. However, due to the above-mentioned convexity properties, already the simplified, iterative gradient method in Fig. 4.1 converges extremely fast to $\bar{\boldsymbol{q}}(\boldsymbol{\theta})$. Now, one can formulate a passive controller with PD components for minimizing the position error and selective dissipation of kinetic energy:

$$\boldsymbol{\tau}_m = \boldsymbol{g}(\bar{\boldsymbol{q}}(\boldsymbol{\theta})) - \boldsymbol{J}_{\bar{\boldsymbol{q}}}^T(\boldsymbol{\theta}) \boldsymbol{K}_p (\bar{\boldsymbol{q}}(\boldsymbol{\theta}) - \boldsymbol{q}_d) - \boldsymbol{K}_d \dot{\boldsymbol{\theta}}. \tag{4.7}$$

The matrices $\boldsymbol{K}_p$ and $\boldsymbol{K}_d$ are the positive definite, symmetric P- and D-gains. A gravity compensation term $\boldsymbol{g}(\bar{\boldsymbol{q}}(\boldsymbol{\theta}))$ also based on the static equivalent completes the control law.
In this section, we exemplarily specify to control the steady state of the link coordinates $\boldsymbol{q}$. The approach is not restricted to this particular choice but gives great flexibility regarding output coordinates. An alternative, very popular choice is a control of Cartesian coordinates.

4.1.2. Statically Equivalent Cartesian Coordinates

A task can be generally formulated to control m independent output variables $\boldsymbol{y} = \boldsymbol{h}(\boldsymbol{\theta}, \boldsymbol{q})$ to desired constant values $\boldsymbol{y}_\mathrm{d} \in \mathbb{R}^m$. In the following, the well known set of Cartesian coordinates is considered. These task coordinates are defined by a mapping $\boldsymbol{x} = \boldsymbol{f}(\boldsymbol{q}) \in \mathbb{R}^m$. An important relation can be derived using the Jacobian matrix $\boldsymbol{J}(\boldsymbol{q}) = \frac{\partial \boldsymbol{f}(\boldsymbol{q})}{\partial \boldsymbol{x}}$ to

$$\dot{\boldsymbol{x}} = \boldsymbol{J}(\boldsymbol{q})\dot{\boldsymbol{q}}. \tag{4.8}$$

In this formulation, the Cartesian task coordinates depend upon the non-collocated joint variables $\boldsymbol{q}$. To achieve a collocated version of the relation, the same approach from the section before can be used. The statically equivalent output coordinates are given by $\bar{\boldsymbol{x}}(\boldsymbol{\theta}) = \boldsymbol{f}(\bar{\boldsymbol{q}}(\boldsymbol{\theta}))$: considering the control law

$$\boldsymbol{\tau}_m = \boldsymbol{g}(\bar{\boldsymbol{q}}(\boldsymbol{\theta})) - \boldsymbol{J}_{\bar{\boldsymbol{x}}}^T(\boldsymbol{\theta})\boldsymbol{K}_p(\bar{\boldsymbol{x}}(\boldsymbol{\theta}) - \boldsymbol{x}_d) - \boldsymbol{K}_d\dot{\boldsymbol{\theta}} \tag{4.9}$$

the equilibrium equations (c.f. 4.1)

$$\boldsymbol{f}_{\boldsymbol{\theta}}(\boldsymbol{\theta}, \boldsymbol{q}) = \boldsymbol{f}_{\boldsymbol{\theta}}(\boldsymbol{\theta}, \bar{\boldsymbol{q}}(\boldsymbol{\theta})) - \boldsymbol{J}_{\bar{\boldsymbol{x}}}^T(\boldsymbol{\theta})\boldsymbol{K}_p(\bar{\boldsymbol{x}}(\boldsymbol{\theta}) - \boldsymbol{x}_d) \tag{4.10a}$$

$$\boldsymbol{f}_{\boldsymbol{q}}(\boldsymbol{\theta}, \boldsymbol{q}) = \boldsymbol{0} \tag{4.10b}$$

result for the static case $\dot{\boldsymbol{x}} = \boldsymbol{0}$. The fulfilled conditions (4.2) allow to concluded that there exists a unique $\boldsymbol{q} = \bar{\boldsymbol{q}}(\boldsymbol{\theta})$ and a global diffeomorphic relation between $\boldsymbol{\theta}$ and $\bar{\boldsymbol{q}}(\boldsymbol{\theta})$ is given. The partial derivative of $\bar{\boldsymbol{x}}(\boldsymbol{\theta}) = \boldsymbol{f}(\bar{\boldsymbol{q}}(\boldsymbol{\theta}))$ is

$$\frac{\partial \boldsymbol{f}(\bar{\boldsymbol{q}}(\boldsymbol{\theta}))}{\boldsymbol{\theta}} = \frac{\partial \boldsymbol{f}(\bar{\boldsymbol{q}}(\boldsymbol{\theta}))}{\bar{\boldsymbol{q}}(\boldsymbol{\theta})}\frac{\partial \bar{\boldsymbol{q}}(\boldsymbol{\theta})}{\partial \boldsymbol{\theta}} = \boldsymbol{J}(\bar{\boldsymbol{q}}(\boldsymbol{\theta}))\boldsymbol{J}_{\bar{\boldsymbol{q}}} = \boldsymbol{J}_{\bar{\boldsymbol{x}}}(\boldsymbol{\theta}). \tag{4.11}$$

This defines a global diffeomorphism if the Jacobian $\boldsymbol{J}_{\bar{\boldsymbol{x}}}(\boldsymbol{\theta})$ is non-singular and $n = m$, which is fulfilled if

$$\left\|\boldsymbol{J}_{\bar{\boldsymbol{x}}}(\boldsymbol{\theta})^{-1}\right\| = \left\|\boldsymbol{J}_{\bar{\boldsymbol{q}}}^{-1}\right\| \left\|\boldsymbol{J}(\bar{\boldsymbol{q}}(\boldsymbol{\theta}))^{-1}\right\| < \alpha_4 \quad \forall \boldsymbol{\theta} \tag{4.12}$$

holds. The boundedness of $\left\|\boldsymbol{J}_{\bar{\boldsymbol{q}}}^{-1}\right\|$ is given by (4.6). In contrast, the mapping $\boldsymbol{J}(\bar{\boldsymbol{q}}(\boldsymbol{\theta}))$ can be singular for some configurations. Therefore, it is assumed that

$$\exists \boldsymbol{x} \in \mathbb{R}^k \text{ such that } \sup\|\boldsymbol{J}(\bar{\boldsymbol{q}}(\boldsymbol{\theta}))^{-1}\| < \infty, \boldsymbol{f}(\bar{\boldsymbol{q}}(\boldsymbol{\theta})) = \boldsymbol{x}, \forall \boldsymbol{\theta} \in \mathbb{R}^n \tag{4.13}$$

is true in the following. This can be enforced by standard singularity avoiding techniques [19]. From (4.10a) it follows that the controller is converging to $\bar{\boldsymbol{x}}(\boldsymbol{\theta}) = \boldsymbol{x}_d$.
This result is the basis for the approaches in Chapter 5.

4.1.3. Experimental Results and Discussion

The joint equivalent control $\bar{\boldsymbol{q}}(\boldsymbol{\theta})$ has been demonstrated in experiments on the DLR Hand Arm System. Measurements are plotted in Fig. 4.2. In the upper plots, a direct, non-collocated

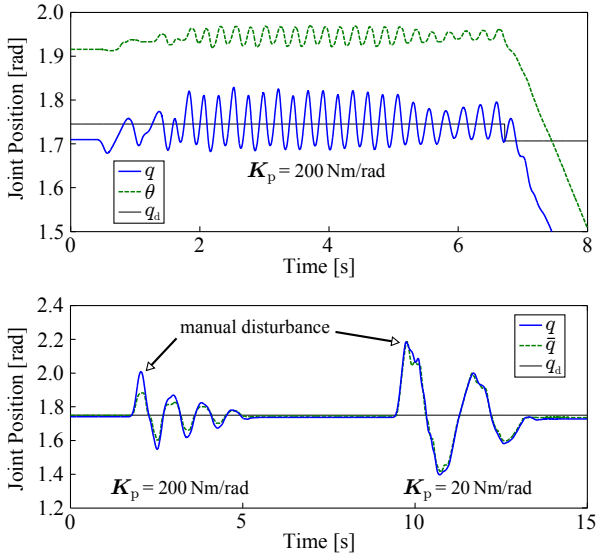

Figure 4.2.: Link position control using non-collocated (top) and collocated state variables (bottom). In the upper plots, the non-collocated feedback of the link side position q destabilizes the system. In the bottom plots, a collocated, static equivalent of the link side position $\bar{q}(\theta)$ is applied. In the latter case, arbitrarily low controller gains are adjustable.

feedback of the link side position $\boldsymbol{q}$ has been used in the controller. The system shows an evidently unstable behavior for a stiffness of 200 Nm/rad. The lower plots illustrate the system behavior while using $\bar{\boldsymbol{q}}(\boldsymbol{\theta})$ and the controller (4.7). Manual disturbances are compensated for rapidly. The capability to adjust arbitrarily low stiffnesses is shown at $t = 10\,\mathrm{s}$ as the proportional gain $\boldsymbol{K}_p$ is lowered to 20 Nm/rad.

Notice the importance of the use of $\bar{\boldsymbol{q}}(\boldsymbol{\theta})$ for VSA robots. While in the case of torque controlled robots the relatively high joint stiffness leads to minor position errors only, the low stiffness of VSA robots causes large errors even without additional load, see Fig. 4.2 (top).

Results of the Cartesian controller (4.9) are presented in Chapter 5.

The control approach has several major advantages: first, the use of $\bar{\boldsymbol{q}}(\boldsymbol{\theta})$ enables stable and statically correct link position control. The static effects of the elasticity are compensated for. The dynamics originated by the elastic element do not have to be taken into account explicitly. Second, arbitrarily low controller gains can be adjusted even for large displacements from the equilibrium since gravity is always compensated accurately. This property shows the flexibility of the controller, as low gains normally let the robot collapse under gravitational loads. The controller parametrized with zero stiffness $\boldsymbol{K}_p = \boldsymbol{0}$ enables the so-called "gravity compensation mode" which lets the robot appear gravity free. This mode is popular for robot demonstration or teaching tasks. Third, the approach provides great versatility for the choice of task coordinates.

Joint control and Cartesian control are described here. The extension to further output variables $\boldsymbol{y} = \boldsymbol{h}(\boldsymbol{\theta}, \boldsymbol{q})$ is straight forward where the presented conditions have to be fulfilled. Another advantage is the robustness of the controller with respect to model uncertainties. This is due to its passivity properties.

4.1.4. Remarks on VSA Link Positioning Accuracy

The link side equivalent (4.3) requires high model accuracy to provide good performance. Especially friction effects may result in a loss of performance. The requirement of VS joints to show low joint damping is beneficial for the positioning quality using the $\bar{\boldsymbol{q}}$ approach.

4.2. Kinetic Energy Shaping

The preceding section is based on the static robot case and collocated measurements to derive $\bar{\boldsymbol{q}}(\boldsymbol{\theta})$. By adding non-collocated feedback, the transient performance of the robot can be improved, however stability is an issue. Advanced controllers to improve the dynamic robot behaviour are discussed in Chapter 6 in detail, while an energy shaping based controller known from flexible link robots is presented, here.
The torque feedback

$$\boldsymbol{\tau}_{\mathrm{m}} = \boldsymbol{B}\boldsymbol{B}_{\theta}^{-1}\boldsymbol{u} + (\boldsymbol{I} - \boldsymbol{B}\boldsymbol{B}_{\theta}^{-1})\boldsymbol{\tau}, \tag{4.14}$$

as proposed in [97], can be interpreted as a virtual motor inertia shaping from $\boldsymbol{B}$ to $\boldsymbol{B}_{\theta}$. It provides non-collocated feedback, while still remaining in a passivity framework and thereby guaranteeing stability. The controller can be directly applied for VSA robots, as the joint torques can be estimated by (2.12). A classical application is the virtual reduction of the usually large perceived motor inertia on the link side due to high reduction ratios. This results in faster motor side dynamics and thereby increased transparency - the robot system feels 'lighter'. An advantageous property of the controller is that it preserves the general robot model structure (2.21). Only the motor inertia is scaled to $\boldsymbol{B}_{\theta}$ and the new motor input is denoted by $\boldsymbol{u}$.

4.2.1. Discussion

The ability of variable stiffness actuators to estimate joint torques constitutes an important similarity to flexible joint robots. Thereby, the generalization of torque control concepts to variable stiffness robots is possible, as demonstrated for two energy shaping techniques. The first generalized controller allows to compensate the deflections of the elastic elements originated by the gravitational load. The method is based on collocated motor coordinate feedback and thereby stability guarantees can be given. In this work the method is applied for variable stiffness robots and extended to Cartesian coordinates. The Cartesian formulation of the collocated control law finds application in stiffness design, Chapter 5. The measurements of experiments conducted on

the DLR Hand Arm System proof the high quality link side configuration control in the static case. The result provides a simple yet powerful way to overcome the position control inaccuracy of elastic joint robots. The second controller is used to shape the kinetic energy of the system. The use of non-collocated feedback is enabled by the passivity of the control law. The controller has been developed for flexible joint robots and is applied in the variable stiffness context, here. It constitutes a basis for e.g. the state feedback damping controller from Section 6.2.

5. Cartesian Stiffness Adjustment

For many robotic tasks it is convenient to specify stiffness and damping properties in the Cartesian space. This approach is known as Cartesian impedance control for torque controlled robots and has meanwhile found its way to industrial applications [13, 14, 15]. The compliance properties are generated algorithmically, where joint torque sensory information is processed in a feedback control loop. In contrast, variable stiffness actuators provide the compliance joint wise on a mechanical level. The passive joint compliance is tunable online, so that link position and stiffness can be adjusted independently. In this chapter Cartesian stiffness adjustment with variable stiffness actuators is treated. It is divided in three parts, where first the achievable Cartesian stiffness performance is analysed and afterwards two control approaches are presented. The chapter is partly based on the author's publication [100].

5.1. Cartesian Stiffness Adjustment

The design goal is to achieve a Cartesian stiffness at the TCP of the multi-joint VSA robot. In this section, we first analyse the achievable Cartesian stiffness performance.

5.1.1. Cartesian Stiffness Transformation

Passive Stiffness

The properties of the transformation of stiffnesses from joint to Cartesian space and vice versa are considered here. First, we are interested in the effect of the passive joint stiffness. Therefore, we assume the gravity to be compensated and the motor positions to be perfectly held.
The Cartesian stiffness behaviour of a general multi-joint robot is described by a constant stiffness matrix[1] $\boldsymbol{K}_C = -\frac{\partial \boldsymbol{f}}{\partial \boldsymbol{x}} \in \mathbb{R}^{m\times m}$ as the relation between the Cartesian wrench $\boldsymbol{f}$ and the Cartesian displacement $\boldsymbol{x}$. Here, m is the number of Cartesian degrees of freedom. The link stiffness is obtained from (2.13) as the force reaction due to a link motion

$$\boldsymbol{K}_J = \frac{\partial \boldsymbol{\tau}_{ext}}{\partial \boldsymbol{q}} = -\frac{\partial \boldsymbol{\tau}}{\partial \boldsymbol{q}} \in \mathbb{R}^{n\times n} \tag{5.1}$$

[1] In the following, $\boldsymbol{K}_\bullet$ and $\boldsymbol{C}_\bullet$ is used for general stiffness/compliance matrices. Subscript 'J' and 'C' denote joint and Cartesian matrices. Subscript 'a' stands for 'active', 'p' for 'passive', 's' for 'serial', and 'd' for 'desired' values.

of the n VSA joints. The mapping from the Cartesian stiffness space to the joint stiffness space is given by $\mathcal{T} : \boldsymbol{K}_J = \mathcal{T}(\boldsymbol{K}_C)$. This transformation can be written as

$$\boldsymbol{K}_J = -\frac{\partial \boldsymbol{\tau}}{\partial \boldsymbol{q}} = \frac{\partial (\boldsymbol{J}(\boldsymbol{q})^T \boldsymbol{K}_C \Delta \boldsymbol{x})}{\partial \boldsymbol{q}} = \boldsymbol{J}(\boldsymbol{q})^T \boldsymbol{K}_C \boldsymbol{J}(\boldsymbol{q}) + \frac{\partial \boldsymbol{J}(\boldsymbol{q})^T}{\partial \boldsymbol{q}} \boldsymbol{K}_C \Delta \boldsymbol{x}, \tag{5.2}$$

where $\boldsymbol{J}(\boldsymbol{q})$ is the manipulator Jacobian (4.8). The Cartesian position error between the desired and the actual position is denoted by $\Delta \boldsymbol{x} = \boldsymbol{x} - \boldsymbol{x}_d$. For further considerations the stiffness is computed at the equilibrium position. As a consequence, $\Delta \boldsymbol{x} = \boldsymbol{0}$ and (5.2) collapses to

$$\boldsymbol{K}_J = \boldsymbol{J}(\boldsymbol{q})^T \boldsymbol{K}_C \boldsymbol{J}(\boldsymbol{q}). \tag{5.3}$$

This relation has only local correctness, as both $\boldsymbol{K}_J$ and $\boldsymbol{J}(\boldsymbol{q})$ depend upon the robot configuration [101]. Furthermore, no external forces are assumed [102].
To calculate the Cartesian stiffness from a given joint stiffness, the inverse problem of (5.3) has to be solved $\boldsymbol{K}_C = \mathcal{T}^{-1}(\boldsymbol{K}_J)$. Therefore, compliance matrices are considered, which are the inverses of the stiffness matrices $\boldsymbol{C}_C = \boldsymbol{K}_C^{-1}$ and $\boldsymbol{C}_J = \boldsymbol{K}_J^{-1}$. Please note that for inversion the matrices $\boldsymbol{K}_C$ and $\boldsymbol{K}_J$ have to be non singular. It follows for the compliance matrices

$$\boldsymbol{C}_C = \boldsymbol{J}(\boldsymbol{q}) \boldsymbol{C}_J \boldsymbol{J}(\boldsymbol{q})^T, \tag{5.4}$$

and the stiffness matrix results to be

$$\boldsymbol{K}_C = (\boldsymbol{J}(\boldsymbol{q}) \boldsymbol{K}_J^{-1} \boldsymbol{J}(\boldsymbol{q})^T)^{-1}. \tag{5.5}$$

It is intuitive, that to achieve an arbitrary desired Cartesian stiffness matrix $\boldsymbol{K}_C$ in general all the elements of the joint stiffness matrix $\boldsymbol{K}_J$ must be non-zero for a given configuration with the Jacobian $\boldsymbol{J}(\boldsymbol{q})$.

Active and Passive Stiffness

The assumption of a fixed motor position is only valid for stiff motor controllers and often an actively compliant behaviour of the drives is generated by control, c.f. Sec 4.1. In this case, two sources of compliance can be identified (see Fig. 5.1) and the force reaction of the motors due to a link displacement has to be incorporated. With a similar approach as in (5.1) it follows

$$\boldsymbol{K}_{Js} = \frac{\partial \boldsymbol{\tau}_{ext}}{\partial \boldsymbol{q}} = -\frac{\partial \boldsymbol{f}(\boldsymbol{\theta} - \boldsymbol{q}, \boldsymbol{\sigma})}{\partial \boldsymbol{q}} = -\frac{\partial \boldsymbol{f}(\boldsymbol{\theta} - \boldsymbol{q}, \boldsymbol{\sigma})}{\partial (\boldsymbol{\theta} - \boldsymbol{q})} \frac{\partial (\boldsymbol{\theta} - \boldsymbol{q})}{\partial \boldsymbol{q}} \tag{5.6a}$$

$$= -\boldsymbol{K}_{Jp} \frac{\partial \boldsymbol{\theta}}{\partial \boldsymbol{q}} + \boldsymbol{K}_{Jp} \tag{5.6b}$$

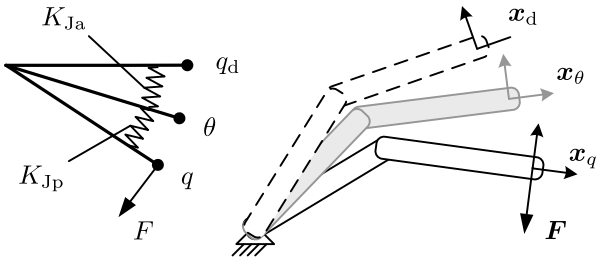

Figure 5.1.: On the left a one link VS joint is sketched. A force F acting at the TCP deflects the link and the motor coordinate. The active stiffness K_{Ja} is acting between the motor and the desired position while the passive stiffness K_{Jp} is mounted between the motor and the link. On the right, the deflection behaviour can be seen for a planar robot. The motor TCP position $\boldsymbol{x}_\theta$ is in between the desired TCP position $\boldsymbol{x}_d$ and the TCP $\boldsymbol{x}_q$.

where $\boldsymbol{K}_{Jp} > 0$ is the passive stiffness matrix of the robot. From (2.21b) and (2.21c) results

$$\boldsymbol{\tau} = \boldsymbol{\tau}_m = \boldsymbol{f}(\boldsymbol{\theta} - \boldsymbol{q}, \boldsymbol{\sigma}) = -\boldsymbol{K}_{Ja}(\boldsymbol{\theta} - \boldsymbol{\theta}_d) \tag{5.7a}$$

$$\frac{\partial \boldsymbol{f}(\boldsymbol{\theta} - \boldsymbol{q}, \boldsymbol{\sigma})}{\partial(\boldsymbol{\theta} - \boldsymbol{q})} \frac{\partial(\boldsymbol{\theta}(\boldsymbol{q}) - \boldsymbol{q})}{\partial \boldsymbol{q}} = -\boldsymbol{K}_{Ja} \frac{\partial \boldsymbol{\theta}(\boldsymbol{q})}{\partial \boldsymbol{q}} \tag{5.7b}$$

$$\boldsymbol{K}_{Jp}\left(\frac{\partial \boldsymbol{\theta}(\boldsymbol{q})}{\partial \boldsymbol{q}} - \boldsymbol{I}\right) = -\boldsymbol{K}_{Ja} \frac{\partial \boldsymbol{\theta}(\boldsymbol{q})}{\partial \boldsymbol{q}} \tag{5.7c}$$

$$(\boldsymbol{K}_{Jp} + \boldsymbol{K}_{Ja}) \frac{\partial \boldsymbol{\theta}(\boldsymbol{q})}{\partial \boldsymbol{q}} = \boldsymbol{K}_{Jp} \tag{5.7d}$$

Equation(5.7d) in (5.6b) results in the total serial stiffness

$$\boldsymbol{K}_{Js} = -\boldsymbol{K}_{Jp}(\boldsymbol{K}_{Jp} + \boldsymbol{K}_{Ja})^{-1} \boldsymbol{K}_{Jp} + \boldsymbol{K}_{Jp}. \tag{5.8}$$

Basic reformulations give

$$\boldsymbol{K}_{Js}^{-1} = \boldsymbol{K}_{Ja}^{-1} + \boldsymbol{K}_{Jp}^{-1}. \tag{5.9}$$

This is the result for the serial combination of the passive VSA stiffness and the active controller stiffness.
With (5.5) the Cartesian serial stiffness

$$\boldsymbol{K}_{Cs} = (\boldsymbol{J}(\boldsymbol{q})(\boldsymbol{K}_{Ja}^{-1} + \boldsymbol{K}_{Jp}^{-1})\boldsymbol{J}(\boldsymbol{q})^T)^{-1}, \tag{5.10a}$$

$$\boldsymbol{K}_{Cs}^{-1} = \boldsymbol{K}_{Ca}^{-1} + \boldsymbol{K}_{Cp}^{-1} \tag{5.10b}$$

is obtained. This is the basis for the analysis in the following sections. It specifies the design freedom to achieve a desired, combined Cartesian stiffness. It allows to formulate the general

global optimization problem

$$\begin{aligned} \min_{\boldsymbol{q}, \boldsymbol{K}_{Jp}, \boldsymbol{K}_{Ca}} & \left\| \boldsymbol{K}_{Cd} - \boldsymbol{K}_{Cs}(\boldsymbol{q}, \boldsymbol{K}_{Ca}, \boldsymbol{K}_{Jp}) \right\|, \\ \text{s.t. } & \boldsymbol{f}(\boldsymbol{q}) = \boldsymbol{x}_d \\ & \boldsymbol{q}^{Min} \leq \boldsymbol{q} \leq \boldsymbol{q}^{Max} \\ & \boldsymbol{K}_{Ja}^{Min} \leq \boldsymbol{K}_{Ja} \leq \boldsymbol{K}_{Ja}^{Max} \\ & \boldsymbol{K}_{Jp}^{Min} \leq \boldsymbol{K}_{Jp} \leq \boldsymbol{K}_{Jp}^{Max} \end{aligned} \tag{5.11}$$

This problem is nonlinear and states are bounded. Several solution possibilities are discussed in the following.
Three different sources of variation can be identified:

- The passive stiffness component $\boldsymbol{K}_{Jp}$.
- The active stiffness component $\boldsymbol{K}_{Ca}$.
- The robot configuration $\boldsymbol{q}$. As it is desired to achieve a certain pose $\boldsymbol{x}_d$, the kinematic nullspace can be varied.

All three possibilities will be evaluated in the following.

5.2. Analysis of Passive Cartesian Stiffness Performance

Following the VSA design idea to achieve a desired task by the mechanical properties of the robot arm, it is analysed what Cartesian stiffness can be achieved by a pure variation of the passive joint stiffness and the adaptation of the robot configuration. The analysis is based upon the general optimization problem (5.11) where only the passive joint stiffness and the configuration are altered. In an earlier work [103] it was investigated what Cartesian stiffness can be achieved by a passive compliant, redundant robot arm with diagonal joint stiffness. Here, the diagonal shape of the stiffness matrix and constraints given by the hardware setup are explicitly incorporated.
To perform the analysis and deduce results from the numerical simulations, we introduce a tool called stiffability maps, which allows us to visualize the stiffness capabilities of a robot. Afterwards, we apply stiffability maps to understand the effect of joint stiffness and nullspace variation.

5.2.1. Stiffability Maps

The concept of stiffability maps is derived from reachability maps [87] which capture the arm's capabilities of reachable workspace. We use them to understand the effects of the optimization parameters on the reachable stiffness for varying TCP positions in the workspace. The high dimensionality of a seven joint robotic arm in the six dimensional Cartesian space still does not

allow for a intuitive visualization. Therefore, we focus on a simplified planar robot with three joints $n = 3$ and a positioning task of the TCP $m = 2$ (no rotations are specified). Gravitation is omitted to understand the effects of the joint stiffness and the role of the robot nullspace configuration. An axial symmetry about the origin of the robot results, which allows to capture the whole Cartesian workspace of the robot by the polar coordinates r and ρ. The stiffness matrices $\boldsymbol{K}_C \in \mathbb{R}^2$ may be represented as ellipses. For tasks the length (eigenvalues λ_1, λ_2) and the rotation (ω) of the axes of the ellipse are varied. We aim to quantify the performance of the achieved stiffness optimized via (5.11), with the restriction to only passive stiffness. The problem complexity allows to achieve the optimal solution using standard optimization algorithms in case of the Frobenius norm (6.47). To be able to interpret the results relative to each other, we use the normalized Forbenius norm

$$E_K = \frac{\|\boldsymbol{K}_{Cd} - \boldsymbol{K}_{Cp}\|_F}{\|\boldsymbol{K}_{Cd}\|_F}. \tag{5.12}$$

The normalization provides the relative deviation off of the desired stiffness value. A value of $E_K = 0$ means perfect tracking of the desired stiffness value. A value of $E_K = 1$ means errors of the magnitude of the desired stiffness values arise. It is to remark, that this normalized error representation is an abstraction necessary to handle the information and provides qualitative results.
The described properties allow to define so-called stiffability maps with the following properties.

- Each stiffability map consists of a grid where the stretch of the arm (the coordinate r) is plotted on the abscissa. The ordinate plots the rotation of the stiffness ellipsoids ω.
- The grid entries represent the optimization results E_K encoded in a color scheme.
- Several stiffability maps are collected in a tiled set, where the axes show varying stiffness values of the main stiffness axes λ_1, λ_2.

The properties of the stiffability plots are depicted in Fig. 5.2.

5.2.2. Joint Stiffness Variation

An obvious variation mechanism is the passive joint stiffness. Most variable stiffness robots are only able to adjust the stiffness in each joint and therefore only a diagonal joint stiffness matrix

$$\boldsymbol{K}_{Jp} = \mathrm{diag}(\boldsymbol{k}_{Jp}) \in \mathbb{R}^{n \times n} \tag{5.13}$$

can be realized. The joint stiffness $\boldsymbol{k}(\boldsymbol{\varphi}, \boldsymbol{\sigma})$ is in this case diagonal represented by the joint stiffness vector by $\boldsymbol{k}_{Jp} \in \mathbb{R}^n$, c.f. (2.13). This is in contrast to the human which has coupling stiffness due to biarticular muscles.[2] Furthermore, the elements of $\boldsymbol{k}_{Jp}$ are restricted to lower and upper stiffness bounds $\boldsymbol{k}_{Jp}^{Min}$ and $\boldsymbol{k}_{Jp}^{Max}$ given by the configuration and mechanism properties.

[2] Recent research efforts point in the direction of developing biarticular robots [90].

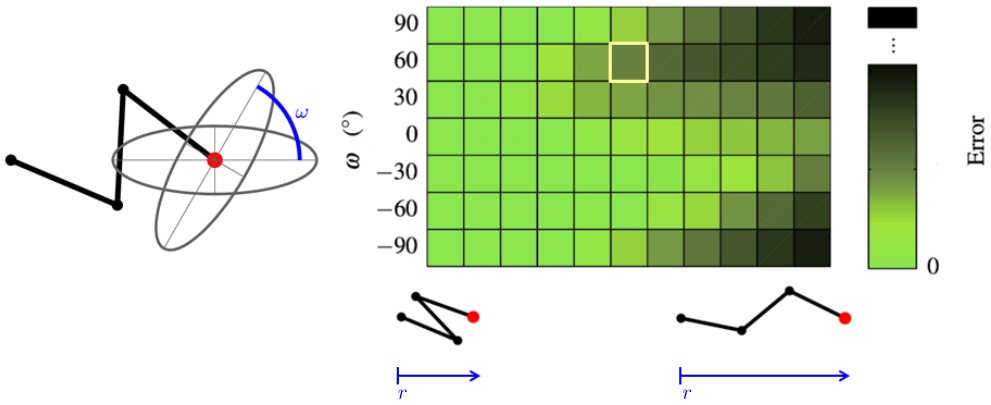

Figure 5.2.: The properties of the stiffability plots.

To give an impression of the achievable Cartesian stiffness range, the stiffability set of the planar three joint robot for a symmetric configuration is plotted in Fig. 5.3. The joint stiffness limits are chosen similarly to the active range of the FS joints of the DLR Hand Arm System.
The stiffability set supports the finding of [103]. It is not possible to achieve arbitrary Cartesian stiffness by pure joint stiffness variation. Furthermore, the tendency can be observed that stiffness ellipses with a dominant axis directed in the polar direction can be achieved with a reasonable quality (see Fig. 5.3, λ_1=500 Nm/rad, λ_2=1500..2500 Nm/rad)). In case where the dominating axis is rotated relative to the polar axis, the performance is reduced.
Concluding it is to say, that with a pure joint stiffness variation a predominate direction arises along which good scaling properties exist. In the other directions, the scaling properties are limited, which leads also to constrained ability to rotate the ellipses.

5.2.3. Nullspace Variation

The second variation possibility evaluated is a reconfiguration of the robot in the nullspace. The robot configuration $\boldsymbol{q}$ is affecting the Cartesian stiffness by the Jacobian matrices. To achieve a pose in the Cartesian space, $m = 6$ task coordinates are required. Many robots are set up in a redundant way, such that more configuration coordinates $n > m$ are available. Such, the DLR Hand Arm system is designed to provide $n = 7$ degrees of freedom. The task of adjusting a Cartesian pose can be achieved while allowing to freely configure the resulting $n-m$ dimensional nullspace. Several solutions for controlling the nullspace motion have been presented in the literature [19].
To evaluate the result of nullspace variations in a stiffability set, it is necessary to chose fixed joint stiffness values. Sets with fixed joint stiffness values of k_{Jp}=100 Nm/rad, k_{Jp}=300 Nm/rad, and k_{Jp}=500 Nm/rad are depicted in Fig. 5.4, Fig. 5.5, and Fig. 5.6, respectively.
In the sets, still a dominance of stiffness ellipses directed in the polar axis can be observed (see

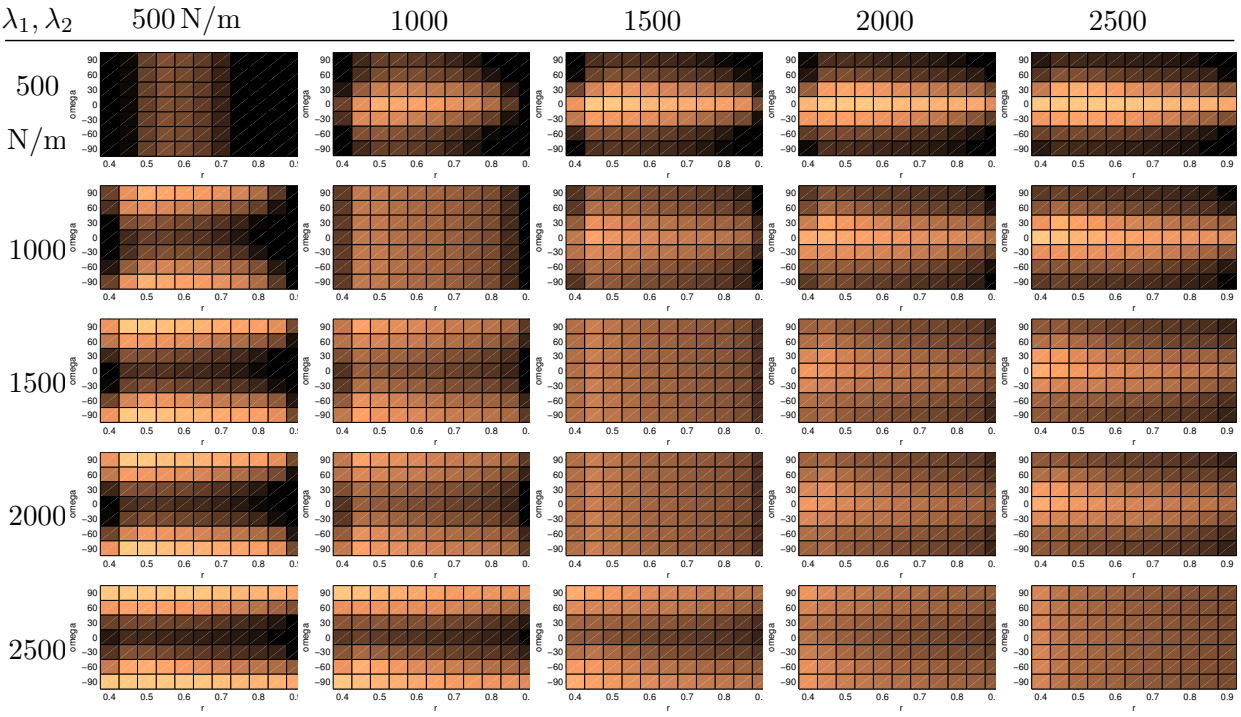

Figure 5.3.: The stiffability set of the planar manipulator. Only joint stiffness optimization is performed with the limits $k_{jp}^{min} = 50\,\mathrm{Nm/rad}$, $k_{jp}^{max} = 500\,\mathrm{Nm/rad}$. The arm configuration has been chosen symmetric, see Fig. 5.2 left.

e.g. Fig. 5.4, Fig. 5.5, and Fig. 5.6, λ_1=500 Nm/rad, λ_2=1500..2500 Nm/rad). In contrast to a joint stiffness optimization, the nullspace variation also enables to adjust stiffness ellipses with equal axis length, at least for some Cartesian stiffness ranges (Fig. 5.4 λ_1=λ_2=500 Nm/rad, Fig. 5.5 λ_1=λ_2=2000 Nm/rad, Fig. 5.6 λ_1=λ_2=2500 Nm/rad). The scaling and rotating of the ellipses depends on the location in the workspace.

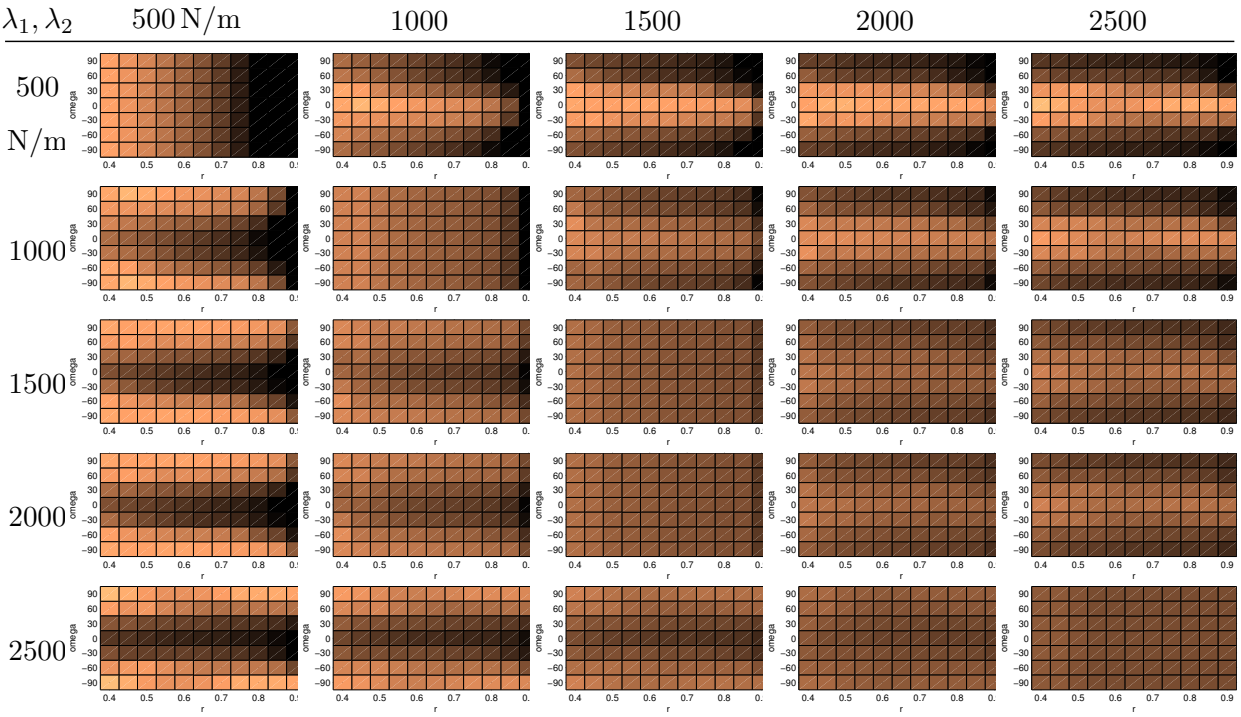

Figure 5.4.: The nullspace configuration is optimized with a fixed stiffness is adjusted to k_{jp}=100 Nm/rad.

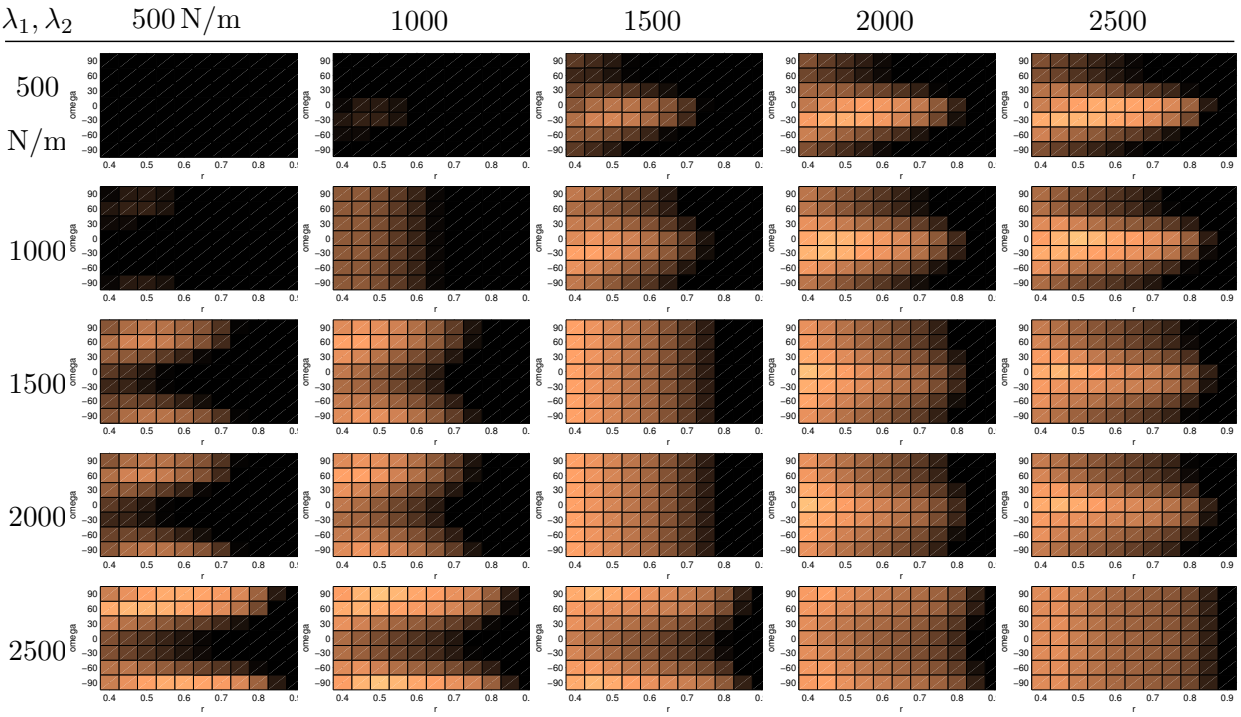

Figure 5.5.: The nullspace configuration is optimized with a fixed stiffness is adjusted to k_{jp}=300 Nm/rad

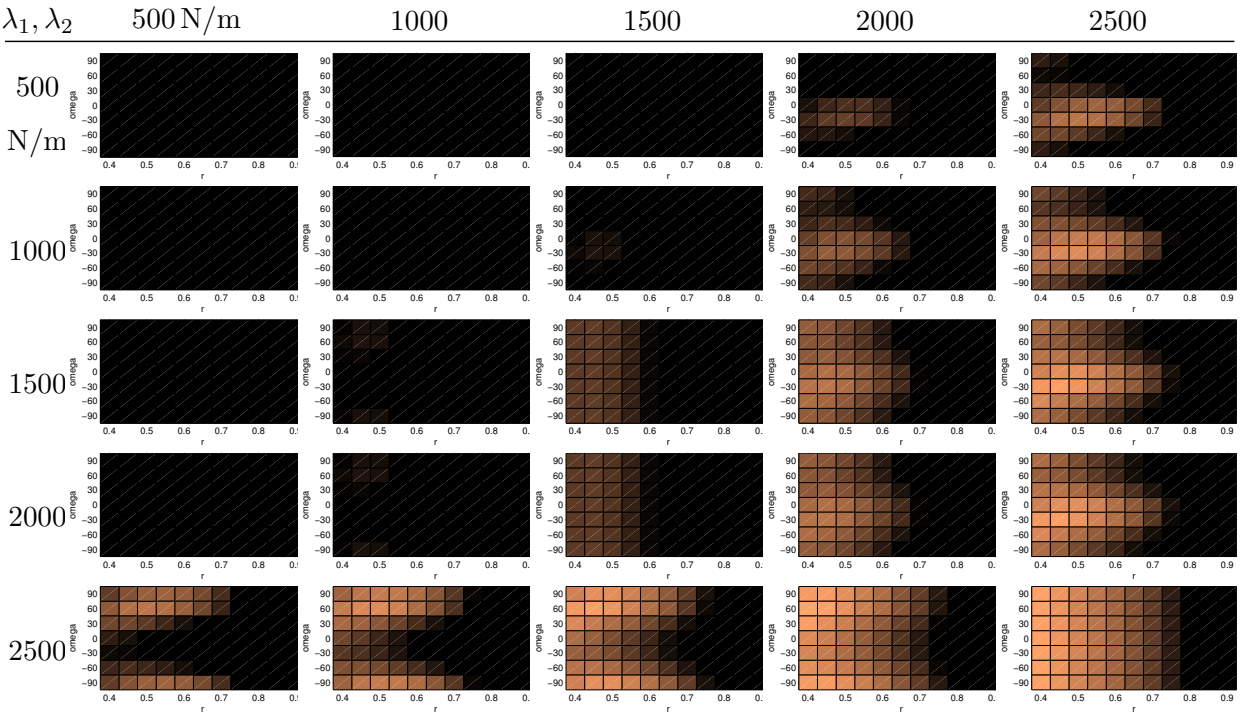

Figure 5.6.: The nullspace configuration is optimized with a fixed stiffness is adjusted to k_{jp}=500 Nm/rad.

5.2.4. Combining Stiffness and Nullspace Variation

The simulation study is concluded with a combination of both, a simultaneous stiffness and nullspace optimization. The set is depicted in Fig. 5.7. It is obvious, that this combined approach improves the achievable stiffness values. Especially for TCP ranges below r =0.5 m high performance is achieved. This can be accredited to good reconfiguration possibilities of the nullspace in this region.

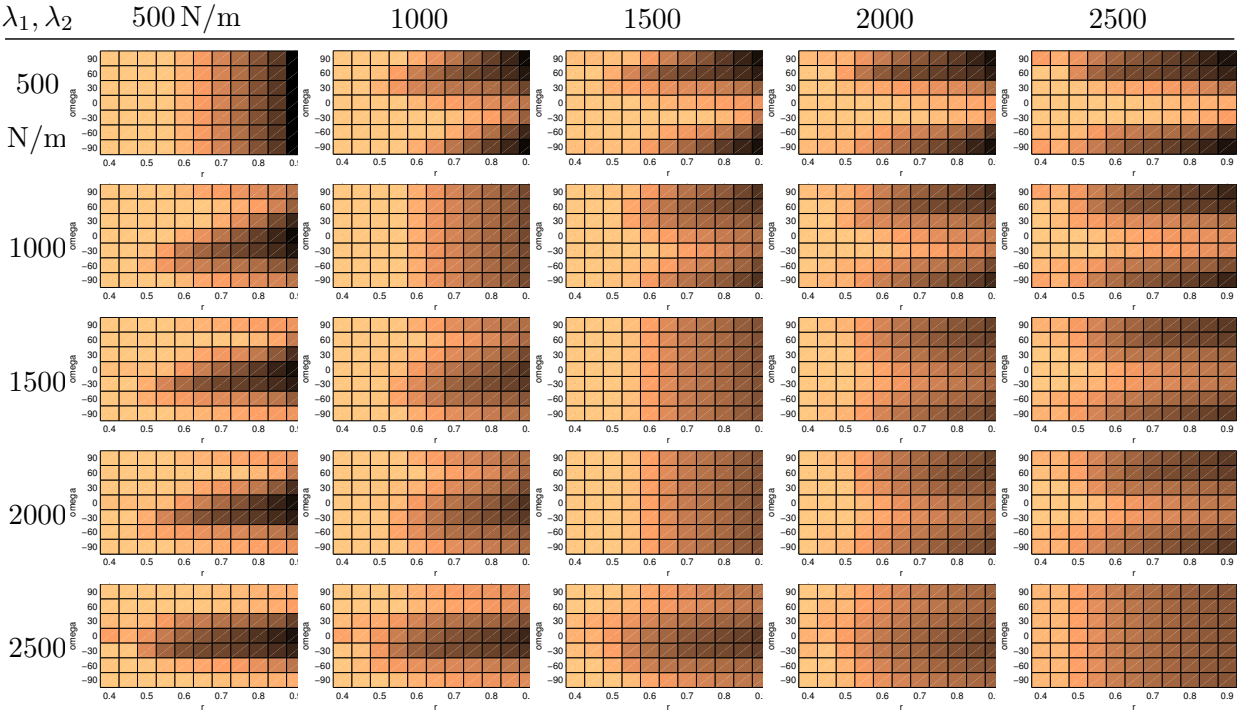

Figure 5.7.: In this set the resulting Cartesian stiffness of the joint stiffness variation and the kinematic nullspace variation is depicted.

5.2.5. Discussion

Stiffability maps as introduced in this section and used in the simulation study provide an intuitive tool to visualize Cartesian stiffness performance. They abstract the underlying stiffness transformation mechanism which allows for an intuitive interpretation of the achievable values. Besides of analysis purposes as presented in this section, an application in an higher level planning stage may be considered.

One result of the analysis is that tracking of Cartesian stiffness matrices is limited using the bounded joint stiffness. Good performance can only be achieved in certain regions of the TCP position range. The impact of joint stiffness variation is dominated by the configuration which mainly affects the dimensions of the stiffness ellipsoids. The analysis highlights the importance

to precisely specify the need of a robotic task. Technological bounds narrow a general use. The joint wise mounting, the upper and lower stiffness bounds, and the severe nonlinearity of the VS joints poses many restrictions and hardens controller design. The balance between benefit and effort has to be thoroughly weighted up.
Nullspace reconfiguration allows to change the dimensions of the stiffness ellipsoids at some TCP positions. Applied in combination with the joint stiffness variation, good Cartesian stiffness tracking can be achieved. A downside is that kinematic reconfiguration may have consequences on planning on a higher level. For example precautions have to be taken to avoid self collision or ensure integrity of the robot and the environment.
In the following two methods to extend the achievable Cartesian stiffness space are discussed. First, the combination of the passive stiffness with an active stiffness is shown. Afterwards, a nullspace optimization controller is presented.

5.3. Active/Passive Stiffness Adjustment

A purely passive stiffness optimization often leads to unsatisfactory Cartesian stiffness results, especially when passive stiffness joint limits are considered. One of the benefits of VSA robots is the applicability of torque control methods. Such, active impedance controllers [18, 96] can be used. The combination of an active impedance controller and the passive joint impedance allows to widely extend the achievable Cartesian stiffness range: the active impedance controller is less limited (e.g. stiffnesses down to 0 N/m can be achieved) and allows for a coupled stiffness matrix. Therefore, it may overcome the limitations of the diagonal and bounded passive joint stiffness even for fixed configurations $\boldsymbol{J}_0 = \boldsymbol{J}(\boldsymbol{q})|_{\boldsymbol{q}=\boldsymbol{q}_0}$. This follows from the serial interconnection of the active and passive stiffness matrices (5.10a). Even if $\boldsymbol{K}_{Jp}$ is only diagonal, the serial stiffness $\boldsymbol{K}_{Cs}$ can be of arbitrary shape due to the active compliance $\boldsymbol{K}_{Ja}$. The design idea is sketched in Fig. 5.8.
Out of these considerations, the general stiffness optimization problem can be derived from (5.11). The desired Cartesian stiffness $\boldsymbol{K}_{Cd}$ shall be achieved by the serial stiffness $\boldsymbol{K}_{Cs}$ for the fixed configuration $\boldsymbol{J}_0$

$$\begin{aligned} \min_{\boldsymbol{K}_{Jp},\boldsymbol{K}_{Ja}} & \left\| \boldsymbol{K}_{Cd} - \boldsymbol{K}_{Cs}(\boldsymbol{K}_{Ja}, \boldsymbol{K}_{Jp}) \right\| . \\ \text{s.t. } & \boldsymbol{K}_{Ja}^{Min} \leq \boldsymbol{K}_{Ja} \leq \boldsymbol{K}_{Ja}^{Max} \\ & \boldsymbol{K}_{Jp}^{Min} \leq \boldsymbol{K}_{Jp} \leq \boldsymbol{K}_{Jp}^{Max} \end{aligned} \tag{5.14}$$

For a solution of this problem, we will make use of a problem description in the compliance space. The serial interconnection in the compliance space is given by

$$\boldsymbol{C}_{Js} = \boldsymbol{C}_{Ja} + \boldsymbol{C}_{Jp}, \tag{5.15}$$

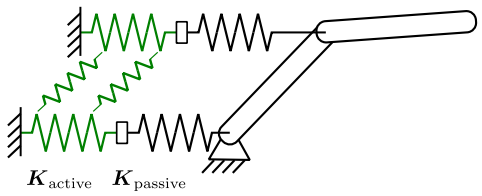

Figure 5.8.: The design idea to use the interconnection of an active impedance controller in series with the passive joint stiffness. As the active stiffness is less limited and may be coupled, it allows to overcome the restriction of the bounded and diagonal passive joint stiffness.

and

$$\boldsymbol{C}_{Cs} = \boldsymbol{J}(\boldsymbol{q})(\boldsymbol{C}_{Ja} + \boldsymbol{C}_{Jp})\boldsymbol{J}(\boldsymbol{q})^T \tag{5.16a}$$

$$\boldsymbol{C}_{Cs} = \boldsymbol{C}_{Ca} + \boldsymbol{C}_{Cp}. \tag{5.16b}$$

The advantage of the formulation in the compliance space is the linearity of the computation. Then, the general compliance optimization problem can be stated

$$\begin{aligned} \min_{\boldsymbol{C}_{Jp}, \boldsymbol{C}_{Ja}} & \left\| \boldsymbol{C}_{Cd} - \boldsymbol{C}_{Cs}(\boldsymbol{C}_{Ja}, \boldsymbol{C}_{Jp}) \right\|, \\ \text{s.t. } & \boldsymbol{C}_{Ja}^{Min} \leq \boldsymbol{C}_{Ja} \leq \boldsymbol{C}_{Ja}^{Max} \\ & \boldsymbol{C}_{Jp}^{Min} \leq \boldsymbol{C}_{Jp} \leq \boldsymbol{C}_{Jp}^{Max} \end{aligned} \tag{5.17}$$

where $\boldsymbol{C}_{Ja}$ is required to be positive definite for controller stability (4.9). This optimization problem is the basis for our active/passive impedance algorithms.
Note that the problem statement in the compliance space mainly influences the optimization norm. The consequence of the formulation in the compliance space is a different weighting of the norm.

5.3.1. Simultaneous Optimization

The norm of the general optimization problem in the compliance space is given by

$$\left\| \boldsymbol{C}_{Cd} - \boldsymbol{C}_{Cs}(\boldsymbol{C}_{Ja}, \boldsymbol{C}_{Jp}) \right\| = \left\| \boldsymbol{C}_{Cd} - \boldsymbol{J}_0(\boldsymbol{C}_{Ja} + \boldsymbol{C}_{Jp})\boldsymbol{J}_0^T \right\|, \tag{5.18}$$

where $\boldsymbol{J}_0 = \boldsymbol{J}(\boldsymbol{q})|_{\boldsymbol{q}=\boldsymbol{q}_0}$.
The problem is of convex nature. This can be seen by rewriting the problem using the Frobenius norm (6.47) into an Euclidian norm. It results

$$\left\| \boldsymbol{A}_1 \boldsymbol{y}_1 + \boldsymbol{A}_2 \boldsymbol{y}_2 - \boldsymbol{b} \right\|_2^G. \tag{5.19}$$

The matrix $\boldsymbol{A}_1 \in \mathbb{R}^{m^2 \times (n^2+n)/2}$ contains the elements of the positive definite matrix $\boldsymbol{C}_{Ca}$ reshaped as a vector and differentiated w.r.t. the active joint compliance vector $\boldsymbol{c}_{Ja}$. The vector $\boldsymbol{c}_{Ja}$ is defined by the upper triangular entries of $\boldsymbol{C}_{Ja}$ which are collected $\boldsymbol{y}_1 = \boldsymbol{c}_{Ja} = \text{triu}(\boldsymbol{C}_{Ja}) \in \mathbb{R}^{(n^2+n)/2}$. If no stiffness couplings between the joints exist, the matrix $\boldsymbol{A}_2 \in \mathbb{R}^{m^2 \times n}$ contains the elements of $\boldsymbol{C}_{Cp}$ reshaped as a vector and differentiated w.r.t. the passive joint compliance vector. Then, the vector $\boldsymbol{y}_2 = \boldsymbol{c}_{Jp} = \text{diag}(\boldsymbol{C}_{Jp}) \in \mathbb{R}^{n/2}$ contains the elements of the diagonal joint compliance matrix. This is the case we assume in the following. If otherwise biarticular couplings exist, the matrix $\boldsymbol{C}_{Jp}$ is not diagonal and $\boldsymbol{A}_2$ and $\boldsymbol{y}_2$ will have a form like $\boldsymbol{A}_1$ and $\boldsymbol{y}_1$. The vector $\boldsymbol{b} \in \mathbb{R}^{m^2}$ contains the desired compliance matrix $\boldsymbol{C}_{Cd}$ reshaped as a vector. The geometric interpretation of the sum is a polyhedron, which can be written in compact form

$$\|\boldsymbol{A}\boldsymbol{y} - \boldsymbol{b}\|_2^G \,, \tag{5.20}$$

where

$$\boldsymbol{A} = \begin{pmatrix} \boldsymbol{A}_1 & \boldsymbol{A}_2 \end{pmatrix}, \; \boldsymbol{y} = \begin{pmatrix} \boldsymbol{y}_1 \\ \boldsymbol{y}_2 \end{pmatrix}. \tag{5.21}$$

Therefore, (5.17) is a standard constrained quadratic program [104], where inequality constraints can be incorporated

$$\begin{aligned} &\min_{\boldsymbol{y}} \boldsymbol{y}^T \boldsymbol{A}^T \boldsymbol{A}\boldsymbol{y} - 2\boldsymbol{b}^T \boldsymbol{A}\boldsymbol{y} + \boldsymbol{b}^T \boldsymbol{b} \\ &\text{s.t. } \boldsymbol{y}^{Min} < \boldsymbol{y} < \boldsymbol{y}^{Max} \end{aligned} \tag{5.22}$$

Recent developments of convex optimization solvers [105], suggest the feasibility of an online solution. In the next section, we show a sequential method, which does not require such complex solvers.

5.3.2. The Sequential Approach

Besides of the combined optimization of the active and passive compliance, here, a sequential approach is presented. It is motivated by the conceptional idea to mainly use the passive compliance properties to achieve a task. First, a passive joint compliance $\boldsymbol{C}_{Jp}$ has to be found such that the desired Cartesian compliance $\boldsymbol{C}_{Cd}$ is achieved 'as good as possible' by the resulting passive Cartesian compliance $\boldsymbol{C}_{Cp}$ (Section 5.3.3). Afterwards, an active impedance controller using $\boldsymbol{C}_{Ca}$ with (5.16b) is designed such that the compliance tracking performance is increased (Section 5.3.4). Using the sequential approach it is possible to formulate a real-time algorithm without the need of additional optimization software.

5.3.3. Sequential Approach: Passive Compliance Optimization

For the first step, the problem formulation from (5.17) is reduced to only contain the passive joint compliance vector:

$$\begin{aligned} &\min_{\boldsymbol{c}_{Jp}} \|\boldsymbol{C}_{Cd} - \boldsymbol{C}_{Cp}(\boldsymbol{c}_{Jp})\| \\ &\text{s.t. } \boldsymbol{c}_{Jp}^{Min} < \boldsymbol{c}_{Jp} < \boldsymbol{c}_{Jp}^{Max} \end{aligned} \tag{5.23}$$

The optimal $\boldsymbol{c}_{Jp}$ is found by searching the extremal regarding the constraints. Therefore, it is transformed into standard least squares form as done in (5.19)

$$\begin{aligned} &\min_{\boldsymbol{c}_{Jp}} \|\boldsymbol{A}_2 \cdot \boldsymbol{c}_{Jp} - \boldsymbol{b}\|_2^G \\ &\text{s.t. } \boldsymbol{c}_{Jp}^{Min} < \boldsymbol{c}_{Jp} < \boldsymbol{c}_{Jp}^{Max}. \end{aligned} \tag{5.24}$$

This inequality constrained least squares problem is solved using an active set algorithm [106]. The algorithm solves the problem as an equality constrained least squares problem where active inequality constraints are treated as equality constraints and inactive inequality constraints are omitted. The algorithm works as following:
In each iteration an equality constrained least squares problem is formulated. Out of the set of inequality constraints denoted by

$$\boldsymbol{B}_0 \, \boldsymbol{c}_{Jp} \geq \boldsymbol{d}, \tag{5.25}$$

where $\boldsymbol{B}_0 = \begin{pmatrix} I \\ -I \end{pmatrix}$ and $\boldsymbol{d} = \begin{pmatrix} \boldsymbol{c}_{Jp}^{Min} \\ \boldsymbol{c}_{Jp}^{Max} \end{pmatrix}$ the active inequality constraints are selected. These are treated as equality constraints forming the working set

$$\boldsymbol{B} \, \boldsymbol{c}_{Jp} = \boldsymbol{d}. \tag{5.26}$$

The problem is now given as the norm of (5.24) with the equality constraints (5.26).
The active set is determined by the following steps:

1. The activeness of each equality constraint is checked by using the Karush-Kuhn-Tucker conditions, which can be done by computing the Lagrange multipliers $\boldsymbol{\lambda}$ defined by

$$\boldsymbol{A}^T(\boldsymbol{A} \, \boldsymbol{c}_{jp} - \boldsymbol{b}) = \boldsymbol{B}^T \boldsymbol{\lambda}. \tag{5.27}$$

   When all Lagrange multipliers are zero or positive, an optimal solution subject to the working set is found. In the case of a negative Lagrange multiplier, the relating equality constraint is not active and the solution is not optimal. Consequently the inactive constraint is removed from the active set and another algorithm iteration is performed.

2. The inequality constraints are checked. The constraints which are not fulfilled are treated as equality constraints and added to the working set. Then, another iteration is executed.

The algorithm terminates, if all equality constraints of the working set are active and all inequality constraints are fulfilled. This gives the passive joint compliance $\boldsymbol{c}_{Jp}^{Best}$ minimizing (5.23) and therefore the passive Cartesian compliance $\boldsymbol{C}_{Cp}$ nearest to the desired Cartesian compliance. Please remark, that the resulting $\boldsymbol{C}_{Cp}$ is positive definite as $\boldsymbol{C}_{Jp} > 0$.

Computation and Application

The active set algorithm is advantageous for real time computations, as the number of computation is upper bounded. At most 2^r least squares optimizations (algorithm iterations) have to be performed, where r is the number of inequality constraints. Assuming a 7 DoF robot, even the worst case of 128 optimization iterations seems tractable with today's computation power.
In most cases the optimization is finished dramatically faster, as often only one algorithm iteration has to be performed. This is, because of in most computation steps the active compliance limits remain the same and therefore the working set remains the same. Regarding the optimization rate of 366 Hz and much lower structural eigen-frequencies of the robot of < 20 Hz which cause the change of limits, the effectiveness of the algorithm can be understood.
If only pure passive impedance behaviour is desired, the relating passive joint stiffness $\boldsymbol{k}_{Jp}^{Best}$ is computed and commanded to the robot with a high gain position controller. As analysed before, the achieved stiffness performance over the workspace is quite limited. To increase the stiffness performance, an active impedance controller is designed to further minimize the norm (5.17), as shown in the next section.

5.3.4. Sequential Approach: Active Compliance Optimization

The sequential approach considers first an optimization of the passive joint compliance. Afterwards, the active compliance is optimized using the approach presented in this section.
Stating the problem of finding the complementing active Cartesian stiffness again as an optimization problem derived from (5.17) gives

$$\begin{aligned} &\min_{\boldsymbol{C}_{Ca}} \|\boldsymbol{C}_{Cd} - \boldsymbol{C}_{Cs}(\boldsymbol{C}_{Ca})\| \\ &\text{s.t.}\, \boldsymbol{C}_{Ca} > 0 \end{aligned} \tag{5.28}$$

The active compliance matrix $\boldsymbol{C}_{Ca}$ is chosen to be positive definite, as otherwise the impedance controller (4.9) is not any more passive. Please remark that in theory even a negative definite $\boldsymbol{C}_{Ca}$ may result in a positive definite serial compliance (5.15) and thereby the interconnection is passive, however non-ideal properties like controller time delays, measurement signal discretization and further effects are not considered and therefore may lead to instability. Furthermore, the main reason for choosing $\boldsymbol{C}_{Ca} > 0$ is that the calculations performed are only valid locally for infinitesimal deflections while in practice of course arbitrary deflections may occur leading to $\boldsymbol{q} \neq \boldsymbol{q}_0$ and $\boldsymbol{C}_{Cp} \neq \boldsymbol{C}_{Cp}^{Best}$. The resulting serial stiffness $\boldsymbol{C}_s$ may not be any more positive definite and may lead to instability.

With (5.16b) and (6.47) the norm in (5.28) can be rewritten by

$$\|\boldsymbol{C}_{Cd} - \boldsymbol{C}_{Cs}\|_F = \|\mathbf{X} - \boldsymbol{C}_{Ca}\|_F \,, \tag{5.29}$$

where we replaced $\boldsymbol{C}_{Cd} - \boldsymbol{C}_{Cp}$ by $\boldsymbol{X}$. Therefore, the minimization problem is reduced to the problem of finding a positive definite matrix $\boldsymbol{C}_{Ca}$ closest to a desired matrix $\boldsymbol{X}$. This is described as a 'matrix nearness problem' in the literature.

Optimization Via a Matrix Nearness Problem

The matrix nearness problem of finding a positive definite matrix involving the Frobenius norm is described in [107]. The key element of the proof and the presented algorithm is to decompose the symmetric part of the goal matrix $\boldsymbol{X}$ into its eigenvalues and to choose only the positive values. The optimal active Cartesian compliance is computed as follows.
First, an eigenvalue transformation of the goal matrix $\boldsymbol{X}$ is computed:

$$\boldsymbol{X} = \boldsymbol{V}\boldsymbol{\Lambda}\boldsymbol{V}^T \tag{5.30}$$

$$\boldsymbol{V}^T\boldsymbol{V} = \boldsymbol{I}; \quad \boldsymbol{\Lambda} = \mathrm{diag}(\boldsymbol{\lambda}). \tag{5.31}$$

Herein, $\boldsymbol{V}$ is the matrix containing the eigenvectors and $\boldsymbol{\Lambda}$ is the diagonal eigenvalue matrix. Second, the active Cartesian compliance matrix $\boldsymbol{C}_{Ca}$ is transformed into this eigenspace:

$$\boldsymbol{C}_Q = \boldsymbol{V}^T\, \boldsymbol{C}_{Ca}\boldsymbol{V} \tag{5.32}$$

Following the proof in [107] to find the positive semi-definite matrix $\boldsymbol{C}_{Ca}$ nearest to $\boldsymbol{X}$, the diagonal entries c_{Qii} of $\boldsymbol{C}_Q$ have to be chosen such that

$$c_{Qii}^{Best} = \begin{cases} \lambda_i, & \lambda_i > 0 \\ 0^+, & \lambda_i \leq 0. \end{cases} \tag{5.33}$$

The value 0^+ represents a value bigger than 0, as in contrast to the proof in [107], we need positive definiteness. The optimal active Cartesian stiffness $\boldsymbol{C}_{Ca}$ results to be

$$\boldsymbol{C}_{Ca}^{Best} = \boldsymbol{V}\boldsymbol{C}_Q^{Best}\boldsymbol{V}^T. \tag{5.34}$$

The optimal active compliance is transformed into stiffness space and directly used in (4.9).

5.3.5. Experimental Setup and Results

Experimental Approach and Procedure

In this section, experimental results of the sequential active/passive approach on the DLR Hand Arm System are shown. The first four degrees of freedom (shoulder joints one and two, the upper arm rotation joint, and the elbow joint) were used to adjust a Cartesian position $\in \mathbb{R}^3$. Rotational stiffness was omitted. All the measurements were done with the robot in a configuration as shown in Fig. 5.9. The experiments were generated using the presented algorithms in the following procedure:

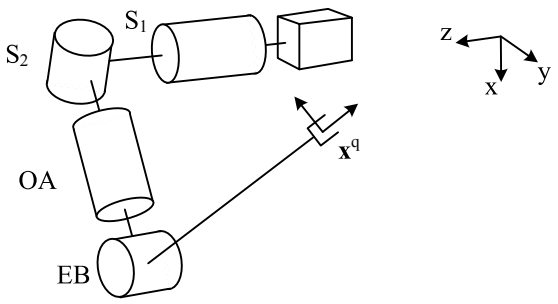

Figure 5.9.: A sketch of the robot configuration, which was used to conduct the experiments. Due to the position of the TCP in front of the arm, the shoulder joint S_1 needs to produce a high torque, resulting in a high stiffness in the x-direction.

Point of time	t_1	t_2	t_3
$\boldsymbol{K}_{Cd}\left[\frac{\mathrm{N}}{\mathrm{m}}\right]$	$\begin{bmatrix} 100 & 0 & 0 \\ 0 & 100 & 0 \\ 0 & 0 & 300 \end{bmatrix}$	$\begin{bmatrix} 100 & 0 & 0 \\ 0 & 100 & 0 \\ 0 & 0 & 300 \end{bmatrix}$	$\begin{bmatrix} \mathbf{100} & 0 & 0 \\ 0 & 100 & 0 \\ 0 & 0 & 300 \end{bmatrix}$
$\boldsymbol{K}_{Cp}\left[\frac{\mathrm{N}}{\mathrm{m}}\right]$	$\begin{bmatrix} 922 & -1695 & 1 \\ -1695 & 8398 & -8 \\ 1 & -8 & 299 \end{bmatrix}$	$\begin{bmatrix} 925 & -1705 & -12 \\ -1705 & 8110 & 65 \\ -12 & 65 & 489 \end{bmatrix}$	$\begin{bmatrix} \mathbf{879} & 592 & -1 \\ 592 & 11092 & 25 \\ -1 & 25 & 324 \end{bmatrix}$
$\boldsymbol{K}_{Ca}\left[\frac{\mathrm{N}}{\mathrm{m}}\right]$	$\begin{bmatrix} 116 & 5 & 0 \\ 5 & 97 & 1 \\ 0 & 1 & 4545 \end{bmatrix}$	$\begin{bmatrix} 116 & 5 & 0 \\ 5 & 97 & 1 \\ 0 & 1 & 4545 \end{bmatrix}$	$\begin{bmatrix} \mathbf{116} & 5 & 0 \\ 5 & 97 & 1 \\ 0 & 1 & 4545 \end{bmatrix}$
$\boldsymbol{K}_{Cs}\left[\frac{\mathrm{N}}{\mathrm{m}}\right]$	$\begin{bmatrix} 96 & 1 & 0 \\ 1 & 95 & 0 \\ 0 & 0 & 280 \end{bmatrix}$	$\begin{bmatrix} 96 & 0 & 0 \\ 0 & 95 & 1 \\ 0 & 1 & 441 \end{bmatrix}$	$\begin{bmatrix} \mathbf{102} & 5 & 0 \\ 5 & 96 & 0 \\ 0 & 0 & 303 \end{bmatrix}$
$\boldsymbol{k}_{Jp}\left[\frac{\mathrm{Nm}}{\mathrm{rad}}\right]$	$\begin{bmatrix} 394^* \\ 123 \\ 113 \\ 161^* \end{bmatrix}$	$\begin{bmatrix} 395 \\ 207 \\ 172 \\ 151 \end{bmatrix}$	$\begin{bmatrix} 541 \\ 122 \\ 124 \\ 250 \end{bmatrix}$

Table 5.1.: Cartesian and joint stiffness at the time instants from the reported experiment. Plotted values from Fig. 5.10 are colorized/bold. Passive joint stiffness $\boldsymbol{k}_{Jp}$ reaching a mechanical limit are marked with a '*'.

1. A desired Cartesian position is commanded and the desired Cartesian stiffness matrix $\boldsymbol{K}_{Cd}$ is specified.

2. The minimum passive joint stiffness vector $\boldsymbol{k}_{Jp}^{Min}$ is configuration dependent due to the progressive stiffness shape. It is achieved using $\boldsymbol{\varphi}_0$ from solving (2.15a) where $\boldsymbol{\tau}_e = \boldsymbol{g}(\boldsymbol{q}_d), \boldsymbol{\sigma} = \mathbf{0}\,\mathrm{rad}$ in (2.13).

3. The optimal passive Cartesian stiffness $\boldsymbol{K}_{Cp}^{Best}$ is computed using the passive stiffness optimization from Section 5.3.3. The optimal stiffness variation parameter $\boldsymbol{\sigma}^{Best}$ are obtained from the $\boldsymbol{k}_{Jp}^{Best}$ at the given configuration

4. The active stiffness optimization from Section 5.3.4 results in the optimal active Cartesian

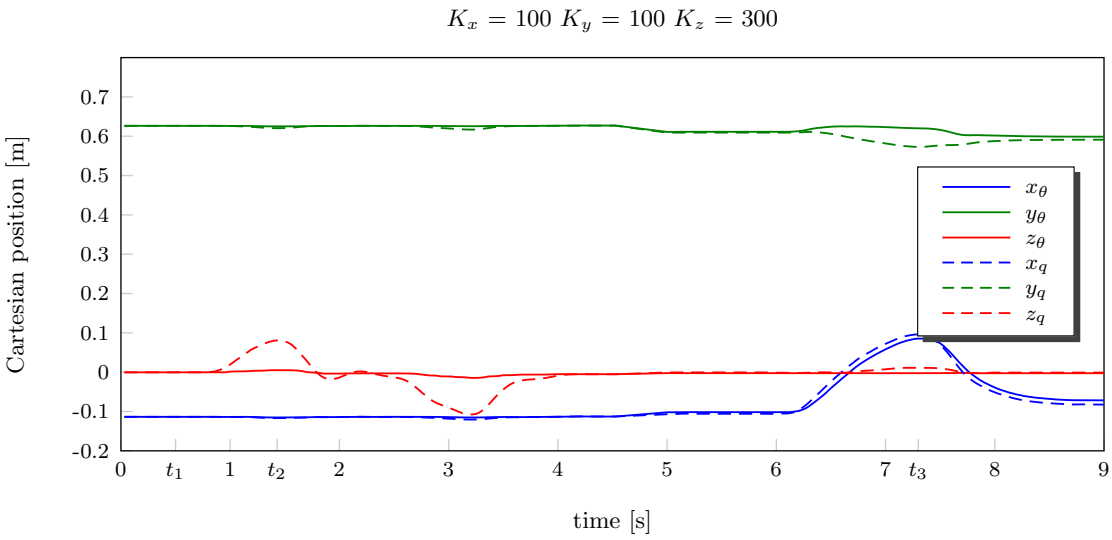

Figure 5.10.: Measurement plots of the TCP position $\boldsymbol{x}_q$ and motor TCP position $\boldsymbol{x}_\theta$. The TCP is deflected in the x- and z-direction. For the case of a low passive stiffness and a high active stiffness (z-direction, time point t_2), the passive stiffness element deflects a lot. For the case vice versa (x-direction, time point t_3), the passive stiffness element deflects very little.

stiffness $\boldsymbol{K}_{Ca}^{Best}$.

The optimization algorithms are computed with a rate of 366 Hz on the real time operating system, see Section 2.1. The user chooses a desired Cartesian stiffness and triggers the parameterization of the controllers. Then, the joint stiffness variation parameter $\boldsymbol{\sigma}^{Best}$ is commanded to the stiffness motors and held constant by a PD-position controller. Also, the active Cartesian stiffness matrix $\boldsymbol{K}_{Ca}^{Best}$ and the equilibrium position $\bar{\boldsymbol{x}}$ are commanded to the active Cartesian impedance controller (4.9) and held constant. The robot stiffness behaviour can now be analysed by deflecting the robot from its equilibrium pose.

Experimental Results

Figure 5.10 shows measurements of the TCP position coordinates $\boldsymbol{x}_q$ and the motor-based TCP position $\boldsymbol{x}_\theta$, where the Cartesian coordinates of the TCP are given by $\boldsymbol{x}_i = (x_i \; y_i \; z_i)^T$. In the latter ones the motor positions instead of the link positions are used to calculate the forward kinematics, see Fig. 5.1. The relating stiffness values for the time instants t_1, t_2 and t_3 are given in Table 5.1. The desired Cartesian stiffness $\boldsymbol{K}_{Cd}$ remains constant throughout the trajectory. $\boldsymbol{K}_{Cp}$ shows the locally valid Cartesian stiffness matrix as it is generated by the passive stiffness joints. At the beginning (t_1), the optimization from Section 5.3.3 was triggered and the necessary

values $\boldsymbol{\sigma}^{Best}$ were set, therefore $\boldsymbol{K}_{Cp} = \boldsymbol{K}_{Cp}^{Best} = \boldsymbol{K}_{Cd}$ should be achieved. However, looking at the diagonal entries, the desired value is only reached satisfactory by the z-coordinate ($K_{Cpzz} = 299\,\mathrm{N/m}$). The x- and y-coordinates are not very close to the desired $\boldsymbol{K}_{Cd}$ values. This is because of the minimal passive joint stiffness bounds prohibit to reach the low Cartesian stiffnesses: The robot configuration requires high joint torques in the first axis to support the robot and from (2.18) with a progressive shape also high joint stiffness results (see Table 5.1, $\boldsymbol{k}_{Jp}$ entries marked with a '*' are reaching the lower bound values). In order to compensate for the high passive Cartesian stiffness entries in $\boldsymbol{K}_{Cp}$, the active compliance optimization computes low stiffness values for the x- and y-component ($K_{Caxx} = 116\,\mathrm{N/m}$, $K_{Cayy} = 97\,\mathrm{N/m}$) and high stiffness for the z-component. Finally, the active and passive stiffness values sum up to a serial stiffness $\boldsymbol{K}_{Cs}$ which is very close to the desired one.

The behaviour of the impedance controller for deflections from the desired position can be seen in the measurements at the time instants t_2 and t_3. At t_2 the TCP is deflected in the z-direction. As the passive stiffness tracking in this direction is very good, most of the deflection is provided by the passive stiffness elements (large motion of z_q in Fig. 5.10), while the high active stiffness prevents the motors from moving (almost no motion of z_θ). The deflection leads to an increase of the passive joint stiffness ($K_{Cpzz} = 489\,\mathrm{N/m}$) because of the progressive shape of the FSJs (see Fig. 2.5) which in turn results in an increase of K_{Cszz}, as the stiffness values are only valid locally (see also Section 5.3.6).

A similar behaviour can be seen at t_3 where a deflection in the x-direction is executed. As the passive joint stiffness in this direction is very high ($K_{Cpxx} = 879\,\mathrm{N/m}$), the TCP deflection is mainly provided by the motor deflection and thereby by the active impedance controller ($K_{Caxx} = 116\,\mathrm{N/m}$). The apparently random change of the y-coordinate stems from a nullspace motion executed by the elbow joint.

Further measurements of experiments of the active/passive impedance controller in action are shown in Fig. 5.11 and Fig. 5.12 . In Fig. 5.11 the stiffness in the x-y plane was set high, while in the z-direction a very low stiffness was chosen. Figure 5.12 shows in contrast a low stiffness in the x-y plane and a high stiffness in the z-direction. In both setups, a commanded high stiffnesses results in a very stiff active impedance controller. A TCP deflection in these stiff directions results in a relatively large deflection of the passive stiffness elements, while the motors move only little. The low stiffness instead is mainly provided by the active impedance controller (the passive impedance is lower bounded), what appears in the plots as a large motion executed by the motors.

For comparability, the stiffability set of the active/passive impedance controller of a setup as used in Section 5.2 is depicted in Fig. 5.13. The stiffness region is vastly extended by the combined approach.

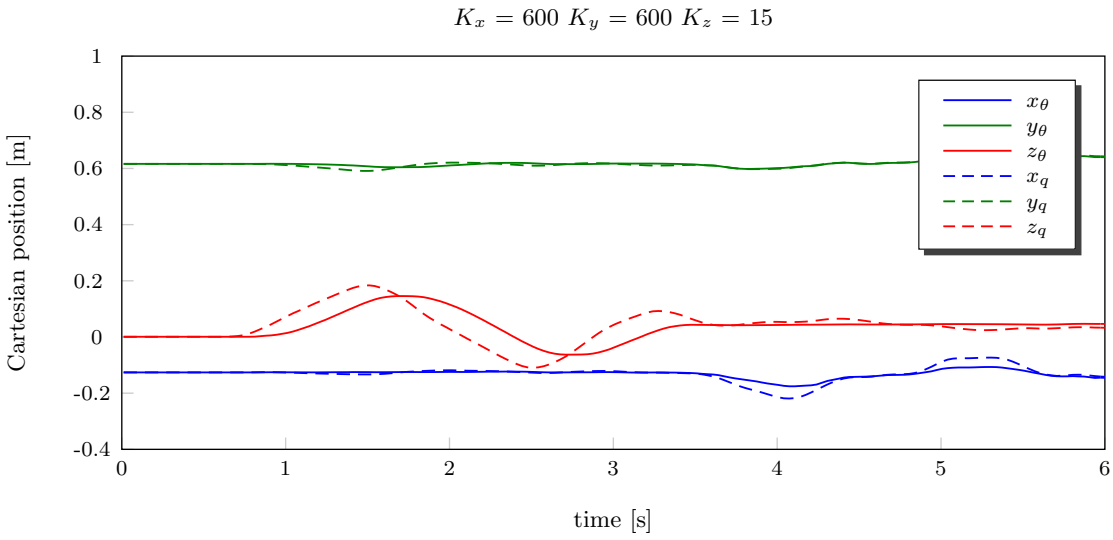

Figure 5.11.: Measurements of the combined impedance controller for specifying the x-y plane to show high stiffness behaviour. The robot can be easily deflected in the z-direction, as here a very low stiffness is commanded.

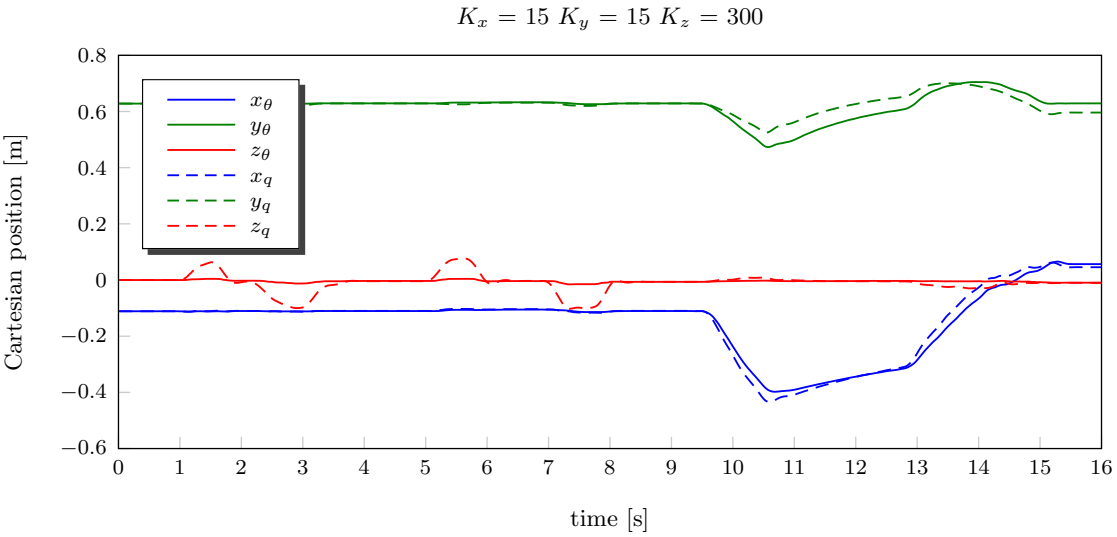

Figure 5.12.: Measurements of the combined impedance controller for high stiffness behaviour in the z-direction. The x- and y-direction show low stiffness, which is generated mostly by the active impedance controller, as the lowest passive stiffness in the direction is relatively high (e.g. $K_{Cpxx} > 10 \cdot K_{Cdxx}$).

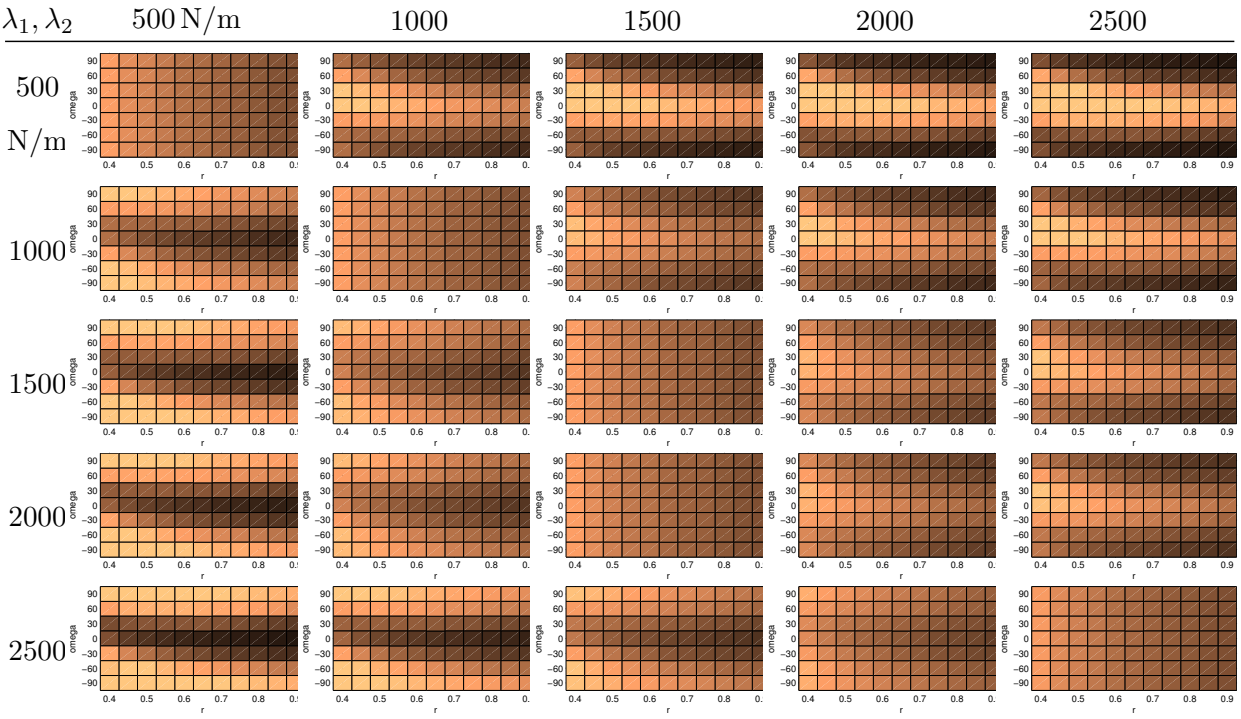

Figure 5.13.: A stiffability set of the serial stiffness approach. The stiffness range of the active impedance controller is k =0..5000 Nm/rad.

5.3.6. Discussion

The combination of the passive joint stiffness with an active impedance controller is an elegant approach to combine the best of both regimes. It allows to make use of the beneficial properties of the passive elastic elements such as robustness and mechanical response. The active controller provides great adaptability and flexibility and thereby allows to overcome bounds imposed by the technical realization.
The combined optimization approach is the choice at hand if high performance stiffness tracking is desired. Disadvantages are more costly computations and an ambiguous contribution of the active and passive stiffness components. In most cases the active/passive impedance approach represents a viable alternative. It focuses on passive stiffness tracking and aims to improve tracking by the active controller. A computational efficient algorithm ensures real-time compatibility. The effectiveness of the presented algorithm can be seen in the conducted experiments and is especially obvious in the stiffability plot Fig. 5.13.

5.4. Configuration Dependent Stiffness Adjustment

The analysis at the beginning of this chapter demonstrates that a pure passive stiffness variation is unsatisfactory to achieve a broad Cartesian stiffness range. A nullspace motion may extend the stiffness performance. In this section, a nullspace variaton method is presented along with an experimental validation.

5.4.1. The Nullspace Optimization Approach

Besides of the stiffness matrices, the Cartesian joint stiffness depends upon the robot configuration. The problem of finding an appropriate robot configuration poses a nonlinear optimization problem (5.11). The global solution of this problem is very hard to find under real-time constraints. Assuming a low dimensional nullspace, sampling approaches may lead to reasonable results. For higher dimensions, this approach is unfeasible as the number of samples grows exponentially. Furthermore, the global solution of this problem might not be applicable to the robot at all times. During trajectory execution, many tasks require the nullspace configuration of the robot to not change erratically. This might happen if minima have a similar error quality and switch their global ranking due to slight motions. For these reasons, we consider a global approach to be more relevant for a motion planning level in an offline layer.
An alternative approach is a local method. Therefore, the general optimization problem (5.11) is reformulated

$$\begin{aligned} &\min_{\boldsymbol{q}} \|\boldsymbol{K}_{Cd} - \boldsymbol{K}_{Cs}(\boldsymbol{q})\| = \min_{\boldsymbol{q}} \|\boldsymbol{G}(\boldsymbol{K}_{Cd}, \boldsymbol{q})\|, \\ &\text{s.t. } \boldsymbol{h}(\boldsymbol{q}) = \boldsymbol{x}_d \\ &\quad \boldsymbol{q}^{Min} \leq \boldsymbol{q} \leq \boldsymbol{q}^{Max}. \end{aligned} \tag{5.35}$$

A locally valid update law can be defined by evaluating the gradient of $\boldsymbol{G}(\boldsymbol{K}_{Cd}, \boldsymbol{q})$ to optimize the joint configuration in the nullspace

$$\boldsymbol{q}_{i+1} = \boldsymbol{q}_i - \alpha \nabla_{\boldsymbol{N_q}} \boldsymbol{G}(\boldsymbol{K}_{Cd}, \boldsymbol{q}). \tag{5.36}$$

The scalar α is determining the step size of the gradient descent. The gradient is computed in the direction of the null space by

$$\nabla_{\boldsymbol{N_q}} \boldsymbol{G}(\boldsymbol{K}_{Cd}, \boldsymbol{q}) = \lim_{h \to 0} \left(\sum_{i=1}^{r} \boldsymbol{n}_i(\boldsymbol{q}) \frac{\boldsymbol{G}(\boldsymbol{K}_{Cd}, \hat{\boldsymbol{q}}) - \boldsymbol{G}(\boldsymbol{K}_{Cd}, \boldsymbol{q})}{h} \right) \tag{5.37}$$

$$\text{with } \hat{\boldsymbol{q}} = \boldsymbol{q} + h\boldsymbol{n}_i(\boldsymbol{q}) \tag{5.38}$$

Herein, $\boldsymbol{N}(\boldsymbol{q}) = (\boldsymbol{n}_1(\boldsymbol{q}), \ldots, \boldsymbol{n}_r(\boldsymbol{q})) \in \mathbb{R}^{n \times r}$ is the nullspace base matrix [19] with the dimension $r = n - m$. Robotic arms often have a one dimensional nullspace, such also the DLR Hand Arm System. In this case, the nullspace matrix reduces to the row vector $\boldsymbol{n}(\boldsymbol{q})$. The gradient iteration involves the numerical computation of local joint stiffness values, as a dependency upon the robot configuration exists.
The gradient descent algorithm converges to the local optimal null space pose $\boldsymbol{q}_0$. The optimal nullspace pose can be used to generate a joint space nullspace controller

$$\boldsymbol{\tau}_n = -\boldsymbol{D}_n \dot{\boldsymbol{\theta}} - \boldsymbol{K}_n(\bar{\boldsymbol{q}} - \boldsymbol{q}_0), \tag{5.39}$$

where $\boldsymbol{K}_n \in \mathbb{R}^{n \times n}$ and $\boldsymbol{D}_n \in \mathbb{R}^{n \times n}$ are positive definite gain matrices and $\dot{\boldsymbol{\theta}} \in \mathbb{R}^n$ is the motor velocity.
This controller is applied on the robot using the superposition principle [10] in addition to the Cartesian impedance controller.

5.4.2. Experimental Results

Three experiments have been conducted to evaluate the nullspace optimization controller in combination with a passive stiffness adjustment 5.3.3. The first four joints of the DLR Hand Arm System were used in the experiments.
In a **first experiment** the local disturbance properties of the nullspace optimization controller in combination with a passive stiffness adjustment control approach were tested. Therefore, a TCP position and a desired Cartesian stiffness matrix of $\boldsymbol{K}_{Cd} = \text{diag}(600, 2000, 500)$ N/m were commanded. The time course of the error norm of the measurements is depicted in Fig. 5.14. The robot is in steady state in two different configurations at the time instants t_1, t_3, t_5 and t_4. In between, the robot is manually disturbed at the elbow. From t_3 to t_4 and t_4 to t_5 the disturbance leads to a change of the local nullspace minimum. The related configurations are illustrated in Fig. 5.15, where the main axes of the desired Cartesian stiffness are shown in red color and the achieved Cartesian stiffness is illustrated in blue color. In the steady states at t_1, t_3, t_5 and t_4 the stiffness tracking is reasonable. During the disturbance, e.g. at t_2 the error grows considerably, depicted in Fig. 5.15(b). The error is about three times bigger than at the optimum position. The nullspace reconfiguration can be observed in the joint position measurements Fig. 5.16.

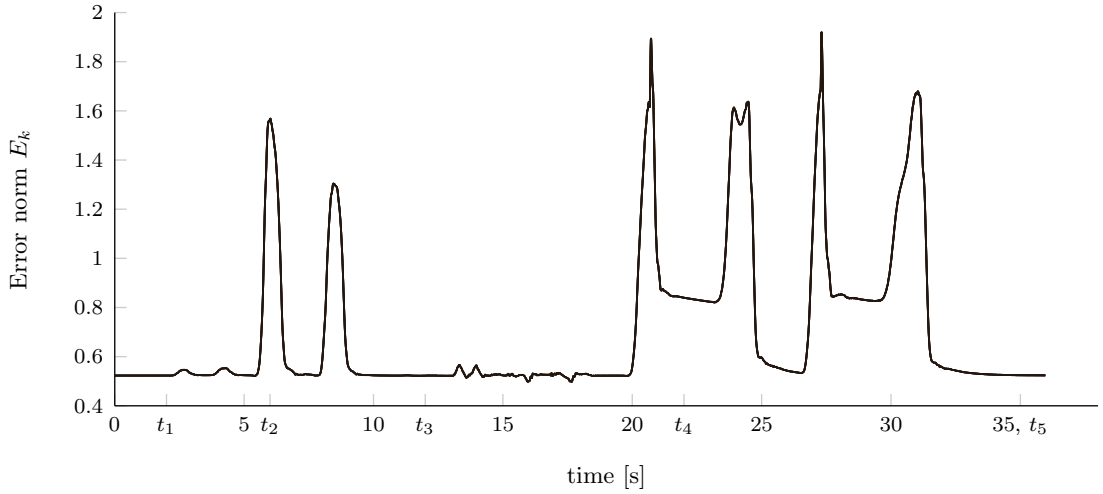

Figure 5.14.: The error norm of the nullspace optimization controller in combination with the passive stiffness adjustment throughout the first experiment. The second local optimum at t_4 has a larger error than the first local optimum at t_1,t_3 and t_5.

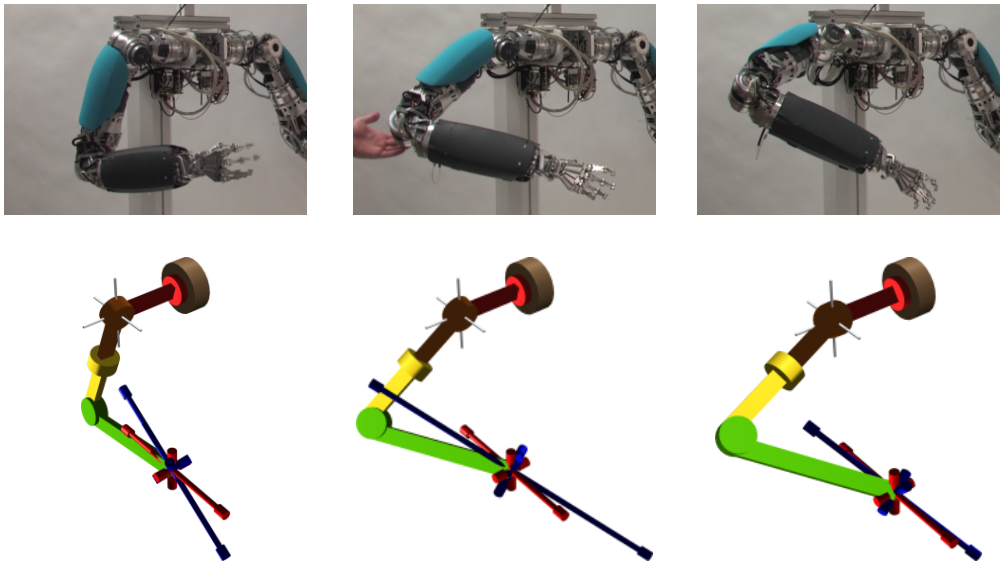

(a) First local optimum from t_1, t_3, t_5.

(b) Disturbance at elbow.

(c) Second local optimum from t_4.

Figure 5.15.: Robot poses and Cartesian stiffness values ($\boldsymbol{K}_{Cd}$ in red, $\boldsymbol{K}_C$ in blue) of the first experiment. By pulling the elbow up, the robot can be moved from one local minimum (a) to another one (c).

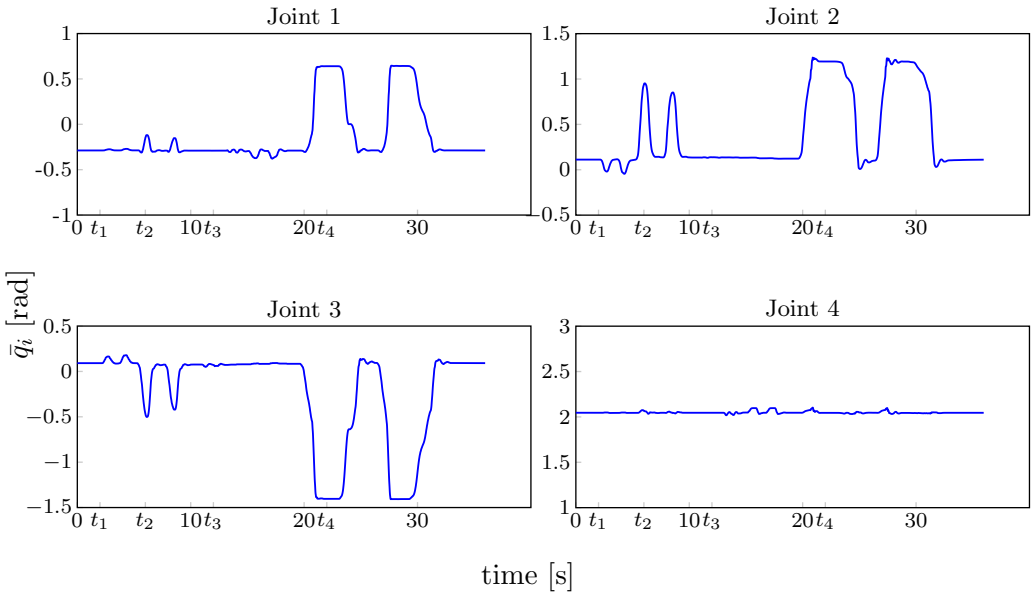

Figure 5.16.: Joint positions $\bar{\boldsymbol{q}}$ throughout the first experiment.

In a **second experiment** a Cartesian trajectory was commanded as it could be used in a scenario to wipe a table. The cyclic trajectory is depicted in Fig. 5.17. The motion is executed from the front of the robot (t_0, t_3) to its side (t_1). The stiffness matrix $\boldsymbol{K}_{Cd} = \mathrm{diag}(2000, 600, 500)\,\mathrm{N/m}$ is chosen with a high stiffness in the normal direction of the table. Four different controller scenarios have been tested. The time courses of the error norms are plotted in Fig. 5.18. A first run has been executed with no stiffness controller at all. The measurements are illustrated in Fig. 5.19, where again the desired stiffness axes are colored red and the achieved ones are colored blue. The big error occuring at t_2 in the error norm plot is visible in Fig. 5.19(b) by a very large main stiffness axis. In the second run, only the joint stiffness was optimized and not the joint nullspace motion. The measurements show, that the performance gain compared to no optimization is low, see Fig. 5.18, joint stiffness optimization (JSO). The reason is the lower limit of the joint stiffness values, which is increased by the arm loading and the progressive stiffness curves of the variable stiffness joints. The mechanical stiffness is relatively high especially in joint 2, as the measurements plotted in Fig. 5.20 show. The third run executed with an activated nullspace optimization controller, shows big performance improvements, see Fig. 5.18, nullspace optimization (NSO). The controller reconfigures the robot such that the joint stiffness limits are lowered, see Fig. 5.21. An additional slight improvement gives the combination of the nullspace optimization and the joint stiffness optimization (NSO + JSO). In the illustration in Fig. 5.22 the reconfiguration and good stiffness tracking is visible. This experiment highlights the importance of the nullspace optimization approach. It also shows, that in some cases the joint stiffness optimization has minor leverage on the achievable stiffness performance due to the narrow bounds of the progressive VSA joint stiffness.

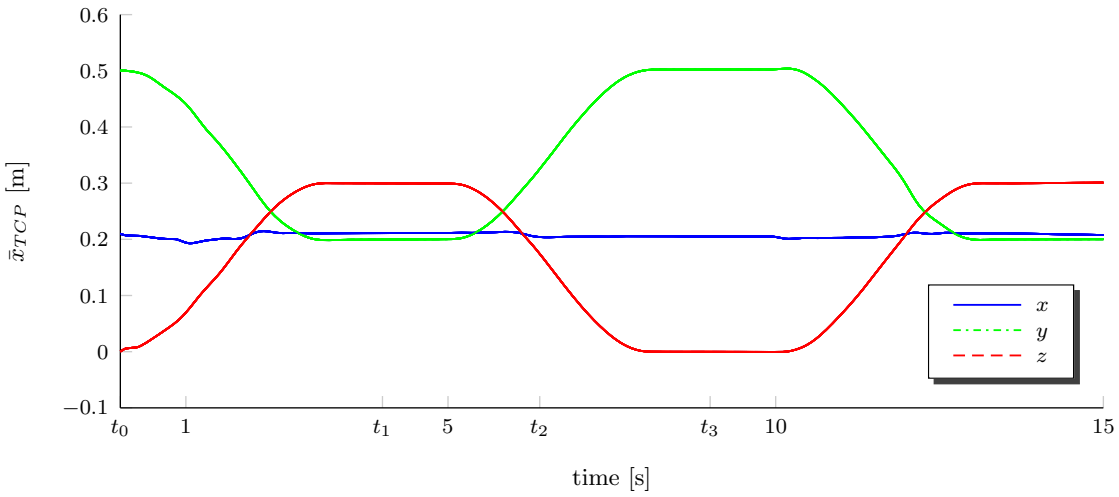

Figure 5.17.: Cartesian TCP trajectory throughout the wiping motion of the second experiment.

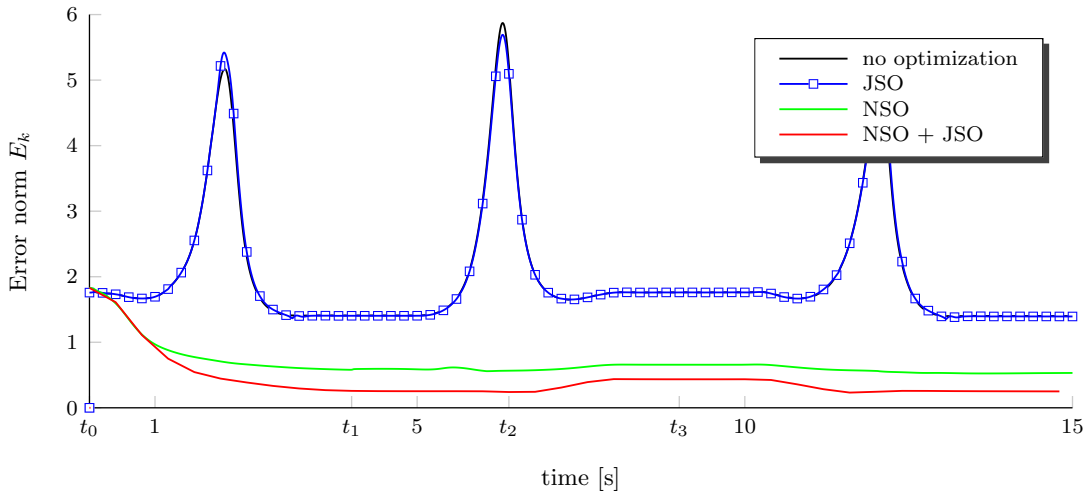

Figure 5.18.: The error norms obtained from the measurements during the wiping experiment. The wiping was executed with four combinations of controllers. The best result gave the combined nullspace and joint stiffness optimization. JSO: Joint stiffness optimization. NSO: Nullspace optimization.

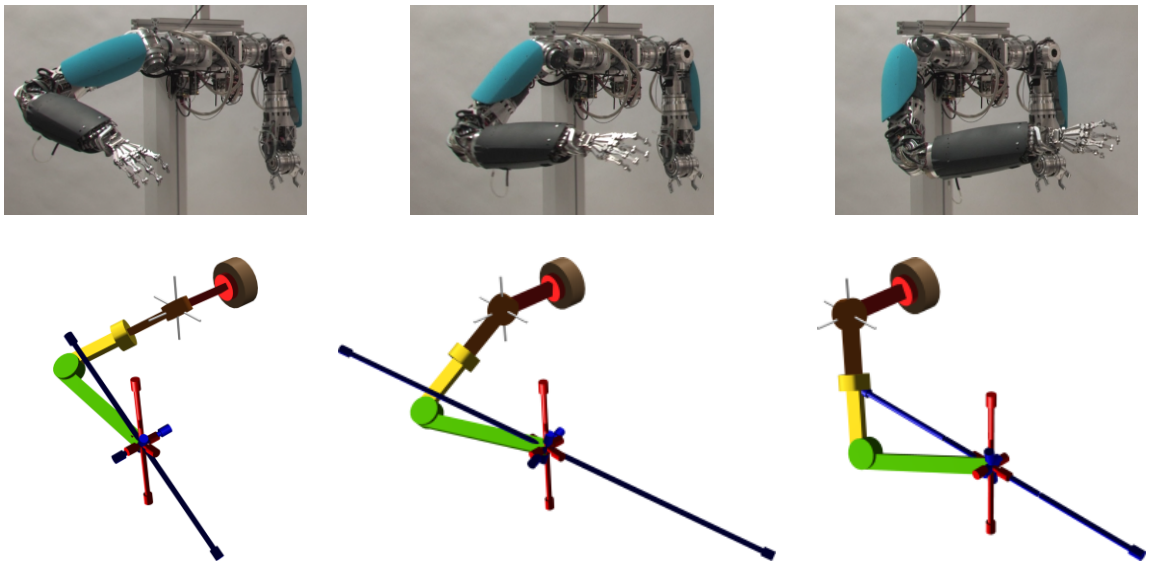

(a) Point of time t_1. (b) Point of time t_1. (c) Point of time t_1.

Figure 5.19.: Illustrations of the desired and achieved Cartesian stiffness ellipsoids ($\boldsymbol{K}_{Cd}$ in red, $\boldsymbol{K}_C$ in blue) during the wiping experiment without any optimization. Large stiffness errors occur.

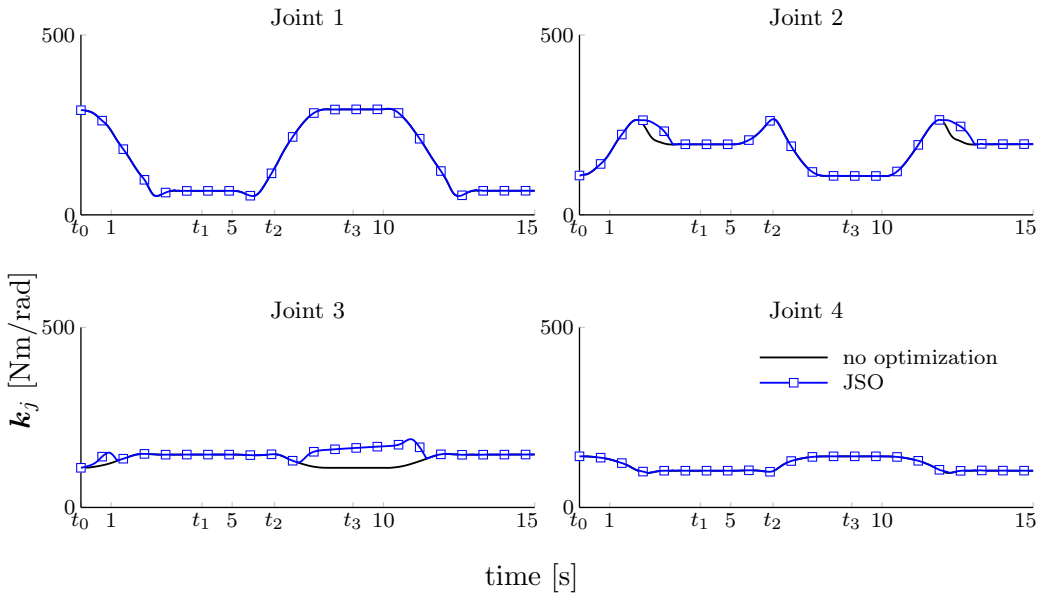

Figure 5.20.: Passive joint stiffness values $\boldsymbol{k}_{Jp}$ throughout the wiping experiment with no optimization and with joint stiffness optimization (JSO). This plot reveals the reason for the bad performance of the JSO controller: It cannot command lower stiffness values as the minimum joint stiffness is increased by the arm loading and the progressive stiffness shape.

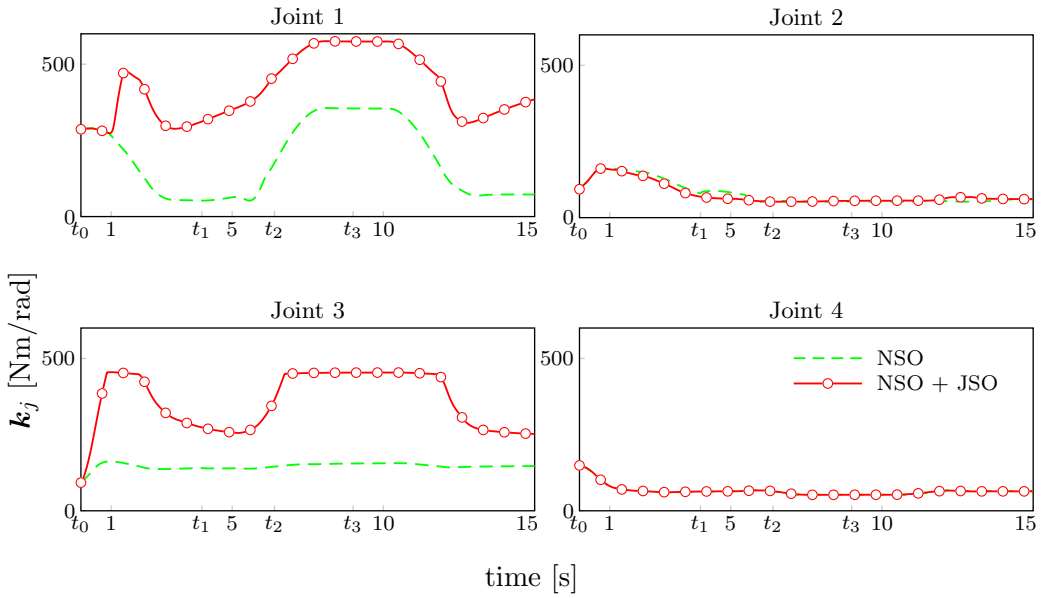

Figure 5.21.: Passive joint stiffness values $\boldsymbol{k}_{Jp}$ throughout the wiping experiment with nullspace and joint stiffness optimization (NSO and JSO). The reconfiguration of the robot lowers the loading of the joints and thereby reduces the minimal joint stiffness values.

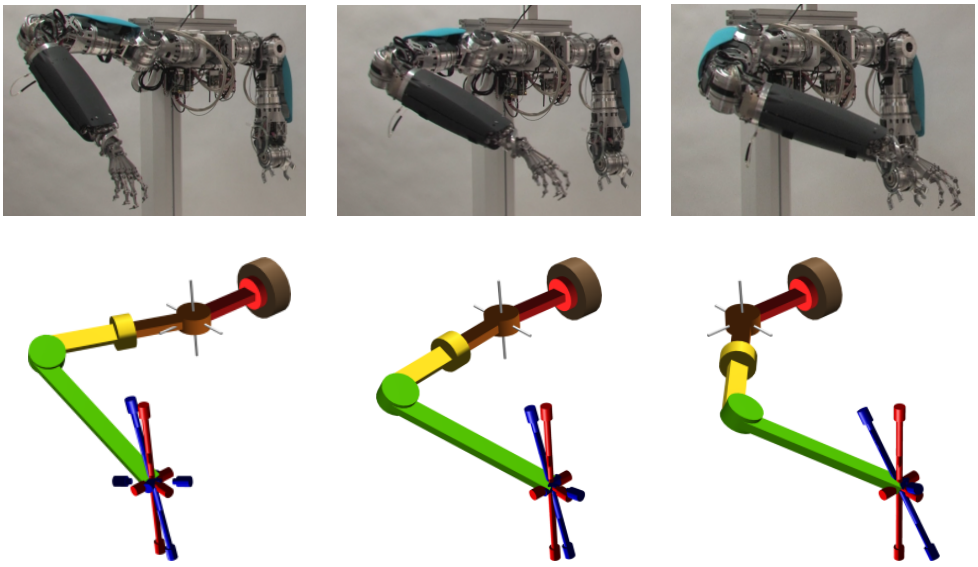

(a) Point of time t_1. (b) Point of time t_1. (c) Point of time t_1.

Figure 5.22.: Illustrations of the desired and achieved Cartesian stiffness ellipsoids ($\boldsymbol{K}_{Cd}$ in red, $\boldsymbol{K}_C$ in blue) during the wiping experiment with nullspace and joint stiffness optimization enabled. The nullspace reconfiguration lowers the joint loading and enables effective joint stiffness optimization resulting in very good stiffness tracking.

The **third experiment** aims to track a changing desired Cartesian stiffness matrix. Therefore, it is switched between the two desired stiffness matrices $\boldsymbol{K}_{Cd1} = \mathrm{diag}(600, 2000, 500)\,\mathrm{N/m}$ and $\boldsymbol{K}_{Cd2} = \mathrm{diag}(2000, 600, 500)\,\mathrm{N/m}$, resembling a rotation by $\pi/2$ along the z-axis. The course of the error norm without optimization, with only joint stiffness optimization (JSO), and with nullspace and joint stiffness optimization (NSO + JSO) is plotted in Fig. 5.23. The stiffness matrix $\boldsymbol{K}_{Cd1}$ is commanded at t_1, and $\boldsymbol{K}_{Cd2}$ at t_3. The robot motion is illustrated in Fig. 5.24. A pure joint stiffness optimization leads to only small advancements. The nullspace optimization reconfigures the elbow such that the main axes are tracked with better accuracy. At t_2 neither optimization is improving the error norm result. This is attributed to a tracking error of the quickly rotating stiffness ellipsoid.

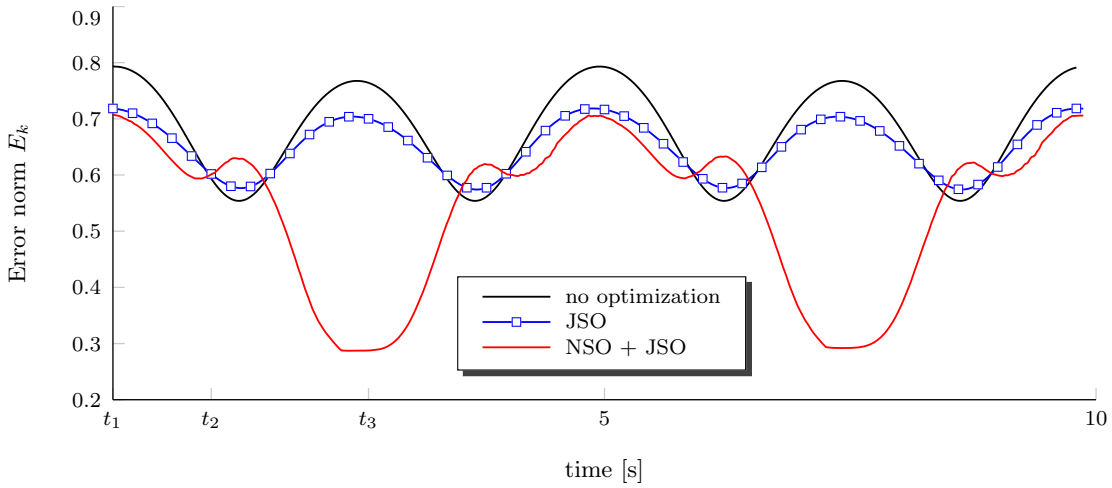

Figure 5.23.: Comparison of the error norms during the third experiment with and without the controllers being enabled.

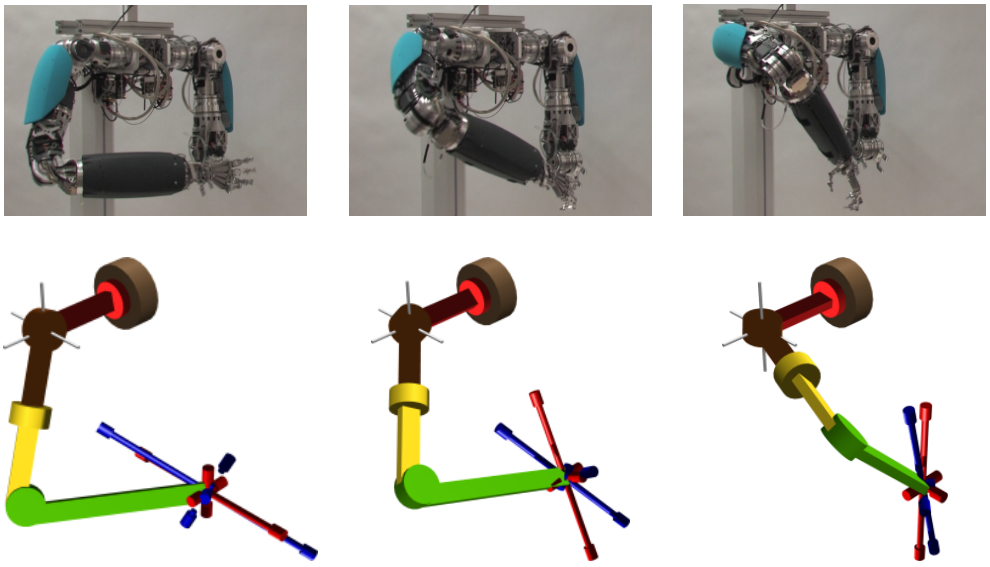

(a) Point of time t_1. (b) Point of time t_2. (c) Point of time t_3.

Figure 5.24.: Illustrations of the desired and achieved Cartesian stiffness ellipsoids ($\boldsymbol{K}_{Cd}$ in red, $\boldsymbol{K}_C$ in blue) during the stiffness ellipsoid rotating experiment with nullspace and joint stiffness optimization enabled. The nullspace reconfiguration is a major factor in ensuring the tracking of the main stiffness axis.

5.4.3. Discussion

The nullspace optimization problem per se is highly nonlinear and hard to solved during real-time operation of the robot. The alternative presented here is a local approach using a nullspace gradient. The advantages of the approach are versatile. It can be applied for robots with highly dimensional nullspace. The method can be easily integrated via well known nullspace projection approaches in the impedance control framework. The resulting robot motion is smooth and convergence rates can be designed by the user. Last but not least, it is feasible for real-time computation. The local properties of the controller allow for a combination with joint based stiffness optimization algorithms, such as the sequantial approach.
The effect of the controller is clearly visible in the results of the experiments. The arm reconfiguration improves stiffness axis tracking and improves the effect of joint stiffness optimization.
Drawback of the nullspace approach is the required reconfiguration of robot arm. Safe reconfiguration has to be ensured e.g. at a higher level planning stage.

6. Damping Control

It is common for the treated VSA systems that the joint elements inhere as little damping as possible. The slightly damped robots tend to show oscillations, which can be easily exaggerated. Many robotic applications require an adjustable damping behavior e.g. for fast positioning accuracy. Integrating an additional variable damping element in each joint would further increase the mechanism complexity and size [108]. For that reason, in the DLR Hand Arm System the approach to inject damping via control was pursued. Furthermore, the use of an active control system is very beneficial because the powerful actuators allow for fast adjustment of the damping behavior ranging from very low damping as provided by the pure mechanical friction in the joints up to the practically highest damping, i. e. (over)critical damping in case of emergency stops.
A vibration damping controller for VSA robots has to meet several requirements. The dynamic multi-input multi-output VSA robot model is highly coupled and nonlinear, conditioned by the inertial properties and the VS elastic elements, resulting in large parameter variations[1]. Furthermore, there are several practical restrictions in controller realization due to the technical implementation. Dominating are actuator saturation, transmission delays, measurement noise, and real-time computation constraints. A main consequence are practical upper and lower limits on controller gains, which are very challenging from controller design perspective. Independent of the exact controller structure, it has been found that the choice of controller gains to remain in a limited range is crucial and very challenging for stability and practicability.
A first category of controllers which can cope with the VSA plant in a mathematical correct way are e. g. feedback linearization or backstepping. Both approaches heavily rely on the robot model, where already small deviations may lead to big control errors. In detail, feedback linearization uses a local diffeomorphism to transform the nonlinear system into a linear dynamics [27]. The control of the achieved linear dynamics is a standard issue. However, it is well known that the feedback linearization approach is very sensitive regarding modeling errors. The resulting total feedback gains vary heavily and the given gain limitations of the system are hard to meet. Backstepping controllers are able to cope with plant parameter variations and such a controller is presented and discussed below. In both approaches the control action is computed by shaping or decoupling the model differential equations through the torque inputs. Therefore it is required to derive sensor signals multiple times, which is practically difficult due to sensor quantization and noise. A further possibility of this category are linear parameter varying (LPV) controllers, which are, however, limited to small parameter variations [109].

[1] Such as eigenfrequencies.

Another controller category are gain scheduling controllers, which use a linearization of the nonlinear dynamics obtained at a high rate (typically above 1 kHz), see [110]. Beneficial is that the controller gains can be adjusted to the fast changing plant parameters. Furthermore, the use of high state derivatives can be avoided by using a state feedback structure. Although widely applied in research and industrial applications, stability can only be guaranteed for limited parameter rates.
A third type of controllers aims at not relying on exact model knowledge. Instead, assumptions on the model structure are made and state signals are used to achieve the control goal. Such an approach is a tradeoff between resulting performance and controller robustness.
All three types of controllers have been developed in this thesis and are presented in the following. Thereby, the range from theoretical elaborate and highly model based controller, over a practically sound version, to a model free approach is shown. It is to remark, that it was an important concern in this thesis that all the developed controllers are applicable to multi-joint robots.
Section 6.1 describes the backstepping approach from [111]. The physical motivated gain design is presented in Section 6.2 and based on [112]. In Section 6.3 the state based damping approach is given, as presented in [113].

6.1. Backstepping

In general, a control approach for VSA robots has to close the gap between theoretical soundness and practical applicability. On the one hand, the approach has to be able to cope with the nonlinearities given by the robot dynamics and the actuators. On the other hand the controller has to regard practical limitations of the feedback systems such as sensor quantization and noise, actuator limitations, signal delays, and unmodeled dynamics.
A control approach which is capable of handling these requirements is backstepping. It allows to specify a physically interpretable control law at the highest state level (the robot link side position/velocity) and guarantees stability in the subsequent levels. Backstepping is well known in the literature. Besides of general introduction of the topic (e.g. [114]), backstepping has been applied in the robotic context. An algorithm for flexible joint robots has been presented in [115, 116], where tracking control on joint level is discussed. A similar type of systems is treated in [19], where impedance control in the Cartesian space is considered.

6.1.1. Model

To use the model (2.23) for backstepping it must be transformed to strict feedback form

$$\ddot{\boldsymbol{q}} = -\boldsymbol{M}^{-1}(\boldsymbol{q})\left(\boldsymbol{C}(\boldsymbol{q},\dot{\boldsymbol{q}})\dot{\boldsymbol{q}} + \boldsymbol{g}(\boldsymbol{q})\right) + \boldsymbol{M}^{-1}(\boldsymbol{q})\boldsymbol{T}\boldsymbol{\tau} \tag{6.1a}$$

$$\dot{\boldsymbol{\tau}} = -\boldsymbol{k}(\boldsymbol{\varphi},\boldsymbol{\sigma})\boldsymbol{T}^T\dot{\boldsymbol{q}} + \boldsymbol{k}(\boldsymbol{\varphi},\boldsymbol{\sigma})\dot{\boldsymbol{\theta}} \tag{6.1b}$$

$$\ddot{\boldsymbol{\theta}} = -\boldsymbol{B}^{-1}\boldsymbol{\tau} + \boldsymbol{B}^{-1}\boldsymbol{\tau}_m. \tag{6.1c}$$

6.1.2. PD$^+$ & Backstepping

Backstepping control design allows to use an arbitrary control law for the first subsystem as long as this closed loop system is asymptotically stable and a Lyapunov function is provided. A basic goal of VSA robots is to adapt the robot on a mechanical level to the task and use additional control only if additional features are needed. Therefore, the structure of the dynamic model of the robot shall be preserved. To achieve this, a control law choice suggested here is the augmented PD controller [117, 78]. The PD$^+$ control law is a tracking controller similar to the computed torque (inverse dynamics) controller. The difference is an inner, decoupled PD feedback loop running at an higher rate plus an outer dynamics compensation loop. This generates a dynamics similar to (2.23a) and additionally allows to provide configuration dependent damping.

Controller Design

The backstepping approach is based on the fact that in each equation one of the coordinates acts as a virtual input to the system. The coordinate has to appear in an affine way in each equation. This is given for the VSA model (6.1) by the elastic torque $\boldsymbol{\tau}$, the motor velocity $\dot{\boldsymbol{\theta}}$, and the motor torque $\boldsymbol{\tau}_m$, respectively.
The PD$^+$ control law for the link side dynamics (6.1a) is chosen as

$$\boldsymbol{\tau}_d = \boldsymbol{T}^+(\boldsymbol{M}(\boldsymbol{q})\ddot{\boldsymbol{q}}_{des} + \boldsymbol{C}(\boldsymbol{q},\dot{\boldsymbol{q}})\dot{\boldsymbol{q}}_{des} + \boldsymbol{g}(\boldsymbol{q}) - \boldsymbol{K}_d\dot{\boldsymbol{e}} - \boldsymbol{K}_p\boldsymbol{e}). \tag{6.2}$$

Herein, the control gains are $\boldsymbol{K}_p, \boldsymbol{K}_d \in \mathbb{R}^{n\times n}$ both positive definite. The errors are given by $\boldsymbol{e} = \boldsymbol{q} - \boldsymbol{q}_{des}$ and $\dot{\boldsymbol{e}} = \dot{\boldsymbol{q}} - \dot{\boldsymbol{q}}_{des}$. The matrix $\boldsymbol{T}^+$ is a pseudo inverse[2] of $\boldsymbol{T}$.
It is assumed that the reference torque $\boldsymbol{\tau}_d$ is tracked, such that the closed loop dynamics

$$\boldsymbol{T}(\boldsymbol{\tau} - \boldsymbol{\tau}_d) = \boldsymbol{M}\ddot{\boldsymbol{e}} + \boldsymbol{C}\dot{\boldsymbol{e}} + \boldsymbol{K}_p\boldsymbol{e} + \boldsymbol{K}_d\dot{\boldsymbol{e}} \tag{6.3}$$

results. For ideal tracking $\boldsymbol{\tau} = \boldsymbol{\tau}_d$, this dynamics constitutes a gravity compensated and PD controlled robot behavior. The choice of the PD$^+$ control law gets clear here, as it sustains the natural dynamics of the plant. To achieve optimal damping in every configuration [19] $\boldsymbol{K}_d$ is calculated by

$$\boldsymbol{K}_d = \xi\left(\boldsymbol{M}^{\frac{1}{2}}\boldsymbol{K}_p^{\frac{1}{2}} + \boldsymbol{K}_p^{\frac{1}{2}}\boldsymbol{M}^{\frac{1}{2}}\right) \tag{6.4}$$

with $\xi \in (0,1]$, $\boldsymbol{M}^{\frac{1}{2}}\boldsymbol{M}^{\frac{1}{2}} = \boldsymbol{M}$ and $\boldsymbol{K}_p^{\frac{1}{2}}\boldsymbol{K}_p^{\frac{1}{2}} = \boldsymbol{K}_p$.
The backstepping formalism requires the recursive formulation of the subsequent control laws aiming at two goals. First, the higher level control laws have to be generated. Secondly, the stability of the closed loop system has to be ensured.

[2] $\boldsymbol{T}$ specifies the load distribution between the drives. The choice of the pseudo inverse results in different motor loading. In the practical application we use the Moore-Penrose pseudo inverse ensuring equal loading of the motors.

The second control law is given by

$$\dot{\boldsymbol{\theta}}_d = \boldsymbol{k}^{-1}(\boldsymbol{\tau}) \left(\boldsymbol{k}(\boldsymbol{\tau}, \boldsymbol{\sigma}) \boldsymbol{T}^T \dot{\boldsymbol{q}} + \dot{\boldsymbol{\tau}}_d - \boldsymbol{K}_1 (\boldsymbol{\tau} - \boldsymbol{\tau}_d) - \boldsymbol{T}^T \dot{\boldsymbol{e}} \right). \tag{6.5}$$

When we assume tracking of $\dot{\boldsymbol{\theta}}_d$, with (6.1b) the error dynamics becomes

$$\boldsymbol{k}(\boldsymbol{\tau}, \boldsymbol{\sigma})(\dot{\boldsymbol{\theta}} - \dot{\boldsymbol{\theta}}_d) = \dot{\boldsymbol{\tau}} - \dot{\boldsymbol{\tau}}_d + \boldsymbol{K}_1 (\boldsymbol{\tau} - \boldsymbol{\tau}_d) + \boldsymbol{T}^T \dot{\boldsymbol{e}}. \tag{6.6}$$

This allows for an interpretation of the control law (6.5). The first term in the parentheses in (6.5) cancels the link velocity dynamics in (6.1b). The second and third term ensure the torque tracking, where $\boldsymbol{K}_1 > 0 \in \mathbb{R}^{m \times m}$ is a so-called backstepping gain. The last term is a compensation term ensuring stability, as elaborated later on.
Following a similar reasoning as before, we obtain the third control law as

$$\boldsymbol{u} = \boldsymbol{B} \left(\boldsymbol{B}^{-1} \boldsymbol{\tau} + \ddot{\boldsymbol{\theta}}_d - \boldsymbol{K}_2 (\dot{\boldsymbol{\theta}} - \dot{\boldsymbol{\theta}}_d) - \boldsymbol{k}(\boldsymbol{\tau}, \boldsymbol{\sigma})(\boldsymbol{\tau} - \boldsymbol{\tau}_d) \right). \tag{6.7}$$

Enforcing $\boldsymbol{\tau}_m = \boldsymbol{u}$ leads to the closed loop equation

$$\boldsymbol{0} = \ddot{\boldsymbol{\theta}} - \ddot{\boldsymbol{\theta}}_d + \boldsymbol{K}_2 (\dot{\boldsymbol{\theta}} - \dot{\boldsymbol{\theta}}_d) + \boldsymbol{k}(\boldsymbol{\tau}, \boldsymbol{\sigma})(\boldsymbol{\tau} - \boldsymbol{\tau}_d). \tag{6.8}$$

The interpretation of the controller terms is analog to (6.5), where $\boldsymbol{K}_2 > 0 \in \mathbb{R}^{m \times m}$ is a backstepping gain. This concludes the controller design. The next step is to prove the controller stability which will also explain the compensation terms.

Stability Analysis

The stability of the closed loop system can be analysed using a Lyapunov function. The tracking errors are defined as

$$\boldsymbol{x}_0 = \boldsymbol{e}, \quad \boldsymbol{x}_1 = \dot{\boldsymbol{e}}, \quad \boldsymbol{x}_2 = \boldsymbol{\tau} - \boldsymbol{\tau}_d, \quad \boldsymbol{x}_3 = \dot{\boldsymbol{\theta}} - \dot{\boldsymbol{\theta}}_d, \tag{6.9}$$

and the closed loop dynamics result by rearranging (6.3), (6.6), and (6.8)

$$\dot{\boldsymbol{x}}_0 = \dot{\boldsymbol{e}} = \dot{\boldsymbol{q}} - \dot{\boldsymbol{q}}_{des} \tag{6.10a}$$

$$\dot{\boldsymbol{x}}_1 = \ddot{\boldsymbol{e}} = \boldsymbol{M}^{-1}(\boldsymbol{q}) \left(-\boldsymbol{K}_d \boldsymbol{x}_1 - \boldsymbol{C}(\boldsymbol{q}, \dot{\boldsymbol{q}}) \boldsymbol{x}_1 - \boldsymbol{K}_p \boldsymbol{x}_0 + \boldsymbol{T} \boldsymbol{x}_2 \right) \tag{6.10b}$$

$$\dot{\boldsymbol{x}}_2 = -\boldsymbol{T}^T \boldsymbol{x}_1 - \boldsymbol{K}_1 \boldsymbol{x}_2 + \boldsymbol{k}(\boldsymbol{\tau}, \boldsymbol{\sigma}) \boldsymbol{x}_3 \tag{6.10c}$$

$$\dot{\boldsymbol{x}}_3 = -\boldsymbol{k}(\boldsymbol{\tau}, \boldsymbol{\sigma}) \boldsymbol{x}_2 - \boldsymbol{K}_2 \boldsymbol{x}_3, \tag{6.10d}$$

with the initial conditions $\boldsymbol{x}_0(0) = \boldsymbol{e}(0)$, $\boldsymbol{x}_1(0) = \dot{\boldsymbol{e}}(0)$, $\boldsymbol{x}_2(0) = \boldsymbol{\tau}(0) - \boldsymbol{\phi}_0(0)$, and $\boldsymbol{x}_3(0) = \dot{\boldsymbol{\theta}}(0) - \boldsymbol{\phi}_1(0)$.
The Lyapunov candidate function is based on a potential function of the first control law plus quadratic terms of the tracking errors,

$$V = \frac{1}{2} \left(\boldsymbol{x}_0^T \boldsymbol{K}_p \boldsymbol{x}_0 + \boldsymbol{x}_1^T \boldsymbol{M}(\boldsymbol{q}) \boldsymbol{x}_1 + \boldsymbol{x}_2^T \boldsymbol{x}_2 + \boldsymbol{x}_3^T \boldsymbol{x}_3 \right) > 0, \quad (\boldsymbol{x}_0, \boldsymbol{x}_1, \boldsymbol{x}_2, \boldsymbol{x}_3) \neq \boldsymbol{0}. \tag{6.11}$$

By deriving (6.11) and substituting (6.10) it follows

$$\dot{V} = -\boldsymbol{x}_1^T \boldsymbol{K}_d \boldsymbol{x}_1 - \boldsymbol{x}_2^T \boldsymbol{K}_1 \boldsymbol{x}_2 - \boldsymbol{x}_3^T \boldsymbol{K}_2 \boldsymbol{x}_3 \leq 0, \quad (\boldsymbol{x}_0, \boldsymbol{x}_1, \boldsymbol{x}_2, \boldsymbol{x}_3) \neq \boldsymbol{0}. \tag{6.12}$$

The action of the compensation terms becomes clear by calculating (6.12). The last term in (6.10b) constitutes the torque error and is cancelled by the first term of the subsequent dynamics (6.10c). Similarly, the last term in (6.10c) represents the velocity error and is cancelled with the first term in (6.10d).
The resulting function is negative semidefinite. As the PD$^+$ controller is asymptotically stable and the remainder of the derivative of the Lyapunov function (6.12) is of quadratic nature, the stability proof from [78] is valid, too, without going into details. Thus asymptotic stability for the closed loop system is given.

6.1.3. Command Filtered Backstepping

A problematic point of backstepping tracking controllers is the need for higher order derivatives of the low level control laws and of state measurements (first n derivatives for n-th order systems). Derivatives of the low level control laws can be easily obtained analytically for robots, while no straight forward way for the state derivatives exists. In [118] an approach to generate the lower level control laws without explicit computation using filters is presented. Here, this approach is adapted to obtain higher order state derivatives while ensuring system stability.
Evaluating the third control law (6.7) it results that the following derivatives of the signals are needed:

- up to 4th order of $\boldsymbol{q}_{des}$
- 3rd order of $\boldsymbol{q}$
- 1st order of $\boldsymbol{k}(\boldsymbol{\tau}, \boldsymbol{\sigma})$
- 1st order of $\boldsymbol{\theta}$

While $\boldsymbol{q}_{des} \in \mathcal{C}^4$ can be obtained from a trajectory generator, see Section 6.4, especially obtaining $\boldsymbol{q}^{(3)}$ is challenging. Possible ways to calculate the derivatives are numerically or model based. Due to the measurement noise numerical derivation is critical and influences system stability. Model based derivatives are problematic because they depend highly on the model, which is very difficult to identify accurately enough. That makes backstepping of higher order systems with sensor signals exposed to noise very hard in practice. A method to cope with this problem is to use special signal filters called command filters.
Originally, command filtered backstepping was proposed for omitting the complex derivation of the control laws which are needed when using backstepping, see [118]. So-called command filters are filtering the output of control laws resulting from backstepping. Here, we use it for filtering measurement noise. In [118] command filtered backstepping is used with SISO-systems,

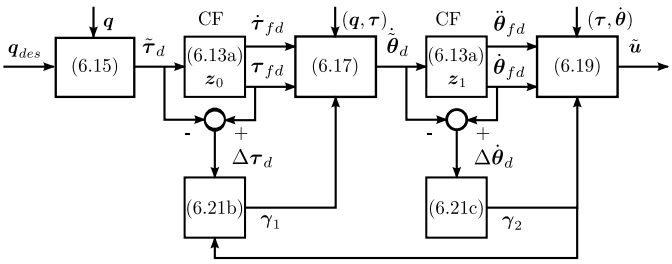

Figure 6.1.: A block diagram of the command filtered backstepping approach.

where subsystems are of first order and the first control law is a feedback linearization law. This is extended here for the MIMO system (6.1), the possibly multiple subsystems, and the PD$^+$ control law (6.2).

Controller Design

The command filters used here are second order low pass filters. Written in state feedback form with the state vector $\boldsymbol{z}_i$ they are

$$\dot{\boldsymbol{z}}_i = \omega_n \begin{pmatrix} 0 & 1 \\ -1 & -2\zeta \end{pmatrix} \boldsymbol{z}_i + \omega_n \begin{pmatrix} 0 \\ 1 \end{pmatrix} \tilde{\boldsymbol{\phi}}_i, \tag{6.13a}$$

$$\begin{pmatrix} \boldsymbol{\phi}_{fi} \\ \dot{\boldsymbol{\phi}}_{fi} \end{pmatrix} = \begin{pmatrix} 1 & 0 \\ 0 & \omega_n \end{pmatrix} \boldsymbol{z}_i, \tag{6.13b}$$

where $\boldsymbol{\phi}_i$, $i \in 1..3$ refers to the control laws $\boldsymbol{\tau}_d$, $\boldsymbol{\theta}_d$, and $\boldsymbol{u}$, respectively. Modified versions of the original laws will be developed below, denoted by a tilde above $\tilde{\boldsymbol{\phi}}_i$ and beeing input to the filters. After filtering, the output is $\boldsymbol{\phi}_{fi}$. The parameter $\omega_n > 0$ denotes the natural frequency, $\zeta \in (0, 1]$ the damping parameter, and $\boldsymbol{z}_i(0) = [\tilde{\boldsymbol{\phi}}_i(0), 0]^T$ the initial value. The state variables of the command filter between the first and second control law are denoted by $\boldsymbol{z}_0$ and between the second and third control law by $\boldsymbol{z}_1$.

The filtering introduces the error $\Delta\phi_i = \phi_{fi} - \tilde{\phi}_i$. This error destructs the validity of the backstepping approach, as the original control laws are distorted. To still be able to ensure stability, the error is fed back (compensated) creating the concept of a compensator $\boldsymbol{\gamma}_i$. The setup of the modified control laws and the compensators is shown now. For an overview, see Fig. 6.1.

First, new tracking errors are defined using the filtered values

$$\tilde{\boldsymbol{x}}_0 = \boldsymbol{e}, \tilde{\boldsymbol{x}}_1 = \dot{\boldsymbol{e}}, \tilde{\boldsymbol{x}}_2 = \boldsymbol{\tau} - \boldsymbol{\tau}_{fd}, \tilde{\boldsymbol{x}}_3 = \dot{\boldsymbol{\theta}} - \dot{\boldsymbol{\theta}}_{fd}. \tag{6.14}$$

The first modified control law is equal to the original control law as it does not require higher state derivatives

$$\tilde{\boldsymbol{\tau}}_d = \boldsymbol{\tau}_d = \boldsymbol{T}^+(\boldsymbol{M}(\boldsymbol{q})\ddot{\boldsymbol{q}}_{des} + \boldsymbol{C}(\boldsymbol{q}, \dot{\boldsymbol{q}})\dot{\boldsymbol{q}}_{des} + \boldsymbol{g}(\boldsymbol{q}) - \boldsymbol{K}_d\dot{\boldsymbol{e}} - \boldsymbol{K}_p\boldsymbol{e}). \tag{6.15}$$

The error dynamics is similar to the original error dynamics, c.f. (6.10b),

$$\dot{\tilde{\boldsymbol{x}}}_1 = \ddot{\boldsymbol{e}} = \boldsymbol{M}^{-1}(\boldsymbol{q})(-\boldsymbol{K}_d\tilde{\boldsymbol{x}}_1 - \boldsymbol{C}(\boldsymbol{q},\dot{\boldsymbol{q}})\tilde{\boldsymbol{x}}_1 - \boldsymbol{K}_p\tilde{\boldsymbol{x}}_0 + \boldsymbol{T}\tilde{\boldsymbol{x}}_2 + \boldsymbol{T}\Delta\boldsymbol{\tau}_d), \tag{6.16}$$

with an additional difference term $\boldsymbol{T}\Delta\boldsymbol{\tau}_d$ and $\boldsymbol{\tau}_{fd} = \Delta\boldsymbol{\tau}_d + \tilde{\boldsymbol{\tau}}_d$. This term arises due to the error introduced by the filtering of the state signals. Before going into detail about the effect of this term, first the two subsequent control laws and dynamics are introduced.
The second control law contains the filtered first control law $\boldsymbol{\tau}_{fd}$ and an additional compensator term $\boldsymbol{\gamma}_1$

$$\dot{\tilde{\boldsymbol{\theta}}}_d = \boldsymbol{k}^{-1}(\boldsymbol{\tau})(\boldsymbol{k}(\boldsymbol{\tau},\boldsymbol{\sigma})\boldsymbol{T}^T\dot{\boldsymbol{q}} + \dot{\boldsymbol{\tau}}_{fd} - \boldsymbol{K}_1(\boldsymbol{\tau} - \boldsymbol{\tau}_{fd}) - \boldsymbol{T}^T(\dot{\boldsymbol{e}} - \boldsymbol{\gamma}_1)). \tag{6.17}$$

The error dynamics is

$$\dot{\tilde{\boldsymbol{x}}}_2 = -\boldsymbol{T}^T(\tilde{\boldsymbol{x}}_1 - \boldsymbol{\gamma}_1) - \boldsymbol{K}_1\tilde{\boldsymbol{x}}_2 + \boldsymbol{k}(\boldsymbol{\tau},\boldsymbol{\sigma})\tilde{\boldsymbol{x}}_3 + \boldsymbol{k}(\boldsymbol{\tau},\boldsymbol{\sigma})\Delta\dot{\boldsymbol{\theta}}_d, \tag{6.18}$$

with $\dot{\boldsymbol{\theta}}_{fd} = \Delta\dot{\boldsymbol{\theta}}_d + \dot{\tilde{\boldsymbol{\theta}}}_d$. The differences to (6.10c) are the compensation term $\boldsymbol{\gamma}_1$ and a difference term due to the filtering.
The third control law is

$$\tilde{\boldsymbol{u}} = \boldsymbol{B}(\boldsymbol{B}^{-1}\boldsymbol{\tau} + \ddot{\boldsymbol{\theta}}_{fd} - \boldsymbol{K}_2(\dot{\boldsymbol{\theta}} - \dot{\boldsymbol{\theta}}_{fd}) - \boldsymbol{k}(\boldsymbol{\tau},\boldsymbol{\sigma})(\boldsymbol{\tau} - \boldsymbol{\tau}_{fd} - \boldsymbol{\gamma}_2)), \tag{6.19}$$

resulting in the error dynamics

$$\dot{\tilde{\boldsymbol{x}}}_3 = -\boldsymbol{k}(\boldsymbol{\tau},\boldsymbol{\sigma})(\tilde{\boldsymbol{x}}_2 - \boldsymbol{\gamma}_2) - \boldsymbol{K}_2\tilde{\boldsymbol{x}}_3, \tag{6.20}$$

where an additional compensator term $\boldsymbol{\gamma}_2$ arises, compared to (6.10d). For all error dynamics the initial conditions $\tilde{\boldsymbol{x}}_0(0) = \boldsymbol{e}(0)$, $\tilde{\boldsymbol{x}}_1(0) = \dot{\boldsymbol{e}}(0)$, $\tilde{\boldsymbol{x}}_2(0) = \boldsymbol{\tau}(0) - \boldsymbol{\tau}_{fd}(0)$, and $\tilde{\boldsymbol{x}}_3(0) = \dot{\boldsymbol{\theta}}(0) - \dot{\boldsymbol{\theta}}_{fd}(0)$ are assumed.
The similarity of (6.14), (6.16), (6.18), and (6.20) to (6.10) is now exploited to ensure and proof stability of the command filtered backstepping controller. Therefore, the compensators $\boldsymbol{\gamma}_i$ are chosen according to the differential equations

$$\dot{\boldsymbol{\gamma}}_0 = \boldsymbol{\gamma}_1 \tag{6.21a}$$
$$\dot{\boldsymbol{\gamma}}_1 = \boldsymbol{M}^{-1}(\boldsymbol{q})(-\boldsymbol{K}_d\boldsymbol{\gamma}_1 - \boldsymbol{C}(\boldsymbol{q},\dot{\boldsymbol{q}})\boldsymbol{\gamma}_1 - \boldsymbol{K}_p\boldsymbol{\gamma}_0 + \boldsymbol{T}\Delta\boldsymbol{\tau}_d + \boldsymbol{T}\boldsymbol{\gamma}_2) \tag{6.21b}$$
$$\dot{\boldsymbol{\gamma}}_2 = -\boldsymbol{K}_1\boldsymbol{\gamma}_2 + \boldsymbol{k}\Delta\dot{\boldsymbol{\theta}}_d, \tag{6.21c}$$
$$\dot{\boldsymbol{\gamma}}_3 = 0. \tag{6.21d}$$

The initial values are $\boldsymbol{\gamma}_0(0) = \boldsymbol{0}$, $\boldsymbol{\gamma}_1(0) = \boldsymbol{0}$ and $\boldsymbol{\gamma}_2(0) = \boldsymbol{0}$. The compensators fulfill two purposes. First, they enable a coordinate transformation to the new set of compensated tracking errors defined as

$$\boldsymbol{v}_0 = \tilde{\boldsymbol{x}}_0 - \boldsymbol{\gamma}_0, \boldsymbol{v}_1 = \tilde{\boldsymbol{x}}_1 - \boldsymbol{\gamma}_1, \boldsymbol{v}_2 = \tilde{\boldsymbol{x}}_2 - \boldsymbol{\gamma}_2, \boldsymbol{v}_3 = \tilde{\boldsymbol{x}}_3 - \boldsymbol{\gamma}_3. \tag{6.22}$$

Second, they remove the Δ terms from (6.16) and (6.18). Both actions become clear by evaluating the compensated tracking errors

$$\dot{\boldsymbol{v}}_0 = \dot{\tilde{\boldsymbol{x}}}_0 - \dot{\boldsymbol{\gamma}}_0 = \boldsymbol{v}_1 \tag{6.23a}$$

$$\dot{\boldsymbol{v}}_1 = \dot{\tilde{\boldsymbol{x}}}_1 - \dot{\boldsymbol{\gamma}}_1 = \boldsymbol{M}^{-1}(\boldsymbol{q})\left(-\boldsymbol{K}_d\boldsymbol{v}_1 - \boldsymbol{C}(\boldsymbol{q},\dot{\boldsymbol{q}})\boldsymbol{v}_1 - \boldsymbol{K}_p\boldsymbol{v}_0 + \boldsymbol{T}\boldsymbol{v}_2\right) \tag{6.23b}$$

$$\dot{\boldsymbol{v}}_2 = \dot{\tilde{\boldsymbol{x}}}_2 - \dot{\boldsymbol{\gamma}}_2 = -\boldsymbol{T}^T\boldsymbol{v}_1 - \boldsymbol{K}_1\boldsymbol{v}_2 + \boldsymbol{k}(\boldsymbol{\tau},\boldsymbol{\sigma})\boldsymbol{v}_3 \tag{6.23c}$$

$$\dot{\boldsymbol{v}}_3 = \dot{\tilde{\boldsymbol{x}}}_3 = -\boldsymbol{k}(\boldsymbol{\tau},\boldsymbol{\sigma})\boldsymbol{v}_2 - \boldsymbol{K}_2\boldsymbol{v}_3, \tag{6.23d}$$

with the initial conditions $\boldsymbol{v}_i(0) = \tilde{\boldsymbol{x}}_i(0), i = 0,\ldots,3$. The coordinate transformation results in exactly the same form as in (6.10) with the coordinates $\boldsymbol{v}_i$, enabling a similar Lyapunov based stability proof.

Stability Analysis

To show stability of the command filtered backstepping approach first the convergence of the compensated tracking errors is shown. Afterwards, the stability for the whole system can be proved through Tichonov's Theorem [114]. The proof is similar to the one presented in [118], with extensions for the PD$^+$ control law and the MIMO system setup.
The stability of the compensated tracking errors can be shown using the Lyapunov function candidate (c.f. (6.11))

$$\tilde{V} = \frac{1}{2}\left(\boldsymbol{v}_0^T\boldsymbol{K}_p\boldsymbol{v}_0 + \boldsymbol{v}_1^T\boldsymbol{M}(\boldsymbol{q})\boldsymbol{v}_1 + \boldsymbol{v}_2^T\boldsymbol{v}_2 + \boldsymbol{v}_3^T\boldsymbol{v}_3\right) > 0, \quad (\boldsymbol{v}_0,\boldsymbol{v}_1,\boldsymbol{v}_2,\boldsymbol{v}_3) \neq \boldsymbol{0}. \tag{6.24}$$

Its derivative is given by

$$\dot{\tilde{V}} = -\boldsymbol{v}_1^T\boldsymbol{K}_d\boldsymbol{v}_1 - \boldsymbol{v}_2^T\boldsymbol{K}_1\boldsymbol{v}_2 - \boldsymbol{v}_3^T\boldsymbol{K}_2\boldsymbol{v}_3 \leq 0, \quad (\boldsymbol{v}_0,\boldsymbol{v}_1,\boldsymbol{v}_2,\boldsymbol{v}_3) \neq \boldsymbol{0}. \tag{6.25}$$

Also the convergence result is similar to (6.12). Hence the compensated tracking errors converge asymptotically.
From this it is not yet possible to conclude the convergence of the tracking errors $(\tilde{\boldsymbol{x}}_0, \tilde{\boldsymbol{x}}_1, \tilde{\boldsymbol{x}}_2, \tilde{\boldsymbol{x}}_3)$. To proof it singular perturbation theory is used. For brevity, we reference here to the comprehensive formulation of Theorem 11.2 in [114].[3]
First the tracking errors and the compensators are combined to a vector denoted by

$$\hat{\boldsymbol{x}} = [\tilde{\boldsymbol{x}}_0, \tilde{\boldsymbol{x}}_1, \tilde{\boldsymbol{x}}_2, \tilde{\boldsymbol{x}}_3, \boldsymbol{\gamma}_0, \boldsymbol{\gamma}_1, \boldsymbol{\gamma}_2]^T \in \mathbb{R}^{2n+2m+2n+m} \tag{6.26}$$

and the command filters are combined and denoted by $\hat{\boldsymbol{z}} = [\boldsymbol{z}_0, \boldsymbol{z}_1]^T \in \mathbb{R}^{2m+2m}$. This allows to write them in the form of the standard singular perturbation problem as

$$\dot{\hat{\boldsymbol{x}}} = \hat{\boldsymbol{f}}(t, \hat{\boldsymbol{x}}, \hat{\boldsymbol{z}}, \epsilon) \tag{6.27}$$

$$\epsilon\dot{\hat{\boldsymbol{z}}} = \hat{\boldsymbol{g}}(t, \hat{\boldsymbol{x}}, \hat{\boldsymbol{z}}, \epsilon). \tag{6.28}$$

[3] The following preconditions must be met. It is considered a compact set $\mathcal{D}_{\hat{x}} \times \mathcal{D}_{\hat{z}}$ with a convex $\mathcal{D}_{\hat{x}} \subset \mathbb{R}^{4n+3m}$, $\mathcal{D}_{\hat{z}} \subset \mathbb{R}^{4m}$ with $\boldsymbol{0} \in \mathcal{D}_{\hat{z}}$ and a time interval $t \in [t_0, t_1]$.

with (6.14), (6.21) and (6.13). The perturbation parameter ϵ is dependent on the filter parameter as $\omega_n = 1/\epsilon$.
The functions $\hat{\boldsymbol{f}}$ and $\hat{\boldsymbol{g}}$ meet the requirents of Condition 1 of the Theorem 11.2 in [114], because their initial conditions $\hat{\boldsymbol{x}}(0)$ and $\hat{\boldsymbol{z}}(0)$ are independent of ϵ, the model (6.1) and the command filters are w.r.t. to their state variables $(\boldsymbol{q}, \boldsymbol{\tau}, \dot{\boldsymbol{\theta}})$ and $(\boldsymbol{z}_0, \boldsymbol{z}_1)$ and the time t continuous and continuously differentiable and the desired trajectory $\boldsymbol{q}_{des}$ is continuously differentiable.
For $\epsilon = 0$ the unique solution of (6.28) is given by

$$\bar{\boldsymbol{z}} = \boldsymbol{h}(t, \hat{\boldsymbol{x}}) = \begin{pmatrix} \tilde{\phi}_j \\ \mathbf{0} \end{pmatrix} \tag{6.29}$$

for $j = 0, 1$, which also fulfills Condition 1 of Theorem 11.2 in [114].
The reduced system

$$\dot{\bar{\boldsymbol{x}}}(t) = \hat{\boldsymbol{f}}(t, \bar{\boldsymbol{x}}, \boldsymbol{h}(t, \hat{\boldsymbol{x}}), 0) \tag{6.30}$$

has a unique solution $\bar{\boldsymbol{x}}(t) \in \mathcal{S} \subset \mathcal{D}_x$, which meets the requirements of Condition 2 of Theorem 11.2 in [114].
With $\boldsymbol{y} = \hat{\boldsymbol{z}} - \boldsymbol{h}(t, \hat{\boldsymbol{x}})$ the boundary layer model

$$\frac{d\boldsymbol{y}}{d\nu} = \hat{\boldsymbol{g}}(t, \hat{\boldsymbol{x}}, \boldsymbol{y} + \boldsymbol{h}(t, \hat{\boldsymbol{x}}), 0) \tag{6.31}$$

with $\nu = t\epsilon$ and fixed $(t, \hat{\boldsymbol{x}})$ can be evaluated to

$$\frac{d\boldsymbol{y}}{d\nu} = \boldsymbol{\Psi}\boldsymbol{y}. \tag{6.32}$$

Herein, $\boldsymbol{\Psi}$ is a block diagonal matrix whose m blocks consist of the system matrices

$$\begin{pmatrix} 0 & 1 \\ -1 & -2\zeta \end{pmatrix} \tag{6.33}$$

of the command filters. The matrix $\boldsymbol{\Psi}$ is Hurwitz. Therefore, the origin is an exponentially stable equilibrium of the boundary layer model, which meets the requirements of Condition 3 of Theorem 11.2 in [114].
Following results for the tracking errors and the filtered signals

$$|\tilde{\boldsymbol{x}}_i(t, \epsilon) - \boldsymbol{x}_i(t)| = \mathcal{O}(\epsilon) \tag{6.34}$$

$$|\boldsymbol{z}_{j,1} - \boldsymbol{\phi}_j| = \mathcal{O}(\epsilon) \tag{6.35}$$

$$|\boldsymbol{z}_{j,2} - \dot{\boldsymbol{\phi}}_j| = \mathcal{O}(\epsilon) \tag{6.36}$$

with $i = 0, 1, 2$ and $j = 0, 1$ hold.
The reduced system is related to the backstepping approach without command filters (6.10) with an additional dynamics resulting from the command filters (6.21) and has the asymptotically stable equilibrium $(\boldsymbol{x}_0, \boldsymbol{x}_1, \boldsymbol{x}_2, \boldsymbol{x}_3) = \mathbf{0}$. So the approach with command filters is also asymptotically stable.

Param.	Value	Unit	Description
J	1.36×10^{-2}	kg m^2	Link inertia
m	0.56	kg	Beam mass
l	0.27	m	Beam length
d	0.55	kg/s	Viscose link friction
b	10^{-2}	kg m^2	Motor inertia
g	9.81	m/s^2	Gravity constant

Table 6.1.: The physical parameters of the experimental BAVS setup.

Param.	Value	Unit	Description
k_p	50	Nm/rad	P-gain of PD$^+$-law
ξ	1	-	damping parameter of PD$^+$-law
$\boldsymbol{K}_1$	$\left(\begin{smallmatrix}20 & 0\\ 0 & 20\end{smallmatrix}\right)$	1/s	1. backstepping gain
$\boldsymbol{K}_2$	$\left(\begin{smallmatrix}1500 & 0\\ 0 & 1500\end{smallmatrix}\right)$	Nm s	2. backstepping gain
$\boldsymbol{\omega}_{n1}$	$250\left[\begin{smallmatrix}1\\ 1\end{smallmatrix}\right]$	Hz	1. CFs frequency
$\boldsymbol{\omega}_{n2}$	$1000\left[\begin{smallmatrix}1\\ 1\end{smallmatrix}\right]$	Hz	2. CFs frequency.

Table 6.2.: The controller parameters of the experimental BAVS setup.

6.1.4. Simulations and Experimental Results

The presented control approaches have been tested in simulation and on two different test rigs. The results are reported below.

BAVS Joint

A set of tests has been conducted using a bidirectional antagonistic variable stiffness joint, see Chapter 3. The experimental setup is shown in Fig. 6.2. The mechanical properties are given in Tab. 6.1 and the controller parameters are shown in Tab. 6.2. Furthermore, $\boldsymbol{T} = \left(\begin{smallmatrix}1 & 1\end{smallmatrix}\right)$. These values have been used for the simulations, too.
First, the disturbance behavior of the controller was analysed in simulation and on the testbed. An external disturbance of $\tau_{ext} = -5.2$ Nm was imposed for 0.8 s. The simulation and experimental result show an asymptotic decay of the errors, see Fig. 6.3. Static and dynamic errors arise in the measurements. The static deviations are attributed to friction and hysteresis effects

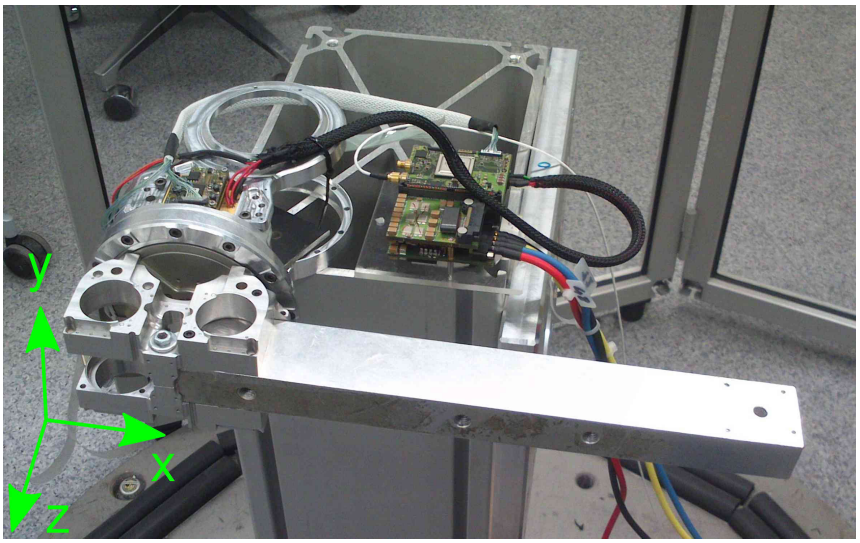

Figure 6.2.: The BAVS joint setup as used for the experimental validation of the backstepping controller. The aluminium beam is connected to the link of the joint.

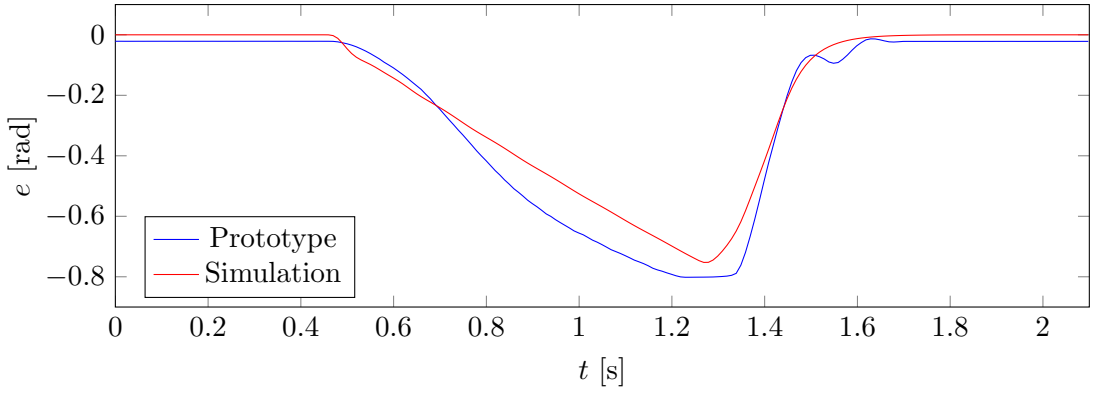

Figure 6.3.: Position error measurement of the disturbance experiment as conducted in simulation and on the BAVS joint. Errors decay asymptotically.

in the joint, but are relatively small. The dynamic differences from the ideal behavior arise among others due to unmodeled dynamics and saturation effects. Overall, it can be concluded, that the experiments match the simulations very well.
Finally, the tracking behavior of the system is validated. Therefore, a desired trajectory is generated according to

$$q_{des}(t) = \frac{1}{4}\pi \sin(4t). \tag{6.37}$$

The desired trajectory q_{des} together with the results is shown in Fig. 6.4. The simulation result is given by e_s and the measurement from the testbed by e_r. To approximate the testbed behavior,

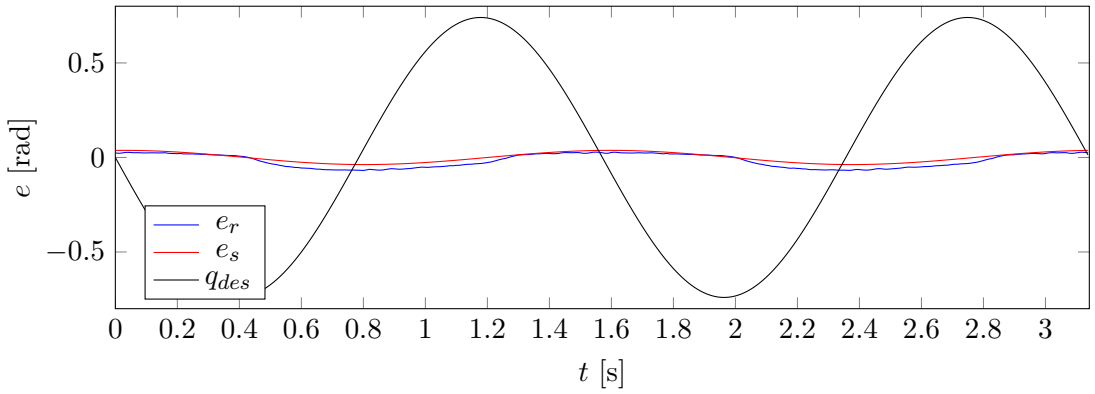

Figure 6.4.: The desired trajectory, the position error measurement of the BAVS setup and simulation results. The tracking errors can be traced back to unmodeled friction effects.

viscose friction of $d = 0.55$ Ns/m on the link side is introduced.
The errors indicate that the link is not perfectly tracking the desired trajectory. This result can be explained by friction effects, as also visible by comparing the simulation and experiment.

Param.	Value	Unit	Description
$\boldsymbol{K}_p$	$\begin{pmatrix} 50 & 0 & 0 & 0 \\ 0 & 50 & 0 & 0 \\ 0 & 0 & 50 & 0 \\ 0 & 0 & 0 & 50 \end{pmatrix}$	Nm/rad	P-gain of PD$^+$-law
ξ	0.5	-	damping parameter of PD$^+$-law
$\boldsymbol{K}_1$	$\begin{pmatrix} 200 & 0 & 0 & 0 \\ 0 & 200 & 0 & 0 \\ 0 & 0 & 200 & 0 \\ 0 & 0 & 0 & 200 \end{pmatrix}$	1/s	1. backstepping gain
$\boldsymbol{K}_2$	$\begin{pmatrix} 300 & 0 & 0 & 0 \\ 0 & 300 & 0 & 0 \\ 0 & 0 & 300 & 0 \\ 0 & 0 & 0 & 300 \end{pmatrix}$	Nm s	2. backstepping gain
$\boldsymbol{\omega}_{n1}$	$1000 \begin{bmatrix} 1 \\ 1 \\ 1 \\ 1 \end{bmatrix}$	Hz	1. CFs frequency
$\boldsymbol{\omega}_{n2}$	$300 \begin{bmatrix} 1 \\ 1 \\ 1 \\ 1 \end{bmatrix}$	Hz	2. CFs frequency

Table 6.3.: The controller parameters as used for the experiments on the DLR Hand Arm System.

DLR Hand Arm System

A second set of tests has been conducted on the DLR Hand Arm System, see Section 2.1. Therefore, the first four joints (shoulder 1 & 2, upper arm rotation joint, elbow joint) have been used. The used controller parameters are given in Tab. 6.3. The disturbance reaction of the system was analysed adjusting a desired position $\boldsymbol{q}_{des} = [\frac{\pi}{2}, \frac{\pi}{2}, \frac{-\pi}{2}, \frac{\pi}{2}]$. The response to an induced collision by an experimenter can be seen in Fig. 6.5. Asymptotic convergence results on all axes. The static and dynamic deviations are attributed to modeling errors and friction effects.
Furthermore, the tracking behaviour of the system was tested. A desired trajectory with a smoothed trapezoidal shape, starting at $\boldsymbol{q}_{des} = \boldsymbol{0}$ moving to the via point $\boldsymbol{q}_{des} = [\frac{\pi}{2}\,\frac{\pi}{2}\,\frac{-\pi}{2}\,\frac{\pi}{2}]^T$ and returning to $\boldsymbol{q}_{des} = \boldsymbol{0}$, has been generated. In Fig. 6.6 the desired trajectory and the simulation and experimental results are depicted.
It is to remark that especially the first axis deviates off the desired trajectory. This is attributed to two reason. First, the values of the dynamic model are not perfectly known. Second, proportional gains of the PD$^+$ law have been chosen low, which follows from a practical confinement, as explained in the discussion.

6.1.5. Discussion

The effectiveness of the chosen backstepping approach is validated by the simulations and experimental results. The general formulation allows to adapt the controller to various robots, such as the BAVS joint or the multi-axis DLR Hand Arm System.
The controller shows several advantageous features. The performance in the case of disturbance is very good. Any errors are reacted for rapidly and the system settles in an asymptotic way. Another advantage of the approach is the consistent way to handle trajectory tracking. The

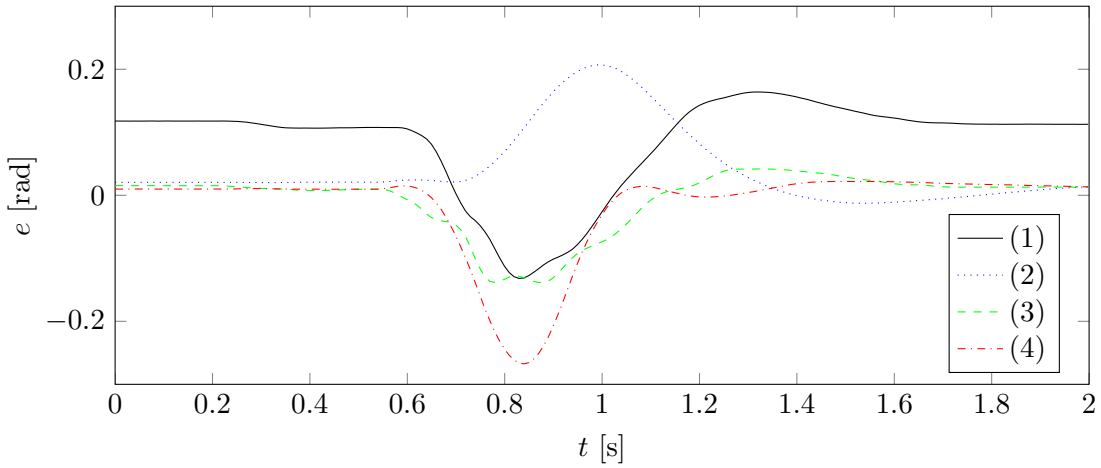

Figure 6.5.: The disturbance reaction of the controller on the four axes of the DLR Hand Arm System. The controller reacts to a hand induced collision, where the errors decline asymptotically.

controller formulation allows to include the trajectory information and the compelling approach to include state filters enables the generation of the reference values. Global stability of the approach is guaranteed under certain assumptions (see also the description of limitations below). The approach allows to include a robot model somewhat close to the physical robot. It can be accounted for the varying link mass and Coriolis and centrifugal terms. Thereby, the analysis can be conducted on a physically intuitive level without too much abstraction, which would harden the controller interpretation.

On the one side, the use of the robot model enables the clean theoretical formulation. On the other side the controller performance is only as good as the model used which is limiting the approach. Effects are visible in the measurements, Fig. 6.6, where errors in the robot model lead to errors in the achieved trajectory. One major drawback of the backstepping approach are input and state constraints. Such limitations, naturally imposed by the technical realization, are not incorporated in the controller design. Especially the cascaded structure of the control laws (6.15), (6.17), and (6.19) requires the exact tracking of subsequent dynamics. Strong link side disturbances may cause tracking errors which lead to high response signals which are prone to saturation effects. These, the controller can not handle and instability may result. In practice this is limiting the deployability of the approach on real robotic systems. The cascaded structure has one more severe consequence, as the highest control law may only depend on link side coordinates $\boldsymbol{q}$, c.f. (6.19). The general VSA stiffness (and also the joint elements of the FSJ) depend additionally upon the motor coordinate $\boldsymbol{\theta}$. Therefore, the passive joint stiffness behaviour cannot be incorporated in the control approach completely, and a linear approximation has to be used. As a link side stiffness higher than the mechanical joint stiffness generally tends to unstable behaviour [19], the controller gains $\boldsymbol{K}_p$ have to be chosen close to the lowest possible

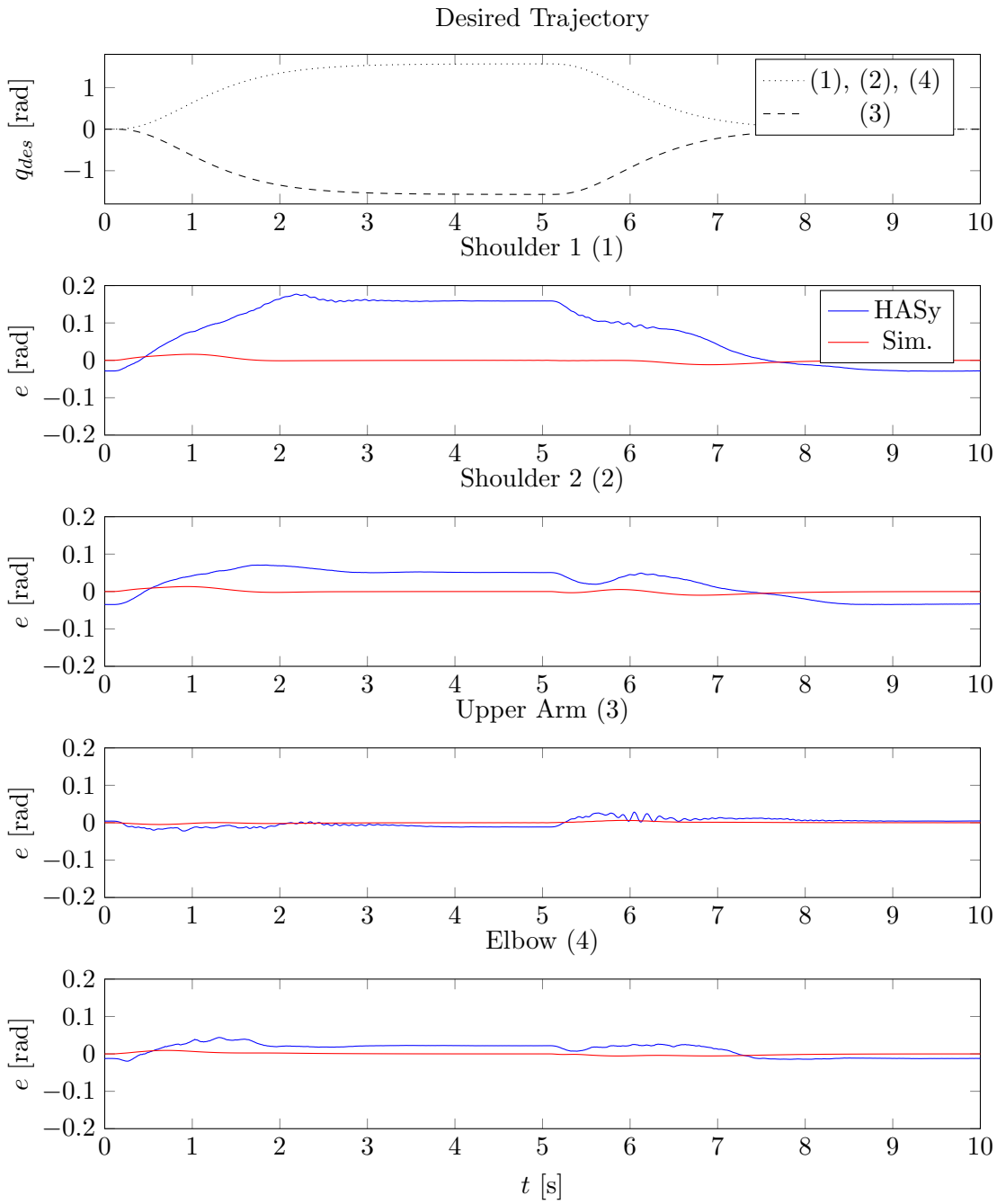

Figure 6.6.: Trajectory tracking experiment on the first four axes of the DLR Hand Arm System.

passive stiffness values. The nonlinear shape of the FSJ joint stiffness (see Fig. 2.13) has its minimal value at about $k(0,0) = 52\,\mathrm{Nm/rad}$. This requires a choice of $k_p \approx 52\,\mathrm{Nm/rad}$ joint wise. For good position tracking this is a low value. If higher controller gains are required, the joint stiffness has to be increases, too.

6.2. State Feedback Control

The theoretical performance of the feedback linearization approach [27] and the backstepping approach (Section 6.1) is originated by the mathematical abstraction, among others. This abstraction hardens the incorporation of the mentioned practical limitations such as bounds on the controller gains, as the reduced model is somewhat different from the robotic system. An approach presented here is the design of a controller which is exploiting the physical structure of the robot. The idea is to interpret the robot model and add the desired damping components, but introduce as least abstraction as possible. The basis is physically motivated gain design. It relies on designing the gains in a sound way based on the physical robot model. Thereby, the smoothness of the gains can be ensured, parameter variations can be accounted for, and gains in a limited range result, simultaneously. The gains are applied in a state feedback control structure. The effectiveness of the controller is visible in the conducted experiments.

6.2.1. Simplified Arm Model

For the controller design, a linearized version of (2.21) along a nominal trajectory is considered. In absence of external torques, the linearized dynamics are

$$\begin{bmatrix} \boldsymbol{M} & \boldsymbol{0} \\ \boldsymbol{0} & \boldsymbol{B} \end{bmatrix} \begin{bmatrix} \Delta\ddot{\boldsymbol{q}} \\ \Delta\ddot{\boldsymbol{\theta}} \end{bmatrix} + \begin{bmatrix} \boldsymbol{K} & -\boldsymbol{K} \\ -\boldsymbol{K} & \boldsymbol{K} \end{bmatrix} \begin{bmatrix} \Delta\boldsymbol{q} \\ \Delta\boldsymbol{\theta} \end{bmatrix} + \underbrace{\begin{bmatrix} \frac{\partial \boldsymbol{g}(\boldsymbol{q})}{\partial \boldsymbol{q}} + \boldsymbol{F}_1(\boldsymbol{q}, \dot{\boldsymbol{q}}, \boldsymbol{\theta}) \\ \boldsymbol{F}_2(\boldsymbol{q}, \dot{\boldsymbol{q}}, \boldsymbol{\theta}) \end{bmatrix}}_{\boldsymbol{R}} = \begin{bmatrix} \boldsymbol{\tau}_{\text{ext}} \\ \boldsymbol{\tau}_m \end{bmatrix}, \tag{6.38}$$

with the instantaneous stiffness matrix $\boldsymbol{K} = \text{diag}(\boldsymbol{k}) \in \mathbb{R}^{n \times n}$, c.f. (2.13).
The terms $\boldsymbol{F}_i(\boldsymbol{q}, \boldsymbol{\theta})$ collect higher order terms resulting from the linearizaton of the link inertia matrix and/or the nonlinear elastic elements. Furthermore the Coriolis/centrifugal terms are included. It is assumed, that the remainder term $\boldsymbol{R}$ can be regarded as a disturbance, and therefore it is ignored $\boldsymbol{R} = \boldsymbol{0}$. The effects of this simplification are discussed in Section 6.2.5.

6.2.2. Gain Design

Due to the dynamic coupling of the robot arm, the controller design must cope with the tightly coupled system. Therefore, a multi-input multi-output state feedback controller based on eigenmode decoupling is developed. In a first step, torque feedback is used to shape the motor inertia, such that normal modes of the arm dynamics can be identified and independently controlled. Then, the system is transformed into a decoupled form, in which the dynamics satisfy a set of independent fourth order differential equations. SISO control design tools are applied to the decoupled system to achieve the desired damping behavior resembling two critically damped second order systems. Finally, the controller is transformed back into the original coordinate system. The design idea is sketched in Fig. 6.7.

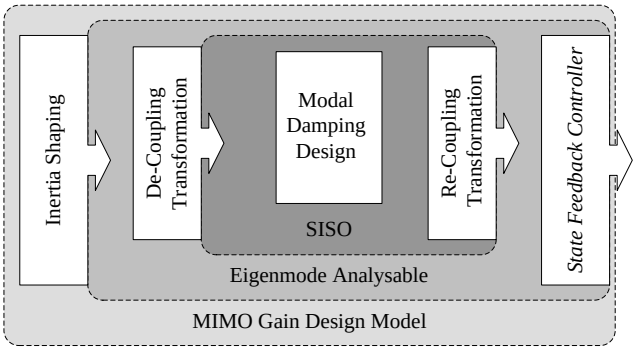

Figure 6.7.: The damping control algorithm consists of three main parts. First, torque feedback provides motor inertia shaping. This enables to use the eigenmode decoupling in a second step. Finally SISO control tools can be applied to ensure proper joint damping.

Modal Decoupling

The decoupling approach makes use of the generalized eigenvalue problem known from matrix algebra:
Given a symmetric and positive definite matrix $\boldsymbol{M} \in \mathbb{R}^{n\times n}$ and a symmetric matrix $\boldsymbol{K} \in \mathbb{R}^{n\times n}$, a nonsingular matrix $\boldsymbol{Q} \in \mathbb{R}^{n\times n}$ can be be found such that

$$\boldsymbol{M} = \boldsymbol{Q}^{-T}\boldsymbol{M}^{Q}\boldsymbol{Q}^{-1}, \tag{6.39a}$$
$$\boldsymbol{K} = \boldsymbol{Q}^{-T}\boldsymbol{Q}^{-1}, \tag{6.39b}$$

with the diagonal matrix $\boldsymbol{M}^{Q}$.
This theorem allows to diagonalize two matrices, here applied to the mass matrix $\boldsymbol{M}$ and the stiffness matrix $\boldsymbol{K}$. By using the coordinate transformation

$$\boldsymbol{q}^{Q} = \boldsymbol{Q}^{-1}\boldsymbol{q} \tag{6.40a}$$
$$\boldsymbol{\theta}^{Q} = \boldsymbol{Q}^{-1}\boldsymbol{\theta} \tag{6.40b}$$
$$\boldsymbol{\tau}^{Q} = \boldsymbol{Q}^{T}\boldsymbol{\tau} \tag{6.40c}$$

the reduced arm dynamics from (6.38) can be rewritten as

$$\boldsymbol{M}^{Q}\ \ddot{\boldsymbol{q}}^{Q} - \boldsymbol{I}(\boldsymbol{\theta}^{Q} - \boldsymbol{q}^{Q}) = \boldsymbol{\tau}_{Q\mathrm{ext}} \tag{6.41a}$$
$$\underbrace{\boldsymbol{Q}^{T}\boldsymbol{B}\boldsymbol{Q}}_{\boldsymbol{B}^{Q}}\ \ddot{\boldsymbol{\theta}}^{Q} + \boldsymbol{I}(\boldsymbol{\theta}^{Q} - \boldsymbol{q}^{Q}) = \boldsymbol{\tau}^{Q}. \tag{6.41b}$$

Here, $\boldsymbol{I} \in \mathbb{R}^{n\times n}$ is the unity matrix. Supposing that also $\boldsymbol{B}^{Q}$ is diagonal, (6.41) represents a completely decoupled system and SISO control design tools can be applied for each subsystem.

To achieve this, it is desired that the transformation

$$\boldsymbol{B}^Q = \boldsymbol{Q}^T \boldsymbol{B} \boldsymbol{Q} \tag{6.42}$$

produces a transformed motor inertia matrix $\boldsymbol{B}^Q$ with diagonal shape. Therefore, the matrix $\boldsymbol{B}$ is shaped by control in advance, such that it is diagonalized by the eigenmode transformation.

Minimal System Modification Choice of Transformed Coordinates

The eigenmode analysis allows to diagonalize the matrices $\boldsymbol{M}$ and $\boldsymbol{K}$. A torque feedback controller (4.14) is used subsequently to reshape the motor inertia matrix $\boldsymbol{B}$ into a form $\boldsymbol{B}_\theta$ such that it can be expressed as the weighted sum of $\boldsymbol{M}$ and $\boldsymbol{K}$,

$$\boldsymbol{B}_\theta = \alpha\ \boldsymbol{M} + \beta\ \boldsymbol{K}, \tag{6.43}$$

where α and β are scalars. The decoupling of $\boldsymbol{B}_\theta$ results with the eigenmode transformation (6.39) from (6.42)

$$\boldsymbol{B}^Q = \boldsymbol{Q}^T \boldsymbol{B}_\theta \boldsymbol{Q} \tag{6.44a}$$

$$\boldsymbol{B}^Q = \alpha\ \boldsymbol{Q}^T \boldsymbol{M} Q + \beta\ \boldsymbol{Q}^T \boldsymbol{K} \boldsymbol{Q} \tag{6.44b}$$

$$\boldsymbol{B}^Q = \alpha\ \boldsymbol{M}^Q + \beta\ \boldsymbol{I} = \mathrm{diag}(\boldsymbol{b}^Q). \tag{6.44c}$$

As $\boldsymbol{M}^Q$ and $\boldsymbol{I}$ are diagonal, also $\boldsymbol{B}^Q$ is diagonal. Therefore, the transformed system is of diagonal shape and suitable for SISO control design.
To achieve the shaped motor inertia $\boldsymbol{B}_\theta$ we use the torque feedback controller (4.14) and define

$$\boldsymbol{K}_{Tcasc} = (\boldsymbol{I} - \boldsymbol{B}\boldsymbol{B}_\theta^{-1}) \tag{6.45}$$

where $\boldsymbol{K}_{Tcasc}$ is the torque feedback gain of the cascaded structure.
The question arises how to choose the parameters α and β in (6.44c). For the experimental implementation on the robot it is important that the feedback gains are in a practically feasible range. It is especially interesting to keep the torque feedback gain matrix $\boldsymbol{K}_{Tcasc}$ low, as it changes the impedance of the actuators. Minimal change of the motor inertia $\boldsymbol{B}$ towards the decoupling motor inertia $\boldsymbol{B}_\theta$ is desired, i.e.,

$$\min_{\alpha,\beta} \|\boldsymbol{B} - \boldsymbol{B}_\theta\|_F\,. \tag{6.46}$$

We use the Frobenius norm defined by

$$\|\boldsymbol{A}\|_F^G = \sqrt{\sum_{i,j} g_{ij} a_{ij}^2}, \tag{6.47}$$

where a_{ij} denotes the ij'th element of the matrix $\boldsymbol{A}$ and $\boldsymbol{G}$ is a weighting matrix. The matrix $\boldsymbol{G} = \boldsymbol{I}$ is chosen here, which is denoted as $\|\|_F$.

We rewrite $\boldsymbol{B}$, $\boldsymbol{B}_\theta$, $\boldsymbol{M}$, and $\boldsymbol{K}$ as well as (6.43) in vector form

$$\boldsymbol{B}_v = \begin{bmatrix} b_{11} \\ b_{12} \\ \vdots \\ b_{nn} \end{bmatrix}, \boldsymbol{B}_\theta = \begin{bmatrix} m_{11} & k_{11} \\ m_{12} & k_{12} \\ \vdots & \vdots \\ m_{nn} & n_{nn} \end{bmatrix} \begin{bmatrix} \alpha \\ \beta \end{bmatrix} = \boldsymbol{A}_v \boldsymbol{x}. \tag{6.48}$$

The minimization problem (6.46) becomes

$$\min_{\alpha,\beta} \left\| \boldsymbol{B}_v - \boldsymbol{A}_v \boldsymbol{x} \right\|_2 . \tag{6.49}$$

It requires to find a proper choice of the parameters α and β. This can be done by solving (6.49) for $\boldsymbol{x}$

$$\boldsymbol{x} = \boldsymbol{A}_v^+ \boldsymbol{B}_v \tag{6.50}$$

using the Moore-Penrose pseudo inverse $\boldsymbol{A}_v^+$ calculated by

$$\boldsymbol{A}_v^+ = \boldsymbol{A}_v^T (\boldsymbol{A}_v \boldsymbol{A}_v^T)^{-1}. \tag{6.51}$$

As a result, the diagonal matrix $\boldsymbol{B}_\theta$ is "as close as possible" to the original motor inertia matrix $\boldsymbol{B}$ and thereby the change of the system is as small as possible. With (6.50), $\boldsymbol{B}_\theta$ can be obtained from (6.43).
The decoupled system is

$$\boldsymbol{M}^Q \ \ddot{\boldsymbol{q}}^Q - \boldsymbol{I}(\boldsymbol{\theta}^Q - \boldsymbol{q}^Q) = \boldsymbol{\tau}_{ext}^Q \tag{6.52a}$$

$$\boldsymbol{B}_\theta^Q \ \ddot{\boldsymbol{\theta}}^Q + \boldsymbol{I}(\boldsymbol{\theta}^Q - \boldsymbol{q}^Q) = \boldsymbol{u}^Q \tag{6.52b}$$

with the new input variable $\boldsymbol{u}^Q = \boldsymbol{Q}^T \boldsymbol{u}$. Equations (6.52) and (6.41) are very similar with the important difference, that the transformed motor inertia matrix $\boldsymbol{B}_\theta^Q$ is diagonal.
In a final design step, a state feedback controller is applied and control gains for the decoupled system are calculated.

6.2.3. State Feedback Controller Design

The torque feedback enables to use the eigenmode analysis based decoupling control approach which results in a set of SISO systems. For each of the decoupled systems a state controller is designed by

$$\boldsymbol{u}^Q = \ \boldsymbol{K}_P^Q \tilde{\boldsymbol{\theta}}^Q - \boldsymbol{K}_D^Q \dot{\boldsymbol{\theta}}^Q - \boldsymbol{K}_T^Q (\boldsymbol{\theta}^Q - \boldsymbol{q}^Q) - \boldsymbol{K}_S^Q (\dot{\boldsymbol{\theta}}^Q - \dot{\boldsymbol{q}}^Q), \tag{6.53}$$

where $\tilde{\boldsymbol{\theta}}^Q$ is defined as the transformed regulation error $\tilde{\boldsymbol{\theta}}^Q = \boldsymbol{\theta}_d^Q - \boldsymbol{\theta}^Q$ with $\boldsymbol{\theta}_d^Q$ the transformed desired motor position. To compensate for the passive elasticity, the link side static equivalent

solution according to (4.3) is often used. The gains $\boldsymbol{K}_P^Q$, $\boldsymbol{K}_D^Q$, $\boldsymbol{K}_T^Q$ and $\boldsymbol{K}_S^Q$ are all $\in \mathbb{R}^{n\times n}$ and of diagonal shape.
To achieve the desired damping behavior of the arm, a proper choice of the feedback gains is necessary. The idea is to select the feedback gains such that the arm dynamics and the control system behave like two damped second order systems, see also [72]. Herein, the controller must provide the necessary damping of the low damped variable stiffness elements. Each decoupled subsystem and its feedback controller represents a fourth order system

$$\begin{aligned}-\boldsymbol{K}^Q\boldsymbol{K}_P^Q - \boldsymbol{K}^Q\boldsymbol{K}_D^Q s - (\boldsymbol{B}^Q\boldsymbol{K}^Q + \boldsymbol{K}^Q\boldsymbol{M}^Q + \boldsymbol{K}_P^Q\boldsymbol{M}^Q + \boldsymbol{K}^Q\boldsymbol{K}_T^Q\boldsymbol{M}^Q)s^2 \\ -(\boldsymbol{K}_D^Q\boldsymbol{M}^Q + \boldsymbol{K}^Q\boldsymbol{K}_S^Q\boldsymbol{M}^Q)s^3 - \boldsymbol{B}^Q\boldsymbol{M}^Q s^4 = \boldsymbol{0}.\end{aligned} \tag{6.54}$$

The four control gains in (6.54) allow to place four poles of the system by specifying a desired characteristic polynomial of the form

$$(s^2 + 2\xi_1\omega_1 s + \omega_1^2)(s^2 + 2\xi_2\omega_2 s + \omega_2^2). \tag{6.55}$$

The controller position proportional gain $\boldsymbol{K}_P$ is chosen first. One possibility is to adjust $\boldsymbol{K}_P$ as high as possible in order to overcome motor friction and to have a compliance behavior introduced mainly by the mechanics. In practice, a trade off between high gains for positioning accuracy and gain limitations due to the sample and actuation system has to be found. Another possibility is to aim for a desired total stiffness given by the serial interconnection of controller stiffness $\boldsymbol{K}_P$ and mechanical stiffness, see Chapter 5. As the controller is designed in the decoupled space, $\boldsymbol{K}_P^Q$ has to be diagonal. To achieve such a diagonal $\boldsymbol{K}_P^Q$ as close as possible to the desired $\boldsymbol{K}_P$, an optimization problem can be stated, $\min_{\boldsymbol{K}_P^Q} ||\boldsymbol{K}_P - \boldsymbol{Q}^{-T}\boldsymbol{K}_P^Q\boldsymbol{Q}^{-1}||$, which is convex for the choice of the Frobenius norm. So far, the system behaves like a two-mass, two-spring system, with the two aforementioned elasticities and the two inertias $\boldsymbol{M}^Q$ and $\boldsymbol{B}^Q$. These parameters determine the eigenmodes of the decoupled systems and therefore ω_1 and ω_2 in (6.55). Then, the damping coefficients $\boldsymbol{K}_D^Q$ ad $\boldsymbol{K}_S^Q$ are chosen such that the system is damped according to specified values[4] of $\xi_1 = \xi_2 = 0.7$. The torque feedback gain is set to zero $\boldsymbol{K}_T^Q = 0$, i.e. torque feedback is required only for motor inertia shaping (6.45).

Re-Coupling Transformation to Original Coordinates

As the gain design is done in decoupled coordinates, it is necessary to transform the gains back with

$$\boldsymbol{K}_p = \boldsymbol{Q}^{-T}\boldsymbol{K}_P^Q\boldsymbol{Q}^{-1}, \tag{6.56a}$$
$$\boldsymbol{K}_D = \boldsymbol{Q}^{-T}\boldsymbol{K}_D^Q\boldsymbol{Q}^{-1}, \tag{6.56b}$$
$$\boldsymbol{K}_T = \boldsymbol{Q}^{-T}\boldsymbol{K}_T^Q\boldsymbol{Q}^{T}, \tag{6.56c}$$
$$\boldsymbol{K}_S = \boldsymbol{Q}^{-T}\boldsymbol{K}_S^Q\boldsymbol{Q}^{T}. \tag{6.56d}$$

[4] A recursive procedure is needed, since the values $\xi_1 = \xi_2 = 0.7$ cannot be attained for arbitrary values of $\boldsymbol{K}_P^Q$.

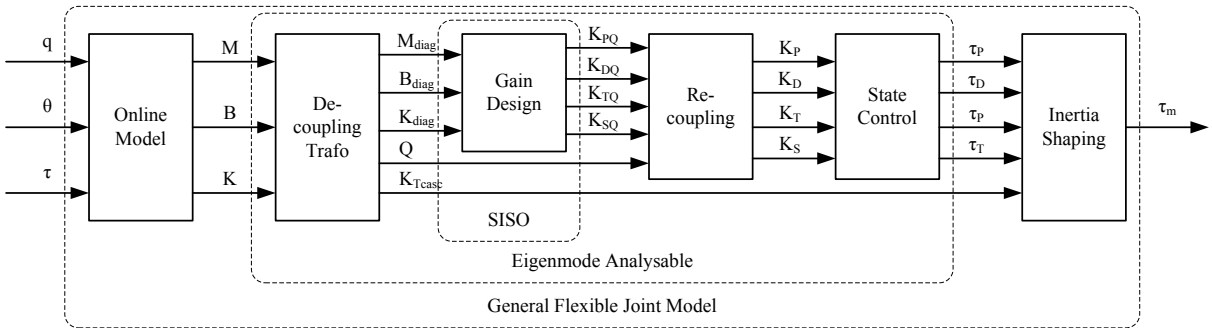

Figure 6.8.: The controller structure as it is implemented in Matlab/Simulink. The steps from Fig. 6.7 are indicated.

These gains are used with the state feedback controller

$$\boldsymbol{u} = \boldsymbol{K}_P\tilde{\boldsymbol{\theta}} - \boldsymbol{K}_D\dot{\boldsymbol{\theta}} - \boldsymbol{K}_T\boldsymbol{K}(\boldsymbol{\theta} - \boldsymbol{q}) - \boldsymbol{K}_S\boldsymbol{K}(\dot{\boldsymbol{\theta}} - \dot{\boldsymbol{q}}). \tag{6.57}$$

Furthermore, the cascaded torque gain (6.45) is used with the torque feedback controller (4.14). Obviously, the control gains are not diagonal in these coordinates.
The control algorithm is summed up in Fig. 6.8, as it is implemented in Matlab/Simulink. The single steps from Fig. 6.7 are also indicated.

6.2.4. Simulations and Experimental Results

The state feedback damping controller (6.57) was compared with the collocated controller (4.7) on the first three joints of the DLR Hand Arm System in simulations (Fig. 6.9) and experiments (Fig. 6.10). The motor positions are shown in the top graphs and the link side positions in the bottom graphs. First, the PD control law was evaluated (Fig. 6.9(a) and Fig. 6.10(a)) for a step like trajectory of the motor position of about 0.52 rad of the upper arm joint. The proportional gains are set to $\boldsymbol{K}_P = 8000\,\mathrm{Nm/rad}$ and the derivative gains are set to $\boldsymbol{K}_D = 250\,\mathrm{Nms/rad}$. Long lasting link oscillations due to the low intrinsic damping of the mechanical elastic elements occur. The excitation of the other joints due to the inertial couplings in $\boldsymbol{M}(\boldsymbol{q})$ and the Coriolis/centrifugal couplings in $\boldsymbol{C}(\boldsymbol{q}, \dot{\boldsymbol{q}})$ is well visible (MIMO system property). In a second experiment the proposed state feedback damping controller with damping ratios of $\xi_{i,j} = 1/\sqrt{2}$ in each modal direction was tested (see Fig. 6.9(b) and Fig. 6.10(b)). With activated damping all oscillations are suppressed rapidly and the settling time is significantly shorter. If one compares the motor position plots of the damped and the undamped system it is noticeable, that only a slight, neat change is required to result in totally different link side behaviors.
The controller response to a motor step trajectory is visualized in the long time exposure photo Fig. 6.11. The exposure time is 4 s, and a stroboscope flash lights the scene with a frequency of 7 Hz. The trajectory starts in the upper left part of the picture and ends in the lower right corner following a curved line (red). In case of motor based control oscillations happen when

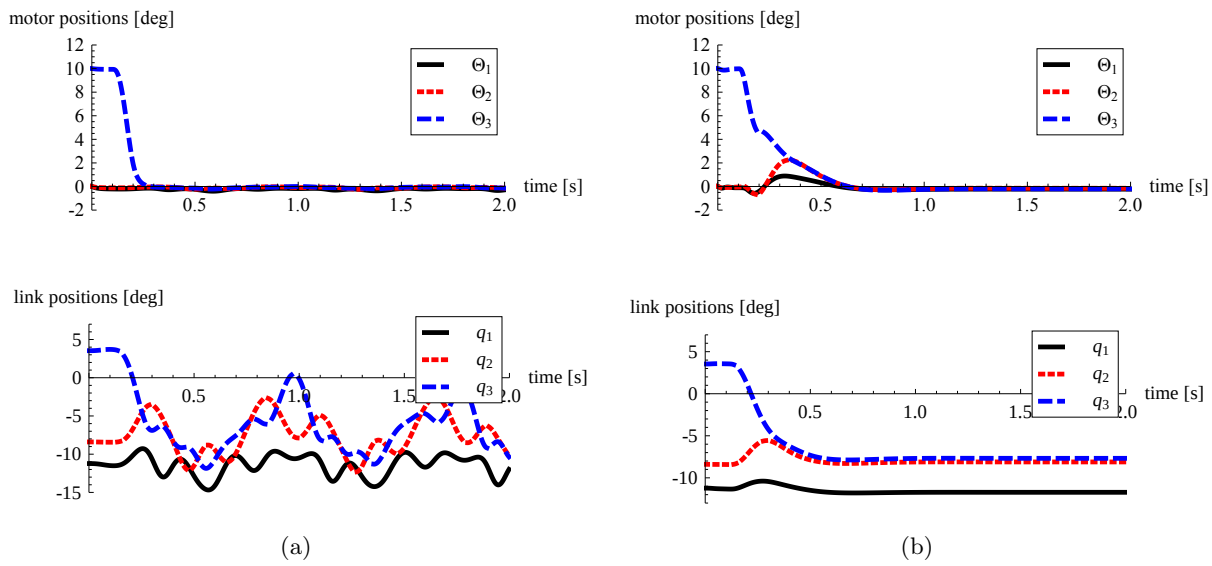

Figure 6.9.: Plots of the simulations of the DLR Hand Arm System with deactivated damping (a) and activated damping controller (b). A step motion is executed by motor θ_3 at $t = 0.1\,\mathrm{s}$. The MIMO properties of the system are visible as the link motion of q_3 couples to the other two joints q_1 and q_2. The damping controller damps out any link oscillations.

decelerating the TCP again, see Fig. 6.11(a). The state feedback damping controlled robot shows well damping with only small overshoot, see Fig. 6.11(b). Moreover, it is noticeable that not only the trajectories differ in both cases, but also the temporal behavior.
To demonstrate the need for a VSA damping controller and the effectiveness of the presented approach, a task was defined which aims to draw a logo on a flat surface, see Fig. 6.12. A path of the logo in Cartesian coordinates was transformed to joint space trajectories using an inverse kinematics mapping. For both pictures, the same desired trajectory was commanded by $\bar{\boldsymbol{q}}(\boldsymbol{\theta})$. In Fig. 6.12(a), a PD scheme was used whereas in Fig. 6.12(b), the damping controller was activated. Without damping, the elasticities in the joints get excited and the natural dynamics lead to oscillatory, out-of-plane motions. This can be seen as the pen leaves the surface at some points of the trajectory. The damped motion instead precisely follows the desired path and straight Cartesian lines are achieved. It is to remark, that redrawing the same trajectory is possible without noticing differences, which demonstrates the repeatability of the system despite of the very elastic joints.

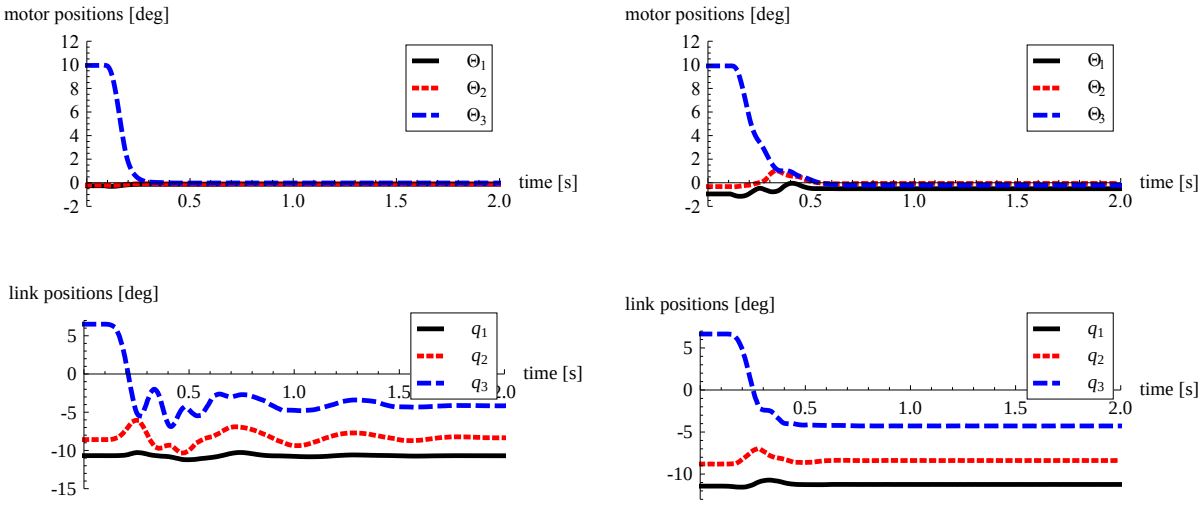

Figure 6.10.: Experiments conducted on the DLR Hand Arm System with deactivated damping (a) and activated damping controller (b). The same step motion as in Fig. 6.9 was performed. Due to friction effects, the link motion is more damped in comparison to the simulations. However, the fast and effective vibration suppression provided by the damping controller is obvious.

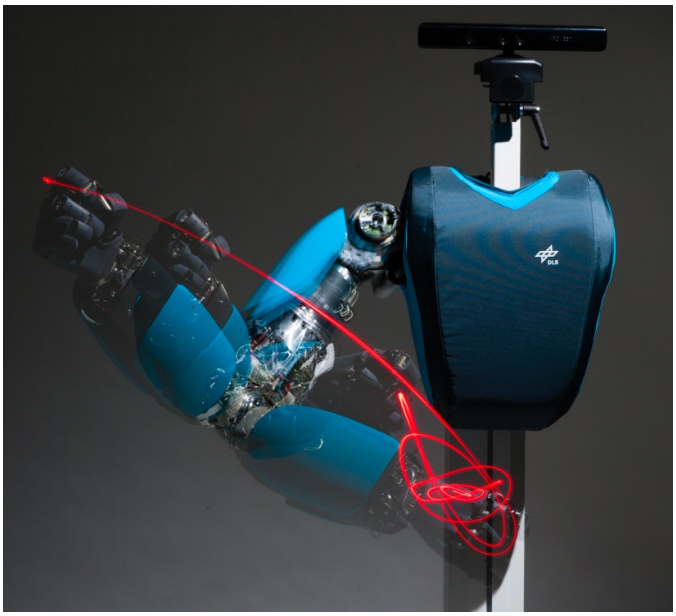

(a)

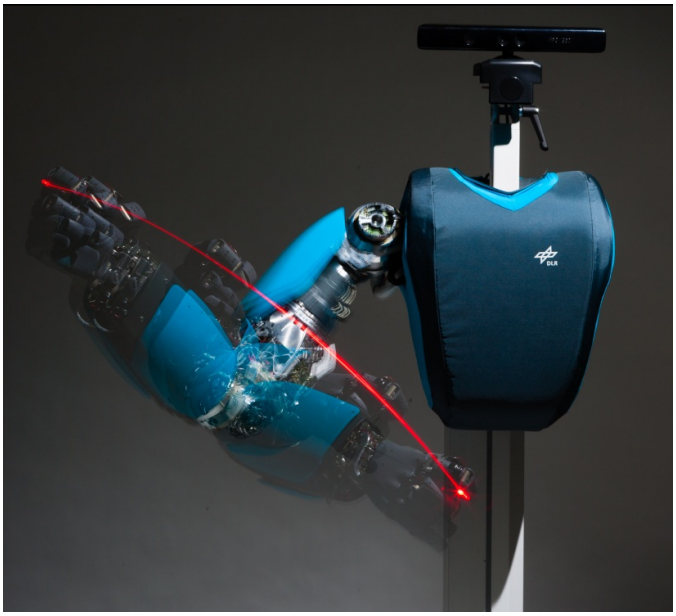

(b)

Figure 6.11.: Long time exposure pictures of the DLR Hand Arm System following a curved line trajectory from upper left to the lower right corner. motor based control is shown in (a), the state feedback controller is applied in (b). The exposure time is 4 s, a stroboscope flash lights the scene with 7 Hz. The state feedback controller follows the trajectory significantly better than the motor based controller which causes overshootings instead.

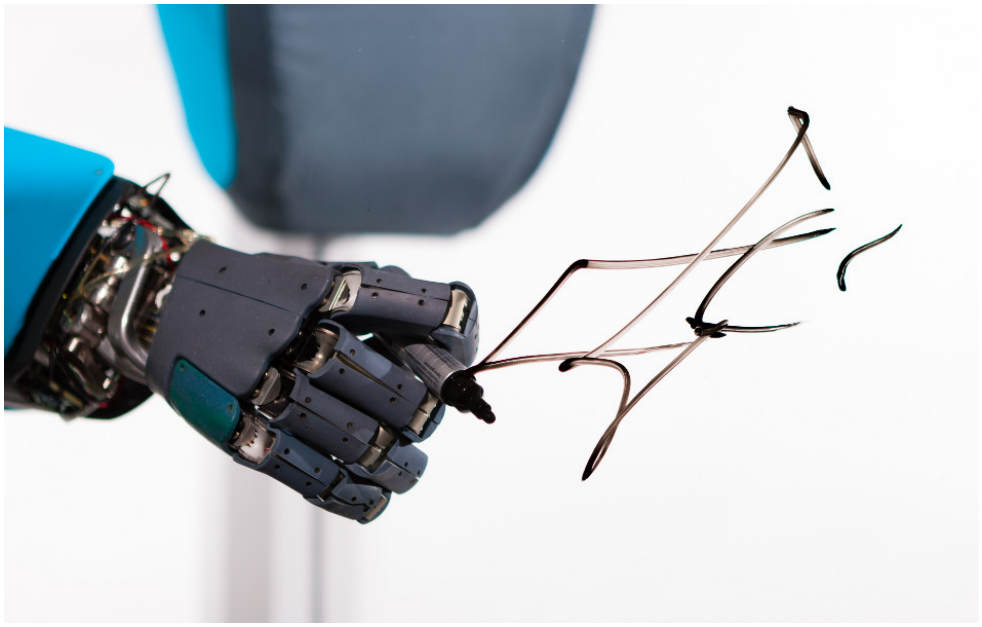

(a)

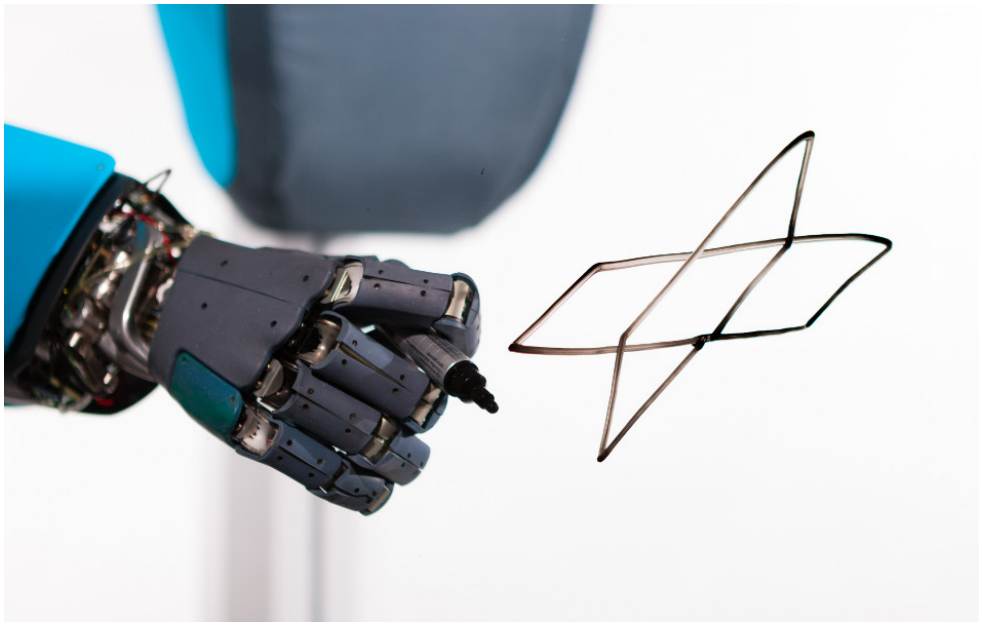

(b)

Figure 6.12.: The DLR logo is drawn on a flat surface (window). In the PD controller is used. As the dynamics of the VSA and the link side are not incorporated, drawing quality is insufficient. If the state feedback damping controller is activated as shown in (b), the results are as desired.

6.2.5. Discussion

The simulations and experimental results validate the effectiveness of the decoupling control approach. We want to highlight the consistency of the data of the simulations and the experiments. Little quantitative differences can be seen. Only small residual oscillations remain at the end of the damping trajectories.

The approach shows several advantages. Outstanding damping behaviour is achieved. Any oscillations, stemming from external disturbance or from commanded motor trajectories, are effectively suppressed. A key element of the algorithm is the physically motivated gain design. The algorithm modifies the system as little as possible to ensure low feedback gains while achieving the control goal. The decoupled system dynamics correspond to the eigenmodes of the physical system. The subsequent controller only damps the vibrations while shifting the eigenmode frequencies as little as possible. The system properties are not cancelled but shaped. This leads to low controller gains and increased robustness. High positioning accuracy is reached, as the motor position is enforced by a high controller gain. The same positioning performance as for the $\bar{q}$-controller (4.7) can be achieved, as the active damping controller acts independent of the $\bar{q}$ approach. This results as damping is only injected if $\dot{\boldsymbol{q}} \neq \mathbf{0}$, which is fulfilled for the static case and the damping controller produces the same behaviour as the PD controller. The controller can easily be combined with feed forward trajectory tracking, see Section 6.4.1. The combination of the open loop and the closed loop controller results in improved tracking behaviour, although the controller is only designed for the regulation case.

Minor limitations of the approach can be seen in the small residual oscillations as they appear in the measurements. This may result due to several reasons. In Section 6.2.1 a linearized version of the nonlinear dynamics was derived. The remainder term $\boldsymbol{R}$ was assumed to be negligible. This assumption has some effects but in practically relevant cases only minimal deviations are visible as can be seen from the simulations and experiments. Another error source are unmodeled dynamics. The time varying terms of the decoupling approach are neglected. Especially friction plays a role as can be seen by the comparison of Fig. 6.9 and Fig. 6.10. The decoupling approach via the generalized eigenvalue problem prohibits to include friction effects of arbitrary form, as a decoupling of such terms is not ensured. An important issue is the precise identification of the robot model, as it constitutes the basis for the control algorithm. The approach of physically motivated gain design proofs to be somewhat robust against model uncertainty. For a quantification of this behaviour, further evaluation needs to be done.

6.3. State Based Approach

A common property of both presented controllers from Section 6.1 and Section 6.2 is their reliance on a good mathematical robot model. On the one hand, this enables the theoretical control process and guarantees good performance. On the other hand, models are always prone to errors, stemming from imprecisions in the representation itself and/or parameter inaccuracies. Additionally, real-time control at a high rate (> 1 kHz) of the high dimensional models and controllers poses quite high demands on the computational infrastructure. For high end prototypes these requirements are many times easier to fulfill as in most cases robot design data can be obtained, powerful computational infrastructure is available, and sensory information is highly precise. This is often contrary for cost effective systems and complex model based control approaches are then not applicable. But still the need for damping control is present.
In the following, we discuss a model-free damping control approach, which complies with the necessity of a simple yet effective damping controller. The approach makes use of the joint elasticities to convert kinetic energy injected by disturbances into elastic energy, which is then dissipated by the joint actuators. The approach only requires state information of the robot. It is easy to implement, has low computational demands, and is also applicable to multi-joint robots. It can be applied on both, torque controlled and position/velocity controlled systems. The control system is energetically passive and exploits the natural mechanical response of the robot hardware. Therefore, it is well suited for human-robot interaction tasks.
This section is based upon the publication [113] of the author.

6.3.1. Basic Concept: Position Input System

To explain the controller idea, a flexible single joint in the absence of gravity as it is sketched in Fig. 6.13 is assumed. The robot be in the static state, where the spring is completely re-

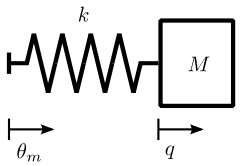

Figure 6.13.: A simplified robotic joint with the motor position input θ_m.

laxed. Furthermore, the motor is position controlled as used to execute a positioning task. This simplified system can be modeled by

$$M\ddot{q} = k(\theta_m - q), \tag{6.58}$$

where θ_m is the motor position. A short disturbance impulse acting on the link will accelerate the link and thereby induce kinetic energy into the system. The elastic element is naturally resisting

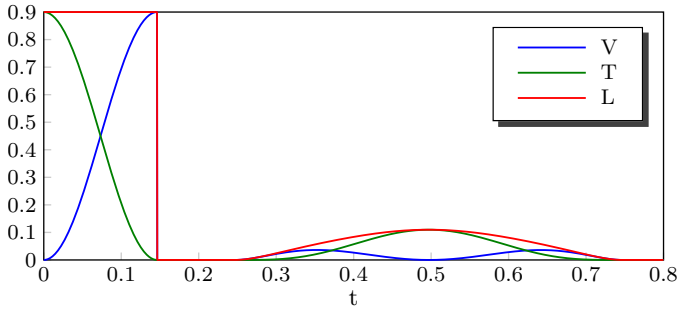

Figure 6.14.: The kinetic and potential energy of the disturbed system (6.58). The initial kinetic energy (initial link velocity, see also Fig. 6.15) is transformed into potential energy by the spring. Once the link is at rest, the controller kicks in and removes the complete energy, effectively suppressing oscillations. To re-establish the original link position a bring back motion is performed.

the disturbance and decelerating the link. In this process the kinetic energy is transformed into potential energy and stored in the spring. The mechanical energy is given by (c.f. 2.5)

$$L = V + T = \frac{1}{2}k(\theta_m - q)^2 + \frac{1}{2}M\dot{q}^2. \tag{6.59}$$

As the system is undamped, the system energy is constant and oscillations occur infinitely. The goal to stop the oscillation can be achieved by removing all the energy out of the system. A main aspect of the concept is the observation that there exist points on the oscillatory trajectory, where the system energy L is given completely by the potential energy expression V, see Fig. 6.14. This allows to derive a simple yet effective damping control law: By commanding a position jump of θ_m to q at times when $\dot{q} = 0$, the system energy can be completely removed to $L = 0$, see Fig. 6.15. No oscillations occur anymore. The control law is

$$\theta_m = q \quad \text{if } (\theta_m - q) \neq 0 \ \& \ \dot{q} = 0. \tag{6.60}$$

As the system is at rest now, the damping goal is fulfilled. To also re-establish the desired goal position, the system state has to be brought back. This bring back task is easy to achieve, as the system state is precisely known at this point. Several controllers can be thought of or e.g. an open loop trajectory can be used, as discussed later.
To sum up, after a link disturbance the controller holds the motor position and uses the elastic element passively to transform the system energy. At the right time, when all the energy is potential, the motor relaxes the spring, removes the energy and thereby damps the system. Afterwards, the desired system state is re-established by a bring back controller.

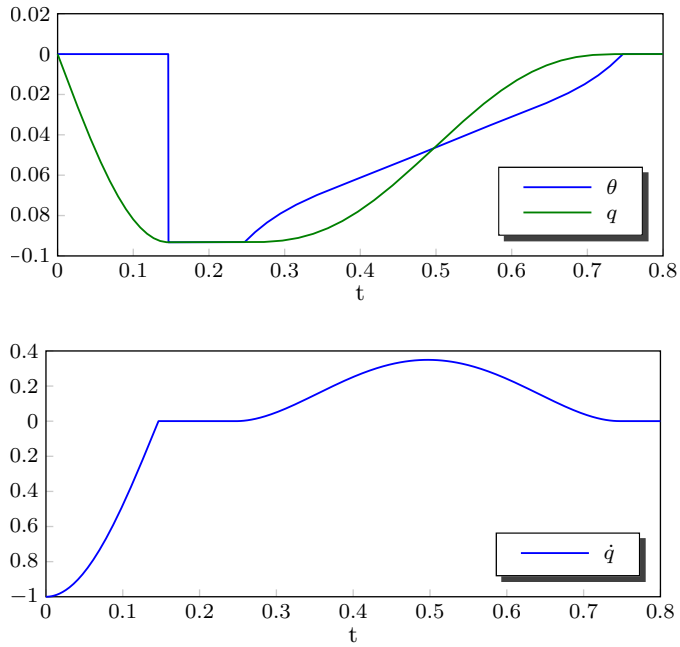

Figure 6.15.: The states of the system (6.58). After a disturbance, the motor position is held constant and the initial link velocity is continuously reduced by the elastic element action. Once it is zero $\dot{q} = 0$, the controller kicks in and removes the potential energy by setting $\theta_m = q$. Afterwards, a bring-back motion re-establishes the desired system state.

6.3.2. Extended Setup: Velocity Input System

The controller concept from Section 6.3.1 needs to be adapted to be implemented on a VSA system. It is assumed, that a position interface on the motor position is provided. Gravity compensation can be achieved by an approach as used in (4.7). Further, the motor dynamics hinder to achieve position jumps of the motor position. Therefore, we extend the damping idea to a motor velocity controlled system. This reflects practical confinements like limited motor velocity and is a good approximation to the PD-controlled system.

Velocity Input Damping Law

The velocity input model of a general VSA system is given by (c.f. (2.21))

$$\boldsymbol{M}(\boldsymbol{q})\ddot{\boldsymbol{q}} + \boldsymbol{C}(\boldsymbol{q}, \dot{\boldsymbol{q}})\dot{\boldsymbol{q}} + \boldsymbol{g}(\boldsymbol{q}) = \boldsymbol{f}(\boldsymbol{\varphi}, \boldsymbol{\sigma}) = \boldsymbol{\tau} \tag{6.61a}$$

$$\dot{\boldsymbol{\theta}} = \boldsymbol{u}, \tag{6.61b}$$

where $\boldsymbol{u} \in \mathbb{R}^n$ represents the input to the system. The controller idea to suppress oscillations by removing energy from the system at states where the kinetic energy is low can be analysed by

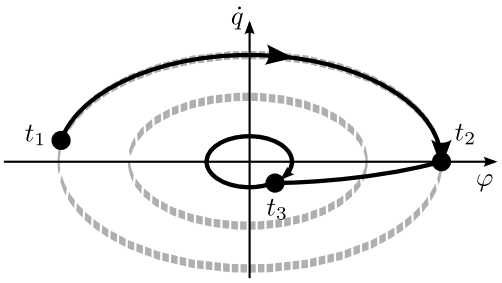

Figure 6.16.: Phase plots of the system (6.61) and the velocity damping controller (6.65). The grey ellipses are energy levels and the black curve is the trajectory. After an initial disturbance at t_1 the motor position is held, until the link is decellerated by the spring at t_2. Then, the spring is relaxed by a motor trajectory in finite time t_2-t_3. This releases parts of the potential energy and damps further oscillations. To completely remove all the system energy, the controller has to be repeatedly applied (after t_3).

energetic considerations. The mechanical system energy is given by

$$L = V + T = V_k + V_g + \dot{\boldsymbol{q}}^T \boldsymbol{M}(\boldsymbol{q})\dot{\boldsymbol{q}} \tag{6.62}$$

where V_k is the energy of the spring and V_g the energy of the gravitation potential. The rate of change of the energy function is given by

$$\dot{L} = \frac{\mathrm{d}V_k}{\mathrm{d}t} + \frac{\mathrm{d}V_g}{\mathrm{d}t} + \dot{\boldsymbol{q}}^T \boldsymbol{M}(\boldsymbol{q})\ddot{\boldsymbol{q}} + \frac{1}{2}\dot{\boldsymbol{q}}^T \dot{\boldsymbol{M}}(\boldsymbol{q})\dot{\boldsymbol{q}} \tag{6.63a}$$

$$= \boldsymbol{\tau}^T(\dot{\boldsymbol{\theta}} - \dot{\boldsymbol{q}}) + \boldsymbol{g}(\boldsymbol{q})^T\dot{\boldsymbol{q}} + \dot{\boldsymbol{q}}^T(\boldsymbol{\tau} - \boldsymbol{C}(\boldsymbol{q},\dot{\boldsymbol{q}})\dot{\boldsymbol{q}} - \boldsymbol{g}(\boldsymbol{q})) + \frac{1}{2}\dot{\boldsymbol{q}}^T \dot{\boldsymbol{M}}(\boldsymbol{q})\dot{\boldsymbol{q}} \tag{6.63b}$$

$$= \boldsymbol{\tau}^T\dot{\boldsymbol{\theta}}. \tag{6.63c}$$

From (6.63) and the mechanical joint stiffness properties it follows, that the system energy is reduced whenever

$$\dot{L} \leq 0 \quad \text{if } (\boldsymbol{\theta} - \boldsymbol{q})^T\dot{\boldsymbol{\theta}} \leq 0. \tag{6.64}$$

According to (6.64) energy is always dissipated if the spring is getting relaxed. The controller exploits this and damps the link side at the same time: To achieve strong link side deceleration, the motor position is not relaxing the spring instantaneously but holds its position and the controller just kicks in when the link is at rest. Thereby, first the link is stopped and then the system energy is removed. The velocity control law to release energy is given by (c.f. (6.60) and Fig. 6.16)

$$\boldsymbol{u} = \begin{cases} < \mathbf{0} & \text{if } (\boldsymbol{\theta} - \boldsymbol{q}) > \mathbf{0} \ \& \ \dot{\boldsymbol{q}} \ \geq \mathbf{0} \\ > \mathbf{0} & \text{if } (\boldsymbol{\theta} - \boldsymbol{q}) < \mathbf{0} \ \& \ \dot{\boldsymbol{q}} \ \leq \mathbf{0} \\ \mathbf{0} & \text{else.} \end{cases} \tag{6.65}$$

A control cycle proceeds as follows. A disturbance deflects the link. The induced kinetic energy is transformed into potential energy in the spring. At the point, where the joint elastic element is maximally tensioned, the motor is controlled to move towards the link and thereby reduces the system energy. To avoid injecting energy into the system again, the motor is stopped once the spring is relaxed. As the motor velocity is limited in the practical case, the controller will not be able to bring the system to a complete rest. Nevertheless, a certain amount of energy will be dissipated and thereby a damping action is achieved. To completely dissipate the system energy, the controller is repeatedly applied. Once the system is at rest and thereby in an undisturbed state, an additional strategy is used to bring the system state back to the desired state. Possible alternatives are discussed in Section 6.3.4.

6.3.3. Velocity Input Damping Controllers

The velocity control law (6.65) is providing qualitative bounds on how to achieve a damping behaviour of the controller. As similar for many control concepts, it provides room for quantitative interpretation, which can be compared to gain design. Gain design rules normally depend not only on theoretical considerations but also on practical and user or task specific needs. Therefore, we analysed two possible controller designs, discuss their properties and show simulation results.

Cascaded Structure Controller

Before going into details of the velocity control laws, we introduce the structure of the used controller which makes it applicable to the general torque controlled system (2.21). The below discussed velocity control laws provide command trajectories. The trajectories are not open loop, as the system state is fed back to generate these trajectories. Still they are realized by an underlying PD-motor controller in a cascaded structure, as depicted in Fig. 6.17. To obtain a desired motor position, the velocity signal is integrated

$$\theta_c(t) = \int_0^t u(\tau) \ \mathrm{d}\tau. \tag{6.66}$$

The separation into a velocity controller and the torque controller requires a two-time-scale-system. Such a system can virtually be split up in two coupled subsystems, one with a faster and one with a slower part (see e.g. [19]). The assumption is considered as mild in the practical case. As described by (6.63), the system energy is reduced in any case when the motor velocity $\dot{\boldsymbol{\theta}}$ is opposing the spring deflection $\boldsymbol{\theta} - \boldsymbol{q}$. For most systems, motor velocity limits $\underline{\dot{\boldsymbol{\theta}}} < \dot{\boldsymbol{\theta}}_m < \overline{\dot{\boldsymbol{\theta}}}$ can be found, such that the motor performance is approximated.

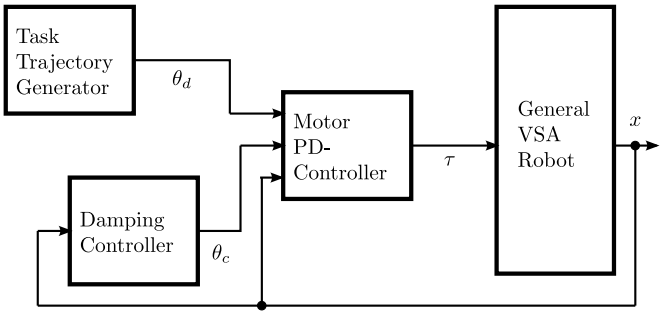

Figure 6.17.: The velocity command damping controller is used in a cascaded structure with a motor PD controller. The damping controller realizes the damping and state recovery action on a velocity level, where the PD-controller acts on torque level.

	Parameters		Init Values
M	4.05 kg	$q(t=0)$	0 rad
B	0.31 kg	$\dot{q}(0)$	-1.0 rad/s
K	207 N/m	$\theta(0)$	0 rad
K_P	8000 Nm/rad/s	$\dot{\theta}(0)$	0 rad/s
K_D	200 Nm/rad/s		

Table 6.4.: The parameters and initial conditions of the simulation study of the cascaded damping controller from Fig. 6.17 on system (6.61) with a linear spring.

State Proportional Control

A solution inspired by (6.65) is

$$\boldsymbol{u} = \begin{cases} -(\boldsymbol{\theta}-\boldsymbol{q})^T \boldsymbol{K}_U \dot{\boldsymbol{q}} & \text{if } (\boldsymbol{\theta}-\boldsymbol{q}) > \mathbf{0} \;\&\; \dot{\boldsymbol{q}} \geq \mathbf{0} \\ (\boldsymbol{\theta}-\boldsymbol{q})^T \boldsymbol{K}_U \dot{\boldsymbol{q}} & \text{if } (\boldsymbol{\theta}-\boldsymbol{q}) < \mathbf{0} \;\&\; \dot{\boldsymbol{q}} \leq \mathbf{0} \\ \mathbf{0} & \text{else.} \end{cases} \tag{6.67}$$

Herein, $\boldsymbol{K}_U$ is a constant gain value. An advantage is the smoothness of the control law caused by the smoothness of the state variables. To demonstrate the velocity input damping controller, it was tested on a one joint system (6.61) with the parameters from Tab. 6.4. The system states are plotted in Fig. 6.18. The system is disturbed by the initial link side velocity $\dot{q}(0) = -1.0$ rad/s. The controller effectiveness can be clearly followed in the system energy plot Fig. 6.19. Once, the initial kinetic energy T is transformed to potential energy V, the controller acts to damp the system. After the first oscillation period almost 90% of the energy is removed, and after the second one more than 98%. It is to remark, that the damping used in the simulations

is lower than for most practical systems.

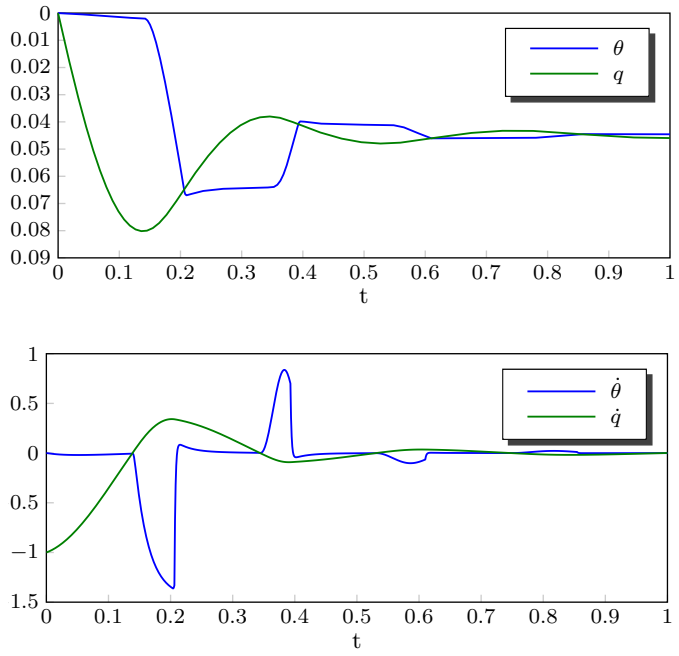

Figure 6.18.: Simulations of the state proportional controller (6.67) on the system (2.21). The motor velocity is changing smoothly and the oscillations are damped. The effect of the underlying PD-motor controller can be seen in the motor position curves.

State Triggered Control

Another solution complying with the damping control law (6.65) is

$$\boldsymbol{u} = \begin{cases} \underline{\dot{\boldsymbol{\theta}}} & \text{if } (\boldsymbol{\theta} - \boldsymbol{q}) > \mathbf{0} \;\&\; \dot{\boldsymbol{q}} \geq \mathbf{0} \\ \overline{\dot{\boldsymbol{\theta}}} & \text{if } (\boldsymbol{\theta} - \boldsymbol{q}) < \mathbf{0} \;\&\; \dot{\boldsymbol{q}} \leq \mathbf{0} \\ \mathbf{0} & \text{else,} \end{cases} \tag{6.68}$$

where $\underline{\dot{\boldsymbol{\theta}}} < \dot{\boldsymbol{\theta}}_m < \overline{\dot{\boldsymbol{\theta}}}$ are the motor velocity limits. Advantages of this controller are that no gains at all have to be tuned and that the system states are only triggering the controller action and are not needed for continuous feedback. The last point may be beneficial if sensor quality (noise, resolution, etc.) is limited.

6.3.4. Bring Back Methods

Once the system is brought to a rest the system state is usually different than desired. The task of the bring back method is to re-establish a desired state $\boldsymbol{q} = \boldsymbol{q}_d$. Therefore, several solutions

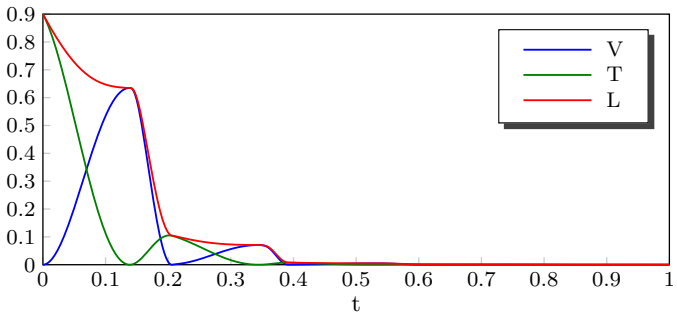

Figure 6.19.: The potential energy V, the kinetic energy T, and the system energy L. Once, the initial kinetic energy T is transformed to potential energy V, the controller acts to damp the system. After the first oscillation period almost 90% of the energy are removed and after the second one more than 98%.

are possible, three presented in the following. They range from state based methods to model based open loop trajectories and damping controllers.

1. A state based bring back motion generator can be realized by using a so-called leaky integrator instead of the normal one in (6.66), here, written as Laplace transfer function

$$G(s) = \frac{1}{1 + s\ T_c}, \tag{6.69}$$

   where T_c is a time constant. It actually works as low pass filter and ensures that the wrong state resulting from the velocity damping controller is forgotten with time. Resulting, the original desired state is recovered.

   The stability of this method is again based on the singular perturbation assumption. The stability of linear control methods for slowly varying nonlinear systems is well known [110]. Furthermore, our modeling assumptions neglect the existence of mechanical parasitic link and spring damping. In general, these effects can be modeled as energy dissipating terms in (2.21) and therefore support the action of damping controllers.

   This solution is state free but requires tuning and adaptation to the robot properties to ensure performance. Its implementation simplicity and the fact that no model knowledge needed justifies the application in some systems.

2. A model based method is to use a pre-planned velocity trajectory to bring the system state back to the desired state. Therefore, an open-loop trajectory is designed by a model inversion approach, see Section 6.4.1.

3. Another model based possibility is to use a passive damping controller. Such a controller normally feed-backs not only the motor velocity and position, but also the link velocity and position. There exist controllers ensuring the passivity property, however a frequent

problem is their limited performance to damp out link oscillations. In a setup with the velocity damping controller as presented here, the problem of limited performance is of minor relevance, as most of the energy injected by a disturbance is dissipated by this controller. A subsequent passive damping controller is only damping out residual oscillations and guaranteeing a well damped bring back motion.

6.3.5. Gravity and Multi-DoF Extension

Gravity Effects

The considerations until this point did not discuss the influence of gravity, as it occurs in (2.21). It was assumed that the equilibrium of the controlled robot only depends on the joint elasticity, and such on the potential energy $V(\boldsymbol{x})$. Therefore, the motor and link position coincide there $\boldsymbol{\theta} = \boldsymbol{q}$. In the presence of gravity, the link is deflected from the motor position $\boldsymbol{\theta} \neq \boldsymbol{q}$ due to the garvity forces $\boldsymbol{g}(\boldsymbol{q})$. The link side equivalent controller $\bar{\boldsymbol{q}}(\boldsymbol{\theta})$ (4.7) can be used to extend the approach, as it allows to control the system such that $\boldsymbol{q} = \bar{\boldsymbol{q}}(\boldsymbol{\theta})$ for $\dot{\boldsymbol{x}}$ can be achieved. By using $\boldsymbol{q} = \bar{\boldsymbol{q}}(\boldsymbol{\theta})$ in (6.65)[5] the controller is directly applicable in the presence of gravity.
This result can be intuitively understood as the controller idea relies on the fact that kinetic energy is transferred into potential energy and then parts of the potential energy are dissipated. Gravity has an effect on the energy levels and its equilibrium position. However, what the exact values are is not primarily relevant for the success of the controller.

The Multi-Joint Case

The main result in Section 6.3.2 about power dissipation by spring relaxation (6.65), can be similarly stated in the multi-joint case: Energy can be dissipated from the multi-joint system by a joint wise relaxation of the deflected elastic elements[6]. The same controllers can be used to damp out the oscillations, see the experiments conducted in the next section and Fig. 6.23. The link inertia $\boldsymbol{M}(\boldsymbol{q})$ and Coriolis/centrifugal matrix $\boldsymbol{C}(\boldsymbol{q}, \dot{\boldsymbol{q}})$ introduce a coupling between the joints which is not accounted for by the controller. Therefore, the damping performance is somewhat limited, but the goal to damp out the oscillations is eventually achieved. A possible solution for improvement is by designing the controller in a modal coordinate, see e.g. Section 6.2.

6.3.6. Experimental Results

Two sets of experiments with this controller have been conducted on the DLR Hand Arm System. In contrast to the experiments in Section 6.1 and Section 6.2, here, only the regulation case is treated.

[5] And subsequently also the control laws (6.67) and (6.68).

[6] Please note, although here, we are assuming uncoupled joint elasticities, the approach is also valid for coupled (biarticular) joints.

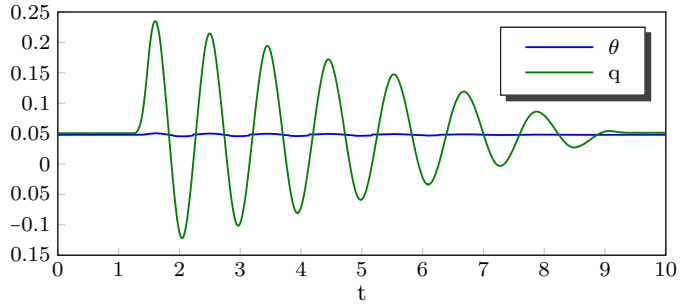

Figure 6.20.: Reference experiments of the disturbed system, with only position control and q_d = const. After a disturbance, long lasting link oscillations occur.

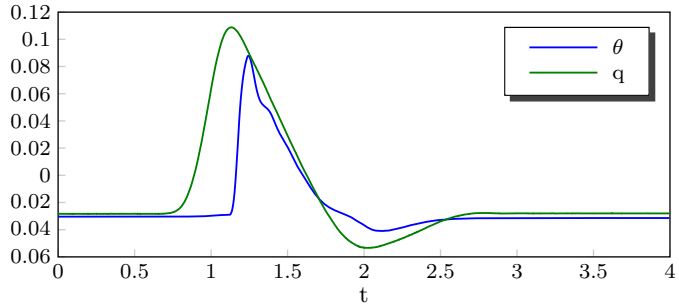

Figure 6.21.: The link is passively decellerated by the spring, until the state proportional damping controller (6.67) kicks in and removes potential energy. Afterwards, the system is brought back to the desired state by the leaking integrator bring back method (6.69).

The robot was configured such that the controller could be tested on a single axis without the effect of gravity. In a first experiment no damping controller has been activated and the motor has been position controlled. The disturbance resulted in long lasting oscillations of the link side, see Fig 6.20. Damping experiments have been conducted with both, the state proportional control law (see Fig. 6.21) and the state triggered control law (see Fig. 6.22). In both cases the oscillations are damped, and the leaky integrator approach re-establishes the desired system state.
Furthermore, experiments on two axes without gravity have been conducted, see Fig. 6.23. The state triggered control law was used again. Although the energy coupling due to the link inertia and Coriolis/centrifugal effects, the system is well damped.

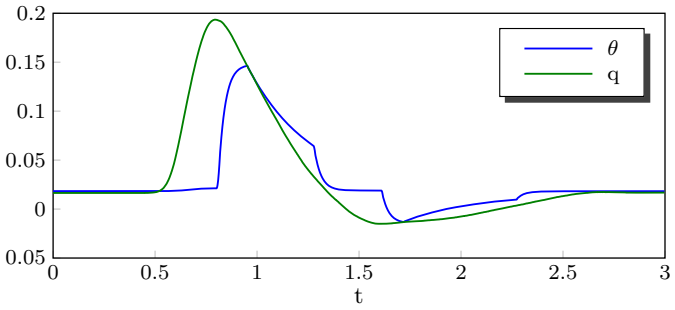

Figure 6.22.: Similar experiments as in Fig. 6.21, this time with the state triggered control law (6.68).

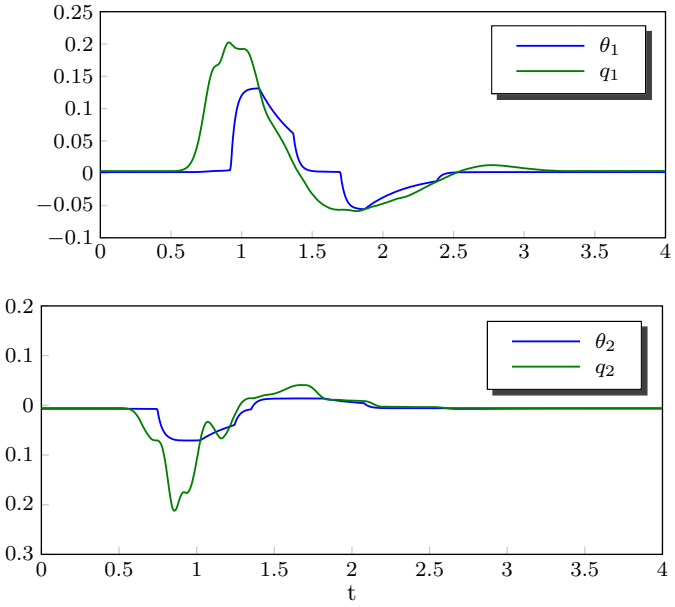

Figure 6.23.: Experiments on two axes of the DLR Hand Arm System with joint wise application of the damping controller (6.67). The damping performance is lowered as couplings introduced by the link inertia and Coriolis/centrifugal matrices $\boldsymbol{M}(\boldsymbol{q}), \boldsymbol{C}(\boldsymbol{q}, \dot{\boldsymbol{q}})$ lead to power flow between the joints. Still, after few cycles the links come to rest and the original state can be recovered.

6.3.7. Discussion

To be able to compare the state baed damping control approach with the other damping controllers we discuss some of its important properties in the following.
A great advantage of the controller is its independence of a system model. It uses purely state measurements to achieve link damping. Even more, the controller reacts in an energetically passive way and thereby, stability is ensured. The process to wait for the kinetic energy to be transformed into potential energy is relying on the natural robot dynamics. The disturbance reaction of this controller is dominated by the natural action of the joint elasticities. VSA systems are build to be mechanically tuned to the desired task. Additional control action can distort this natural mechanical reaction. The state based controller aims to preserve the natural robot behaviour for a big portion of the disturbance event: the controller does not intervene the disturbance until a late moment and thereby, the natural robot behaviour is responding. This goes in line with the concept of physical embodiment. Another advantage of the control scheme is its relative independence of state measurements. We discussed the issues resulting in controller gain limitations before. As with this controller it is possible to formulate algorithms which are only triggered by state events (single state measurements, see (6.68)), somewhat a robustness to state signal errors can be achieved.
A limitation of the controller is its performance. The approaches from Section 6.1 and Section 6.2 allow for better damping performance, which can be easily understood. This is especially revealed in the multi-DoF case, as the inertia couplings are not accounted for. Still, the damping performance is very good, as the experiments validate. The controller requires the knowledge of the equilibrium state of the robot. It can be measured if the robot is in steady state. Tracking tasks require the continuous knowledge of the equilibrium position, which seems to be unfeasible to achieve without a system model in practice. Therefore, the controller is limited to the regulation case.

6.4. Further Approaches

6.4.1. Feed Forward Controller Design

The presented feed back controllers provide effective disturbance rejection. Often it is sufficient to assume the undisturbed case if good trajectory tracking is desired. If the arm is not exposed to disturbances, the tracking task can be fulfilled using an open loop control approach.
In this case, the desired trajectory is specified by $\boldsymbol{q}_d(t)$. Solving (2.21a) for $\boldsymbol{\theta}_d(t)$ with (2.15a) results in

$$\boldsymbol{\theta}_d = \boldsymbol{f}^{-1}\left(\boldsymbol{M}(\boldsymbol{q}_d)\ddot{\boldsymbol{q}}_d + \boldsymbol{C}(\boldsymbol{q}_d, \dot{\boldsymbol{q}}_d)\dot{\boldsymbol{q}}_d + \boldsymbol{g}(\boldsymbol{q}_d)\right) + \boldsymbol{q}_d. \tag{6.70}$$

Assuming perfect motor tracking, this equation allows to obtain dynamically compensated motor

trajectories. Feed forward commands for the motor velocity

$$\dot{\boldsymbol{\theta}} = \dot{\boldsymbol{q}}_d + \boldsymbol{k}(\boldsymbol{\varphi})^{-1} \left(\dot{\boldsymbol{M}}(\boldsymbol{q}_d)\ddot{\boldsymbol{q}}_d + \boldsymbol{M}(\boldsymbol{q}_d)\boldsymbol{q}_d^{(3)} + \dot{\boldsymbol{C}}(\boldsymbol{q}_d, \dot{\boldsymbol{q}}_d)\dot{\boldsymbol{q}}_d + \boldsymbol{C}(\boldsymbol{q}_d, \dot{\boldsymbol{q}}_d)\ddot{\boldsymbol{q}}_d + \dot{\boldsymbol{g}}(\boldsymbol{q}_d) \right) \tag{6.71}$$

and motor torque

$$\ddot{\boldsymbol{\theta}}_d = \ddot{\boldsymbol{q}}_d + \boldsymbol{k}(\boldsymbol{\varphi})^{-1} \Big(\ddot{\boldsymbol{M}}(\boldsymbol{q}_d)\ddot{\boldsymbol{q}}_d + 2\dot{\boldsymbol{M}}(\boldsymbol{q}_d)\boldsymbol{q}_d^{(3)} + \boldsymbol{M}(\boldsymbol{q}_d)\boldsymbol{q}_d^{(4)} + \ddot{\boldsymbol{C}}(\boldsymbol{q}_d, \dot{\boldsymbol{q}}_d)\dot{\boldsymbol{q}}_d \tag{6.72}$$

$$2\dot{\boldsymbol{C}}(\boldsymbol{q}_d, \dot{\boldsymbol{q}}_d)\ddot{\boldsymbol{q}}_d + \boldsymbol{C}(\boldsymbol{q}_d, \dot{\boldsymbol{q}}_d)\boldsymbol{q}_d^{(3)} + \ddot{\boldsymbol{g}}(\boldsymbol{q}_d) - \boldsymbol{j}(\boldsymbol{\varphi})\dot{\boldsymbol{\varphi}}^2 \Big) \tag{6.73}$$

can be calculated by subsequent derivation of the dynamics. We use

$$\boldsymbol{j}(\boldsymbol{\varphi}, \boldsymbol{\sigma}) = \frac{\partial^2 \boldsymbol{f}(\boldsymbol{\varphi}, \boldsymbol{\sigma})}{\partial \boldsymbol{\varphi}^2} \tag{6.74}$$

as the second derivative of the joint torque function.
The trajectory needs to fulfill $\boldsymbol{q}_d(t) \in \mathcal{C}^4$ as to avoid jumps in the motor torque. A standard trajectory generation method allowing to specify bounds on the fourth derivative and to specify start and end position is given by a polynomial approach [119].

6.5. Comparative Overview of the Approaches

Each of the discussed approaches has its advantages and drawbacks for its own. Here, we provide a qualitative comparison. Of course the properties depend upon the exact implementation and the relations can only be seen as a general guidance. Also, the feed forward approach is an open loop method and will probably be combined with one of the closed loop controllers. The disturbance performance is therefore not fully relevant.

	Disturbance performance	Tracking damping	Model reliance	Noise robustness	Theoretical convergence analysis	Implementation complexity
Backstepping	+	+	-	-	+	-
State Feedback	+	+	-	+	-	-
State Based	+	-	+	+	+	+
Feed Forward	-	+	+	+	+	+

Table 6.5.: Qualitative comparison of the discussed control approaches.

7. Oscillatory Motions

The energy storage properties of passive compliance could be beneficial for solving highly dynamical tasks such as fast point-to-point movements, throwing, walking and running, and other. Some work has been done to exploit the elastic elements to gain increased end effector velocity [23] or tune the resulting oscillatory behaviour to a predefined trajectory [120, 26, 121]. The mentioned work mainly uses optimization and iterative methods to adjust the joint stiffness and torque to achieve the desired action. A central goal of variable stiffness actuation is to embody tasks in the system by using natural properties of the robot to fulfill them. Therefore, we focuses on an approach to exploit the natural system dynamics.
It is aimed to exploit the joint compliance of multiple degrees of freedom series elastic actuated (SEA) robots by identifying and shaping intrinsic resonance properties of the system. The basic idea is to generate trajectories producing coordinated motion of the multi-DoF robot manipulator. Therefore, a desired system is formulated which contains one multiple eigenmode and makes use of the intrinsic eigenmodes of the linearized robot dynamics. To excite the oscillatory system, negative damping is used as energy input. A controller is developed which allows to apply the approach to systems that can be modelled by the reduced flexible joint model.
This chapter is based upon the publication [122]

7.1. Eigenmode Shaping and System Eexcitation

The presented method is based on linear oscillation theory and will be introduced for an idealized system. Therefore, the homogeneous second order linear differential equation

$$\boldsymbol{M}\,\ddot{\boldsymbol{q}} + \boldsymbol{K}_d\,\boldsymbol{q} = \boldsymbol{0} \tag{7.1}$$

is considered as the linearized model of the multi-joint robot manipulator without motor dynamics, where the linearization is around an equilibrium position, c.f. (6.38).

7.1.1. Eigenmode Shaping

In a first step, the eigenmodes of the system (7.1) are chosen such that n repeated eigenvalues arise. Therefore, the general eigenvalue problem

$$\boldsymbol{K}_d\,\boldsymbol{q} = \lambda\,\boldsymbol{M}\,\boldsymbol{q} \tag{7.2}$$

is considered. From (7.2) the following condition is deduced: for $i = 1, 2, \ldots, n$ there exist a pair $(\lambda_i, \boldsymbol{q}_i)$, such that

$$\boldsymbol{K}_d \, \boldsymbol{q}_i = \lambda_i \, \boldsymbol{M} \, \boldsymbol{q}_i. \tag{7.3}$$

It is desired that alle eigenvalues are similar $\lambda_0 = \lambda_i, \forall i$, so we can rewrite

$$\boldsymbol{K}_d \, \boldsymbol{Q} = \lambda_0 \, \boldsymbol{M} \, \boldsymbol{Q}, \tag{7.4}$$

where $\boldsymbol{Q} = (\boldsymbol{q}_1, \boldsymbol{q}_2, \ldots, \boldsymbol{q}_n)$; consequently the system (7.1) is shaped in one eigenmode, if the stiffness matrix is proportional to the mass matrix, i.e.

$$\boldsymbol{K}_d = \lambda_0 \, \boldsymbol{M}. \tag{7.5}$$

This implies that $\boldsymbol{Q}$ is regular.

7.1.2. System Excitation

The system (7.1), where condition (7.5) holds, consists of only first modes. To obtain an oscillatory motion energy needs to be injected into the system. Therefore, a damping term will be introduced, which leads to

$$\boldsymbol{M} \, \ddot{\boldsymbol{q}} + \boldsymbol{D}_d \, \dot{\boldsymbol{q}} + \boldsymbol{K}_d \, \boldsymbol{q} = \boldsymbol{0}. \tag{7.6}$$

By setting the damping matrix $\boldsymbol{D}_d \in \mathbb{R}^{n \times n}$ to be negative or positive definite, the system energy will be increased or decreased, respectively.
To excite the joints of the system synchronously in resonance, the damping matrix is designed in decoupled modal coordinates. The general eigenvalue decomposition from (6.39) is used[1] with (7.5) resulting in

$$\boldsymbol{Q}^T \, \boldsymbol{K}_d \, \boldsymbol{Q} = \lambda_0 \, \boldsymbol{Q}^T \, \boldsymbol{M} \, \boldsymbol{Q} = \lambda_0 \, \boldsymbol{I}, \tag{7.7}$$

where the modal matrix $\boldsymbol{Q}$ decouples the system (7.6). The damping matrix in coupled joint coordinates is designed by

$$\boldsymbol{D}_d = 2 \, \boldsymbol{Q}^{-T} \, \mathrm{diag} \left(\xi_i \, \sqrt{\lambda_0} \right) \, \boldsymbol{Q}^{-1}. \tag{7.8}$$

By choosing the damping factors $\xi_i = \xi_1 = \ldots = \xi_n = \xi$ to be negative, the damping matrix $\boldsymbol{D}_d$ becomes negative definite and all joints of the system (7.6) will be excited.

[1] Here we normalize w.r.t. $\boldsymbol{M}$.

7.2. One-Mode Shaping for the Nonlinear Reduced Flexible Joint Model

In the following, the linear eigenmode design presented in Section 7.1 is applied to a series elastic actuated robot manipulator. Therefore, it is assumed, that the manipulator dynamics can be modeled by the reduced flexible joint model, c.f. 2.21, [73]:

$$\boldsymbol{M}(\boldsymbol{q})\,\ddot{\boldsymbol{q}} + \boldsymbol{c}(\boldsymbol{q},\dot{\boldsymbol{q}}) = \boldsymbol{\tau} \tag{7.9a}$$

$$\boldsymbol{B}\,\ddot{\boldsymbol{\theta}} + \boldsymbol{\tau} = \boldsymbol{\tau}_m \tag{7.9b}$$

$$\boldsymbol{\tau} = \boldsymbol{K}(\boldsymbol{\theta} - \boldsymbol{q}) + \boldsymbol{D}(\dot{\boldsymbol{\theta}} - \dot{\boldsymbol{q}}) \tag{7.9c}$$

The structure of the system (7.9) differs substantially from the linear one-mode dynamics (7.6). To still apply the algorithm, a dynamic trajectory generation algorithm is used to shape the system to the desired form. It consists of serially interconnected subsystems (see Figure 7.1), where asymptotic stability of each subsystem will be proven.

7.2.1. Trajectory Generation and Tracking

Oscillation control of the system (7.9) is achieved in two steps. First, a command trajectory is generated, which excites the system along the one-mode dynamics. Therefore, the one-mode system

$$\boldsymbol{M}(\boldsymbol{q})\,\ddot{\boldsymbol{q}} + \boldsymbol{D}_d(\boldsymbol{q})\,\dot{\boldsymbol{q}} + \boldsymbol{K}_d(\boldsymbol{q})\,\boldsymbol{q} = \boldsymbol{0} \tag{7.10}$$

is considered. The system is evaluated by numerical simulation to obtain a link side trajectory $\boldsymbol{q}_d(t)$. The damping gain $\boldsymbol{D}_d(\boldsymbol{q})$ is computed by (7.8). The stability of the system is analysed in the following section. The second step is to ensure that the system (7.9) follows the desired trajectory $\boldsymbol{q}_d(t)$. If a controller can be found that ensures tracking of a desired joint torque $\boldsymbol{\tau} = \boldsymbol{\tau}_d$, the choice

$$\boldsymbol{\tau}_d = \boldsymbol{K}\left(\boldsymbol{\theta}_d - \boldsymbol{q}_d\right) + \boldsymbol{D}\left(\dot{\boldsymbol{\theta}}_d - \dot{\boldsymbol{q}}_d\right) \tag{7.11a}$$

$$= -\boldsymbol{D}_d(\boldsymbol{q}_d)\,\dot{\boldsymbol{q}}_d - \boldsymbol{K}_d(\boldsymbol{q}_d)\,\boldsymbol{q}_d + \boldsymbol{c}(\boldsymbol{q}_d,\dot{\boldsymbol{q}}_d), \tag{7.11b}$$

results with (7.9a) in (7.10) for $\boldsymbol{q} = \boldsymbol{q}_d(t)$. Such a controller is given by

$$\boldsymbol{\tau}_c = \boldsymbol{B}\,\ddot{\boldsymbol{\theta}}_d - \boldsymbol{K}_P\,\tilde{\boldsymbol{\theta}} - \boldsymbol{K}_D\,\dot{\tilde{\boldsymbol{\theta}}} + \boldsymbol{\tau}_u, \tag{7.12}$$

as it can be verified by equating $\boldsymbol{\tau}_m = \boldsymbol{\tau}_c$ and $\boldsymbol{\tau}_u = \boldsymbol{\tau}_d$. Here, $\tilde{\boldsymbol{\theta}} = \boldsymbol{\theta} - \boldsymbol{\theta}_d$ is the control error, $\boldsymbol{\tau}_u$ a torque feed forward term, and $\boldsymbol{K}_P \in \mathbb{R}^{n\times n}$ and $\boldsymbol{K}_D \in \mathbb{R}^{n\times n}$ are the constant, symmetric and positive definite controller gain matrices, respectively. The controller (7.12) ensures tracking of a motor trajectory and contains the desired torque terms. The motor trajectory $\boldsymbol{\theta}_d(t)$ can be obtained from the desired link trajectory $\boldsymbol{q}_d(t)$ by solving

$$\boldsymbol{D}\dot{\boldsymbol{\theta}}_d + \boldsymbol{K}\boldsymbol{\theta}_d = (\boldsymbol{D} - \boldsymbol{D}_d)\dot{\boldsymbol{q}}_d + (\boldsymbol{K} - \boldsymbol{K}_d)\boldsymbol{q}_d + \boldsymbol{c}(\boldsymbol{q}_d,\dot{\boldsymbol{q}}_d), \tag{7.13}$$

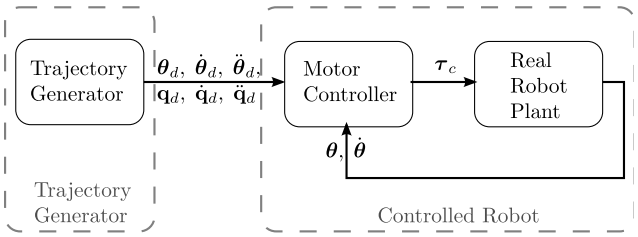

Figure 7.1.: Structure of the complete system: trajectory generator, motor PD controller and real robot plant. Two uncoupled subsystems are marked.

which follows from (7.11). From (7.13) it follows, that the desired dynamics is obtained by reshaping the stiffness and damping matrices and cancelling out the Coriolis/centrifugal forces in the link side dynamics (7.9a). Assuming that the motor side dynamics are sufficiently fast[2], the desired form of (7.10) can be obtained by following the desired trajectory $\boldsymbol{\theta}_d(t)$.
Compared to a design procedure as backstepping Section 6.1 the measured link positions are not used to compute the motor trajectories. To prove stability of the complete system, this will be of major importance.

7.2.2. Stability Analysis of the Complete System

The complete approach can be divided in three parts: a trajectory generator, a motor PD controller and the real robot plant. Figure 7.1 depicts the structure. By treating the PD controller and plant as one unit, two decoupled subsystems can be identified. This partitioning permits to analyse the stability of each subsystem separately, where stability of the complete system can be deduced, if both serially interconnected subsystems for itself are stable.
As generally known (see, e.g. [123, 95]), the motor PD controller stabilizes the flexible joint system (7.9) by local asymptotic convergence. In the following, the stability of the trajectory generator is analysed.
The closed loop dynamics (7.10) can be rewritten as

$$\ddot{\boldsymbol{q}} + \boldsymbol{M}(\boldsymbol{q})^{-1}\, \boldsymbol{D}_d(\boldsymbol{q})\, \dot{\boldsymbol{q}} + \lambda_0\, \boldsymbol{q} = \mathbf{0}, \tag{7.14}$$

where the one-mode shaping relation (7.5) $\boldsymbol{K}_d(\boldsymbol{q}) = \lambda_0 \boldsymbol{M}(\boldsymbol{q})$ is substituted. For the system (7.14) a positive definite Lyapunov function is

$$V(\boldsymbol{q}, \dot{\boldsymbol{q}}) = \frac{1}{2}\, \dot{\boldsymbol{q}}^T\, \dot{\boldsymbol{q}} + \frac{1}{2}\, \lambda_0\, \boldsymbol{q}^T\, \boldsymbol{q}, \tag{7.15}$$

which has a semi negative definite derivative

$$\dot{V}(\boldsymbol{q}, \dot{\boldsymbol{q}}) = \dot{\boldsymbol{q}}^T\, \ddot{\boldsymbol{q}} + \lambda_0\, \dot{\boldsymbol{q}}^T\, \boldsymbol{q} = -\dot{\boldsymbol{q}}\, \boldsymbol{M}(\boldsymbol{q})^{-1}\, \boldsymbol{D}_d(\boldsymbol{q})\, \dot{\boldsymbol{q}} \tag{7.16}$$

[2]More precisely we suppose that $\boldsymbol{\theta}_d \equiv \boldsymbol{\theta}$ for all time, i.e. the singular perturbation assumption (see e.g. [114]) holds.

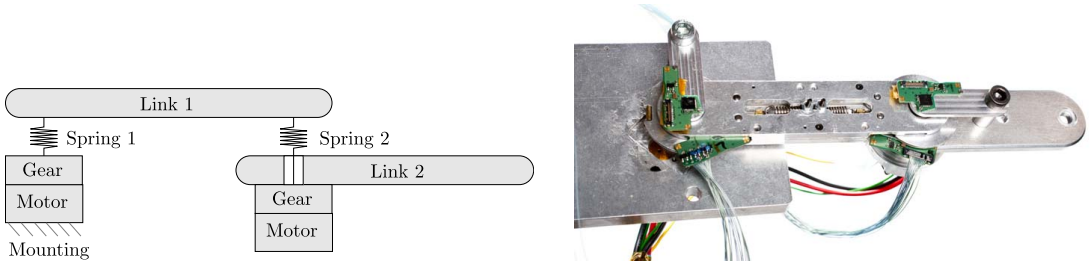

(a) (b)

Figure 7.2.: A sketch and a photo of the SEA robot setup used for the oscillation control tests.

Table 7.1.: Model parameters

i	$m_i\ (kg)$	$CM_i\ (m)$	$J_i\ (kgm^2)$	$k_i\ (Nm)$	$d_i\ (Nms)$
1	0.066	0.042	0.00021	2.4 . . . 6.5	0.01
2	0.118	0.012	0.00009	2.4 . . . 6.5	0.01

if

$$\forall \boldsymbol{y} \neq \boldsymbol{0},\ \forall \boldsymbol{q},\ \boldsymbol{y}^T\, \boldsymbol{M}(\boldsymbol{q})^{-1}\, \boldsymbol{D}_d(\boldsymbol{q})\, \boldsymbol{y} > 0. \tag{7.17}$$

Combining (7.7) and (7.8) yields

$$\boldsymbol{M}(\boldsymbol{q})^{-1}\, \boldsymbol{D}_d(\boldsymbol{q}) = \xi \sqrt{\lambda_0}\, \boldsymbol{Q}\, \boldsymbol{Q}^T\, \boldsymbol{Q}^{-T}\, \boldsymbol{Q}^{-1} = \xi \sqrt{\lambda_0}\, \boldsymbol{I} \tag{7.18}$$

where $\xi \sqrt{\lambda_0} > 0$ as long as $\xi > 0$. $V(\boldsymbol{q}, \dot{\boldsymbol{q}})$ is radially unbounded and for $\xi > 0$, $\dot{V}(\boldsymbol{q}, \dot{\boldsymbol{q}}) \leq 0$. Since $\dot{\boldsymbol{q}} = \boldsymbol{0}, \boldsymbol{q} \neq \boldsymbol{0}$ is not the largest invariant set, the system converges to $\dot{\boldsymbol{q}} = \boldsymbol{0}, \boldsymbol{q} = \boldsymbol{0}$. This implies that $\boldsymbol{q} = \boldsymbol{0}, \dot{\boldsymbol{q}} = \boldsymbol{0}$ is a global asymptotic stable equilibrium point [114].

7.3. Simulation and Experimental Results

The trajectory generation approach has been evaluated on a planar two-link serial elastic actuated (SEA) robot manipulator prototype. The setup is sketched in Fig. 7.2(a) and depicted in Fig. 7.2(b). The parameters of the two link SEA manipulator are listed in Table 7.1. m_i, CM_i and J_i denotes the mass, the distances to the center of mass (w.r.t. the joint axis) and the mass moments of inertia (w.r.t. the joint axis) of each link i. The joint stiffness k_i can be varied by replacing the springs and the joint damping is assumed to be constant.
The method was validated in simulations and experiments on a prototype setup by commanding the desired motor trajectory $\boldsymbol{\theta}_d(t)$ obtained in a numerical offline computation, see Fig. 7.3(c) and Fig. 7.3(d). The joint stiffness was set to $(k_1 = 7.0\,Nm, k_2 = 2.4\,Nm)$. The proportional gain of the motor PD controller was $\boldsymbol{K}_P = \mathrm{diag}(1000, 1000)$, and the differential gain $\boldsymbol{K}_D$ was

chosen such that the closed loop system is critically damped. Finally, the desired controller torques $\boldsymbol{\tau}_c$ were directly commanded to the current controllers of the motors.
Figure 7.3 shows the results of the simulations and experiments[3]. The trajectory consists of three parts, see Fig. 7.3(e). First, the system is excited from rest position by a negative damping coefficient. Once the desired oscillation amplitude is reached, the damping is set to zero and the system sustains the motion. Finally, the oscillation is stopped by a positive damping factor.
As the system is designed to contain one repeated eigenvalue, the motions of the two links are exactly coincident in the simulation. The experimental measurements show very similar performance as the simulation and the position and velocity plots of the two link motions are accurately matching. The desired motor motions computed by the algorithm are different in amplitude and slightly phase shifted from the measured ones. This is as to generate the desired one-mode behaviour and excite the system, an adapted trajectory is necessary. In the experiment, the motor PD controller precisely tracks the desired motion.
The oscillation amplitudes which can be reached by the real hardware setup are restricted trough maximal elongation of the springs. Thus, the behavior shown in Fig. 7.3 is quasi-linear.

[3]Measured velocities are obtained by low pass filtering at 30 Hz and deriving the position measurements numerically.

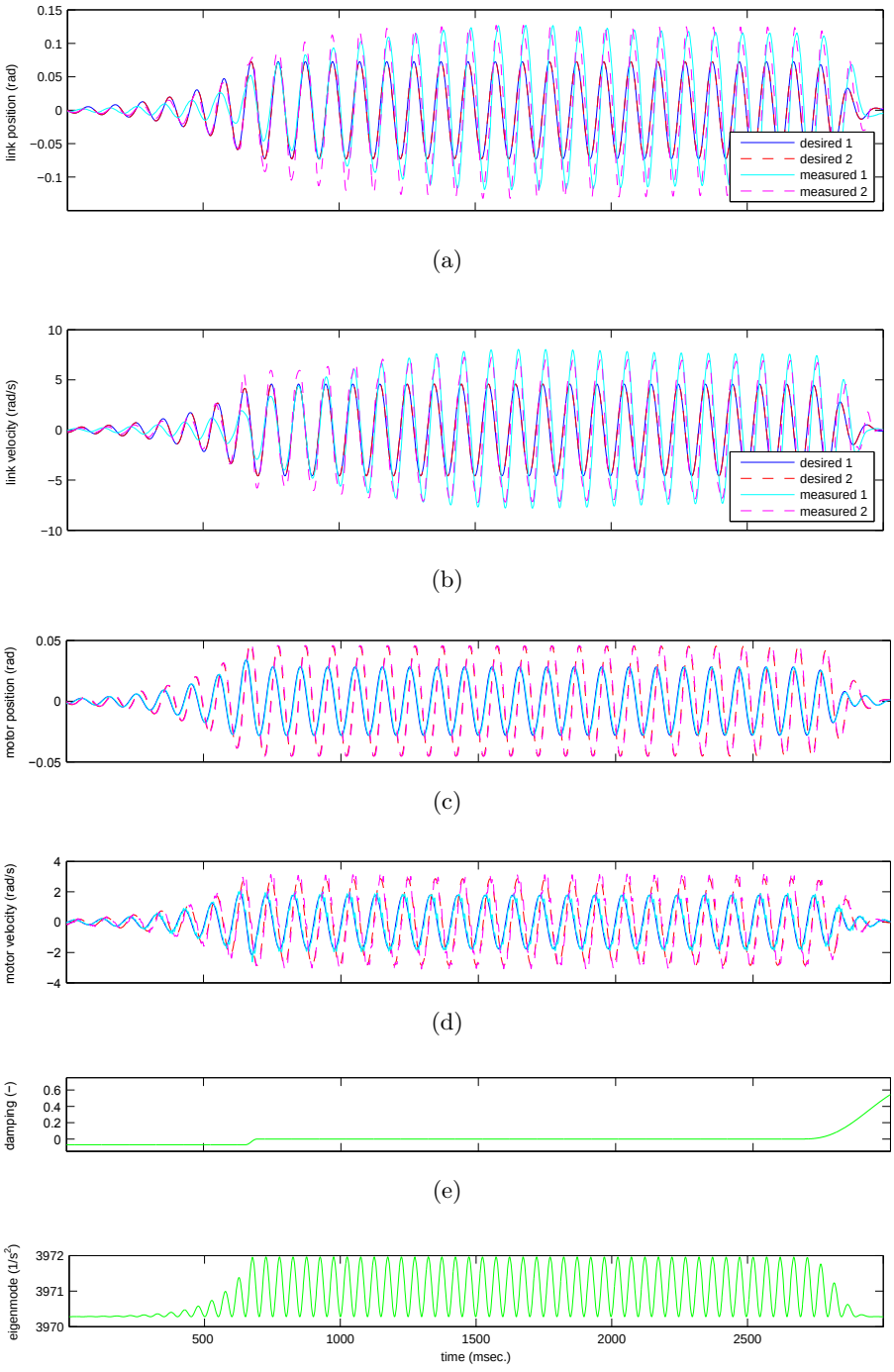

Figure 7.3.: Comparison of the simulated and measured trajectories. The measurements show very good matching of the predicted and achieved behaviour. The three motion parts oscillation excitation, oscillation conservation and damping are induced by the damping factor.

7.4. Discussion

The presented method is an effort to generate oscillatory motions for multi-joint system. Fundamental for the approach are the one-mode shaping and the excitation of the system by using a negative damping coefficient. The only-first-modes dynamics allow to identify points in the resulting trajectory at which all the energy of the system is potential or kinetic. For example the passive springs are relaxed at zero crossings of the link position and all the energy is kinetic. Thereby, coordinated motion is achieved which can be used e.g. for pick and place tasks. Furthermore, the reduction from n-eigenmodes to only one eigenmode provides an abstraction mechanism which allows to extend methods which are designed for single-DoF systems and use them on multi-DoF systems such as input shaping (an approach using feedback linearization was presented in [124]).

A fundamental aim of the algorithm is to exploit the natural dynamics of the robot. Therefore, the goal dynamics are chosen such that is resembles the dynamics of the original system. If the natural system properties are very different from the desired properties, the system inputs have to be used to shape the dynamics. As a result, the system performance is limited. The oscillations are induced and amplified over several periods exploiting the energy storage capabilities of the mechanical elastic elements. As a result the maximum system energy is only limited by hardware maximum ratings (e.g. system end stops, load capability) and not by power restrictions of the energy source.

The approach has several restrictions. The only-first-mode requirement leads to rather big feedback torques. Furthermore, the sequential approach to first produce a trajectory and afterwards track it reduces the flexibility for instantaneous use, as for example a controller provides. Last, the approach is 'economically' limited to series elastic actuators: in principle it is also applicable to variable stiffness actuators, however it would require to shape to nonlinear dynamics of the elastic elements to the linear desired dynamics. The effort to do so annihilates the advantages achieved by exploiting the natural robot dynamics. The considerations have been used to design several advancement of the presented approach. So the mode shaping idea has been improved [125]. Further, new ways to excite oscillations have been developed [126, 127]. Concluding it is to say that the approach can be seen as a first step towards achieving oscillatory motions and exploiting the intrinsic system dynamics of variable stiffness actuators.

8. Conclusions

8.1. Contributions

The variable stiffness actuation technology promises many benefits and advantages. The focus of this work is the VSA performance in classical impedance control tasks, in particular adjusting the equilibrium position, the robot stiffness, and damping properties. A concise analysis of the bidirectional antagonistic variable stiffness joint and a method to induce mechanical oscillations for manipulation or locomotion purposes round off the work. An important point was the thorough experimental validation off all theoretical concepts described. In detail, the contributions are:

8.1.1. System Modeling, Analysis, and Design

System modeling constitutes the basis for controller design. In this work, we provide a thorough overview of VSA robot modeling. Serial and parallel type VS joints have been treated. Various stiffness characteristics and important properties regarding uniqueness of solutions have been discussed. The resulting robot model provides an abstract view. Further practical effects relevant for controller design have been given additionally. The contribution is the presentation of the different variable stiffness joint setups and modeling of the complete VSA robot in a condensed and integral form also relating to concepts reported in the literature.
The described model properties are deepened in a case study of a particular joint solution, the bidirectional antagonistic variable stiffness joint. An analytical model has been developed describing the torque and stiffness behaviour of the setup. This model was used to analyse the joint properties and revealed the existence of two operating modes of BAVS joints. The first operating mode is a co-contraction mode well known from the standard antagonistic setup. By generating internal torques the joint stiffness can be varied. The additional operating mode is called 'helping mode' as there, unidirectional torques are produced by the motors to compensate for an external load. By distributing the load between the motors it is still possible to change the link stiffness in the helping mode. A major result of the analysis is the need for proper torque-stiffness curve design to enable stiffness variation even in helping mode. Out of these considerations, a synthesis method to analytically design the torque-stiffness performance of BAVS joints has been developed. The practical implications of the torque-stiffness curves have been evaluated in a cam-disc based BAVS joint setup. Three implementation variants have

been treated, where the contribution is again the analytical approach. Cam-discs arrangements with 2 and 4 cam-discs, 1 or 2 elastic elements, and symmetric or asymmetric shape have been investigated. The gained insights have been used for the design of a BAVS joint as mounted in the DLR Hand Arm System. Experimental validation has thereby been conducted by robot design and measurements.
The BAVS case study fulfills two goals in this work. First, it provides deep insight in the setup and the properties of VS actuators important for controller design. Second, it is a contribution to the field of VS actuator development and outlines the capabilities of the BAVS joint technology.

8.1.2. Impedance Control Concepts

Energy Shaping

Extensive research on energy shaping methods has been done in the robotic field and especially flexible joint robots are well explored. One of the fundamental properties of VSA robots is their ability to measure joint torques. This constitutes a similarity of VS actuators and flexible joint actuators and suggests to transfer some of the torque control methods developed for the latter. In this work two energy shaping methods are adapted to VS robots. Potential energy shaping relies on defining a static link side equivalent coordinate, which is collocated to the motor torque input. This coordinate enables quasi link side control by well known motor coordinate based controllers and ensures controller stability. The importance of this link side equivalent method to enable precise configuration control is highlighted: it provides an effective way to avoid the inacceptable deviations arising due to the elongation of the elastic elements under gravitational load which inevitable occur for pure motor coordinate control. The strengths of the approach are the convexity of the problem formulation and the flexibility of the goal coordinate choice. The former enables fast computation in the real-time environment while the latter is used in this work to design collocated, statically equivalent Cartesian coordinates. Thereby, a Cartesian impedance controller is designed. The performance of the approach is demonstrated by experiments on the DLR Hand Arm System. The second approach is kinetic energy shaping. In a passivity framework, non-collocated feedback control is used to shape the motor inertia. The superposition principle of the impedance control formulation enables a seamless integration with other compatible controllers. Therefore, both approaches depict a fundamental basis and are widely used for several of the controllers developed in the thesis.
Using elastic elements to estimate joint torques simplifies the robot setup as it obviates the need for additional strain gauges. However, the practicality of such an approach and the allegedly positioning inaccuracy due to the low stiffness of the elastic elements has been cause for criticism of such a concept. The transfer of the two energy shaping methods as performed in this work and the obtained results prove the validity and the performance of the approach. It is clearly demonstrated that a carefully designed system in combination with advanced control methods allows for high quality position and torque control in joint and Cartesian coordinates.

Stiffness Adjustment

A popular modality of torque controlled robots in the impedance control framework is the ability to adjust the robots stiffness. This mode allows to fulfill several tasks. Well known is the use for indirect force control which is especially advantageous during contact situations. Human-robot interaction profits from the flexibility of robot stiffness adjustment. For example zero stiffness adjustment with gravity compensation enables easy teach-in tasks. An important extension is Cartesian impedance control, which allows to specify the equilibrium position and the stiffness properties in Cartesian coordinates. The joint stiffness of VSAs can be varied on a mechanical level by an additional control input. The joint-wise deployment and bounded stiffness range due to mechanism properties require the modification of the Cartesian impedance control formulation to incorporate the VSA characteristics. The contribution is a concise analysis of the Cartesian VSA performance and the development of control approaches to extend the robot capabilities. The influencing parameters, which are the passive joint stiffness variation and nullspace reconfiguration, are identified. Stiffability maps are introduced, which capture the robot arm's capability to render Cartesian stiffness values. Two control approaches are presented to extend the insufficient Cartesian stiffness performance of pure passive joint stiffness adjustment. First, the combination of the passive stiffness with an active impedance controller is suggested. This allows to overcome the mechanical joint limitations and the joint wise actuator mounting. The Cartesian stiffness optimization problem and the counterpart in the compliance space are formulated. A convex formulation, optimizing the active and passive stiffness simultaneously, is presented. Furthermore, a sequential approach has been developed aiming at high task embodiment by approaching the desired stiffness as good as possible by the passive stiffness and complementing the residual by an active control component. The second adjustment parameter relevant to achieve high Cartesian stiffness tracking is configuration adjustment. A local method has been formulated exploiting the nullspace configuration of the robot. The effects of the approaches are shown using the stiffability maps. Additionally, the effectiveness along with its real-time applicability of both approaches has been verified by a series of experiments conducted on the DLR Hand Arm System.
Contributions of this work are the analysis and control tools to adjust the Cartesian stiffness of multi-joint variable stiffness actuated robots. These methods allow to achieve high quality Cartesian stiffness regulation with similar performance as torque controlled robots.

Damping Adjustment

The third property relevant for task execution success is the ability to adjust the robot damping. The low damping of variable stiffness joints is elementary for dynamic performance and torque estimation. However, for many manipulation tasks proper damping of the overall system is required. The nonlinearity and the high system dimensions of a multi-joint VSA robot are highly demanding for controller design. Three different damping controllers are presented and evaluated in this thesis. A first controller is based upon a backstepping control law. A PD^+

control law is chosen on the highest level. The choice provides configuration dependent damping and preserves the intrinsic structure of the robot dynamics to a maximal extend. The use of command filters solves the stability problems associated to low pass signal filtering. Higher order state derivatives can be obtained by command filters in a stable framework. Several experiments have been conducted on various systems. The flexibility of the backstepping approach has been validated on a bidirectional antagonistic variable stiffness test bench. The multi-joint properties are verified on the DLR Hand Arm System. A second approach is based upon a state feedback controller and physically motivated gain design. The state feedback structure avoids feedback of higher order state derivatives and controller gains can be matched to specific sensors. Gain design is a key factor for controller performance. The developed gain design algorithm aims to add the desired damping properties and modify the robot as little as possible by control. Eigenmode decoupling and optimized torque feedback are used to ensure minimal feedback interaction. The excellent controller performance is validated on several experiments on the DLR Hand Arm System. A third controller is designed to rely as little as possible on model knowledge of the robot system. The controller idea is derived from observations of the kinetic and potential energy transfer process during a disturbance. Thereby, only basic state information and input modalities are required such as link side measurements and motor position or velocity inputs. No system model is needed even for the multi-joint case and stability can be guaranteed. The controller has been tested on the DLR Hand Arm System. Furthermore, an open loop feed forward approach is discussed.
The coherent representation of the three completely different control approaches provides a contribution itself. The presentation allows to easily compare the theoretical effort, constraints of the approaches, and experimental results. Thereby, it is possible to evaluate the suitability of the controller for the complete range of robots, be it a high end system or robots where hardware and computational restrictions exist. Together with the link side equivalent controller the damping control approaches are elementary contributions to achieve precise and fast position regulation performance of VSA robots.

8.1.3. Oscillation Control

Exploiting the energy storing capabilities of the elastic elements allows to achieve highly dynamic or energy efficient motions. Link velocities exceeding the motor velocities or cyclic motions requiring only little energy input can be obtained. The decoupling of the motor and the link by the elastic element and its energy storage capabilities are exploited. While the main focus of this work are impedance control tasks, some of the used methods may be adapted to dynamic and energy efficient motions useful for cyclic tasks such as hammering or running. Such, the physically motivated gain design algorithm as used in the state feedback damping controller relies on modal decoupling of the system dynamics. By using negative damping gains in combination with the modal decoupling, the oscillatory system can be intentionally excited. A method to excite stable oscillations in a series elastic actuated system is presented. It can be seen as the starting point

for a series of research efforts aiming to exploit the energy storage properties of elastic elements in a feedback controller structure.

8.2. Final Remarks and Future Work

The work presented in this thesis covers several of the system analysis and control problems and questions which arose in the context of the development of variable stiffness actuated robots. An initial focus was the modeling and the joint case study and is accounted to the recent development of the VS technology. Thereby, a deep understanding of the capabilities of such systems could be acquired. The difference to the flexible joint setup is mainly the elastic element with its nonlinear stiffness. Indeed, the advantageous features are enabled by this spring element and the separated structure of the motor and link. Main challenges for controller design arise from the nonlinear stiffness and dynamics and the multi-dimensionality of the VSA robot setup. Criticisms of the VSA concept are possible configuration imprecision due to the elastic elements and easily excitable oscillations due to the low intrinsic damping. Both these questions have been tackled in this work, where several control concepts to overcome these disadvantages have been developed. The thorough experimental evaluation shows that the approaches in combination with the careful mechanical VSA robot design allow to achieve high performance position and damping control while providing mechanical robustness. A further effort of this thesis was the validation of the torque control ability of VSA robots. The transfer and evaluation of several well-known energy shaping techniques showes the power of the VSA setup. A highlight is the combination of the passive joint stiffness with an active impedance controller. Increased flexibility regarding coordinate choice and stiffness adjustability show the advantages of the joining of both methods. The effect of robot configuration on the stiffness performance is another topic explore and shows high potential. Subsuming it can be said, that the presented concepts to adjust the impedance parameters, namely the equilibrium position, the robot stiffness, and the system damping, allow to achieve similar performance as torque controlled robots. The treatment of oscillation control is an outlook into the interesting and open field of exciting and actively utilizing the energy storage capability of VSA systems. The development of efficient and intuitively adjustable and parameterisable controllers can be the goal for further research.
The VSA concept itself is also topic of ongoing research and modifications are likely to happen. Such development steps are also visible in this work, where several joint concepts are treated. An advantage of the presented control methods is their generality resulting in independence from a particular joint realization. For example the active/passive stiffness adjustment approach only requires the ability to adjust the active and passive joint stiffness - which particular joint realization is used is of minor relevance. Another example are the damping approaches. Be it the backstepping approach, the state feedback approach or the state based damping, all the approaches only pose quite general requirements on the joint setup. Therefore, these damping approaches can be used in a straight forward manner also on SEA joints. An important point of

this work is the strong focus on real world application of the developed concepts on multi-joint VSA systems. Numerous experiments proof the real-time applicability and characteristics of the approaches. This thorough experimental evaluation on a multi-joint VSA robot is a highlight of this work.
This work demonstrates the range and capability of the VSA joint concept. A task to be completed is to develop and integrate a set of identification and control methods and to tune it to the mechanic and electric robotic setup. The focus should be robustness, simplicity, and performance, both, on a control and mechatronic level.
The author is convinced that many of the robotic tools required therefore have been developed and a careful combination will lead to a versatile, robust, and performant service robotic system.

A. Curriculum Vitae

Florian Petit was born in München, Germany, on September 21st, 1982. He holds a Diplom Ingenieur (Dipl.-Ing.) degree from the Technische Universität München. He is currently pursuing a PhD at the Institute of Robotics and Mechatronics at the German Aerospace Center (DLR) under the supervision of Prof. Alin Albu-Schäffer and is a member of the Sensory-Motor Systems Lab at ETH Zürich under the supervision of Prof. Robert Riener.

Florian Petit's research focus is the analysis and control of torque controlled robots and nonlinear systems in general. In particular, he is interested in the system design of variable stiffness robots, as well as model-based control methods which can be summarized as impedance control methods.

Previous projects include fibre Bragg grating interrogation with a tunable laser at the Institute for Measurement Systems and Sensor Technology of TU München of Prof. A. W. Koch in 2006 and the simulation of efficient quadrupedal walking at the Autonomous Systems Lab at ETH Zürich under supervision of Prof. Roland Siegwart in 2007. From April until September 2008 he was a visiting scholar in the Locomotion Lab of Prof. Kenneth Waldron at Stanford University, where he worked on the analysis and design of a foot-ankle system. In July 2011 he co-organized the "Summer School on Impedance" at Frauenchiemsee.

B. List of Publications

Journals

- **F. Petit**, W. Friedl, H. Höppner and M. Grebenstein. Analysis and Synthesis of the Bidirectional Antagonistic Variable Stiffness Mechanism, *IEEE Transactions on Mechatronics*, 2014.
- **F. Petit**, A. Dietrich and A. Albu-Schäffer, Generalizing Torque Control Concepts to Variable Stiffness Robots, *conditionally accepted: IEEE Robotics & Automation Magazine*, 2014.
- **F. Petit**, A. Daasch and A. Albu-Schäffer. Backstepping Control of Variable Stiffness Robots, *IEEE Transactions on Control System Technology*, 2014.
- D. Lakatos, **F. Petit** and A. Albu-Schaffer. *Nonlinear Oscillations for Cyclic Movements in Human and Robotic Arms*, IEEE Transactions on Robotics, 2014.
- D. J. Braun, **F. Petit**, F. Huber, S. Haddadin, P. van der Smagt, A. Albu-Schaffer and S. Vijayakumar. Robots Driven by Compliant Actuators: Optimal Control Under Actuation Constraints, *IEEE Transactions on Robotics*, 2013.
- B. Vanderborght, A. Albu-Schaeffer, A. Bicchi, E. Burdet, D.G. Caldwell, R. Carloni, M. Catalano, O. Eiberger, W. Friedl, G. Ganesh, M. Garabini, M. Grebenstein, G. Grioli, S. Haddadin, H. Hoppner, A. Jafari, M. Laffranchi, D. Lefeber, **F. Petit**, S. Stramigioli, N. Tsagarakis, M. Van Damme, R. Van Ham, L.C. Visser and S. Wolf. Variable impedance actuators: A review, *Robotics and Autonomous Systems*, 2013.
- M. S. Müller, L. Hoffmann, T. Bodendorfer, F. Hirth, **F. Petit**, M. P. Plattner, T. C. Buck and A. W. Koch: Fiber Bragg Grating interrogation based on monolithic tunable laser diode. *IEEE Transactions on Instrumentation and Measurement*, 2009.

Conferences

- **F. Petit**, Ch. Ott and A. Albu-Schäffer. A Model-Free Approach to Achieve Damping via Vibration Suppression for Intrinsically Elastic Robots, *IEEE Int. Conf. on Robotics and Automation*, 2014.

- D. Lakatos, **F. Petit** and A. Albu-Schäffer. Nonlinear Oscillations for Cyclic Movements in Variable Impedance Actuated Robotic Arms, *Proc. IEEE Int. Conf. on Robotics and Automation*, 2013.

- D. Lakatos, G. Garofalo, **F. Petit**, Ch. Ott and A. Albu-Schäffer. Modal Limit Cycle Control for Variable Stiffness Actuated Robots, *Proc. IEEE Int. Conf. on Robotics and Automation*, 2013.

- D. Lakatos, M. Görner, **F. Petit**, A. Dietrich and A. Albu-Schäffer. A modally adaptive control for multi-contact cyclic motions in compliantly actuated robotic systems, *Proc. IEEE/RSJ Int. Conf. on Intelligent Robots and Systems*, 2013.

- A. Albu-Schäffer, Ch. Ott and **F. Petit**. Energy Shaping Control for a Class of Underactuated Euler-Lagrange Systems, *10th IFAC Symposium on Robot Control*, 2012.

- **F. Petit**, D. Lakatos, W. Friedl and A. Albu-Schäffer. Dynamic Trajectory Generation for Serial Elastic Actuated Robots, *10th IFAC Symposium on Robot Control*, 2012.

- B. Vanderborght, A. Albu-Schäffer, A. Bicchi, E. Burdet, D. Caldwell, R. Carloni, M. Catalano, G. Gowrishankar, M. Garabini, G. Grioli, S. Haddadin, A. Jafari, M. Laffranchi, D. Lefebre, **F. Petit** , S. Stramigioli, M. Grebenstein, N. Tsagarakis, M. van Damme, R. van Ham, L. Visser and S. Wolf. Variable Impedance Actuators: Moving the Robots of Tomorrow, *Proc. IEEE Int. Conf. on Robotics and Automation*, 2012.

- D. J. Braun, **F. Petit**, F. Huber, S. Haddadin, P. van der Smagt, A. Albu-Schaffer and S. Vijayakumar. *Optimal torque and stiffness control in compliantly actuated robots*, IEEE International Conference on Intelligent Robots and Systems, 2012.

- **F. Petit** and A. Albu-Schäffer. Cartesian Impedance Control For A Variable Stiffness Robot Arm, *Proc. of the IEEE/RSJ International Conference on Intelligent Robots and Systems*, 2011.

- **F. Petit** and A. Albu-Schäffer. State Feedback Damping Control For A Multi DOF Variable Stiffness Robot Arm, *Proc. IEEE Int. Conf. on Robotics and Automation*, 2011.

- M. Grebenstein, A. Albu-Schäffer, T. Bahls, M. Chalon, O. Eiberger, W. Friedl, R. Gruber, S. Haddadin, U. Hagn, R. Haslinger, H. Höppner, S. Jörg, M. Nickl, A. Nothhelfer, **F. Petit**, J. Reill, N. Seitz, T. Wimböck, S. Wolf, T. Wüsthoff and G. Hirzinger. The DLR Hand Arm System, *Proc. IEEE Int. Conf. on Robotics and Automation*, 2011.

- W. Friedl, H. Höppner, **F. Petit** and G. Hirzinger. Wrist and Forearm Rotation of the DLR Hand Arm System: Mechanical Design, Shape Analysis and Experimental Validation, *Proc. of the IEEE/RSJ International Conference on Intelligent Robots and Systems*, 2011.

- D. Lakatos, **F. Petit** and P. van der Smagt. *Conditioning vs. excitation time for estimating impedance parameters of the human arm*, IEEE International Conference on Humanoid Robots, 2011.
- A. Albu-Schäffer, S. Wolf, O. Eiberger, S. Haddadin, **F. Petit** and M. Chalon. Dynamic Modelling and Control of Variable Stiffness Actuators, *Proc. IEEE Int. Conf. on Robotics and Automation*, 2010.
- **F. Petit**, M. Chalon, W. Friedl, M. Grebenstein, A. Albu-Schäffer and G. Hirzinger. Bidirectional Antagonistic Variable Stiffness Actuation: Analysis, Design & Implementation, *Proc. IEEE Int. Conf. on Robotics and Automation*, 2010.
- C. D. Remy, K. Buffinton, **F. Petit** and R. Siegwart. Passive dynamic walking with quadrupeds, *Workshop at the "Robotics: Science and Systems" Conference*, 2008.

Bibliography

[1] L. Takayama, W. Ju, and C. Nass, "Beyond dirty, dangerous and dull: what everyday people think robots should do," Proceedings of the 3rd international conference on Human robot interaction, pp. 25–32, 2008. Cited on page 11.

[2] M. Mason, "Compliance and force control for computer controlled manipulators," Transactions on Systems, Man, and Cybernetics, vol. 11, no. 6, pp. 418–432, 1981. Cited on page 11.

[3] M. A. Peshkin, "Programmed compliance for error corrective assembly," IEEE Transaction on Robotics and Automation, vol. 6, no. 4, pp. 473–482, 1990. Cited on page 12.

[4] A. Albu-Schäffer, O. Eiberger, M. Grebenstein, S. Haddadin, C. Ott, T. Wimböck, S. Wolf, and G. Hirzinger, "Soft robotics: From torque feedback-controlled lightweight robots to intrinsically compliant systems," IEEE Robotics and Automation Magazine, vol. 15, no. 4, pp. 20–30, 2008. Cited on page 12.

[5] K. Laurin-Kovitz, J. Colgate, and S. Carnes, "Design of components for programmable passive impedance," in Proc. IEEE Int. Conf. on Robotics and Automation, vol. 2, 1991, pp. 1476–1481. Cited on pages 12 and 15.

[6] C.-P. Chou and B. Hannaford, "Measurement and modeling of mckibben pneumatic artificial muscles," IEEE Transactions on Robotics and Automation, vol. 12, no. 1, pp. 90–102, 1996. Cited on pages 12 and 15.

[7] T. L. De Fazio, D. S. Seltzer, and D. Whitney, "The instrumented remote center of compliance," Industrial Robot, vol. 11, no. 4, pp. 238–242, 1984. Cited on page 12.

[8] Schunk GmbH Co. KG. (2013, 6) Flexible force-torque sensor. [Online]. Available: http://www.schunk.com/schunk$_$files/attachments/OM$_$AU$_$FTC$__$EN.pdf Cited on page 12.

[9] P. B. Siciliano and P. O. Khatib, Eds., Springer Handbook of Robotics. Springer Berlin Heidelberg, 2008. Cited on page 12.

[10] N. Hogan, "Impedance Control: An Approach to Manipulation: Part I - Theory, Part II - Implementation, Part III - Applications," ASME Journal of Dynamic Systems, Measurement, and Control, vol. 107, pp. 1–24, 1985. Cited on pages 12, 15, and 85.

[11] E. D. Fasse and J. F. Broenink, "A spatial impedance controller for robotic manipulation," IEEE Transaction on Robotics and Automation, vol. 13, pp. 546–556, 1997. Cited on page 12.

[12] G. Hirzinger, N. Sporer, A. Albu-Schäffer, M. Hähnle, R. Krenn, A. Pascucci, and M. Schedl, "DLR's torque-controlled light weight robot III - are we reaching the technological limits now?" in Proc. IEEE Int. Conf. on Robotics and Automation, 2002, pp. 1710–1716. Cited on pages 12, 16, and 25.

[13] Daimler AG. (2009, 12) Mercedes-Benz Werk Untertuerkheim: Leichtbauroboter im Piloteinsatz. [Online]. Available: http://media.daimler.com/dcmedia/0-921-657591-49-1257618-1-0-1-0-0-0-11701-614316-0-1-0-0-0-0-0.html Cited on pages 12 and 62.

[14] ——. (2012, 12) Mensch-roboter-kooperation: Innovatives zusammenspiel von mensch und roboter bei mercedes-benz. [Online]. Available: http://media.daimler.com/dcmedia/0-921-656186-49-1556286-1-0-0-0-0-0-11694-614232-0-0-0-0-0-0-0.html Cited on pages 12 and 62.

[15] KUKA Roboter GmbH. (2013, 11) Irex: Curtain up for the lbr iiwa! [Online]. Available: http://www.kuka-robotics.com/germany/en/pressevents/news/NN_131106_iREX.htm Cited on pages 12, 16, and 62.

[16] O. Khatib, "A unified approach for motion and force control of robot manipulators: The operational space formulation." International Journal of Robotics and Automation, vol. 3, no. 1, pp. 43–53, 1987. Cited on page 12.

[17] C. Dumas, S. Caro, S. Garnier, and B. Furet, "Joint stiffness identification of six-revolute industrial serial robots," Robot. Comput.-Integr. Manuf., vol. 27, no. 4, pp. 881–888, 2011. Cited on page 12.

[18] A. Albu-Schäffer, C. Ott, and G. Hirzinger, "A unified passivity based control framework for position, torque and impedance control of flexible joint robots," International Journal of Robotics Research, vol. 26, no. 1, pp. 23–39, 2007. Cited on pages 12, 25, 55, and 73.

[19] C. Ott, Cartesian Impedance Control of Redundant and Flexible-Joint Robots, ser. Springer Tracts in Advanced Robotics. Springer, 2008, vol. 49. Cited on pages 12, 58, 67, 85, 97, 98, 109, and 126.

[20] A. De Luca, A. Albu-Schäffer, S. Haddadin, and G. Hirzinger, "Collision detection and safe reaction with the dlr-iii lightweight manipulator arm," in Proc. IEEE/RSJ Int. Conf. on Intelligent Robots and Systems, 2006, pp. 1623–1630. Cited on page 12.

[21] KUKA Laboratories GmbH, KUKA System Software 5.6 lr Bedien- und Programmieranleitung für Systemintegratoren, 2011. Cited on page 12.

[22] M. Grebenstein, M. Chalon, W. Friedl, S. Haddadin, T. Wimböck, G. Hirzinger, and R. Siegwart, "The hand of the DLR Hand Arm System: Designed for interaction," The International Journal of Robotics Research, vol. 31, no. 13, pp. 1531–1555, 2012. Cited on pages 13, 16, and 41.

[23] D. J. Braun, F. Petit, F. Huber, S. Haddadin, P. van der Smagt, A. Albu-Schäffer, and S. Vijayakumar, "Robots driven by compliant actuators: Optimal control under actuation constraints," IEEE Transactions on Robotics, vol. 29, no. 5, pp. 1085–1101, 2013. Cited on pages 13, 28, and 135.

[24] M. Raibert, Legged Robots that Balance. MIT Press, 1986. Cited on page 13.

[25] B. Vanderborght, N. Tsagarakis, R. Van Ham, I. Thorson, and D. Caldwell, "MACCEPA 2.0: Compliant actuator used for energy efficient hopping robot chobino 1D," Autonomous Robots, vol. 31, no. 1, pp. 55–65, 2011. Cited on pages 13, 16, and 26.

[26] L. C. Visser, S. Stramigioli, and A. Bicchi, "Embodying desired behavior in variable stiffness actuators," in 2011 Congress of the International Federation of Automatic Control, 2011, pp. 9733–9738. Cited on pages 13 and 135.

[27] G. Palli, C. Melchiorri, and A. De Luca, "On the feedback linearization of robots with variable joint stiffness," in Proc. IEEE Int. Conf. on Robotics and Automation, 2008, pp. 1753 – 1759. Cited on pages 14, 96, and 111.

[28] R. Schiavi, G. Grioli, S. Sen, and A. Bicchi, "VSA-II: a novel prototype of variable stiffness actuator for safe and performing robots interacting with humans," in Proc. IEEE Int. Conf. on Robotics and Automation, 2008, pp. 2171 – 2176. Cited on pages 14 and 16.

[29] A. De Luca, F. Flacco, A. Bicchi, and R. Schiavi, "Nonlinear decoupled motion-stiffness control and collision detection/reaction for the VSA-II variable stiffness device," in Proc. IEEE/RSJ Int. Conf. on Intelligent Robots and Systems, 2009, pp. 5487 – 5494. Cited on page 14.

[30] C. Semini, V. Barasuol, T. Boaventura, M. Frigerio, and J. Buchli, "Is active impedance the key to a breakthrough for legged robots?" in Proceedings of International Symposium of Robotics Research (ISRR), 2013. Cited on pages 15 and 17.

[31] B. Tondu and P. Lopez, "Modeling and control of mckibben artificial muscle robot actuators," IEEE Control Systems Magazine, vol. 20, no. 2, pp. 15–38, 2000. Cited on page 15.

[32] F. Carpi, R. Kornbluh, P. Sommer-Larsen, and G. Alici, "Electroactive polymer actuators as artificial muscles: are they ready for bioinspired applications?" Bioinspiration & biomimetics, vol. 6, no. 4, 2011. Cited on page 15.

[33] R. H. Baughman, C. Cui, A. A. Zakhidov, Z. Iqbal, J. N. Barisci, G. M. Spinks, G. G. Wallace, A. Mazzoldi, D. D. Rossi, A. G. Rinzler, O. Jaschinski, S. Roth, and M. Kertesz, "Carbon nanotube actuators," Science, vol. 284, no. 5418, pp. 1340–1344, 1999. Cited on page 15.

[34] T. Morita and S. Sugano, "Design and development of a new robot joint using a mechanical impedance adjuster," in Proc. IEEE Int. Conf. on Robotics and Automation, vol. 3, 1995, pp. 2469–2475. Cited on pages 15 and 17.

[35] ——, "Development and evaluation of seven dof mia arm," in Proc. IEEE Int. Conf. on Robotics and Automation, vol. 1, 1997, pp. 462–467. Cited on pages 15 and 17.

[36] K. Koganezawa, Y. Watanabe, and N. Shimizu, "Antagonistic muscle-like actuator and its application to multi-dof forearm prosthesis," Advanced Robotics, vol. 12, no. 7, pp. 771–789, 1999. Cited on pages 15 and 31.

[37] K. Koganezawa, "Mechanical stiffness control for antagonistically driven joints," in Proc. IEEE/RSJ Int. Conf. on Intelligent Robots and Systems, 2005, pp. 1544–1551. Cited on page 15.

[38] C. English and D. Russell, "Mechanics and stiffness limitations of a variable stiffness actuator for use in prosthetic limbs," Mechanism and Machine Theory, vol. 34, no. 1, pp. 7 – 25, 1999. Cited on page 15.

[39] M. Okada, Y. Nakamura, and S. Ban, "Design of programmable passive compliance shoulder mechanism," in Proc. IEEE Int. Conf. on Robotics and Automation, vol. 1, 2001, pp. 348–353 vol.1. Cited on page 15.

[40] A. Bicchi, S. Rizzini, and G. Tonietti, "Compliant design for intrinsic safety: general issues and preliminary design," Proc. of the IEEE/RSJ Int. Conf. on Intelligent Robots and Systems, vol. 4, pp. 1864 – 1869, 2001. Cited on page 16.

[41] A. Bicchi and G. Tonietti, "Fast and soft-arm tactics," IEEE Robotics & Automation Magazine, vol. 11, no. 2, pp. 22–33, 2004. Cited on page 16.

[42] J. W. Hurst, J. Chestnutt, and A. Rizzi, "An actuator with physically variable stiffness for highly dynamic legged locomotion," in Proc. IEEE Int. Conf. on Robotics and Automation, 2004, pp. 4662 – 4667. Cited on page 16.

[43] G. Tonietti, R. Schiavi, and A. Bicchi, "Design and control of a variable stiffness actuator for safe and fast physical human/robot interaction," in Proc. IEEE Int. Conf. on Robotics and Automation, 2005, pp. 526 – 531. Cited on page 16.

[44] M. Grebenstein, "Antagonistische Schwenkvorrichtung," German Patent No. DE 10 2006 016 958 A1, 2006. Cited on page 16.

[45] R. Van Ham, B. Vanderborght, M. V. Damme, B. Verrelst, and D. Lefeber, "Maccepa, the mechanically adjustable compliance and controllable equilibrium position actuator: Design and implementation in a biped robot," Robotics and Autonomous Systems, vol. 55, no. 10, pp. 761 – 768, 2007. Cited on pages 16 and 26.

[46] S. Wolf and G. Hirzinger, "A new variable stiffness design: Matching requirements of the next robot generation," in Proc. IEEE Int. Conf. on Robotics and Automation, 2008, pp. 1741 – 1746. Cited on pages 16, 19, 23, and 41.

[47] O. Eiberger, S. Haddadin, M. Weis, A. Albu-Schäffer, and G. Hirzinger, "On joint design with intrinsic variable compliance: Derivation of the DLR QA-joint," in Proc. IEEE Int. Conf. on Robotics and Automation, 2010, pp. 1687 – 1694. Cited on pages 16, 23, and 41.

[48] S. Wolf, O. Eiberger, and G. Hirzinger, "The DLR FSJ: Energy based design of variable stiffness joints," in Proc. IEEE Int. Conf. on Robotics and Automation, 2011, pp. 5082 – 5089. Cited on pages 16, 21, 23, 26, and 41.

[49] M. G. Catalano, R. Schiavi, and A. Bicchi, "Mechanism design for variable stiffness actuation based on enumeration and analysis of performance," in Proc. IEEE Int. Conf. on Robotics and Automation, 2010, pp. 3285 – 3291. Cited on pages 16 and 21.

[50] A. Jafari, N. G. Tsagarakis, B. Vanderborght, and D. G. Caldwell, "A novel actuator with adjustable stiffness (AwAS)," Proc. IEEE/RSJ Int. Conf. on Intelligent Robots and Systems, pp. 4201 – 4206, Oct 2010. Cited on page 16.

[51] M. Laffranchi, N. G. Tsagarakis, and D. G. Caldwell, "A variable physical damping actuator (vpda) for compliant robotic joints," in Proc. IEEE Int. Conf. on Robotics and Automation, 2010, pp. 1668 – 1674. Cited on page 16.

[52] G. A. Pratt and M. M. Williamson, "Series elastic actuators," in Proc. IEEE/RSJ Int. Conf. on Intelligent Robots and Systems, Pittsburg, PA, USA, 1995, pp. 399–406. Cited on pages 16 and 25.

[53] L. Visser, R. Carloni, R. Unal, and S. Stramigioli, "Modeling and design of energy efficient variable stiffness actuators," in Proc. IEEE Int. Conf. on Robotics and Automation, 2010, pp. 3273 – 3278. Cited on page 16.

[54] S. Groothuis, G. Rusticelli, A. Zucchelli, S. Stramigioli, and R. Carloni, "The vsaUT-II: a novel rotational variable stiffness actuator," in Proc. IEEE Int. Conf. on Robotics and Automation, 2012, pp. 3355 – 3360. Cited on pages 16 and 25.

[55] M. Grebenstein and P. van der Smagt, "Antagonism for a highly anthropomorphic hand arm system," Advanced Robotics, no. 22, pp. 39 – 55, 2008. Cited on page 16.

[56] R. Van Ham, T. G. Sugar, B. Vanderborght, K. W. Hollander, and D. Lefeber, "Compliant actuator designs," IEEE Robotics and Automation Magazine, vol. 16, pp. 81–94, 2009. Cited on page 16.

[57] N. L. Tagliamonte, F. Sergi, D. Accotom, G. Carpino, and E. Guglielmelli, "Double actuation architectures for rendering variable impedance in compliant robots: A review," Mechatronics, vol. 22, pp. 1187–1203, 2012. Cited on page 16.

[58] B. Vanderborght, A. Albu-Schäffer, A. Bicchi, E. Burdet, D. Caldwell, R. Carloni, M. Catalano, O. Eiberger, W. Friedl, G. Ganesh, M. Garabini, M. Grebenstein, G. Grioli, S. Haddadin, H. Höppner, A. Jafari, M. Laffranchi, D. Lefeber, F. Petit, S. Stramigioli, N. Tsagarakis, M. V. Damme, R. V. Ham, L. Visser, and S. Wolf, "Variable impedance actuators: A review," Robotics and Autonomous Systems, vol. 61, no. 12, p. 1601–1614, 2013. Cited on page 16.

[59] "Robonaut 2 fact sheet," National Aeronautics and Space Administration, Tech. Rep. [Online]. Available: http://www.nasa.gov/pdf/464887main_Robonaut2FactSheet.pdf Cited on page 16.

[60] R. A. Brooks, C. Breazeal, M. Marjanovic, B. Scassellati, and M. M. Williamson, "The cog project: Building a humanoid robot," Lecture Notes in Computer Science, vol. 1562, pp. 52–87, 1999. Cited on pages 17 and 25.

[61] A. L. Edsinger, "Robot manipulation in human environments," Ph.D. dissertation, Massachusetts Institute of Technology, 2007. Cited on page 17.

[62] Meka Robotics. [Online]. Available: http://mekabot.com Cited on pages 17 and 25.

[63] Rethink Robotics. [Online]. Available: http://www.rethinkrobotics.com/products/baxter/ Cited on page 17.

[64] T. Morita, H. Iwata, and S. Sugano, "Development of human symbiotic robot: Wendy," in Proc. IEEE Int. Conf. on Robotics and Automation, vol. 4, 1999, pp. 3183–3188. Cited on page 17.

[65] H. Iwata and S. Sugano, "Design of human symbiotic robot twendy-one," in Proc. IEEE Int. Conf. on Robotics and Automation, 2009, pp. 580 – 586. Cited on page 17.

[66] T. Sugaiwa, H. Iwata, and S. Sugano, "New visco-elastic mechanism design for flexible joint manipulator," in International Conference on Advanced Intelligent Mechatronics, 2008, pp. 235 – 240. Cited on page 17.

[67] G. Metta, L. Natale, F. Nori, G. Sandini, D. Vernon, L. Fadiga, C. von Hofsten, K. Rosander, M. Lopes, J. Santos-Victor, A. Bernardino, and L. Montesano, "The icub humanoid robot: An open-systems platform for research in cognitive development," Neural Networks, vol. 23, no. 8-9, pp. 1125–1134, 2010. Cited on page 17.

[68] N. G. Tsagarakis, Z. Li, J. Saglia, and D. G. Caldwell, "The design of the lower body of the compliant humanoid robot cCub," in Proc. IEEE Int. Conf. on Robotics and Automation, 2011, pp. 2035 – 2040. Cited on page 17.

[69] M. Laffranchi, N. G. Tsagarakis, and D. G. Caldwell, "Compact arm: a compliant manipulator with intrinsic variable physical damping," in Robotics, Science and Systems (RSS), 2012. Cited on pages 17 and 25.

[70] M. Grebenstein, A. Albu-Schäffer, T. Bahls, M. Chalon, O. Eiberger, W. Friedl, R. Gruber, S. Haddadin, U. Hagn, R. Haslinger, H. Höppner, S. Jörg, M. Nickl, A. Nothhelfer, F. Petit, J. Reill, N. Seitz, T. Wimböck, S. Wolf, T. Wüsthoff, and G. Hirzinger, "The DLR Hand Arm System," in Proc. IEEE Int. Conf. on Robotics and Automation, 2011, pp. 3175 – 3182. Cited on pages 17, 19, and 23.

[71] R. M. Murray, Z. X. Li, and S. S. Sastry, A Mathematical Introduction to Robotic Manipulation. CRC Press, 1994. Cited on page 22.

[72] A. Albu-Schäffer, S. Wolf, O. Eiberger, S. Haddadin, F. Petit, and M. Chalon, "Dynamic modelling and control of variable stiffness actuators," in Proc. IEEE Int. Conf. on Robotics and Automation, 2010, pp. 2155 – 2162. Cited on pages 23 and 115.

[73] M. Spong, "Modeling and control of elastic joint robots." Transactions of the ASME: Journal of Dynamic Systems, Measurement, and Control, vol. 109, pp. 310–319, 1987. Cited on pages 23, 25, 26, 27, and 137.

[74] A. Jafari, N. G. Tsagarakis, and D. G. Caldwell, "A novel intrinsically energy efficient actuator with adjustable stiffness (AwAS)," IEEE Transactions on Mechatronics, vol. 18, no. 1, pp. 355 – 365, 2013. Cited on page 25.

[75] L. Le Tien, A. Albu-Schäffer, A. De Luca, and G. Hirzinger, "Friction observer and compensation for control of robots with joint torque measurement," in Proc. IEEE/RSJ Int. Conf. on Intelligent Robots and Systems. IEEE, 2008, pp. 3789 – 3795. Cited on page 28.

[76] S. Haddadin, F. Huber, and A. Albu-Schäffer, "Optimal control for exploiting the natural dynamics of variable stiffness robots," in Proc. IEEE Int. Conf. on Robotics and Automation, 2012, pp. 3347 – 3354. Cited on page 28.

[77] R. Findeisen, F. Allgöwer, and L. Biegler, Eds., Assessment and Future Directions of Nonlinear Model Predictive Control, ser. Lecture Notes in Control and Information Sciences. Springer Publishing Company, Berlin Heidelberg, 2007, vol. 358. Cited on page 28.

[78] B. Paden and R. Panja, "Globally asymptotically stable 'PD+' controller for robot manipulators," International Journal of Control, vol. 47, no. 6, pp. 1697–1712, 1988. Cited on pages 29, 98, and 100.

[79] A. Baehr, "Speed acquisition methods for high-bandwidth servo drives," Ph.D. dissertation, TU Darmstadt, 2004. Cited on page 29.

[80] F. Petit, M. Chalon, W. Friedl, M. Grebenstein, A. Albu-Schäffer, and G. Hirzinger, "Bidirectional antagonistic variable stiffness actuation: Analysis, design & implementation," in Proc. IEEE Int. Conf. on Robotics and Automation, 2010, pp. 4189–4196. Cited on page 30.

[81] F. Petit, W. Friedl, H. Höppner, and M. Grebenstein, "Analysis and synthesis of the bidirectional antagonistic variable stiffness mechanism," IEEE Transactions on Mechatronics, pp. 1–12, 2014. Cited on page 30.

[82] G. Tonietti and A. Bicchi, "Adaptive simultaneous position and stiffness control for a soft robot arm," Proc. IEEE Int. Conf. on Robotics and Automation, vol. 2, pp. 1992 – 1997, 2002. Cited on page 31.

[83] F. Szufnarowski and A. Schneider, "Compliant piezo-flex drives for muscle-like, antagonistic actuation of robot joints," in International Conference on Biomedical Robotics and Biomechatronics, 2010, pp. 381 – 388. Cited on page 31.

[84] K.-H. Nam, B.-S. Kim, and J.-B. Song, "Compliant actuation of parallel-type variable stiffness actuator based on antagonistic actuation," Journal of Mechanical Science and Technology, vol. 24, no. 11, pp. 2315–2321, 2010. Cited on page 31.

[85] S. A. Migliore, E. A. Brown, and S. P. DeWeerth, "Biologically inspired joint stiffness control," in Proc. IEEE/RSJ Int. Conf. on Intelligent Robots and Systems, 2005, pp. 4519–4524. Cited on pages 31 and 41.

[86] R. Shadmehr and M. A. Arbib, "A mathematical analysis of the force-stiffness characteristics of muscles in control of a single joint system," Biological Cybernetics, vol. 66, no. 6, pp. 463–477, 1992. Cited on pages 38 and 54.

[87] F. Zacharias, C. Borst, and G. Hirzinger, "Capturing robot workspace structure: Representing robot capabilities," in Proc. IEEE/RSJ Int. Conf. on Intelligent Robots and Systems, 2008, pp. 3229 – 3236. Cited on pages 40 and 65.

[88] W. Friedl, H. Höppner, F. Petit, and G. Hirzinger, "Wrist and forearm rotation of the dlr hand arm system: Mechanical design, shape analysis and experimental validation," in Proc. of the IEEE/RSJ Int. Conf. on Intelligent Robots and Systems, 2011, pp. 1836 – 1842. Cited on pages 41 and 44.

[89] H. V. Quy, L. Aryananda, F. Sheikh, F. Casanova, and R. Pfeifer, "A novel mechanism for varying stiffness via changing transmission angle," in Proc. IEEE Int. Conf. on Robotics and Automation, 2011, pp. 5076–5081. Cited on page 41.

[90] H. Höppner, W. Wiedmeyer, and P. van der Smagt, "A new biarticular joint mechanism to extend stiffness ranges," in Proc. IEEE Int. Conf. on Robotics and Automation, 2014, pp. 3403 – 3410. Cited on pages 49 and 66.

[91] M. Takegaki and S. Arimoto, "A new feedback method for dynamic control of manipulators," Journal of Dynamic Systems Measurement and Control, vol. 103, no. 2, pp. 119–125, 1981. Cited on page 55.

[92] R. Ortega and M. W. Spong, "Adaptive motion control of rigid robots: a tutorial," in 27th IEEE Conference on Decision and Control, vol. 2, 1988, pp. 1575 – 1584. Cited on page 55.

[93] P. Tomei, "A simple pd controller for robots with elastic joints," Automatic Control, IEEE Transactions on, vol. 36, no. 10, pp. 1208–1213, 1991. Cited on page 55.

[94] R. Ortega, M. W. Spong, F. Gomez-Estern, and G. Blankenstein, "Stabilization of a class of underactuated mechanical systems via interconnection and damping assignment," IEEE Transactions on automatic control, vol. 47, no. 8, pp. 1218–1233, 2002. Cited on page 55.

[95] A. De Luca, B. Siciliano, and L. Zollo, "Pd control with on-line gravity compensation for robots with elastic joints: Theory and experiments," Automatica, vol. 41, no. 10, pp. 1809–1819, 2005. Cited on pages 55 and 138.

[96] L. Zollo, B. Siciliano, A. De Luca, E. Guglielmelli, and P. Dario, "Compliance control for an anthropomorphic robot with elastic joints: Theory and experiments," Journal of Dynamic Systems, Measurement, and Control, vol. 127, pp. 321–328, 2005. Cited on pages 55 and 73.

[97] C. Ott, A. Albu-Schäffer, A. Kugi, and G. Hirzinger, "On the Passivity-Based Impedance Control of Flexible Joint Robots," IEEE Transactions on Robotics, vol. 24, no. 2, pp. 416–429, 2008. Cited on pages 55 and 60.

[98] A. Albu-Schäffer, C. Ott, and F. Petit, "Energy shaping control for a class of underactuated euler-lagrange systems," in 10th IFAC Symposium on Robot Control, 2012, pp. 567–575. Cited on pages 55, 56, and 57.

[99] J. Holterman, "Vibration control of high-precision machines with active structural elements," Ph.D. dissertation, University of Twente, 2002. Cited on page 56.

[100] F. Petit and A. Albu-Schäffer, "Cartesian impedance control for a variable stiffness robot arm," in Proc. of the IEEE/RSJ Int. Conf. on Intelligent Robots and Systems, 2011, pp. 4180–4186. Cited on page 62.

[101] J. Salisbury, "Active stiffness control of a manipulator in cartesian coordinates," in IEEE Conference on Decision and Control, 1980, pp. 95–100. Cited on page 63.

[102] S.-F. Chen and I. Kao, "Conservative congruence transformation for joint and cartesian stiffness matrices of robotic hands and fingers," The International Journal of Robotics Research, vol. 19, no. 9, pp. 835–847, 2000. Cited on page 63.

[103] A. Albu-Schäffer, M. Fischer, G. Schreiber, F. Schöppe, and G. Hirzingers, "Soft robotics: What cartesian stiffness can we obtain with passively compliant, uncoupled joints?" in Proc. IEEE/RSJ Int. Conf. on Intelligent Robots and Systems, vol. 4, 2004, pp. 3295 – 3301. Cited on pages 65 and 67.

[104] S. Boyd and L. Vandenberghe, Convex Optimization. Cambridge University Press, 2004. [Online]. Available: http://www.stanford.edu/~boyd/cvxbook/ Cited on page 75.

[105] A. Domahidi, E. Chu, and S. Boyd, "Ecos: An socp solver for embedded systems," in Control Conference (ECC), 2013 European, 2013, pp. 3071–3076. Cited on page 75.

[106] A. Björck, Numerical Methods for Least Squares Problems. SIAM, 1996. Cited on page 76.

[107] N. J. Higham, "Computing a nearest symmetric positive semidefinite matrix," in Linear Algebra and its Applications, vol. 103, 1998, p. 103–118. Cited on page 78.

[108] M. Laffranchi, N. G. Tsagarakis, and D. G. Caldwell, "Analysis and development of a semiactive damping system," IEEE Transactions on Mechatronics, vol. 18, no. 2, pp. 744 – 753, 2012. Cited on page 96.

[109] F. Saupe, "Linear parameter varying control design for industrial manipulators," Ph.D. dissertation, Technical University Hamburg-Harburg, 2012. Cited on page 96.

[110] J. S. Shamma and M. Athans, "Gain scheduling: Potential hazards and possible remedies," Control Systems, vol. 12, pp. 101 – 107, 1992. Cited on pages 97 and 129.

[111] F. Petit, A. Daasch, and A. Albu-Schäffer, "Backstepping control of variable stiffness robots," IEEE Transactions on control system technology, 2014. Cited on page 97.

[112] F. Petit and A. Albu-Schäffer, "State feedback damping control for a multi dof variable stiffness robot arm," in Proc. IEEE Int. Conf. on Robotics and Automation, 2011, p. 5561–5567. Cited on page 97.

[113] F. Petit, Christian Ott, and A. Albu-Schäffer, "A model-free approach to achieve damping via vibration suppression for intrinsically elastic robots," in IEEE Int. Conf. on Robotics and Automation, 2014, pp. 2176 – 2182. Cited on pages 97 and 122.

[114] H. K. Khalil, Nonlinear systems, 3rd ed. Upper Saddle River, NJ, USA: Prentice Hall, 2002. Cited on pages 97, 103, 104, 138, and 139.

[115] J. H. Oh and J. S. Lee, "Control of flexible joint robot system by backstepping design approach," in Proc. IEEE Int. Conf. on Robotics and Automation, vol. 4, 1997, p. 3435–3440. Cited on page 97.

[116] J. Oh and J. Lee, "Backstepping control design of flexible joint manipulator using only position measurements," IEEE Conference on Decision and Control, vol. 1, pp. 931 – 936, 1998. Cited on page 97.

[117] D. Koditschek, "Natural motion for robot arms," in Proc. IEEE Conf. on Decision and Control, vol. 23, 1984, pp. 733 –735. Cited on page 98.

[118] J. A. Farrell, M. Polycarpou, M. Sharma, and W. Dong, "Command filtered backstepping," IEEE Transactions on Automatic Control, vol. 54, no. 6, pp. 1391–1395, 2009. Cited on pages 100 and 103.

[119] J. J. Craig, Introduction to Robotics: Mechanics and Control, 2nd ed. Boston, MA, USA: Addison-Wesley Longman Publishing Co., Inc., 1989. Cited on page 134.

[120] M. Uemura and S. Kawamura, "Resonance-based motion control method for mulit-joint robot through combining stiffness adaptation and iterative learning control," in Proc. IEEE Int. Conf. on Robotics and Automation, 2009, pp. 1543 – 1548. Cited on page 135.

[121] M. Uemura, H. Goya, and S. Kawamura, "Motion control with stiffness adaptation for torque minimization in multijoint robots," IEEE Transactions on Robotics, vol. 30, no. 2, pp. 352–364, 2014. Cited on page 135.

[122] F. Petit, D. Lakatos, W. Friedl, and A. Albu-Schäffer, "Dynamic trajectory generation for serial elastic actuated robots," in 10th IFAC Symposium on Robot Control, 2012, pp. 636–643. Cited on page 135.

[123] A. Albu-Schäffer and G. Hirzinger, "State feedback controller for flexible joint robots: a globally stable approach implemented on dlr's light-weight robots," in Proc. IEEE/RSJ Int. Conf. on Intelligent Robots and Systems, vol. 2, 2000, pp. 1087–1093. Cited on page 138.

[124] A. K. Banerjee and W. E. Singhose, "Command shaping in tracking control of a two-link flexible robot," Journal of Guidance, Control, and Dynamics, vol. 21, pp. 1012–1015, 1998. Cited on page 142.

[125] D. Lakatos, G. Garofalo, F. Petit, C. Ott, and A. Albu-Schäffer, "Modal limit cycle control for variable stiffness actuated robots," in Proc. IEEE Int. Conf. on Robotics and Automation, 2013, pp. 4934 – 4941. Cited on page 142.

[126] D. Lakatos, F. Petit, and A. Albu-Schäffer, "Nonlinear oscillations for cyclic movements in variable impedance actuated robotic arms," in Proc. IEEE Int. Conf. on Robotics and Automation, 2013, pp. 508–515. Cited on page 142.

[127] D. Lakatos, M. Görner, F. Petit, A. Dietrich, and A. Albu-Schäffer, "A modally adaptive control for multi-contact cyclic motions in compliantly actuated robotic systems," in Proc. IEEE/RSJ Int. Conf. on Intelligent Robots and Systems, 2013, pp. 5388–5395. Cited on page 142.